Ultrasound-based Motion Modelling for the Lungs in Scanned Proton Therapy

Inaugural dissertation

to
be awarded the degree of

Dr. sc. med.

presented at
the Faculty of Medicine
of the University of Basel

by
Alina Giger
from Niedergösgen, Switzerland

Basel, 2021

Approved by the Faculty of Medicine
on application of

Prof. Dr. Philippe C. Cattin, University of Basel – *primary advisor*
Prof. Dr. Antony J. Lomax, Paul Scherrer Institute – *secondary advisor*
Prof. Dr. Orçun Göksel, ETH Zurich – *external expert*
Dr. Christoph Jud, University of Basel – *further advisor*

Basel, the 2nd of November 2020

Prof. Dr. Primo Schär
Dean

To my parents
Gianna & Stefan.
For their endless love and support.

Contents

Acronyms

3D CRT three-dimensional conformal radiotherapy. 10–12

4D CBCT respiratory-correlated CBCT. 16, 26

4D CT respiratory-correlated CT. 16–20, 26, 27, 34

4D CT(MRI) synthetic time-resolved 4D CT. 28

4D MRI time-resolved volumetric MRI. xv, 3, 4, 18, 20, 22, 26–28, 35, 55, 65, 79, 119, 120

ABC active breath control. 18, 22

ADC adenocarcinoma. 5, 6

AJCC American Joint Committee on Cancer. 5

AP anterior-posterior. 16

AR autoregressive. 34, 120

BEV beam's-eye-view. 23

CAiM Computer-assisted Applications in Medicine. xii, 122

CBCT cone-beam CT. 15, 24

cGAN conditional generative adversarial network. xv, 33, 55

CIAN Center for medical Image Analysis & Navigation. xii, 4

CLUST Challenge on Liver Ultrasound Tracking. 29

CT computed tomography. xv, 3, 7, 15, 19, 22, 23, 26, 28, 79, 119

CTV clinical target volume. 18

DIR deformable image registration. 29, 30, 121

DVF deformation vector field. 29, 55, 119–121

EMTS electromagnetic tracking system. 22

FM fiducial markers. 22, 23

GP Gaussian process. 32

GPR Gaussian process regression. xv, 4, 30, 32, 79, 99, 119, 120, 122

GRNN generalised regression neural network. 33

GSI GSI Helmholtz Centre for Heavy Ion Research. 20, 24

HIFU high intensity focused ultrasound. 24

HIMAC Heavy Ion Medical Accelerator in Chiba. 22

IASLC International Association for the Study of Lung Cancer. 5

ICRU International Commission on Radiation Units & Measurements. 18

IGRT image-guided radiation therapy. 21

IMPT intensity modulated proton therapy. 12, 13, 18

IMRT intensity modulated radiation therapy. 10–13, 17

ITV internal target volume. 18, 19

LCLC large-cell lung carcinoma. 5

Linac linear accelerator. 20

LR left-right. 16

MICCAI the International Conference on Medical Image Computing and Computer Assisted Intervention. 29, 55, 65

MR magnetic resonance. xi, xii, xv, 3, 28, 33, 35, 55, 122

MR-linac magnetic resonance linear accelerator. 23, 26

MRgHIFU magnetic resonance guided high intensity focused ultrasound. 3

MRI magnetic resonance imaging. xi, xv, 3, 4, 16, 23–28, 119

NSCLC non-small cell lung carcinoma. 5, 6, 8, 9, 11–14, 17

OAR organs at risk. 1, 10, 12, 13, 21

OLS ordinary least squares. 31

OTS optical tracking system. 22, 28

PBS pencil beam scanning. 3, 4, 12, 13, 15, 17–20, 22, 23, 25, 28, 29, 32, 34, 79, 119, 122

PCA principal component analysis. 29, 30, 79, 121

PSI Paul Scherrer Institute. xi–xiii, 4, 13, 19, 20, 23, 28, 34, 79, 99

PSPT passively scattered proton therapy. 12, 13, 20

PTCOG Particle Therapy Co-Operative Group. 9, 18

RBF radial basis function. 32

RNN recurrent neural network. 33

ROI region of interest. 29

RTOG Radiation Therapy Oncology Group. 12, 14

SABR stereotactic ablative radiation therapy. 10, 11, 16

SBRT stereotactic body radiation therapy. 11

SCLC small cell lung carcinoma. 5, 6, 8, 9

SEER Surveillance, Epidemiology, and End Results. 5, 11

SFUD single-field uniform dose. 13, 18

SI superior-inferior. 16, 24, 121

SNR signal-to-noise ratio. 29

SNSF Swiss National Science Foundation. xiii, 4

SOBP spread-out Bragg peak. 12

SqCC squamous cell carcinoma. 5, 6

SVD singular value decomposition. 30

UICC Union for International Cancer Control. 5

US ultrasound. xi, xii, 2–4, 23, 24, 27–31, 33, 35, 55, 65, 79, 119–122

US-4DMRI ultrasound-based 4D MRI. 35

VATS video-assisted thoracoscopic surgery. 8

WEPL water-equivalent pathlength. 17

WHO World Health Organization. 7

Acknowledgements

First and foremost my gratitude goes to Prof. Dr. Philippe Cattin for providing me with the opportunity to pursue my doctoral studies on this interesting and exciting project. Despite being a very sought-after person, his door was always open and his willingness to lend an ear when needed unchanged. His insightful pieces of advice and our constructive discussions were indispensable for successfully completing this project. In that regard, I further extend my thanks to Dr. Christoph Jud, advisor and colleague, for his continuous support, advice, and motivation, and our countless inspiring discussions concerning technical challenges and beyond. He answered all my questions in detail, with great expertise and patience.

This project being inherently multi-disciplinary would not have been possible without the support and expertise of many project partners from a broad variety of institutions and research fields. I am particularly indebted to my project partners at the Paul Scherrer Institute (PSI) in Villigen, Switzerland, namely Prof. Dr. Tony Lomax, Dr. Miriam Krieger, and Dr. Ye Zhang. The close collaboration, especially towards the end of the project, was a deeply inspiring and instructive experience. The numerous meetings and fruitful discussions provided insight into the field of proton therapy and broadened my understanding of the overall project. Special thanks go to Dr. Miriam Krieger for her invaluable contributions during data acquisition and the integration of our motion model into the dose calculation and tumour tracking simulations. Having her as project partner has made work a great pleasure – from our first encounter in Groningen to the end of this project and hopefully beyond. I further thank Prof. Dr. Tony Lomax for his support and advice as second supervisor.

The data acquisition was only possible thanks to Prof. Dr. Rares Salomir and his team, especially Pauline Guillemin, from the Image Guided Interventions Laboratory at the University of Geneva. I owe them my gratitude for providing the knowledge and facility for simultaneous US/MRI acquisitions, and their willingness and time to perform experiments late into the night. Moreover, this work is based on MRI sequences which were developed by Prof. Dr. Oliver Bieri and his team of the Magnetic Resonance Physics and Methodology Group (MRPM) at the University of Basel. In particular, I am grateful to Dr. Damien Nguyen, Dr. Grzegorz Bauman, and Dr. Zarko Celicanin for developing and adapting the MRI sequences according to our needs, and Dr. Francesco Santini and Dr. Orso Pusterla for their unceasing support regarding the integration of our MR-compatible US probe within the experimental setup.

This US probe was developed at the Fraunhofer IBMT, Sulzbach, Germany, by Christian Degel and Daniel Speicher. I am deeply indebted to Bruno Sempéré, former software developer at Fukuda Denshi, Basel, Switzerland, and thereafter scientific developer in our group, for

sharing his deep knowledge in the field of US imaging, his thorough explanations of the US system, his support with the formulation of the technical specifications for our US probe, and his assistance and time spent with parameter tuning and safety evaluation of this probe. I further extend my gratitude to Dieter Schweizer, former director of Fukuda Denshi, Basel, Switzerland, for providing the necessary documents and electronic parts for our newly developed US probe and his generosity for providing additional components. We thank Prof. Dr. Orçun Göksel and Dieter Schweizer from the Computer-assisted Applications in Medicine (CAiM) Group at ETH Zurich, Switzerland, for the opportunity to perform the required safety tests of our probe using their acoustic measurement bench and additional test equipment. I further thank Prof. Dr. Orçun Göksel for agreeing to be my external examiner and for reviewing this thesis.

With the arrival of our MR-compatible US probe, the process of integrating it within our experimental setup was not at all straightforward but rather we have faced system synchronisation issues and image artefacts. I am sincerely grateful for the help of many more people who assisted us in this endeavour, namely: Domenico Ferrara from Fukuda Denshi and CAiM, for his assistance during the electromagnetic and thermal safety tests; Lina Marcela Beltran Bernal from the University of Basel for providing the equipment for thermal imaging; Dr. Flavio Carinci, Dr. Pablo Fernandez Carmona, Gilles Martin, Marco Menghini, and Roman Kaminski from PSI for their contributions towards system synchronisation and image artefact reduction; Orane Lorton from the University of Geneva for providing the plans for the 3D printed US holder; Florian Spiess from the Unversity of Basel for developing image processing algorithms to eliminate the remaining stripe artefacts within the US images. I further extend my gratitude to Dr. Emma Colvill and Dr. Marta Peroni for their assistance during data acquisition in general, and to Alisha Dütschler for her support with image processing, all from PSI.

Moreover, my warm thanks go to my former and current colleagues of CIAN. I am especially thankful to Dr. Simon Pezold for reviewing and criticising many of my paper drafts and in general for shaping my view of good scientific practice; Dr. Robin Sandkühler for his valuable support with image registration and for sharing his excellent programming skills; Marek Zelechowski for organising numerous after-work pints and for strengthening social bonds within the group; and Dr. Frank Preiswerk for laying the foundations of this work with his excellent preceding PhD project. Special thanks belong to my fellow students and colleagues who have turned my doctoral studies into a wonderful and memorable adventure, from CIAN: Dr. Adrian Schneider, Dr. Antal Horváth, Balázs Faludi, Bruno Sempéré, Carlo Seppi, Dr. Christoph Jud, Eva Schnider, Florentin Bieder, Dr. Frank Preiswerk, Jörg Wagner, Julia Wolleb, Karim Ayadi, Dr. Lilian Witthauer, Lorenzo Iafolla, Marek Zelechowski, Massimiliano Filipozzi, Dr. Nadia Möri, Dr. Natalia Chicherova, Negin Sahraei, Norbert Zentai, Peter von Niederhäusern, Philippe Valmaggia, Dr. Robin Sandkühler, Samaneh Manavi, Dr. Sara Freund, Dr. Simon Andermatt, Dr. Simon Pezold, Dr. Stephan Wyder, Tiziano Ronchetti, Dr. Uri Nahum; and beyond: Esther Zoller, Griffin Rodgers, Dr. Kyung-won Baek, Ludovic Amruthalingam, Maksym Yushchenko, Manuela Eugster, Dr. Marzia Buscema, Prof. Dr. Mathieu Sarracanie, Dr. Matthias Weigel, Mohammad Khair Nahhas, Prof. Dr. Najat Salameh, Po-Jui Lu, Dr. Reinhard Wendler, and Dr. Sylvia Nyilas. I further extend my thanks to the current and former members of the technical and administrative support team, namely Aydin Ürgen, Dr. Beat Fasel, Corinne Eymann-Baier, Dr. Daniela Vavrecka-Sidler, Dr. Gabriela Oser Duss, Hannah Heissler, and Patrick Mayrock.

Finally, my deep gratitude belongs to my family, especially my parents Gianna and Stefan and my siblings Laura and Nicolas, for their constant support beyond work; to my beloved partner Mathias for his unconditional love, reassurance, humour, and above all for his critical mind and eagerness to learn; and to all my friends.

The overall project was financially supported by the Swiss National Science Foundation (SNSF) and conducted under the lead of Prof. Dr. Damien Charles Weber from PSI.

Summary

Respiratory motion poses a major challenge in image acquisition and image-guided interventions of thoracic and abdominal organs, such as the liver or lungs. In the field of radiotherapy, accurate knowledge of the organ motion is essential for precise radiation of the target volume while sparing surrounding healthy tissue and organs at risk. In this thesis, we present different tools and methods towards ultrasound-guided lung tumour tracking in scanned proton therapy with the main focus on respiratory motion modelling.

We start off with introducing an ultrasound-based 4D magnetic resonance imaging (4D MRI) method for which simultaneously acquired ultrasound and partial MRI data is used to retrospectively reconstruct a time-resolved volumetric MR image. In the following, different motion modelling approaches are presented where 2D abdominal ultrasound images serve as a surrogate signal to predict complete lung motion information. First, we propose a novel approach based on a conditional generative adversarial network (cGAN) in conjunction with a state-of-the-art navigator-based 4D MRI. Second, we investigate the performance of a polynomial regression model when subject to ultrasound probe repositioning as required for fractionated treatments. Third, we propose a motion model based on Gaussian process regression (GPR) and analyse the impact of prediction errors on proton dose distributions with and without tumour tracking. All of these studies are based on simultaneously acquired ultrasound and 4D MRI data sets of two to eight healthy volunteers. For the dosimetric analysis, the motion patterns extracted from 4D MRI of healthy volunteers were combined with computed tomography (CT) scans of two lung cancer patients.

In general, the mean or median prediction error was found to be below $3\,\mathrm{mm}$ for intra-fractional motion modelling. Moreover, motion predictions based on GPR were shown to translate into clinically acceptable dose distributions, emphasising the great potential of ultrasound-guidance for motion mitigation in scanned proton therapy. From a treatment point of view, however, the dosimetric benefits of tumour tracking were found to be limited. Tumour tracking alone may not always be sufficient to restore clinically acceptable dose distributions and should be combined with other motion mitigation techniques such as rescanning.

Zusammenfassung

Die Atembewegung stellt eine grosse Herausforderung dar sowohl bei der Bildgebung als auch bei bildgeführten Eingriffen an Brust- und Bauchorganen, wie zum Beispiel der Leber oder der Lunge. In der Strahlentherapie sind genaue Kenntnisse der Organbewegung unerlässlich für eine präzise Bestrahlung des Zielvolumens bei gleichzeitiger Schonung des umliegenden gesunden Gewebes und gefährdeter Organe. In dieser Arbeit stellen wir verschiedene Methoden vor, um die Atembewegung der Lunge anhand von Ultraschallbilder der Leber zu schätzen. Ziel ist es, diese Bewegungsmodelle in der Protonentherapie anzuwenden, sodass der Protonenstrahl dem Tumour folgen kann.

Die Arbeit beginnt mit der Einführung einer neuen Methode für die sogenannte 4D Magnetresonanztomographie (4D-MRT). Dazu werden gleichzeitig erfasste Ultraschallbilder und unvollständige MRT-Daten für die Rekonstruktion eines zeitaufgelösten volumetrischen MRT-Bildes verwendet. Im Folgenden werden verschiedene Bewegungsmodelle präsentiert, bei denen 2D-Ultraschallbilder des Abdomens als Hilfssignal dienen, um die vollständige Lungenbewegung zu schätzen. In einem ersten Schritt stellen wir einen Ansatz vor, der ein neuronales Netzwerk, das sogenannte cGAN, mit einer anerkannten Methode für die 4D-MRT kombiniert. Im zweiten Schritt untersuchen wir ein polynomiales Regressionsmodell für den Spezialfall, wenn die Ultraschallsonde neu positioniert werden muss. Dies ist insbesondere dann erforderlich, wenn die Gesamtdosis auf kleinere Einzeldosen aufgeteilt wird und das Bewegungsmodell folglich über mehrere Tage angewendet wird. Im dritten Schritt schlagen wir ein Bewegungsmodell vor, welches auf einer Gaussprozessregression (GPR) basiert. Wir analysieren die Auswirkungen von den erhaltenen Bewegungsschätzungen auf die Protonendosisverteilungen sowohl mit als auch ohne Tumortracking. Alle Studien basieren auf gleichzeitig aufgenommenen Ultraschall- und 4D-MRT-Datensätzen von zwei bis acht gesunden Freiwilligen. Für die dosimetrische Analyse wurden die aus diesen 4D-MRT extrahierten Bewegungsmuster mit den Computertomographieaufnahmen (CT-Aufnahmen) von zwei Lungenkrebspatienten kombiniert.

Der mittlere Vorhersagefehler lag im Allgemeinen unter $3\,\mathrm{mm}$ ohne Neupositionierung der Ultraschallsonde. Darüber hinaus zeigte sich, dass die Bewegungsschätzungen auf der Basis der GPR zu klinisch akzeptablen Dosisverteilungen führten. Dies unterstreicht das grosse Potenzial der ultraschallbasierten Bewegungmodelle für die Protonentherapie. Die Analyse der Dosisverteilung deutete jedoch auch darauf hin, dass das Tumortracking nur begrenzten Nutzen bringt. Tumortracking allein reicht möglicherweise nicht immer aus, um klinisch akzeptable Dosisverteilungen zu erzielen und sollte daher mit anderen Techniken, wie z.B. dem sogenannten Rescanning, kombiniert werden.

Chapter 1

Introduction

Lung cancer is the most frequently diagnosed cancer and the leading cause of cancer death worldwide. An estimated two million new cases and 1.8 million deaths in 2018 were reported by the International Agency for Research on Cancer (IARC) [26, 71]. The need for early detection and effective treatment strategies is evident and, consequently, much research is conducted to reduce the heavy burden of lung cancer.

1.1 Motivation

Lung cancer is not only the most common cancer worldwide, with a 5-year relative survival rate of $20.5\,\%$ as of 2016 in the United States, it also is one of the most aggressive forms of human cancer [111]. Depending on cancer type and stage, the 5-year overall survival rate greatly varies and so does the treatment of choice. Radiotherapy is one of the three main treatment approaches besides surgery and chemotherapy [186, 234]. Within the field of radiotherapy, there are different types of radiation including, among others, photon beams and proton beams.

In contrast to conventional radiotherapy beams based on photons, proton beams have a locally confined penetration depth at which a large amount of energy is deposited. The significant rise in dose observed at the characteristic depth is called Bragg peak [171, 292]. While the tissue in the beam path proximal to the Bragg peak receives a small dose, beyond the Bragg peak the dose drops to zero within millimetres [171]. By modulating the Bragg peak, high radiation dose can be deposited within the tumour volume while significantly reducing the radiation dose to surrounding normal tissue and organs at risk (OAR) when compared to photon beams. Conformal dose distribution is especially important for radiotherapy in the thorax, containing critical and sensitive structures such as the heart, oesophagus, spinal cord, or normal lung tissue [146]. As such, proton therapy bears the potential to significantly improve lung cancer treatment as first studies suggest [31, 37, 197].

However, physiological organ motion – mainly induced by respiration or the cardiac cycle – hampers the clinical application of abdominal and thoracic proton therapy [145, 276]. In many aspects, organ motion transforms the problem formulations and the questions of interest from three dimensions to four with the fourth dimension being time. This gave rise to interesting but challenging research fields, such as time-resolved imaging or 4D imaging [113, 263], 4D dose

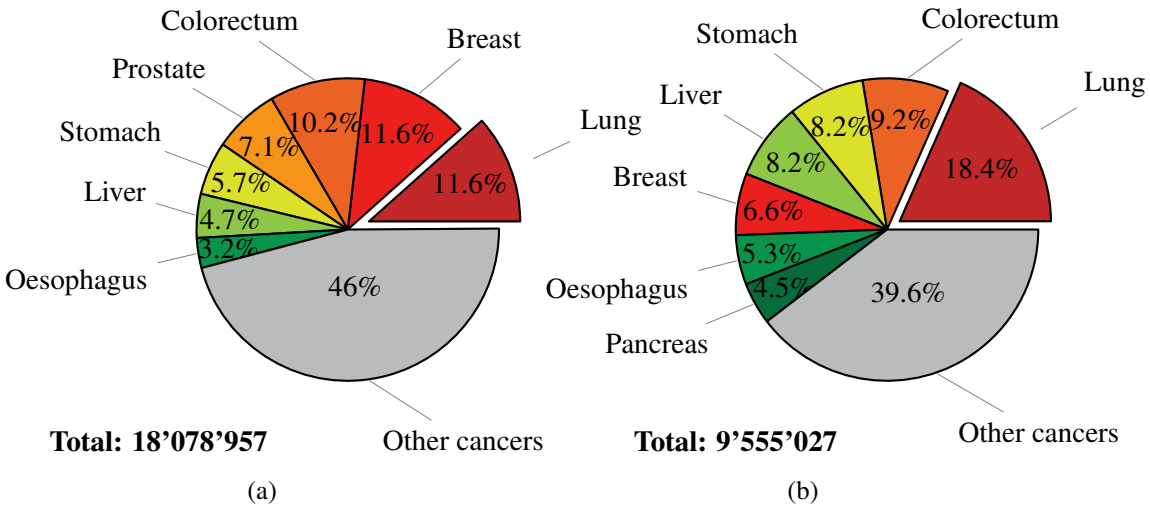

Figure 1.1: Estimated number of (a) new cases, and (b) deaths in 2018 worldwide. The data for this plot was retrieved from [26, 71] and is further available online [72].

calculations [229], and motion modelling [181]. As an additional complication, the physiological motion is not perfectly periodic but rather varies from cycle to cycle, from day to day, and of course from patient to patient [138, 285, 286].

It is thus crucial to mitigate the effects of organ motion in general and respiratory motion in particular for radiotherapy of lung tumours. Possible approaches include breath holding, gating, and tumour tracking [143, 225]. In most cases, some sort of surrogate signal is required in order to identify the respiratory state of the patient. On the one hand, external signals such as respiratory belts, spirometry, or optical surface markers are used [19, 181]. However, it has been shown that the correlation between external signals and internal organ motion may be poor, mainly for two reasons: time-varying phase shifts between the external signal and the internal motion [107], and organ drift [268, 285, 286]. On the other hand, image-based surrogate signals or implanted electromagnetic transponders provide internal information. These approaches, however, are typically invasive in the sense that markers need to be implanted, or the patient is exposed to additional radiation dose [19]. This motivates our research on the use of abdominal ultrasound (US) imaging as respiratory motion surrogate for lung motion prediction: US imaging is non-invasive, non-ionising, relatively inexpensive, and further provides internal organ motion information at a high temporal resolution [73, 205]. Above all, diaphragm motion – clearly visible on abdominal US imaging – is a suitable surrogate for lung tumour motion [35].

1.2 Contribution

Within the scope of this project, we investigate the use of abdominal US imaging for respiratory motion modelling in proton therapy. This work succeeds two closely related projects performed in our group [3, 217]. Although the projects share some common objectives and characteristics, they differ in various key aspects: the target organ, the surrogate signal, and the characteristics of

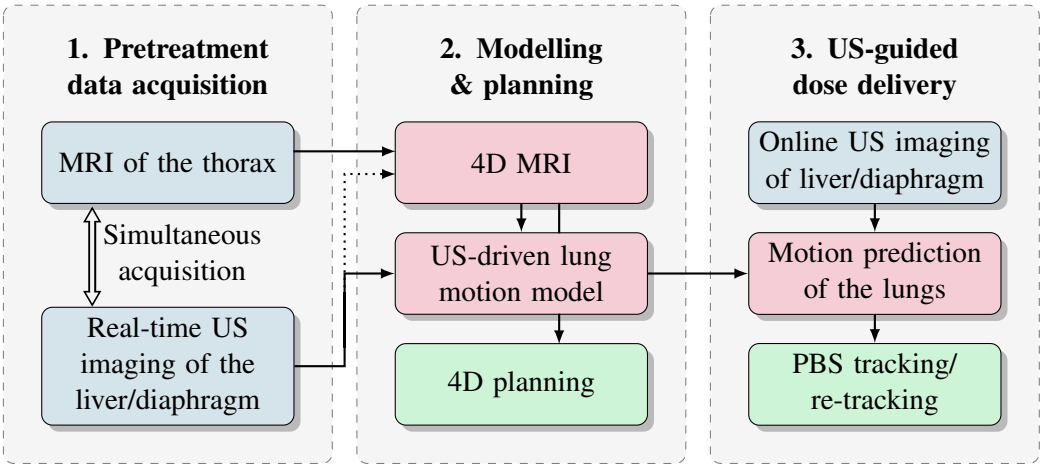

Figure 1.2: Schematics of the overall project. Project parts related to data acquisition are shown in blue, those related to treatment planning and dose delivery are shown in green, while image processing and motion modelling are shown in red.

the motion models. The first project investigated the use of both population-based and patient-specific motion models for the application in magnetic resonance guided high intensity focused ultrasound (MRgHIFU) ablation of liver tumours [3]. Contrary to the present project, the respiratory surrogate was extracted from the magnetic resonance (MR) images directly which to date is not available during proton therapy. The second project proposed population-based statistical motion models for the liver based on abdominal US imaging as a surrogate [217, 219]. In contrast, the goal of the current project is to develop patient-specific motion models for the lungs. Given the limited penetration depth of US waves in air [73, 205], lung tumours cannot be tracked directly – the motion needs to be predicted.

The general approach presented in this work is split into three major parts as shown in Figure 1.2. In a pretreatment phase simultaneous abdominal US and thoracic magnetic resonance imaging (MRI) data sets are acquired in order to ensure temporal correspondence between the two imaging modalities. Based on this data a patient-specific time-resolved volumetric MRI (4D MRI) is retrospectively reconstructed. The 4D MRI and the US-based surrogate signal form the basis for respiratory motion modelling. Moreover, motion information extracted from the 4D MRI together with a corresponding computed tomography (CT) scan may be further used for 4D treatment planning [154, 155]. During dose delivery, online US imaging in combination with the US-driven respiratory motion model may eventually allow for real-time tumour tracking in pencil beam scanning (PBS) proton therapy. The treatment dose is typically delivered in multiple small fractions over a duration of several days [171, 207]. Following the workflow in Figure 1.2, we can summarise the contributions of this work as follows:

- In collaboration with our project partners, we acquired hybrid abdominal US and thoracic 4D MRI data sets of several volunteers which form the basis for the succeeding studies.
- We propose a US-driven 4D MRI allowing for reduced acquisition times and increased

temporal resolution when compared to state-of-the-art navigator-based approaches.

- We investigate different types of respiratory motion models using US-based surrogate signals as input in order to predict dense motion estimates of the thorax.
- US probe repositioning is a prerequisite for a fractionated treatment. In a feasibility study, we assess the impact of US probe repositioning on the prediction accuracy.
- In a joint effort, we evaluate the effects of the presented respiratory motion model on 4D dose distributions in PBS proton therapy and tumour tracking.

This work is part of a joint project between the Center for medical Image Analysis & Navigation (CIAN) at the University of Basel, the Centre for Proton Therapy at the Paul Scherrer Institute (PSI), the Radiological Physics groups at the University Hospitals of Basel and Geneva, and the Department of Radiation Oncology at University Hospital Zurich. It is funded by the Swiss National Science Foundation (SNSF)[1]. The MRI sequences used within the scope of this project were developed at the University Hospital Basel while the data acquisition was predominantly conducted at Geneva University Hospitals. Our project partners at PSI were focusing on treatment planning and dose validation strategies. The findings thereof are described in a separate dissertation [153], although some overlap with the results presented here is evident. The work presented here covers the 4D imaging and motion modelling aspects of the overall project. Our aim is to develop 4D MRI methods and patient-specific respiratory motion models which are tailored towards lung tumour tracking in scanned proton therapy. However, the proposed approaches could be easily transferred to conventional radiotherapy.

1.3 Outline

The remainder of this thesis starts with non-exhaustive literature reviews in Chapters 2 and 3. First, an overview about the medical background of lung cancer, its symptoms and treatment strategies is given in Chapter 2, followed by a characterisation of organ motion, a description of its implications on proton therapy, and possible motion management strategies in Chapter 3. In Chapter 4 the problem formulation is concretised and a broad overview about respiratory motion models is provided. Subsequently, research publications emerging from this project are presented in Chapters 5 to 9. Chapter 5 presents a US-driven 4D MRI method. In Chapter 6 a novel approach to respiratory motion modelling based on deep learning is proposed within the scope of a proof-of-concept study. Chapter 7 investigates the performance of a polynomial regression model subject to US probe repositioning. In Chapter 8 and Chapter 9 a Gaussian process regression (GPR) model is integrated into extensive simulation studies with the aim to investigate the effects of residual motion prediction errors on 4D dose distributions in the lungs in general and within the context of tumour tracking in particular. Chapter 10 concludes this thesis with an overall discussion of the findings, current limitations and possible future developments.

[1]Grant number: 320030_163330/1. Available online at: http://p3.snf.ch/Default.aspx?query=320030_163330, accessed 12 February 2020.

Chapter 2

Medical Background

While lung cancer is the commonly used term when referring to tumours located in the lungs, it describes a complex and heterogeneous group of diseases. In this chapter, we provide a brief introduction to the medical context of the thesis including lung cancer types, causes and symptoms, possible treatment strategies in general, and radiotherapy in particular. Some of the statistical data presented in this chapter are retrieved from the Surveillance, Epidemiology, and End Results (SEER) Program which collects epidemiologic data for the population of the USA [111]. It is noted specifically if the numbers are reported for the USA only.

2.1 Lung cancer

2.1.1 Types

Two major types of lung cancer are distinguished based mainly on histological classification and therapeutic implications; small cell lung carcinoma (SCLC) and non-small cell lung carcinoma (NSCLC). The group of NSCLC is further divided into histological subtypes among which the most important ones are adenocarcinoma (ADC), squamous cell carcinoma (SqCC), and large-cell lung carcinoma (LCLC). Conversely, SCLC forms a group of its own and is generally known to be more aggressive as it tends to spread more rapidly [14]. With the advent of targeted therapy and immunotherapy, further subtyping on a molecular basis has become increasingly important [203, 228].

2.1.2 Staging

The progress of the disease is generally classified according to a standardised cancer staging system as proposed by the International Association for the Study of Lung Cancer (IASLC) Staging Project[1] and implemented by the Union for International Cancer Control (UICC)[2] and the American Joint Committee on Cancer (AJCC)[3]. This staging system is internationally accepted and

[1] Available online at: https://www.iaslc.org/Research-Education/IASLC-Staging-Project, accessed 14 February 2020.

[2] Available online at: https://www.uicc.org/resources/tnm, accessed 14 February 2020.

[3] Available online at: https://www.cancerstaging.org, accessed 14 February 2020.

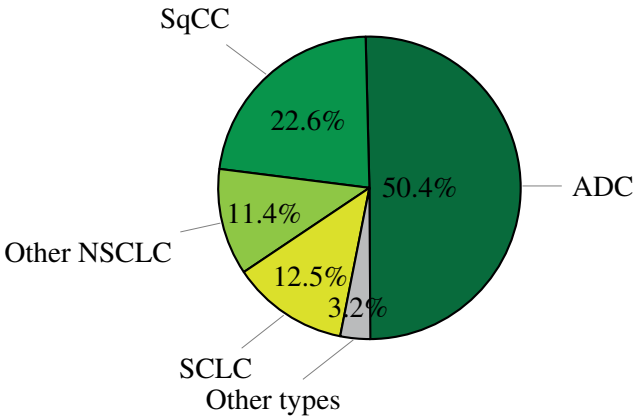

Figure 2.1: Lung cancer: incidence of histological subtypes in the USA as of 2017. The data for this plot was retrieved from [111].

referred to as the TNM classification system where *T* describes the primary tumour site and size, *N* the regional lymph node involvement, and *M* the presence and extent of metastasis [27]. Each descriptor is further divided into numbered categories where in general higher numbers reflect a more advanced stage of the disease.

Given the stage descriptors, stage groups can be assigned ranging from stage IA1 to stage IVB with increasing severity [80]. A similar system is applied for staging in SCLC [198]. Besides histological classification, staging is the most important prognostic factor for recurrence rate and survival times, and decisively shapes the treatment strategy [294].

2.1.3 Epidemiology

Incidence NSCLC accounts for more than $80\,\%$ of all lung cancer cases in the USA among which ADC is the most common subtype with $50.4\,\%$, followed by SqCC with $22.6\,\%$; SCLC ranks third with $12.5\,\%$ of all lung cancer in the USA as shown in Figure 2.1 [111].

Survival Patients diagnosed with clinical stage IA1 NSCLC have a 5-year overall survival chance of $92\,\%$. This number drastically decreases to $60\,\%$ for clinical stage IIA, $36\,\%$ for clinical stage IIIA, and $10\,\%$ for clinical stage IVA [80]. If the cancer is diagnosed at the latest stage, the median survival time is 6 months only and patients are not expected to survive the next five years at all [80]. For SCLC the 5-year overall survival ranges similarly from $93\,\%$ for clinical stage IA1 to $8\,\%$ for clinical stage IV [198].

Although chances of survival are high if the cancer is detected in early stages, the 5-year age-standardised survival rate remains low, for developed and developing regions alike, ranging from $10\,\%$ to $20\,\%$ [2]. The main reason for the poor survival rates of lung cancer is the usually late detection of the disease. Associated symptoms, such as coughing and dyspnea, often only manifest when the cancer has already spread. In only $17\,\%$ of the cases, the lung cancer was diagnosed when it was still confined to the primary site, while for a majority of all patients the

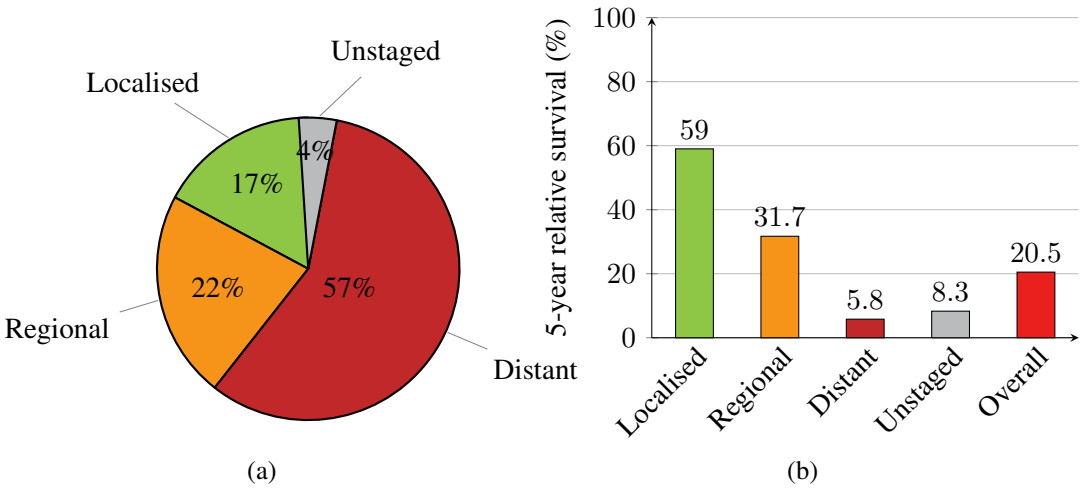

Figure 2.2: (a) Stage distribution at diagnosis and (b) the corresponding 5-year relative survival rate in the USA as of 2016. The data for this plot was retrieved from [111].

disease has spread to distant sites by the time it is diagnosed [111]. As a result, early detection of lung cancer is an active field of research mainly focusing on low-dose CT screening and the development and use of biomarkers [93, 98, 270].

2.1.4 Etiology

The single most important cause of lung cancer is tobacco smoking with tobacco smoke containing at least 69 carcinogens [194]. According to the World Health Organization (WHO), $80\,\%$ to $85\,\%$ of lung cancer cases worldwide are associated with tobacco smoking [289]. With the decline of smoking prevalence in high-income countries, age-adjusted incidence and mortality rates of lung cancer have decreased on average by $2.2\,\%$ and $3.3\,\%$, respectively, each year over the last 10 years in the USA [111].

In the latest version of the World Cancer Report the WHO lists 29 further carcinogens known to cause lung cancer among which are asbestos, silica, several heavy metals, and radon [289]. Furthermore, both indoor and outdoor air pollution have been classified as lung carcinogens with increasing importance in never-smokers. Indoor air pollution is primarily caused by household combustion of coal and wood for cooking and heating in poorly ventilated homes and predominantly found in rural areas [295]. Among outdoor air pollutants, the WHO specifically names diesel engine exhaust as a human carcinogen.

2.1.5 Symptoms

The burden of lung-cancer symptoms in advanced stage patients is high, substantially impairing their quality of life [121, 254]. Among symptoms related to primary lung cancer are cough, shortness of breath (dyspnea), blood in sputum (hemoptysis), and chest discomfort. In advanced lung cancer patients also symptoms associated with intrathoracic or extrathoracic spread are

reported. These are for example chest and bone pain, fatigue, depression, nausea, and vomiting [11, 30, 48, 121, 287]. In a study based on survey data from 2411 lung cancer patients, more than $98\,\%$ of the patients reported at least one symptom regardless of the stage; moderate-to-severe symptoms were experienced by $65.7\,\%$ and $73.5\,\%$ for early stage and late stage lung cancer patients, respectively [287]. Given the high prevalence and burden of symptoms, palliative care and symptom management is considered crucial throughout the course of treatment [254, 287].

2.2 Treatment

The three mainstays of lung cancer treatment are surgery, radiotherapy, and chemotherapy. In recent years, however, targeted therapy and immunotherapy have yielded promising results and therefore have grown in importance for advanced lung cancer [34, 203, 267]. Depending on the type and stage of the disease and the patient's physical condition different treatment strategies are recommended [48].

2.2.1 Surgery

Surgery with curative intent is the treatment of choice for early stage NSCLC with the goal of complete resection of the tumour and possibly metastatic lymph nodes. It plays, however, a limited role in SCLC [202]. There are different types of surgical resection, ranging from wedge resection where only a small wedge-shaped section of lung tissue is removed up to pneumonectomy – the removal of an entire lung. Lung resection is most commonly performed using open thoracotomy or minimally invasive video-assisted thoracoscopic surgery (VATS). Alternatively, median sternotomy might also be applied as a surgical procedure for lung resection [5, 241].

Limited Resection In limited resection, that is wedge resection or segmentectomy, a small part of the lung is removed. Wedge resection describes the surgical approach where the cancerous tissue and a small margin of normal lung parenchyma surrounding the tumour are removed. In segmentectomy, an anatomical division of a specific lobe is removed, usually involving lymph node dissection [110].

Based on a randomised study performed in 1995, limited resection is generally considered to be associated with higher local recurrence and reduced survival when compared to the more invasive lobectomy [79]. More recent studies, however, suggest that the survival for stage I lung cancer patients undergoing limited resection or lobectomy is comparable [192, 293]. Despite the conflicting results, limited resection is currently reserved for early stage lung cancer patients with impaired lung function or increased surgical risk [202].

Lobectomy Lobectomy is the surgical procedure where an entire lobe is removed. It is the treatment of choice for early stage and locally advanced lung cancer with intraparenchymal lesions and the most common type of incision in lung cancer patients [10, 202].

Pneumonectomy and Sleeve Resection For central tumours involving several lobes or the main stem bronchus, the removal of an entire lung – a pneumonectomy – might be required [202]. In some cases, a less invasive incision could be performed as an alternative to pneumonectomy. In a so-called sleeve resection the involved lobe and parts of the involved bronchi are removed [50]. Several studies indicate reduced operative mortality, better long-term survival and improved quality of life for sleeve resection when compared to pneumonectomy [7, 58, 70].

2.2.2 Chemotherapy and Chemo-Radiotherapy

With its tendency towards early and widespread metastases, SCLC is predominantly treated with systemic chemotherapy. However, SCLC often consists of both extremely chemosensitive and chemoresistant clones. Initial good response followed by disease recurrence is therefore frequently observed in SCLC patients [14].

Moreover, chemotherapy is an integral treatment modality in locally advanced or metastatic NSCLC patients [59]. It is applied as a neoadjuvant, adjuvant or definitive treatment modality, often in combination with surgery or radiation. In general, the combination of chemotherapy and radiotherapy, also referred to as chemo-radiotherapy, is considered the standard therapy for stage III NSCLC [60, 234]. Beneficial outcome has been reported for concurrent chemoradiation regimens when compared to sequential therapy [49].

2.2.3 Radiotherapy

Despite surgery being the treatment of choice when medically and technically feasible, radiotherapy plays a crucial role in lung cancer treatment. It is reported that about $80\,\%$ of all lung cancer patients are inoperable at presentation due to tumour location and extension, extrathoracic spread, comorbidities, or poor physical condition [11, 260].

Radiotherapy in general describes the use of ionising radiation in order to damage cancerous cells and to ultimately destroy their reproductive capacity. When radiation is applied to a patient, energy is transferred to the human tissue through ionisation. Yet, the majority of the absorbed energy is converted into heat, having no negative effects on the cells [139, 171]. The probability of permanent tissue damage increases with increasing energy, also referred to as radiation dose. In principle, however, radiation dose affects both cancerous cells and normal tissue. Therefore, it is beneficial to apply conformal radiation therapy techniques and radiation types which are able to precisely deliver the radiation dose to a localised region [171].

In clinical practice, photon beams are the standard type of ionising radiation for all kinds of cancer treatments. Alternatively, a small but rapidly increasing proportion of patients is treated with charged particles [62, 123, 207]. By the end of 2018[4], more than $220{,}000$ patients have been treated with particle therapy of which $85.8\,\%$ received proton radiation followed by carbon ions with $12.6\,\%$. The two types of radiation, photons versus protons, differ greatly in terms of physical properties and the associated depth-dose curves as shown in Figure 2.3. Photons are uncharged, massless particles which cause ionising electrons to be released upon interaction

[4]Statistical data retrieved from the PTCOG website. Available online at: https://www.ptcog.ch/, accessed 11 March 2020.

with matter. As such, photons are classified as indirectly ionising radiation [139, 152]. Different physical effects lead to an attenuation of the photons while they are travelling through the tissue. The characteristic dose-depth curve for photon radiation reaches a maximum after a short build-up phase close to the incidence of the beam. Subsequently, the deposited dose decreases exponentially with depth [207]. Conversely, protons are relatively heavy charged particles which directly cause ionisation by collision [139]. Four different types of physical interactions determine the beam shape and the dose-depth curve characteristics for protons, namely: coulomb interactions with orbiting electrons as well as with atomic nuclei of the medium, and elastic and inelastic nuclear interactions. Of these, by far the most common is the coulomb interaction between the incident protons and the orbiting electrons of the atoms in the medium [171]. On their trajectory through matter, the protons interact with millions of electrons losing a small amount of energy with each interaction. The rate of energy loss per unit path length or stopping power is described by the Bethe-Bloch equation [139, 171]. In a nutshell, the Bethe-Bloch equation reveals two important relationships. First, the radiation dose is a function of the material's density and its chemical composition. Second, the transferred energy is inversely proportional to the square of the proton's velocity [171]. The latter relationship gives rise to the characteristic peak in the depth-dose curve of the proton, the so-called Bragg peak: with increasing depth, and therefore decreasing velocity, increasingly more energy per unit length is deposited within the tissue [139, 171, 207]. Upon entrance, the velocity of the incident protons is relatively high and, consequently, the absorbed dose is limited. Beyond the Bragg peak, the radiation dose drops to zero within millimetres. Furthermore, the position of the Bragg peak in depth is determined by the density of the tissue in the beam path and the initial energy, the latter of which can be tailored towards a specific target [171]. These properties – the finite range, the reduced integral dose, and the sharp Bragg peak – render proton radiation an attractive treatment modality for cancer therapy. It allows to precisely deliver radiation dose to a confined region within the target while sparing healthy tissue and OAR.

External Beam Radiotherapy vs. Brachytherapy As the name implies, in external beam radiotherapy the radiation source is pointed at the patient from outside. In brachytherapy, a sealed source of radiation is placed in close proximity either inside or adjacent to the target [139]. External beam radiation is the most common type of radiotherapy in definitive lung cancer treatment with curative intent; brachytherapy is restricted to highly selected cases mainly with endobronchial lesions [266]. However, in palliative care, brachytherapy may be used to relieve symptoms caused by endobronchial obstruction and therefore to improve the quality of life [254, 258]. In this work, we focus on lung cancer treatment with curative intent. All treatment modalities described below are different types of external beam radiotherapy.

Conventional Radiotherapy

Early stage lung cancer in medically inoperable patients is typically treated with stereotactic ablative radiation therapy (SABR) while locally advanced stage lung cancer is commonly managed with three-dimensional conformal radiotherapy (3D CRT) or intensity modulated radiation therapy (IMRT) as part of definitive concurrent chemo-radiotherapy [234].

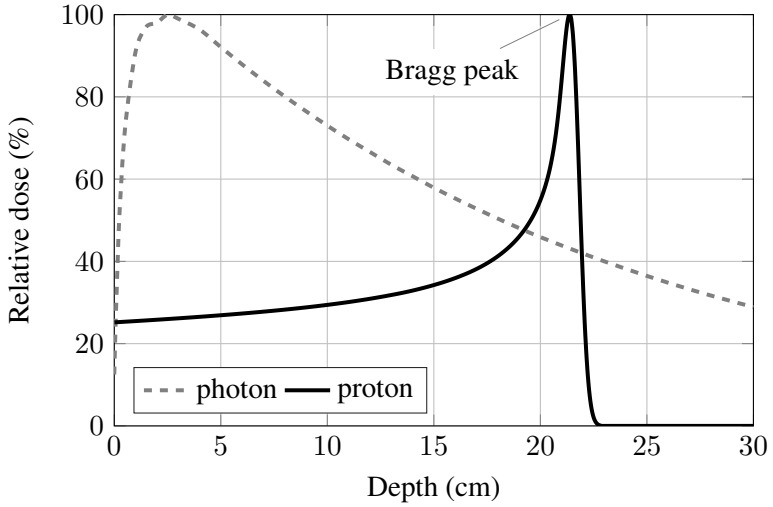

Figure 2.3: Example depth-dose curves in water for a $10\,\mathrm{MV}$ photon beam with a $10 \times 10\,\mathrm{cm}^2$ field size (grey) and a $180\,\mathrm{MeV}$ proton beam (black). The data for the photon beam was retrieved from [139], Appendix 11.1. The data for the proton beam originate from PSI Gantry 2 commissioning, courtesy of Tony Lomax.

Stereotactic ablative radiation therapy (SABR) In the recent past, SABR has emerged as the standard treatment modality for medically inoperable stage I and II NSCLC patients [234]. SABR, also known as stereotactic body radiation therapy (SBRT), is a highly focused treatment method where several radiation fields are delivered from different angles. While each beam considered separately has only limited effect on the tissue, the summation of all radiation at the intersection point allows for high ablative doses, with biologically effective doses exceeding $100\,\mathrm{Gy}$ [39]. Apart from radiation dose, SABR differs from conventional radiotherapy in terms of shorter treatment times and reduced number of fractions [208]. Compared to conventional radiotherapy, SABR has shown beneficial outcome with increased overall survival and local control rates in the range of $90\,\%$ [94, 208, 272, 279]. Furthermore, SABR is associated with low toxicity and a reduced risk of declined quality of life [94, 184, 279].

Based on the promising results of SABR for inoperable early stage NSCLC, its application in medically operable patients is subject of ongoing research and discussion as several correspondences among experts in the field reveal [33, 39, 40, 174, 250, 259, 280].

Three-dimensional conformal therapy (3D CRT) The standard treatment for locally advanced NSCLC is conformal radiotherapy with concurrent chemotherapy [46, 100]. While, historically, 3D CRT was considered the treatment of choice, IMRT has increasingly been applied over the past two decades and has been recommended to be used routinely [46]. Studies based on the SEER-Medicare database[5] report an increase in the share of IMRT from $2\,\%$ to $3\,\%$ in 2002 to about $25\,\%$ in 2009 [43, 100].

[5] Available online at: https://healthcaredelivery.cancer.gov/seermedicare/, accessed 6 March 2020.

Although technically speaking IMRT is a type of 3D CRT, the two treatment approaches differ substantially and therefore are often discussed as separate modalities [116]. Conventional 3D CRT is an advanced form of radiotherapy based on 3D treatment planning procedures. Typically, several differently shaped radiation beams are targeted at the tumour from different angles with the goal to conform the dose distribution to the 3D target volume while sparing surrounding healthy tissue and OAR [116]. Conversely, IMRT applies modulated radiation beams with non-uniform radiation intensities across the geometric field shape. In contrast to conventional 3D CRT, treatment planning for IMRT is generally formulated as an inverse problem [116, 288].

Clinical data showed significantly lower rates of severe pneumonitis and cardiac doses for IMRT when compared to conventional 3D CRT in locally advanced NSCLC [46, 297]. While previous studies report no significant difference in overall survival [43, 100], more recent studies hint at improved survival and improved quality of life for IMRT [46, 122].

Proton Therapy

Owing to its physical properties, notably the characteristic Bragg peak, proton therapy bears the potential to result in more favourable dose distributions as compared to photon radiotherapy. Proton therapy may reduce the dose received by normal lung tissue and critical OAR, such as the heart, oesophagus, spinal cord or main bronchi [36, 146]. This is especially important in lung cancer as shown in the randomised phase III RTOG 0617 trial conducted by the Radiation Therapy Oncology Group [25]. In an attempt to improve local control by dose escalation in concurrent chemo-radiotherapy, a decrease in overall survival was observed for higher radiation dose. Surprising at first, these observations may be explained by increased normal tissue toxicity, emphasising the need for highly conformal treatment strategies [62, 108].

There are two main types of proton therapy, namely passively scattered proton therapy (PSPT) and pencil beam scanning (PBS) proton therapy [36]. Although beam modulation is inherent in proton therapy, inspired by conventional radiotherapy a similar concept has been adopted: intensity modulated proton therapy (IMPT) [169, 170, 172].

Passively scattered proton therapy (PSPT) In PSPT a broad monoenergetic beam is generated using scattering material in the beam path. The beam is shaped to fit the tumour's lateral geometry by applying patient- and field-specific collimators [62]. The Bragg peak is spread along the beam path to match the tumour expansion with the help of a rotating absorber with varying thickness, and shaped to match the distal surface of the tumour via range compensators [207]. This approach results in homogeneous dose distributions within the target due to the so-called spread-out Bragg peak (SOBP). It does, however, lack the possibility to modulate the dose with respect to the proximal tumour surface [207].

For several years, PSPT has been applied in tumours prone to respiratory motion and, among others, in NSCLC [31, 145]. Clinical studies report promising median survival times and tolerable toxicities for PSPT with concurrent chemotherapy in locally advanced NSCLC [37, 197]. A retrospective analysis based on the National Cancer Database[6] further demonstrates improved 5-year overall survival rates for proton therapy when compared to photon-based radiotherapy

[6] Available online at: https://www.facs.org/quality-programs/cancer/ncdb, accessed 29 May 2020.

in general. However, the advantages in overall survival were not statistically significant when PSPT was compared to IMRT [104].

Pencil beam scanning (PBS) In spot scanning or PBS approaches a multitude of proton beamlets are applied in order to irradiate the tumour with a high degree of conformity. The lateral width of an individual beamlet is in the range of a few millimetres, and thus comparable to the size of a pencil. The initial energy, and therefore the position of the Bragg peak within the tissue, is adjusted for each beamlet individually. The lateral position is controlled using varying magnetic fields deflecting the proton beams [207]. As such, the target is scanned spot by spot and layer by layer [62]. The total of all beamlets applied from one direction are summarised in a field [1]. Typically, multiple field plans with 2 to 4 fields are used [36]. There are two conceptual approaches to optimise such treatment plans. In single-field uniform dose (SFUD) plans, the fields are optimised separately such that homogeneous dose distributions are obtained for each field individually [1]. In IMPT, all fields are optimised simultaneously, eventually resulting in a homogeneous overall dose distribution. The individual fields, however, are non-uniform [1, 169, 170, 172]. This additional flexibility in dose sculpting allows IMPT to fully exploit the advantages of protons in radiotherapy.

A virtual clinical study for advanced stage NSCLC patients has demonstrated the potential of IMPT to reduce the dose to normal tissue and OAR when compared to both IMRT and PSPT [301]. Furthermore, it suggests that dose escalation is possible without compromising the sparing of healthy tissue when compared to PSPT. First clinical experiences seem to confirm these findings [38, 193]. However, in an experimental study, it has also been shown that IMPT is less robust towards residual breath-hold motion when compared to SFUD plans [84].

Clinical application Ever since the first clinical application of spot scanning worldwide at PSI in the 1990s [209, 210], the number of clinical facilities has increased rapidly and many more are under construction [123, 207]. Encouraged by the physical advantages of protons and the unprecedented conformity of PBS, many of the newly installed proton facilities are no longer equipped with beam scattering but rather with scanning [145]. Consequently, PBS proton therapy has become increasingly popular also for thoracic and abdominal tumours [145, 276]. However, increased conformity comes at the cost of increased range uncertainty which makes proton therapy in general and active scanning in particular exceptionally challenging in mobile targets [64].

Moreover, proton therapy is associated with 2 to 3 times higher costs per treatment when compared with conventional photon-based therapy [36, 62]. The higher costs are mainly driven by the particle accelerators, such as synchrotrons or cyclotrons, and the gantries used in proton therapy. Proton delivery systems are substantially more expensive and bigger in size than the linear accelerators required for conventional radiotherapy [62, 207].

Despite the physical advantages and the resulting beneficial dosimetric distributions, the limited cost-effective ratio has hampered the widespread application of proton therapy in the clinics [62, 207]. Also, dosimetric advantages do not necessarily translate into clinically relevant improvements as we have seen above for the comparison between PSPT and IMRT [104].

Further randomised trials, such as the RTOG 1308[7], are essential to assess the clinical benefits of proton therapy in NSCLC [36].

[7]Study description available online at: https://clinicaltrials.gov/ct2/show/NCT01993810, accessed 18 March 2020.

Chapter 3

Motion in PBS Proton Therapy

Lung tumours inherently undergo motion and changes. The causes are manifold and differ in magnitude and time scale. In this chapter, we outline the main sources of motion, their implication on particle therapy, and possible motion mitigation strategies. We mainly focus on PBS proton therapy of the lungs, however, whenever necessary or helpful, research regarding other anatomical sites or treatment methods will be considered as well.

3.1 Causes and Characteristics

The causes for lung tumour motion are both physiological and treatment-related, ranging in time scale from milliseconds for cardiac pulsation, through seconds and minutes for respiratory motion and organ drift, up to weeks and months for treatment response or changes in patient condition, such as weight loss or gain [145, 162]. In the context of radiotherapy, the different types of motion are broadly classified into inter- and intra-fractional motion [15, 181]. In addition, patient movement and patient position may contribute to tumour motion also [162]. Body frames and vacuum cushions are commonly applied immobilisation tools to overcome patient movements. Moreover, in-room CT and cone-beam CT (CBCT) are becoming available also in particle therapy facilities, allowing for both on- and off-isocenter imaging in the treatment position for setup verification and target alignment [145, 160, 276]. For the discussion below we assume ideal patient setup and focus on inter- and intra-fractional organ motion, especially on the respiratory motion.

Inter-fractional motion includes changes observed from fraction to fraction and, therefore, over days and weeks [181]. Baseline shifts of several millimetres between fractions were reported which means that the mean tumour position changed with respect to the initially identified position [28, 261]. Moreover, tumour volume decrease in the range of $15\,\%$ to $70\,\%$ was observed over 7 weeks of treatment [28].

Intra-fractional motion includes all changes which occur within a single treatment session and, thus, within seconds to minutes [181]. For lung cancer this involves predominately respi-

ratory motion. Several studies analysed the respiration-induced motion characteristics of lung tumours based on different imaging modalities: implanted gold markers in conjunction with fluoroscopy [201, 252, 255], respiratory-correlated CT (4D CT) [28, 166, 240], respiratory-correlated CBCT (4D CBCT) [261], or dynamic MRI [214]. They consistently identified the main motion component in the superior-inferior (SI) direction, followed by anterior-posterior (AP) and left-right (LR). Among these, the largest study including 166 tumours from 156 patients reports a tumour motion below $13.4\,\mathrm{mm}$, $5.9\,\mathrm{mm}$, and $4.0\,\mathrm{mm}$ in SI, AP, and LR, respectively, for $95\,\%$ of the tumours [166]. A more recent study based on 126 patients reports a median and maximum amplitude in SI direction of $4.0\,\mathrm{mm}$ and $53.0\,\mathrm{mm}$, respectively [240]. The tumour mobility was found to be associated with the diaphragm motion [35] and tends to correlate with tumour location and size: a larger motion was observed for smaller tumours and lower sites [166, 201, 214]. However, while the results were confirmed for the tumour location, another study reported no correlation between tumour motion and tumour size [240]. A summary of respiratory motion characteristics can be found in [138].

Respiratory motion is considered to be quasi-periodic. The breathing period was reported to be in the range of $2.7\,\mathrm{s}$ to $6.6\,\mathrm{s}$ with a mean periodicity of $3.6 \pm 0.8\,\mathrm{s}$ [252, 286]. However, motion variabilities between and within breathing cycles are not negligible. First, it was observed that lung tumours commonly follow different trajectories during inhalation and exhalation. This hysteresis was predominantly found in the sagittal plane and ranged from $1\,\mathrm{mm}$ to $5\,\mathrm{mm}$ [252]. Second, extensive time-resolved MRI acquisitions revealed a drift in abdominal organs: the liver was observed to drift on average between $1.2\,\mathrm{mm}$ to $4.6\,\mathrm{mm}$ and maximally up to $12.8\,\mathrm{mm}$ in inferior direction over $20\,\mathrm{min}$ [285]. For longer time durations of up to $1\,\mathrm{h}$, an average organ drift in the superior direction of $2.4\,\mathrm{mm}$ to $7.1\,\mathrm{mm}$ was reported [286]. Possible sources for organ drift in the liver are peristaltic motion, muscle relaxation, or the change in direction of the gravitational force acting on the organs in the upright and supine position [286]. Similar findings were reported for lung tumours. During SABR, the motion of an implanted fiducial marker near the lung tumour was monitored in 68 patients and 335 fractions [268]. Combining the three anatomical directions, a tumour drift of more than $3\,\mathrm{mm}$ was observed in $42.1\,\%$ and $71.6\,\%$ after $10\,\mathrm{min}$ and $30\,\mathrm{min}$, respectively. Moreover, a tendency for drift towards the posterior and the superior direction was reported.

Besides respiratory motion, cardiac pulsation may account for a non-negligible amount of lung tumour motion. However, contradicting findings were reported regarding the influence of the heartbeat. While one study detected the cardiac impact mainly in tumours close to the heart or the aortic arch [252], a second study did not find a statistically significant correlation of cardiac-induced motion and tumour location in terms of lobe [44]. Nevertheless, the impact of the heartbeat on tumours in the left hemithorax was larger in amplitude when compared to right lung tumours [44].

3.2 Implications

Organ motion poses a great challenge in conformal radiotherapy in general. The benefits of increased conformity only come into play if the target's location and the shape are known precisely at every time point during treatment. In terms of geometrical uncertainties, organ motion

– and particularly respiratory motion – similarly complicate both conformal photon therapy and particle therapy [15, 22, 249]. If not taken into account, organ motion results in a blurring of the dose distribution and consequently in lateral target miss [22]. There are, however, additional adverse implications in particle therapy in general and PBS therapy in particular, namely the influence of motion on the radiological pathlength and the so-called interplay effect [15].

The influence of motion on the radiological pathlength Range uncertainties along the beam path are unique to particle therapy and a direct consequence of the physical interaction of protons with matter and their finite range in tissue [207]. The radiological pathlength, commonly expressed in water-equivalent pathlength (WEPL), is affected both by inter-fractional and intra-fractional organ motion [15]. In particular for lungs, large density differences between tumour tissue and normal lung tissue substantially alter the radiological pathlength and may lead to considerable overshoot while rib cage motion induced by respiration further affects the proton range [207].

To quantify the effects of inter-fractional motion, two 4D CT scans of a stage III NSCLC patient acquired within five weeks were analysed in a simulation study. Tumour shrinkage and lung density variations resulted in a change of $3\,\mathrm{cm}$ and $1.5\,\mathrm{cm}$ WEPL, respectively [189]. For intra-fractional motion, range variations of up to $21.8\,\mathrm{mm}$ WEPL were reported in a similar analysis for 11 patients [190].

Interplay effects The different motion dynamics of respiration-induced tumour motion on the one hand, and dynamic dose delivery techniques on the other hand, interfere. This effect is generally referred to as interplay and manifests in inhomogeneous dose distributions with possibly severe local underdosage and overdosage [15]. As such, the interplay effect is not limited to actively scanned particle therapy but rather can also be observed in IMRT based on photons [22, 249].

The interplay effect was first described for proton therapy with the introduction of clinical spot scanning facilities [213]. Several studies have investigated and quantified the interplay effect for respiratory lung tumour motion ever since [17, 88, 149, 164, 221]. Based on 4D CT data of up to 11 lung cancer patients, all simulation studies identified patient and treatment specific parameters which affect the dose error caused by interplay. A general trend towards increased interplay effect for increasing respiratory motion amplitude was observed. However, also smaller spot size [88], smaller tumour volume [164, 221], or baseline shifts in the inter-fractional setting [149] were reported to amplify the interplay effect. Conversely, multiple-field plans, as opposed to single-field plans, and irregular breathing patterns led to higher dose homogeneity by averaging out the detrimental interplay effects [149]. In an attempt to disentangle the different adverse effects on dose distribution in mobile tumours, the impact of interplay was found to dominate both blurring and range uncertainties [221].

3.3 Motion Mitigation

Pioneered in photon therapy, there are various strategies on how to manage inter-fractional and intra-fractional organ motion as well as patient positioning and immobilisation [15, 143, 225].

For respiratory motion, there are three conceptually distinct stages in the treatment process on where to tackle the problem of motion mitigation: influence the respiratory motion itself, incorporate the motion dynamics into the treatment planning, or lastly adapt the delivery technique to take motion into account. A summary of motion mitigation techniques for PBS proton therapy can further be found in the latest consensus guidelines of the PTCOG thoracic and lymphoma subcommittee [41].

3.3.1 Motion reduction

Motion reduction techniques have been introduced in photon beam radiotherapy and range from mechanical intervention through special breathing manoeuvres to artificial ventilation [15]. Abdominal compression was consistently found to reduce the lung tumour motion, in particular in the SI direction [97, 178, 195], and for lower-lobe lesions [23]. However, also increased interfractional variations [178], and limited dosimetric gains [23] were reported. Other approaches include high-frequency jet ventilation [238] or apneic oxygenation [165]. However, since these methods require general anaesthesia and oral intubation, they impose an additional load on patients and the clinical workflow [15, 106]. Conversely, active breath control (ABC) and voluntary breath hold offer non-invasive alternatives which have been intensively studied for photon beam treatment [8, 20, 99]. Recent simulation studies for PBS proton therapy demonstrate promising results in terms of clinical feasibility and dosimetric robustness [61, 85]. In an experimental study, SFUD plans were shown to be more robust when compared to IMPT plans with respect to residual intra-breath hold motion. This study was performed on an anthropomorphic phantom in conjunction with tumour geometry and motion extracted from lung cancer patients [84]. However, breath hold relies on patient compliance and may not be feasible for all patients, even more so if the lung function is impaired. Several patients had to be excluded from the abovementioned studies either because they were not able to perform reproducible breath hold positions [8], or due to the inability to hold their breath for the required duration of $20\,\mathrm{s}$ [85].

3.3.2 Treatment planning

Image-based volumetric treatment planning is the state of the art in radiotherapy. While this approach is well established for static tumours, it is not straightforward on how to incorporate intra-fractional motion into treatment planning, especially for proton therapy. One approach is to define specific margins to account for motion-induced uncertainties [143]. In clinical practice, different definitions for the target volume are used in order to take into account microscopic spread, setup uncertainties or internal organ motion [222]. According to the International Commission on Radiation Units & Measurements (ICRU) Report 78 [115], the internal target volume (ITV) includes an internal margin to compensate for uncertainties due to "physiologic movements and variations in size, shape, and position of the clinical target volume (CTV)" [187, 224]. Alternative formulations based on water-equivalent volumes were proposed for proton therapy to compensate for range variations [87, 225]. While current ITV approaches are typically based on one average respiratory cycle consisting of 8 to 10 motion states as provided by a 4D CT, in a recent publication a probabilistic ITV was introduced which explicitly incorporates respiratory motion variabilities extracted from extensive 4D MRI data sets [154]. The use of margins or

ITV alone is generally not considered sufficient for PBS proton therapy in particular due to the interplay effect [143]. To ensure target coverage, margins are typically applied in combination with other motion mitigation techniques, such as rescanning or gating [154, 225].

Increased margins as present in the ITV definition aim to ensure target coverage which, however, inherently increase the dose to surrounding normal tissue especially for large motions [15]. As an alternative, the respiratory motion may be included in the treatment optimisation process directly [13, 86, 167]. As such, these 4D treatment planning approaches consider all states of a 4D CT as opposed to a single 3D CT image. However, these techniques heavily rely on the planning 4D CT and generally assume reproducible breathing patterns [86, 167]. To overcome this issue, motion irregularities were explicitly incorporated into the optimisation process [13]. Nevertheless, small deviations from the planning motion, although irregular, resulted in substantially reduced dose homogeneity. A loss of target homogeneity of more than $5\,\%$ was observed for changes in motion amplitude, phase or periodicity of more than $1\,\mathrm{mm}$, $200\,\mathrm{ms}$, and $20\,\mathrm{ms}$, respectively [13].

3.3.3 Treatment delivery

The relative ease with which the beam position can be adapted allows for dedicated treatment delivery strategies in PBS proton therapy. The most promising and widely discussed techniques include rescanning, gating, tracking, or a combination thereof [15, 143, 225].

Rescanning builds on the principle of stochastic and the quasi-periodicity of the respiratory motion. Instead of applying the planned treatment dose in one pass, the target volume is repeatedly scanned with the dose scaled down accordingly [225]. Assuming temporally uncorrelated motion dynamics of the target and the scanning process, respectively, rescanning leads to an averaging of potential local over- and underdosage and, therefore, to a mitigation of the interplay effect. With the introduction of clinical spot scanning devices, rescanning – also known as repainting – has been proposed as a potential motion mitigation technique [213]. Similar averaging effects have been observed for an increased number of fractions [213], and multiple-field plans [144]. Numerous rescanning approaches have been proposed and investigated ever since, many of which at PSI [12, 74, 89, 144, 242, 243, 298, 305].

On the one hand, two main rescanning techniques namely volumetric rescanning and layered rescanning were introduced. While in layered rescanning each iso-energy layer is rescanned several times before the energy is changed, the entire volume is repeatedly scanned in volumetric rescanning [225]. Since volumetric rescanning imposes higher technical requirements on the scanning system, layered rescanning is recommended for slow scanning systems [12]. On the other hand, different approaches on how to divide the dose among the different rescans have been proposed. In scaled rescanning, the total dose is divided by the number of rescans resulting in a constant number of rescans per spot [213]. However, due to large dose variations within an energy layer, scaled rescanning may lead to impractically small doses for low-weighted spots. To overcome this drawback, iso-layered rescanning has been proposed where high-weighted spots are scanned more often than low-weighted ones [298]. Yet, also iso-layered rescanning may result in residual doses which are small and, thus, technically infeasible to be delivered. At PSI

a hybrid rescanning approach is used where the smallest deliverable beam weight is taken into account [153, 305]. Finally, continuous line scanning was compared to discrete spot scanning. Similar dose distributions have been achieved for continuous line scanning, however, with the advantage of reduced treatment times [242].

Rescanning inherently comes at the cost of increased involvement of the surrounding normal tissue [143, 144]. Therefore, it may be favourable to apply rescanning in combination with breath hold, gating, or tracking, especially for large tumour motions [74].

Gating describes the treatment delivery technique in which the tumour is irradiated at specific respiratory states only [143]. The gating window is typically chosen at end-exhalation as this was shown to be the most reproducible respiratory state [281]. While gating has been clinically applied both in conventional radiotherapy [135] and in PSPT [120, 175], studies for scanned proton therapy are mainly based on simulations or phantom experiments [89, 133, 180, 244, 253, 305]. Gating was shown to reduce the dose to the normal lung and to mitigate the interplay effect for the patients under investigation [89]. In general, however, target motion is not fully eliminated in beam gating. Consequently, the residual motion in the gating window has to be considered during treatment planning [16, 225]. Smaller gating windows reduce the residual motion at the cost of increased treatment times [133].

Similar to the above, most analyses using patient geometry were performed on an average 4D CT respiratory cycle [89, 133] or rigid tumour motion [253]. Studies performed on realistic breathing patterns obtained from 4D MRI suggest that neither gating nor rescanning alone is sufficient to achieve clinically acceptable dose distributions. A combination of the two mitigation techniques, however, was found to be feasible and robust in terms of dose homogeneity and treatment times [244, 302, 305].

Tumour tracking is, in principle, the most precise motion mitigation technique for scanned particle therapy but also technically the most challenging [225]. In tumour tracking the proton beam is adapted to track the tumour's motion. Under ideal conditions tumour tracking does not require additional target volume expansions as rescanning does nor does it lead to prolonged treatment times as gating does [92].

The concept of tumour tracking was first introduced for conventional radiotherapy [134] and by now is readily applied in clinical practice through the use of robotic radiosurgery systems [109], multi-leaf collimators [137], or gimbaled Linac systems [56, 105]. Moreover, motion compensation by treatment couch movements has been proposed also [161]. That being said, with lateral adaptions being inherently a key element in scanned particle therapy, the application of PBS proton therapy for tumour tracking seems especially promising. In contrast to photon therapy, however, range variations as a result of motion-induced anatomy changes have to be taken into account as well which demands sufficiently fast energy adaptation [92]. As such, fast energy modulation systems have been developed and implemented for carbon ion at GSI Helmholtz Centre for Heavy Ion Research (GSI) [18, 42, 91], and for proton therapy at PSI [211, 233]. Yet, the clinical feasibility of tumour tracking PBS particle therapy remains unclear. Computer simulations based on a heterogeneous phantom, which includes high-density tissue proximal to the moving target, suggest that tumour tracking is not able to retrieve the nom-

inal dose homogeneity even in the case of perfect knowledge about the tumour position [278]. Dose inhomogeneities are introduced by suboptimal beam weights due to adjustments in the beam position relative to density inhomogeneities during beam tracking. Moreover, the study introduces the concept of retracking – the combination of tracking and rescanning – which has been shown to substantially reduce the sensitivity to position errors when compared to tracking alone in a homogeneous phantom. Retracking was further investigated in a study based on patient geometries and realistic liver motions [304]. The study suggests that tracking alone is not able to fully compensate for motions greater than $10\,\mathrm{mm}$ resulting in substantially increased dose to normal tissue proximal to the target. However, three times retracking has been shown to significantly improve the dose homogeneity within the target volume to the extent of comparable dose distributions as for the static plan.

3.4 Motion Monitoring

With the exception of rescanning, most of the above motion mitigation strategies rely on the knowledge of the respiratory state and, therefore, on some sort of motion monitoring. Similar to mitigation techniques, motion monitoring is more advanced in photon therapy than in particle therapy [145]. The translation of monitoring systems from photon to proton therapy, however, is not necessarily straightforward due to increased accuracy requirements and hardware-related challenges [19]. A recent publication summarises state-of-the-art and clinical motion monitoring systems in radiotherapy [19], while others focus more specifically on particle therapy [145, 157, 276] or motion modelling [181]. Here, motion monitoring techniques are discussed with the main focus on radiotherapy for lung tumours. However, since motion monitoring further is a key element in 4D imaging and motion modelling, literature from these fields are included as well.

To date, no imaging modality exists capable of 4D real-time thorax imaging during dose delivery. Current motion monitoring systems therefore generally rely on surrogate signals, often in combination with a correspondence model [181]. Appropriate surrogate signals exhibit a strong correlation with the motion of the tumour and possibly OAR while being available at high temporal resolution; they may be external or internal, invasive or non-invasive, 1D or multi-dimensional, or image-based, ionising and non-ionising [181, 276]. In the last decades, image-guided radiation therapy (IGRT) has emerged as an active field of research including recent adoptions in particle therapy [32, 147, 160, 206].

3.4.1 External monitoring techniques

External monitoring techniques are often less demanding technically than internal monitoring techniques, and typically advantageous in terms of ease of use and temporal resolution; they are non-invasive and do not introduce additional ionising dose to the patients [19]. However, external surrogates rely on a consistent and reliable relationship between the measured signal and the internal target motion. Consequently, they share their blindness towards phase shifts [107], baseline shifts [28, 261], and organ drift [268, 285, 286], and therefore are often used in combination with direct tumour imaging for verification [45, 140, 251].

Spirometry A spirometer measures the airflow into and out of the lungs through a mouthpiece [19, 181]. The patients wear a nose clip to restrict the respiration to the mouth [107]. Spirometry often suffers from a phase difference between the external signal and the actual tumour motion [107] and from signal drift [176, 299]. Therefore, spirometer-based monitoring was recommended for ABC rather than free breathing gating techniques [299]. As such, commercially available ABC devices have been used clinically for treating mobile targets affected by respiratory motion in general, and lung tumours in particular [183]. Further limitations associated with spirometry are the required training sessions [19, 183] and patients' discomfort and difficulties in tolerating spirometry [107].

Respiratory belt Different pressure sensors such as strain gauges [158] or bellows [264, 277] were examined for motion monitoring. These pressure sensors are integrated into a respiratory belt wrapped around the patient's abdomen and measure the external expansion of the abdomen. Respiratory belts are commercially available and have been applied for both 4D MRI [264, 277] and respiratory-gated radiotherapy of lung tumours [163]. Only recently, such a respiratory belt was commissioned for gated carbon-ion scanning radiotherapy for the Heavy Ion Medical Accelerator in Chiba (HIMAC) [185].

Body surface motion Abdominal displacement or skin surface tracking constitutes the third group of external motion monitoring approaches and comprises various measurement techniques, several of which are commercially available and in clinical use [140, 291]. Among these are laser sensors [269], electromagnetic tracking systems (EMTS) [67, 107], and various optical tracking systems (OTS) [9, 66, 68, 112, 176]. In a study comparing an OTS and an EMTS for PBS proton therapy, it was found that the OTS is better suited for clinical applications even though in controlled laboratory conditions the two systems performed comparably in terms of accuracy and latency [67]. However, the CT scanner and the treatment gantry both induced electromagnetic distortions impairing the tracking precision of the EMTS by several millimetres. Although optical systems are popular solutions for respiratory motion monitoring due to high temporal resolution and usability, the correlation between the external signal and the internal target motion is not always reliable. Comparisons between spirometry and abdominal displacement measurements suggest that the relationship with lung tumour motion is stronger and more reproducible for spirometry [107, 176].

3.4.2 Internal monitoring techniques

Internal monitoring techniques are mostly image-based and may include implanted radio-opaque fiducial markers (FM) while other approaches use electromagnetic tracking of implanted transponder beacons [157]. Common to all image-based approaches is the need for appropriate image processing algorithms to retrieve the motion surrogate [19]. Internal monitoring approaches are generally considered to be superior in terms of target localisation accuracy. However, they impose additional radiation dose in case of ionising imaging modalities, or risks of complications due to marker implantation [19]. Complications following FM implantation were reported to be most prevalent for the lungs when compared to other sites such as pancreas or liver. Of 44 marker

implantation procedures in the lungs, major and minor complications were observed in 7 and 21 cases, respectively, of which pneumothorax was the most common complication [148]. The same study also reported substantial marker migration within the lungs requiring additional procedures [148]. Moreover, FM and electromagnetic transponders may introduce artefacts within the planning CT and interact with the particle beam depending on their material, size and location within the treatment field [15, 95, 157].

Electromagnetic tracking of internal transponders In an electromagnetic tracking system, the implanted transponder beacons contain a miniature electric circuit. The transponders resonate upon excitation with an electromagnetic field which in turn can be measured by sensors [257]. Such an electromagnetic tracking system is commercially available and in clinical use for prostate cancer treatment [257]. Its application in lung tumour treatment with photon radiotherapy has recently been initiated with first clinical trials [21, 247].

Fluoroscopy 2D X-ray imaging is generally available as an in-room imaging modality in particle facilities and may be used in fluoroscopic mode for real-time motion monitoring [19, 160]. Notably, a specifically developed beam's-eye-view (BEV) fluoroscopic system was implemented at PSI enabling online X-ray imaging in beam direction synchronised with proton irradiation [233]. Due to the typically low contrast of abdominal lesions in X-ray projections, radio-opaque FM are often implanted in close proximity to the target to facilitate fluoroscopic tracking [157, 253]. However, also markerless approaches based on diaphragm tracking have been investigated both in simulation studies [303, 305] and in a clinical trial for PBS carbon-ion therapy of 10 patients with lung or liver cancer [188]. While fluoroscopy offers temporally highly-resolved, internal target motion information, it inherently imposes considerable non-therapeutic radiation dose to the patients [188]. In order to reduce the imaging dose, hybrid monitoring systems combining fluoroscopy and an optical tracking system are used clinically for photon therapy [140] and have been investigated in a phantom study for proton therapy [45].

Magnetic resonance imaging MRI is an alternative and versatile imaging modality with great potential for image-guided radiotherapy. Compared to fluoroscopy, MRI provides improved soft-tissue contrast without radiation dose [206]. As such, much research was performed towards magnetic resonance linear accelerator (MR-linac) systems, a combination of an MRI scanner and a radiotherapy accelerator [223]. First MR-linac systems have recently been introduced into the clinics [271]. In proton therapy, however, the proton beams are deflected by the magnetic field of the MRI scanner which distorts the dose distribution if not taken into account [199]. Moreover, the interaction between the magnetic field of the MRI scanner and the beam transport magnets complicate MRI-guidance [246]. In a recent feasibility study, an open low-field MRI scanner was integrated into a static proton research beam line [245]. However, MR-guided particle therapy is still in an early stage of development and subject of ongoing research [19].

Ultrasound imaging Similar to MRI, US imaging provides excellent soft-tissue contrast without ionising radiation dose; US as well as MRI is generally non-invasive and may provide functional information. In addition, US is relatively inexpensive and real-time capable; it enables

2D imaging at a high spatial and temporal resolution [73, 205]. As such, US imaging is attracting increasing interest for image-guided radiotherapy both for inter- and intra-fractional motion management as well as treatment planning [73, 205]. A first commercially available US system for intra-fractional motion monitoring uses 4D transperineal imaging for prostate motion tracking in radiotherapy [159]. In recent studies, the accuracy of this US-guidance system was evaluated in vivo and found to be comparable to other motion monitoring systems [90, 96].

US imaging being a modality especially suited for soft tissue imaging has the potential to reduce treatment margins and therefore to improve intra-fractional motion monitoring for targets in the upper abdomen, such as the liver [51] or pancreas [200]. In a case study, 4D US imaging of the liver was performed on one patient with implanted electromagnetic transponders [117]. Good spatial alignment between the US-based and electromagnetic target localisation was reported for simultaneous acquisitions under free breathing. Another group investigated the use of 4D US imaging of target structures in the upper abdomen to monitor intra-breath hold residual motion [256, 284]. US-based motion monitoring was compared to diaphragm motion in CBCT projections of 13 patients [284]. For a majority of the acquired data, a strong correlation between the two signals has been reported.

Despite the advantages of US-guidance, its application in both particle therapy and lung tumours has been rare [19]. The high attenuation of US in air impedes direct imaging of lung structures and tumours [205]. Therefore, lung tumour tracking based on US imaging has to be performed indirectly. Only recently real-time lung tumour motion estimation based on abdominal US imaging was proposed in a feasibility study with three lung cancer patients [191]. Continuous US imaging was combined with periodic CBCT projection images in order to reduce the imaging radiation dose to the patients. The diaphragm motion was measured with the US system's tracking software and served as an internal respiratory surrogate signal for lung tumour motion estimation in SI direction. The study reports a significant correlation between the diaphragm and lung tumour motions. At GSI, a US-tracking system was integrated into a scanned particle therapy system. It was shown to considerably reduce interplay effects in an experimental phantom study with simplified periodic respiratory motion and beam tracking [216, 248].

Continuous or real-time US signals, however, are not only of interest in the context of radiotherapy. Various studies investigated its application in other fields, such as high intensity focused ultrasound (HIFU) ablation of moving tissue [6, 173], motion modelling [219, 227], motion compensation in medical imaging [239], or the generation of synthetic MRI at high temporal resolution [218, 220]. In the following, we will focus on respiratory motion modelling in general and US-driven models in particular.

Chapter 4

Respiratory Motion Modelling

Motion models are essential when a direct measurement of the motion of interest is not possible at sufficient temporal and spatial resolution [181]. In particular, for PBS proton therapy, the knowledge of the 4D patient motion within the beam path is essential for both dose distribution analysis in offline simulation studies and, eventually, online adaptation of the treatment beam in tumour tracking [19, 145, 276]. In this chapter, we review retrospective 4D MRI approaches and different types of motion models to overcome the lack of real-time 4D imaging of the lungs.

4.1 Problem formulation

Following the definition of McClelland et al. [181], a motion model is "a process that takes some surrogate data as input and produces a motion estimate as output". The surrogate data should be available at high temporal resolution and correlate reliably with the motion of interest [181]. As such, all of the motion monitoring techniques described in Section 3.4 are possible surrogate data with their respective benefits and limitations. Conversely, the motion estimates are typically extracted from imaging data prior to the intended procedure.

Let $\boldsymbol{x}_t \in \mathbb{R}^u$ and $\boldsymbol{y}_t \in \mathbb{R}^v$ denote the surrogate data of dimension u and the motion estimate of dimension v at time t, respectively. Then, the relationship between the input and the output signal can be formulated as a regression model:

$$\boldsymbol{y}_t = f(\boldsymbol{x}_t, \boldsymbol{\theta}) + \boldsymbol{\epsilon}_t, \tag{4.1}$$

where $\boldsymbol{\theta}$ represent the unknown model parameters, and $\boldsymbol{\epsilon}_t \in \mathbb{R}^v$ is an additive error term. In regression analysis, $\boldsymbol{x}_t$ and $\boldsymbol{y}_t$ are generally referred to as independent and dependent variable, respectively. Given a set of m observations $\mathcal{S} = \{(\boldsymbol{x}_t, \boldsymbol{y}_t) \,|\, t = 1, \ldots, m\}$, the aim is to infer the function $f : \mathbb{R}^u \to \mathbb{R}^v$. Depending on the type of surrogate data $\boldsymbol{x}_t$, pre-processing might be necessary or helpful, especially for image-based surrogates. Moreover, for real-time applications it is necessary to predict future motion estimates in order to take inherent system latencies into account. Therefore, the respiratory motion model usually consists of a spatial and a temporal component. In this work, we adopt the notation introduced by McClelland et al. [181] and refer to the spatial regression model in Equation (4.1) as correspondence model. Given that the data

at hand are time series, we use autoregressive models for forcasting as described in Section 4.5. Overall, the motion modelling pipeline for radiotherapy consists of four steps [181]:

1. **Data acquisition:** Prior to the treatment delivery, respiratory motion data of the patient is acquired. Typically, the surrogate signal and the imaging data used for motion estimation are acquired simultaneously to ensure temporal correspondence between the two signals.

2. **Data processing:** Following the data acquisition, both image reconstruction and image registration is normally required to extract the motion estimates $\boldsymbol{y}_t$. These motion estimates may not only be used for motion modelling but also for treatment planning. In the case of image-based surrogate data, image processing and feature extraction are typically required for the surrogate as well to obtain the desired surrogate information $\boldsymbol{x}_t$.

3. **Model fitting:** Depending on the motion model, the surrogate signal $\boldsymbol{x}_t$ may be mapped into a feature space first: $\hat{\boldsymbol{x}}_{\boldsymbol{t}} = \phi(\boldsymbol{x}_t)$. Given a set $\mathcal{S}$ of training data and a predefined motion model $f(\hat{\boldsymbol{x}}_{\boldsymbol{t}}, \boldsymbol{\theta})$, the model parameters $\boldsymbol{\theta}$ are then optimised.

4. **Motion estimation:** During treatment, the surrogate data is acquired and used as input to the model for online motion estimation.

4.2 Data acquisition

Simultaneous acquisition of the surrogate and the imaging data forms the basis for respiratory motion modelling. Alternatively, the surrogate signal can be extracted directly from partial imaging data if available during treatment, as it is done for example in MR-linac systems [264, 265]. In this section we focus on imaging techniques of the thorax and abdomen for intrafractional motion estimation. The different types of surrogate modalities are discussed in detail in Section 3.4.

In order to capture the respiratory motion of the lungs, time-resolved volumetric imaging is essential. Such imaging sequences are generally referred to as 4D imaging techniques, consisting of three spatial dimensions plus time [113]. At present, 4D CT is the clinical standard for motion evaluation and 4D dose calculations [113, 145, 276]. However, alternative imaging modalities, such as 4D MRI or 4D CBCT, have gained increasing interest over the last years [29, 263, 306]. The underlying challenges and principles are the same for all imaging modalities. The time needed for the acquisition of a 3D image is long compared to typical respiratory motion dynamics. This is particularly true if large volumes are scanned, such as the thorax or abdomen. If not accounted for, organ motion leads to modality-specific image artefacts such as blurring, distortion of organ boundaries or incorrect object position, shape, and size [113].

A common approach to cope with respiratory organ motion in 4D imaging is to split the respiratory cycle into a predefined number of states or *bins*, either by phase or by amplitude [113, 263]. Then, partial image data is acquired at high temporal resolution and assigned to a respiratory state based on the surrogate signal. Examples of partial image data are reconstructed 2D slices, projection images in CT [113], or partial k-space data in the case of MRI [263]. Conceptually, such 4D imaging methods can be divided into two major groups: prospective and

retrospective approaches. In prospective approaches, the acquisition is gated and, thus, restricted to a specific respiratory state. In retrospective approaches, a large set of partial image data is acquired and retrospectively sorted into the respective bins. If sufficient image data was acquired per respiratory state, the partial image information is combined or stacked to form a complete 3D image. This so-called binning or stacking approach leads to an inherent trade-off between temporal resolution, acquisition time, and image quality. While a high number of respiratory states demands a large amount of image data, a small number of respiratory states results in increased residual motion within one bin [263]. Moreover, the methods rely on the quasi-periodicity of the respiratory motion and the assumption that the respiratory states are consistent among different respiratory cycles [113]. As such, the resulting 4D image does not reveal respiratory variability but rather must be construed as an average respiratory cycle [276].

In this work, we adopt the notation of *respiratory-correlated* and *time-resolved* 4D imaging methods as introduced for MRI in [206, 263]. We are aware that none of the currently available 4D imaging method is truly real-time in the sense that full 3D images are acquired at sufficiently high temporal and spatial resolution as required for *time-resolved* 4D imaging according to the aforementioned publications [206, 263]. Here, we use the term *respiratory-correlated* when referring to methods which produce one average respiratory cycle with a fixed number of respiratory states as described above. We further use the term *time-resolved* for methods which reconstruct a continuous 4D image beyond one respiratory cycle and which as such are capable of capturing motion variabilities and long term deformations. Although the individual 3D images are reconstructed from partial image data, the forth dimension does arguably describe time rather than respiratory states.

4D CT is the mainstay for clinical 4D treatment planning since it provides density information required for dose calculations [113, 276]. Typically, the temporal resolution is in the range of $1.25\,\mathrm{Hz}$ to $2.5\,\mathrm{Hz}$ resulting in 5 to 10 states for a respiratory cycle of $4\,\mathrm{s}$ [276]. Image artefacts in clinical 4D CT are widespread and manifest in duplicated, overlapping, or incomplete structures [114, 296]. For 4D CT imaging in particular, artefact reduction through increased acquisition times is limited by the increased imaging dose delivered to the patients [114].

4D MRI offers greater flexibility in image orientation [168] and acquisition sequences [263] as well as superior soft-tissue contrast [196] when compared to 4D CT. In the absence of ionising radiation, 4D MRI allows for prolonged acquisition times and, therefore, for the systematic analysis of respiratory variabilities and organ drift in comprehensive time-resolved 4D images [285, 286]. Within the scope of this work we focused on the development and use of *time-resolved* 4D MRI methods for its application in treatment planning and dose analysis in radiotherapy. Recently, we have developed a novel 4D MRI method which is based on 3D partial k-space readouts to estimate the respiratory motion. High-frequency image details are subsequently restored using peripheral k-space patches and image registration [128, 129]. Furthermore, we have presented an US-driven 4D MRI approach where motion information extracted from abdominal US images serve as surrogate for retrospective stacking of 2D MRI slices [78]. This approach together with an extended literature review on 4D MRI is presented in Chapter 5.

4D CT(MRI) describes an approach to combine the benefits of both imaging modalities, namely the density information provided by CT as required for dose calculations and the comprehensive motion information from 4D MRI [24]. The motion information extracted from a time-resolved 4D MRI is used to warp a static 3D CT image resulting in a synthetic time-resolved 4D CT. This method was used at PSI to study the impact of motion variabilities on the dose distribution in combination with various mitigation strategies [302–305]. Moreover, it has been validated experimentally for lung proton treatment planning [156]. In Chapter 8 and Chapter 9 we investigate the use of a motion model for tumour tracking in PBS proton therapy on the basis of such 4D CT(MRI) data sets.

Hybrid US/MRI acquisition is a prerequisite for the motion modelling approach presented in this work. Synchronised acquisitions ensure that the US-based surrogate signal and the motion estimates extracted from the 4D MRI coincide temporally. Mutual interferences between the two imaging devices, however, present technical challenges and may result in image artefacts in either modality [212, 275]. The US transducer needs to be insensitive to the high electromagnetic fields and the radiofrequency pulses emitted by the MRI scanner. Conversely, the MRI scanner itself is susceptible to electromagnetic disturbances caused by the US system [275]. A specifically developed MR-compatible US research platform has been developed at Fraunhofer IBMT where the US system including beamformer unit and display was placed near the MR bore [275]. Other groups have performed hybrid US/MRI measurements on clinical US scanners operating outside the Faraday cage of the MR room [173, 212, 239]. The MR-compatible US transducer was connected to the system using a $7\,\mathrm{m}$ to $8\,\mathrm{m}$ long cable passing through the waveguide. Both the transducer and the cable were electromagnetically shielded and grounded to the Faraday cage. The same setup as described in [239] was used for the data acquisitions in this work. In addition, we are currently developing a novel system setup targeting at prolonged data acquisitions, improved system synchronisation, and online access to the US images via an external computer.

4.3 Data processing

4.3.1 Feature extraction form surrogate signals

For 1D or low-dimensional surrogate signals, such as spirometry, respiratory belts, or OTS, the measurements directly represent the respiratory motion. For higher-dimensional surrogate data, in particular image-based approaches, a lower-dimensional motion signal is normally derived by extracting meaningful features through image processing [181]. A plethora of image processing algorithms have been presented and discussed in the literature for different image modalities. Often, the translational motion of surface points or anatomical structures, such as liver vessels or the diaphragm, were tracked [181]. In fluoroscopic images, for example, edge detection was applied for both implanted fiducial and diaphragm tracking [303], while other approaches rely on an active contour model for the diaphragm [141]. In MRI template matching was proposed for predefined regions in 2D slices [4, 285] or surface structures [302]. Using 3D skin-surface data directly, a 1D surrogate signal was extracted by computing the volume between the surface

and the treatment couch [182].

In abdominal US imaging feature tracking is challenging due to low signal-to-noise ratio (SNR) and image artefacts including acoustic shadowing or mirroring. As such, structure or feature tracking in medical ultrasound for real-time applications forms a research field on its own [53]. Numerous methods have been proposed based on speckle tracking [230], optical flow [6, 177], active contours [300], non-rigid image registration [47, 282], supporters [204], and learning-based approaches using image registration [54] and block matching [55], to name but a few. Furthermore, different tracking algorithms for liver structures were compared at the MICCAI Challenge on Liver Ultrasound Tracking (CLUST) [51, 52]. On a more abstract level, A-mode US signals have been used to extract respiratory motion surrogates [218, 220].

In this work, we have applied different approaches for feature extraction among which are vessel and diaphragm tracking [54] in Chapter 5 and principal component analysis (PCA) in Chapters 7 to 9. Furthermore, in Chapter 6 the input images have been implicitly projected into a low-dimensional feature space due to the encoder-decoder network architecture of the motion model.

4.3.2 Motion estimation from imaging data

The motion estimate may be represented as a low-dimensional motion trajectory of the tumour's centre of mass or as a dense deformation vector field (DVF) [181]. For PBS proton therapy, however, anatomical changes introduced by high- or low-density tissue moving in and out of the beam path substantially influence the radiological pathlength. Therefore, the target motion alone is not sufficient but the whole patient geometry is required [19].

The DVF is a spatial transformation mapping and typically describes the spatial correspondence between two images. In medical imaging, it is generally computed using deformable image registration (DIR) [262]. Let $\mathcal{X} = \{x_i\}_{i=1}^{n}$ be a set of regularly distributed grid points x_i of dimension d. Furthermore, let $I_T, I_R : \mathcal{X} \to \mathbb{R}$ be the target and the reference image, respectively, which map the image domain $\mathcal{X} \subset \mathbb{R}^d$ to intensity values. Further, let $\tilde{u} : \mathcal{X} \to \mathbb{R}^d$ denote the spatial mapping which transforms the reference image grid. Then, the registration problem can be formulated as a regularised minimisation problem [127, 237]:

$$\tilde{u}_* = \arg\min_{\tilde{u}} \mathcal{S}(I_R, I_T, \tilde{u}) + \varphi\mathcal{R}(\tilde{u}), \tag{4.2}$$

with the similarity measure $\mathcal{S}$ between the transformed reference image and the target image, and the regulariser $\mathcal{R}$. The spatial transformation, or the DVF, $\tilde{u}_*$ represents a motion estimate. We rearrange the DVF into the column vector $\boldsymbol{y}_t \in \mathbb{R}^v$ as introduced for the regression problem in Equation (4.1).

While most registration approaches enforce smooth continuous transformations [231], the global smoothness assumption does not necessarily hold in medical imaging [145]. For thoracic images in particular, local discontinuities due to sliding organ motion at the thoracic cavity should be preserved [237]. A common approach to circumvent this complication is to restrict the DIR to the region of interest (ROI) using manually defined image masks [226]. Alternatively, discontinuity preserving image registration approaches have been developed [103, 283], many of which in our group [125–127, 131, 132, 237]. Latest developments employ deep neural networks

for DIR in medical images [101, 235]. In this work, we have used two open source registration frameworks namely AIRLab [236] and plastimatch[1] in Chapter 7, 8, and 9. Moreover, we have applied a discontinuity preserving image registration approach [237] in Chapter 6.

4.3.3 Dimensionality reduction

A widespread approach in respiratory motion modelling – for both surrogate data and motion estimates alike – is the use of PCA for dimensionality reduction [181]. In a nutshell, PCA maps the data onto an orthogonal basis given by the eigenvectors of the sample covariance matrix. The new variables, or the principal components, are linear combinations of the original data and pairwise uncorrelated. The PCA can be described as an eigenproblem which, however, is typically formulated as singular value decomposition (SVD), especially for large data matrices. For dimensionality reduction, only the eigenvectors corresponding to the largest eigenvalues are retained as basis vectors in order to maximise the variance in the data while minimising the information loss [124]. In motion modelling specifically, the use of dimensionality reduction based on PCA has been proposed for surrogate signals [54, 274] and motion estimates [219] separately, but also for the two signals combined [179]. In this work, we have used PCA for both feature extraction in abdominal US imaging and dimensionality reduction of the motion estimates as described in Chapter 7, 8, and 9.

4.4 Correspondence models

The correspondence model $f(\cdot, \boldsymbol{\theta})$ describes the relationship between the surrogate and the motion estimate. Its form needs to be defined based on prior assumptions regarding this relationship and may include an explicit definition of the mapping ϕ. As such, various models have been proposed in the literature, among which are linear and polynomial regression, Gaussian process regression (GPR), or neural networks.

For the descriptions below we assume a set of observation $\mathcal{S} = \{(\boldsymbol{x}_t, \boldsymbol{y}_t) \,|\, t = 1, \ldots, m\}$ and introduce a matrix notation. Let $\boldsymbol{X} = \begin{bmatrix}\boldsymbol{x}_1 \boldsymbol{x}_2 \ldots \boldsymbol{x}_m\end{bmatrix}$ be the $u \times m$ input matrix consisting of the surrogate signal and, analogously, $\boldsymbol{Y} = \begin{bmatrix}\boldsymbol{y}_1 \boldsymbol{y}_2 \ldots \boldsymbol{y}_m\end{bmatrix}$ denote the $v \times m$ output matrix consisting of the motion estimates.

4.4.1 Linear Regression

In linear regression, as the name implies, the motion is assumed to be a linear combination of the surrogate signals. It is the most common approach in the field of respiratory motion modelling [181]. Including a constant to the surrogate, that is $\hat{\boldsymbol{x}}_t^T = \begin{bmatrix}1 & \boldsymbol{x}_t^T\end{bmatrix}$, the model can be written in matrix notation as:

$$\boldsymbol{y}_t = \boldsymbol{\theta} \hat{\boldsymbol{x}}_t + \boldsymbol{\epsilon}_t, \tag{4.3}$$

[1] Available online at: https://www.plastimatch.org, accessed 30 April 2020.

or analogously for all observations:

$$\boldsymbol{Y} = \boldsymbol{\theta}\hat{\boldsymbol{X}} + \boldsymbol{E}, \tag{4.4}$$

with $\boldsymbol{\theta} \in \mathbb{R}^{v\times(u+1)}$, $\hat{\boldsymbol{X}} = \begin{bmatrix}\hat{\boldsymbol{x}}_1\hat{\boldsymbol{x}}_2\dots\hat{\boldsymbol{x}}_m\end{bmatrix} \in \mathbb{R}^{(u+1)\times m}$, and $\boldsymbol{E} = \begin{bmatrix}\boldsymbol{\epsilon}_1\boldsymbol{\epsilon}_2\dots\boldsymbol{\epsilon}_m\end{bmatrix} \in \mathbb{R}^{v\times m}$. There are different methods on how to estimate the unknown model parameters $\boldsymbol{\theta}$. The standard approach, however, is ordinary least squares (OLS) which minimises the sum of the square differences between the observed and the estimated variables $\boldsymbol{y}_t$ and $\tilde{\boldsymbol{y}}_t = \boldsymbol{\theta}\hat{\boldsymbol{x}}_t$, respectively. That is:

$$\boldsymbol{\theta}_* = \arg\min_{\boldsymbol{\theta}} \mathcal{C}(\boldsymbol{y}_t, \tilde{\boldsymbol{y}}_t) = \arg\min_{\boldsymbol{\theta}} \sum_{t=1}^{m} (\boldsymbol{y}_t - \boldsymbol{\theta}\hat{\boldsymbol{x}}_t)^2, \tag{4.5}$$

with cost function $\mathcal{C}$. Assuming a set of linearly independent observation $\mathcal{S}$ with $m > u+1$, the solution is given in closed form:

$$\boldsymbol{\theta}_* = \arg\min_{\boldsymbol{\theta}} \|\boldsymbol{Y} - \boldsymbol{\theta}\hat{\boldsymbol{X}}\|^2 \tag{4.6}$$

$$= \boldsymbol{Y}\hat{\boldsymbol{X}}^T \left(\hat{\boldsymbol{X}}\hat{\boldsymbol{X}}^T\right)^{-1}. \tag{4.7}$$

4.4.2 Polynomial regression

Alternatively, one could assume a polynomial function to model a more complex relationship. Similarly to linear models, polynomial regression is widely used in respiratory motion modelling, among which quadratic and cubic models are the most common ones since higher order polynomials tend to overfit the data [181]. A polynomial model of order n is defined as:

$$\boldsymbol{y}_t = \boldsymbol{\theta}_0 + \boldsymbol{\theta}_1\boldsymbol{x}_t + \boldsymbol{\theta}_2\boldsymbol{x}_t^2 + \dots + \boldsymbol{\theta}_n\boldsymbol{x}_t^n, \tag{4.8}$$

with intercept $\boldsymbol{\theta}_0 \in \mathbb{R}^v$, $\boldsymbol{\theta}_i \in \mathbb{R}^{v\times u},\ \forall i \in \{1,\dots,n\}$, and where $\boldsymbol{x}_t^2 = \boldsymbol{x}_t \odot \boldsymbol{x}_t$, and analogously for $\boldsymbol{x}_t^n$, is defined as the element-wise multiplication or Hadamard product. Equation (4.8) can again be written in matrix notation by projecting the input vector into a higher-dimensional feature space, $\hat{\boldsymbol{x}}_t^T = \begin{bmatrix}1 & \boldsymbol{x}_t^T & (\boldsymbol{x}_t^2)^T & \dots & (\boldsymbol{x}_t^n)^T\end{bmatrix} \in \mathbb{R}^{nu+1}$, analogous to Equation (4.3):

$$\boldsymbol{y}_t = \boldsymbol{\theta}\hat{\boldsymbol{x}}_t + \boldsymbol{\epsilon}_t, \tag{4.9}$$

with $\boldsymbol{\theta} = \begin{bmatrix}\boldsymbol{\theta}_0 & \boldsymbol{\theta}_1 & \dots & \boldsymbol{\theta}_n\end{bmatrix} \in \mathbb{R}^{v\times(nu+1)}$. Although the independent variable $\hat{\boldsymbol{x}}_t$ is not linear in $\boldsymbol{x}_t$, the correspondence model is linear with respect to the unknown parameter $\boldsymbol{\theta}$. As such, from an estimation point of view Equation (4.3) and Equation (4.8) are identical. Thus, the solution of the polynomial regression is given in Equation (4.6) using OLS estimation. Here the mapping ϕ is manually engineered and based on prior assumptions about the data distribution. In Chapter 7 we investigate the performance of such a cubic regression model for the case of US probe repositioning.

4.4.3 Gaussian Process regression (GPR)

Another possibility is to assume that the function f is distributed according to a Gaussian process (GP), that is $f \sim \mathcal{GP}(\mu, k)$ with mean function $\mu : \mathbb{R}^u \to \mathbb{R}^v$ and covariance function or kernel $k : \mathbb{R}^u \times \mathbb{R}^u \to \mathbb{R}^{v \times v}$. Broadly speaking, a GP is defined as a distribution over functions or more specifically, as "a collection of random variables, any finite number of which have a joint Gaussian distribution" [290].

The properties of the *prior* distribution, in particular the shape of the covariance function k, represent our prior assumptions on the function characteristics. Given a number of observations $\mathcal{S}$, the set of possible functions is restricted to those passing through the observed data points. The prior distribution in combination with the observations give rise to the *posterior* distribution $p(f|\mathcal{S})$ with reduced uncertainties close to the observations [290]. Assuming a Gaussian likelihood, the posterior is again a Gaussian process $\mathcal{GP}(\mu_S, k_S)$ with mean μ_S and covariance k_S given in closed form. While the mean solves the regression problem, the covariance additionally allows to estimate a confidence interval. It is worth noting that in the context of tumour treatment a confidence value based on the posterior covariance could serve as a quality measure for the motion estimate and might be incorporated in the mitigation strategy. For more details, we refer to Chapter 8.

In contrast to linear and polynomial models described above, we do not assume a fixed relationship between the input and the output for GPR. As such, a GP is a non-parametric model where the posterior distribution over the function f is shaped given the observations S. The properties of the covariance function k, however, are defined by hyperparameters which need to be determined. Moreover, there exist a multitude of possible covariance functions, among which the Gaussian kernel is probably the most common [290]:

$$k(\boldsymbol{x}_t, \boldsymbol{x}_{t'}) = \theta_0^2 \exp\left(-\frac{\|\boldsymbol{x}_t - \boldsymbol{x}_{t'}\|^2}{2\theta_1^2}\right) \boldsymbol{I}_v, \tag{4.10}$$

with scaling parameter θ_0, length-scale or smoothness parameter θ_1, and the v-dimensional identity matrix $\boldsymbol{I}_v$. In particular, a GP using a Gaussian kernel comprises smooth functions [290]. Following Mercer's theorem, it can be shown that the Gaussian kernel, also known as radial basis function (RBF), can be written in terms of an infinite number of orthonormal basis functions [290]:

$$k(\boldsymbol{x}_t, \boldsymbol{x}_{t'}) = \sum_{i=1}^{\infty} \lambda_i \phi_i(\boldsymbol{x}_t) \phi^*(\boldsymbol{x}_{t'}), \tag{4.11}$$

where * denotes complex conjugation. In other words, here the mapping of the input $\boldsymbol{x}_t$ into the feature space is indirectly defined by the choice of the covariance function $k(\cdot, \cdot)$.

Although GPR is a powerful tool, to the best of our knowledge, this framework has not been widely used in respiratory motion modelling for radiotherapy. In a previous work, GPR has been proposed for liver motion modelling using both a patient-specific motion model and a statistical motion model based on nine volunteers [130]. In a simulation study described in Chapter 8 and Chapter 9, we investigate the impact of GPR on the dose distribution in PBS proton therapy of lung cancers.

4.4.4 Neural networks and deep learning

Neural networks are a nested structure of parametric, non-linear functions $\boldsymbol{h}^{(i)} = f^{(i)}(\boldsymbol{x}_t^{(i)}, \boldsymbol{\theta}^{(i)})$ which are differentiable with respect to the parameters $\boldsymbol{\theta}^{(i)}$. Classical feedforward networks can conceptually be split into different layers i, starting with an input layer, followed by multiple hidden layers, up to the output layer. The number of hidden layers defines the network's depth and, as such, increased numbers of hidden layers gave rise to the common terminology *deep neural networks* [82]. In a forward pass, the given input data $\boldsymbol{x}_t^{(0)} = \boldsymbol{x}_t$ is processed by the input layer; its output is fed to the succeeding layer. The input to the hidden layers typically consists at least of the outputs from the preceding layer, that is $\boldsymbol{x}_t^{(i)} = \boldsymbol{h}^{(i-1)}$. The output of the last layer represents the estimated output $\tilde{\boldsymbol{y}}_{\boldsymbol{t}}$. The operations performed in each hidden layer may include linear combinations of the input variables, normalisation, nonlinearity or activation functions, and down- or upsampling operators. Finally, the last component is the cost or objective function $\mathcal{C}$ subsequent to the output layer. In a supervised learning approach, the cost function can be written in the form $\mathcal{C}(\boldsymbol{y}_t, \tilde{\boldsymbol{y}}_t)$. Analogous to Equation (4.5), finding the optimal parameters $\boldsymbol{\theta}_*$ now reduces to a minimisation problem of the form:

$$\boldsymbol{\theta}_* = \arg\min_{\boldsymbol{\theta}} \mathcal{C}(\boldsymbol{y}_t, \tilde{\boldsymbol{y}}_{\boldsymbol{t}}). \tag{4.12}$$

Using the so-called backpropagation algorithm, the derivative of the cost function with respect to the parameters $\nabla_{\boldsymbol{\theta}}\mathcal{C}$ can be computed efficiently by recursively applying the chain rule for differentiation [232]. Given the gradient, different optimisation techniques, such as stochastic gradient descent or momentum methods, may be used to update the parameters [82]. For such learning approaches, the input data is mapped into a feature space as defined by the architecture of the network and the choice of the operations performed in each layer. However, as opposed to the methods introduced above, the parameters of this mapping function are iteratively learned given a (large) set of training data [82].

While the history of neural networks and deep learning dates back to the 1940s, these models have experienced a resurgence in the last two decades and gained in popularity ever since. The advent of more powerful hardware with increased memory size allowed for increased model sizes and more sophisticated model architectures using large data sets, which in turn resulted in increased accuracy for more complex problem formulations [82]. However, in respiratory motion modelling, only a few works exist where neural networks and deep learning were applied. Early work investigated shallow networks, such as single-layer perceptrons [118, 273] or a generalised regression neural network (GRNN) [81]. In a more recent work, a recurrent neural network (RNN) was proposed to generate synthetic MR images given amplitude mode US signals [218]. In Chapter 6, we investigate the use of a conditional generative adversarial network (cGAN) [83, 119] to predict complete MR volumes in a patient-specific motion model.

4.5 Autoregressive models

Motion modelling for real-time tracking of lung or liver tumours in radiotherapy is further complicated by inherent system latencies. The overall system latency describes the time lag between

the target motion and the corresponding adaption of the treatment beam by the tracking system [150]. System latency may include the delay in surrogate acquisition and processing, computation of the motion estimate and the response of the tracking system [181]. In radiotherapy system latencies range from tens to hundreds of milliseconds: $50\,\mathrm{ms}$ and $115\,\mathrm{ms}$ were reported for the VERO system [57] and the Cyberknife [109], respectively, while the numbers are in the range of $160\,\mathrm{ms}$ to $570\,\mathrm{ms}$ for dynamic multileaf collimator tracking systems [136, 151, 215]. To the best of our knowledge, no closed-loop system response time was reported in the literature for PBS proton therapy systems. However, the time needed for beam adaption gives a first estimate of the system latency in case of tumour tracking. While 2D tracking requires lateral beam adaption only, 3D tracking additionally relies on fast energy changes. Fast energy switching times of about $80\,\mathrm{ms}$ were reported for the Gantry 2 at PSI [211, 233]. Lateral beam adaption is generally much faster and roughly an order of magnitude smaller when compared to changes of the beam energy [233].

In order to compensate for these system latencies, respiratory motion models should be designed to predict future motion states with a prediction horizon in the range of the system latency. A large variety of motion prediction methods have been studied and compared in literature including linear regression and support vector predictors, atlas-based methods, Kalman filters, and neural networks [4, 65, 150, 219]. Most approaches for time series prediction are based on an autoregressive (AR) model of order p. That is, at time point t, the signal $\boldsymbol{x}_{t+n}$ is predicted n steps ahead given a set of p preceding observations $\{\boldsymbol{x}_i\}_{t-p+1}^{t}$ [65]. One comparative study reports that multi-layer perceptrons outperform both linear regression and support vector regression. However, the differences between the analysed approaches are relatively small leading to the conclusion that the choice of the model parameters may outweigh the choice of the prediction model [150]. Focusing on different algorithms, another study suggests that machine learning approaches are better suited for longer prediction horizons while a wavelet-based multiscale autoregression model performs best for prediction horizons of up to $150\,\mathrm{ms}$ [65].

In this work, we have used a linear prediction model in Chapter 7 and Chapter 9, while forecasting has been incorporated in the neural network for the method presented in Chapter 6.

4.6 Population-based approaches

The motion modelling pipeline described above implicitly assumed a patient-specific model. However, various population-based methods, also referred to as cross-population approaches, have been proposed for respiratory motion modelling [4, 63, 69, 102, 130, 142, 219]. The general idea is to learn the global motion characteristics from different individuals and use this prior knowledge to infer patient-specific motion estimates. Population-based motion models have the advantage of eliminating the need for patient-specific 4D imaging and, thus, reduce the imaging burden introduced by 4D CT [181]. However, in one study it was reported that the prediction accuracy of the population-based model was significantly lower for impaired lung motion dynamics when compared to intact lungs [63]. Given the large inter-patient variations in respiratory patterns [138], it is questionable whether a population-based approach will achieve superior accuracy when compared to a patient-specific model. Within the scope of this work, we thus focus on patient-specific motion models.

Chapter 5

Ultrasound-driven 4D MRI

The publication presented in this chapter describes a time-resolved 4D MRI method where abdominal US images serve as a surrogate signal for retrospective sorting of 2D MR images acquired under free respiration, hereinafter referred to as US-4DMRI. The presented method is inspired by and compared to the state-of-the-art navigator-based approach which relies on an interleaved acquisition scheme where data and navigator slices are acquired alternately [285]. We compare two different types of feature extraction methods for the US images; the first approach relies on an intensity-based image similarity metric, while the second approach is based on a fiducial tracking algorithm [54].

The proposed US-4DMRI is evaluated on MR liver scans of eight healthy volunteers. The data for this study was acquired within the scope of a preceding project at our group [219]. Both, qualitative and quantitative analyses show that the US-4DMRI performs as well as the state-of-the-art navigator-based approach. Moreover, the proposed US-4DMRI has an increased temporal resolution and a reduced overall acquisition duration.

Publication. The following paper was published in the journal *Physics in Medicine & Biology* (PMB) on the 16th of July 2018[1] [78]. A minor publishing error was corrected in an erratum[2] [77].

[1]Available online at: https://doi.org/10.1088/1361-6560/aaca1d, accessed 12 May 2020.
[2]Available online at: https://doi.org/10.1088/1361-6560/aad482, accessed 12 May 2020.

Citation Alina Giger *et al* 2018 *Phys. Med. Biol.* **63** 145015

Ultrasound-driven 4D MRI

Alina Giger[1,2], Marc Stadelmann[3], Frank Preiswerk[4], Christoph Jud[1,2], Valeria De Luca[5]‡, Zarko Celicanin[1,6], Oliver Bieri[1,6], Rares Salomir[7] and Philippe C. Cattin[1,2]

[1] Department of Biomedical Engineering, University of Basel, Allschwil, Switzerland
[2] Center for medical Image Analysis & Navigation, University of Basel, Allschwil, Switzerland
[3] Institute for Surgical Technology & Biomechanics, University of Bern, Bern, Switzerland
[4] Department of Radiology, Brigham and Women's Hospital, Harvard Medical School, Boston, MA, USA
[5] Computer Vision Laboratory, ETH Zurich, Zurich, Switzerland
[6] Division of Radiological Physics, Department of Radiology, University of Basel Hospital, Basel, Switzerland
[7] Faculty of Medicine, Radiology, University of Geneva, Geneva, Switzerland

E-mail: `alina.giger@unibas.ch`

Abstract. We present an ultrasound-driven 4D magnetic resonance imaging (US-4DMRI) method for respiratory motion imaging in the thorax and abdomen. The proposed US-4DMRI comes along with a high temporal resolution, and allows for organ motion imaging beyond a single respiratory cycle. With the availability of the US surrogate both inside and outside the MR bore, 4D MR images can be reconstructed for 4D treatment planning and online respiratory motion prediction during radiotherapy.

US-4DMRI relies on simultaneously acquired 2D liver US images and abdominal 2D MR multi-slice scans under free respiration. MR volumes are retrospectively composed by grouping the MR slices corresponding to the most similar US images. We present two different US similarity metrics: an intensity-based approach, and a similarity measure relying on predefined fiducials which are being tracked over time. The proposed method is demonstrated on MR liver scans of 8 volunteers acquired over a duration of 5.5 min each at a temporal resolution of 2.6 Hz with synchronous US imaging at 14 Hz to 17 Hz. Visual inspection of the reconstructed MR volumes revealed satisfactory results in terms of continuity in organ boundaries and blood vessels. In quantitative leave-one-out experiments, both US similarity metrics reach the performance level of state-of-the-art navigator-based approaches.

Keywords: 4D imaging, 4D MRI, hybrid ultrasound/MR imaging, radiotherapy, respiratory motion

Submitted to: *Phys. Med. Biol.*

‡ now at the Novartis Institute for BioMedical Research, Basel, Switzerland

1. Introduction

Time-resolved volumetric imaging, or 4D imaging, is a key factor in respiration induced organ motion quantification and finds use in several clinical applications, such as high-intensity focused ultrasound (HIFU) ablation (Schwenke, Strehlow, Haase, Jenne, Tanner, Langø, Loeve, Karakitsios, Xiao, Levy et al. 2015) or radiotherapy of thoracic and abdominal tumours (Buerger, Clough, King, Schaeffter & Prieto 2012, Stemkens, Tijssen, de Senneville, Lagendijk & van den Berg 2016). In radiotherapy, accurate knowledge about respiratory motion is crucial for both 4D treatment planning and precise tumour tracking during dose delivery. Therefore, 4D imaging is inevitable when high-precision radiotherapy techniques should be translated from static to mobile treatment targets. For example, in active scanning proton therapy, respiration-induced organ deformations in combination with dynamic dose delivery cause interplay effects that adversely affect treatment quality and may lead to inhomogeneous dose distributions (Phillips, Pedroni, Blattmann, Boehringer, Coray & Scheib 1992, Bert & Durante 2011). In this context, 4D imaging can form the basis for respiratory motion models and eventually enable highly conformal radiation procedures.

At present, 4D computed tomography (4D CT) is the preferred imaging modality for treatment planning in radiotherapy (Hugo & Rosu 2012). The main difficulty, however, lies in the inevitable trade-off between radiation dose delivered to the patient and image quality. As 4D CT methods generally assume a constant respiration period, respiration variabilities often lead to serious image artifacts and volume inconsistencies (Yamamoto, Langner, Loo, Shen & Keall 2008, Johnston, Diehn, Murphy, Loo & Maxim 2011). In order to overcome these issues, recent developments have increasingly focused on 4D magnetic resonance imaging (4D MRI). The absence of radiation dose in MRI allows for longer scan durations and superior soft-tissue contrast enhances tumour/tissue delineation (Neto, Elazzazzi, Altun & Semelka 2008). Moreover, MRI offers the possibility of selecting the imaging plane in the main direction of motion, i.e. in sagittal direction, which further reduces motion artifacts (Liu, Yin, Chang, Czito, Palta, Bashir, Qin & Cai 2014).

Although possible, dynamic 3D MRI is not favourable for respiratory motion imaging since it suffers from low temporal or spatial resolution if large volumes need to be scanned (Blackall, Ahmad, Miquel, McClelland, Landau & Hawkes 2006, Dinkel, Hintze, Tetzlaff, Huber, Herfarth, Debus, Kauczor & Thieke 2009). Consequently, various methods based on retrospective binning of partial image data have been proposed. 2D MR images at varying slice positions are continuously acquired while the patient's respiratory motion is recorded either using external surrogates, such as belt respiration sensors (Tryggestad, Flammang, Han-Oh, Hales, Herman, McNutt, Roland, Shea & Wong 2013), or internal image-based metrics which are derived from MR signals directly. Examples of the latter are body area (Cai, Chang, Wang, Segars & Yin 2011, Liu et al. 2014), body boundaries in combination with low-frequency components in the Fourier domain (Hui, Wen, Stemkens, Tijssen, van den Berg,

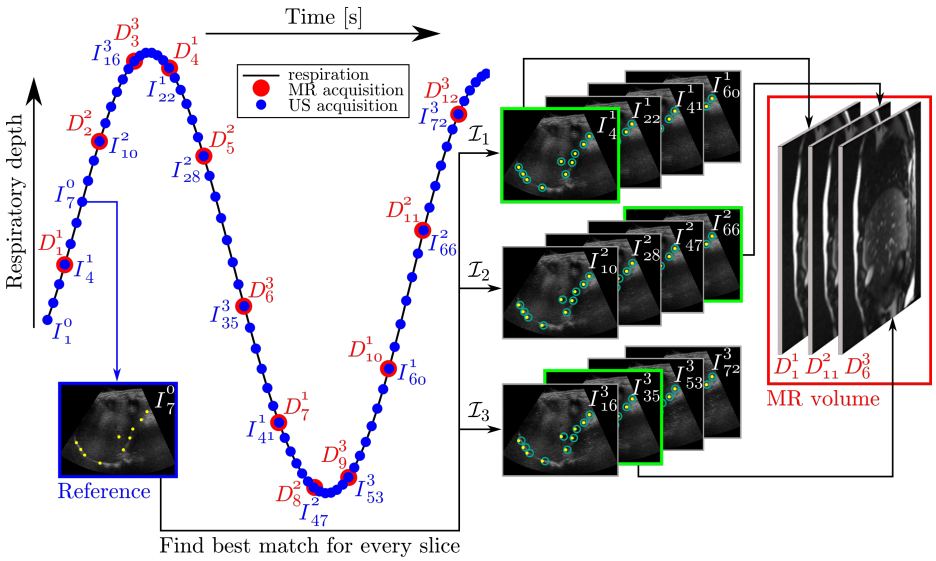

Figure 1: Principle of US-4DMRI: simplified acquisition scheme with $n = 3$ slices per MR volume and US fiducial tracking as surrogate data. For each point of the respiratory cycle (blue dots), one MR volume is reconstructed. To do so, the US images $I^s_{i_{\mathrm{US}}}$, which were acquired simultaneously with an MR scan $D^s_{i_{\mathrm{MR}}}$, are grouped into subsets $\mathcal{I}_s$ according to the MR slice position s. For a given reference (blue frame), the best matching US image for each slice position (green frames) is identified based on automatically tracked US fiducials (marked as yellow dots and green circles). Finally, the corresponding MR scans are stacked into a 3D image (red frame).

Hwang & Beddar 2016), mutual information (Paganelli, Summers, Bellomi, Baroni & Riboldi 2015), manifold learning (Wachinger, Yigitsoy, Rijkhorst & Navab 2012), and deformation fields of interleaved navigator slices (Von Siebenthal, Gamper, Boesiger, Lomax, Cattin et al. 2007). Based on the surrogate data, the MR scans are attributed to different respiratory states and 3D MR volumes are reconstructed. Similarly, retrospective sorting of 3D-acquired k-space data based on MR navigators or self-navigation techniques has also been proposed (Buerger et al. 2012, Stemkens, Tijssen, de Senneville, Heerkens, van Vulpen, Lagendijk & van den Berg 2015, Rank, Heußer, Buzan, Wetscherek, Freitag, Dinkel & Kachelrieß 2017, Mickevicius & Paulson 2017).

External surrogates rely on the correlation between the external signal and internal organ motion which is not always valid (von Siebenthal, Székely, Lomax & Cattin 2007, Stemkens et al. 2015). Conversely, image-based metrics and self-navigation are powerful tools for MR-guided interventions and radiotherapy (Stemkens et al. 2016). However, when it comes to proton therapy, the connection between pretreatment 4D MRI and motion estimation during dose delivery is not straightforward as these

surrogates are not available outside the MR bore. To overcome these issues, hybrid ultrasound (US) and MRI acquisition offers a promising approach since US imaging provides internal organ motion data while being available both inside and outside the MR bore. Only recently, single-element US signals, MRI and regression-based methods have been combined for generating synthetic MR images (Preiswerk, Toews, Hoge, Chiou, Panych, Wells III & Madore 2015, Preiswerk, Toews, Cheng, Chiou Jr, Mei, Schaefer, Hoge, Schwartz, Panych & Madore 2016).

In this work, we introduce 2D US surrogates of the liver and the diaphragm for retrospectively stacking abdominal MR images, as shown in figure 1. By using hybrid US/MRI imaging, we propose an ultrasound-driven 4D MRI (US-4DMRI) with increased temporal resolution and reduced overall acquisition duration as compared to navigator-based approaches. We investigate the applicability of US surrogates for retrospective 4D MRI by formulating two different US similarity metrics, and compare the performance of US-4DMRI with the navigator-based 4D MRI in (Von Siebenthal, Gamper, Boesiger, Lomax, Cattin et al. 2007).

2. Materials and methods

2.1. Simultaneous US and MR data acquisition

The data used in the present work have been acquired as part of a related study (Preiswerk, De Luca, Arnold, Celicanin, Petrusca, Tanner, Bieri, Salomir & Cattin 2014). For details on the experimental setup and acquisition parameters, the reader is referred to (Petrusca, Cattin, De Luca, Preiswerk, Celicanin, Auboiroux, Viallon, Arnold, Santini, Terraz et al. 2013) and (Preiswerk et al. 2014).

Simultaneous US/MR acquisitions were performed in a 1.5 T MR scanner. We applied a balanced steady-state free precession MR pulse sequence and, for validation purposes, an interleaved acquisition scheme (Von Siebenthal, Gamper, Boesiger, Lomax, Cattin et al. 2007), where data and so-called navigator slices were acquired alternatingly. 2D multi-slice MR scans were acquired at a frame rate of $f_{\mathrm{MR}} \approx 5.2\,\mathrm{Hz}$, or $f^d_{\mathrm{MR}} = f_{\mathrm{MR}}/2 \approx 2.6\,\mathrm{Hz}$ for data slices d only, with a spatial resolution of 1.82 mm and a slice thickness of 4.02 mm. The US frame rate was 14 Hz to 17 Hz.

Eight US/MR liver data sets were recorded for a total duration of 5.5 min each. No subject showed signs of hepatic disorders. Sagittal MR slices were positioned to cover the right liver lobe and scanned the region of interest (ROI) in sequential order. The navigator was acquired at a fixed location in the sagittal plane in order to minimize out-of-plane motion of liver vessels during respiration (Rohlfing, Maurer, O'dell & Zhong 2004). The MR-compatible US probe was either placed on the 6th or 7th right intercostal space, respectively, or frontally on the abdomen resulting in sagittal-oblique images. The volume acquisition time t_{vol}, defined as the time needed for a complete scan of the target volume, ranged from 10.1 s to 11.7 s. The signal properties for all subjects k are summarized in table 1.

Table 1: Signal properties of the liver data sets. At each slice position $s \in \{1, \dots, n\}$, a total of $|\mathcal{I}_s|$ MR data scans were acquired; the overall number of data scans is $N^d = n|\mathcal{I}_s|$; the volume acquisition time is $t_{vol} = n/f^d_{\mathrm{MR}}$.

Subject k	1	2	3	4	5	6	7	8
General information [–]								
No. of respiratory cycles	97	61	71	94	96	52	58	63
No. of MR slice positions, n	30	30	30	30	30	30	26	28
No. of MR images per slice pos., $\lvert\mathcal{I}_s\rvert$	28	28	28	28	28	28	30	28
No. of MR data images, N^d	840	840	840	840	840	840	780	784
Volume acquisition time, t_{vol} [s]	11.7	11.7	11.6	11.7	11.6	11.7	10.1	10.9
Temporal resolution [Hz]								
f_{MR} (data and navigator scans)	5.12	5.12	5.16	5.12	5.16	5.12	5.16	5.16
f^d_{MR} (data scans only)	2.56	2.56	2.58	2.56	2.58	2.56	2.58	2.58
f_{US}	16.0	16.0	17.0	17.0	17.0	14.0	15.0	15.0

2.2. Ultrasound-driven 4D MRI

The main principle of US-4DMRI is shown in figure 1. Let f^d_{MR} and f_{US} represent the MR and US acquisition frame rates. Let i_{MR} and i_{US} define the indices of MR data scans and US images, respectively. Then,

- $D^s_{i_{\mathrm{MR}}}$ denotes the MR scan acquired at time $t_{i_{\mathrm{MR}}} = i_{\mathrm{MR}}/f^d_{\mathrm{MR}}$ and slice position s,
- $I^s_{i_{\mathrm{US}}}$ denotes the US image corresponding to $D^s_{i_{\mathrm{MR}}}$, acquired at time $t_{i_{\mathrm{US}}} = i_{\mathrm{US}}/f_{\mathrm{US}}$,
- $I^\circ_{i_{\mathrm{US}}}$ denotes the remaining US images at times $t_{i_{\mathrm{US}}}$ with no corresponding MR scan.

Note that $t_{i_{\mathrm{MR}}}$ and $t_{i_{\mathrm{US}}}$ do not necessarily coincide. However, since f_{US} is considerably higher than f^d_{MR}, we assume that the MR slice $D^s_{i_{\mathrm{MR}}}$ and its temporally closest US image $I^s_{i_{\mathrm{US}}}$ represent the liver in a sufficiently similar state.

For every $t_{i_{\mathrm{US}}}$ of the respiratory motion (blue dots in figure 1), a complete MR volume is reconstructed, resulting in a 4D image frame rate of $f_{4\mathrm{D}} = f_{\mathrm{US}}$. We generate n subsets $\mathcal{I}_s$ each of them comprising all US images associated with the given MR slice position s, that is $\mathcal{I}_s = \{I^{s'}_{i_{\mathrm{US}}} \,|\, s' = s\}$. The US image $I_{i_{\mathrm{US}}}$, being either $I^s_{i_{\mathrm{US}}}$ or $I^\circ_{i_{\mathrm{US}}}$, serves as reference (blue frame in figure 1) in order to find the best matching image $I^s_{j^*_{\mathrm{US}}} \in \mathcal{I}_s$ for each slice position s (green frames in figure 1) by solving

$$j^* = \arg\min_j S(I_{i_{\mathrm{US}}}, I^s_{j_{\mathrm{US}}}), \tag{1}$$

with similarity measure S. Then, the corresponding MR scans $D^s_{j^*_{\mathrm{MR}}}$ build the final MR volume for time $t_{i_{\mathrm{US}}}$. The optimal US image $I^s_{j^*_{\mathrm{US}}}$ is determined by exhaustive search on the subset $\mathcal{I}_s$. Alternatively, the N_{avg} best matching scans could be averaged in order to increase the signal-to-noise ratio (Von Siebenthal, Gamper, Boesiger, Lomax, Cattin et al. 2007).

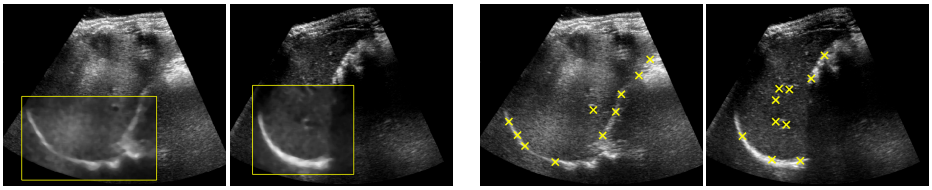

(a) (b)

Figure 2: US surrogate data for two different subjects. (a) The intensity-based similarity metric was computed as the MAD of the image area inside the highlighted rectangle. (b) The selected fiducials are marked as yellow crosses. Since the acoustic window of the left image reveals only few vessel structures, most fiducials were placed on the liver boundary. Conversely, in the right image the fiducials were equally distributed on vessel centers and the diaphragm.

2.2.1. Similarity measure Automatically tracked US fiducials have shown to be suitable surrogates for the respiratory motion model in (Preiswerk et al. 2014). In this work, we examine the applicability of US feature tracking in the context of 4D MRI. Below, we additionally introduce a comparison method which is directly computed on image intensities.

Intensity-based Dealing with mono-modal surrogate images, the mean absolute intensity difference (MAD) represents a computationally efficient similarity metric. In order to further reduce computational time and since the respiratory motion closely correlates with the motion of the diaphragm, we selected a ROI around the liver boundary. A median filter with a fixed window size of 10 was then applied to reduce speckles. Let $\mathcal{R}$ represent the ROI and $\tilde{I}_{i_{\mathrm{US}}}(r) \in \{0, \dots 255\}$ the intensity value of the median filtered US image at pixel location r. Then, the similarity term can be formulated as

$$S_{\mathrm{MAD}}(I_{i_{\mathrm{US}}}, I^s_{j_{\mathrm{US}}}) = \frac{1}{|\mathcal{R}|} \sum_{r \in \mathcal{R}} |\tilde{I}_{i_{\mathrm{US}}}(r) - \tilde{I}^s_{j_{\mathrm{US}}}(r)|. \tag{2}$$

Figure 2a shows sample US images with the cropped and median-filtered ROI overlaid.

Fiducial tracking For each US sequence, we manually selected between 5 and 11 fiducials on a reference image at end-exhalation as shown in figure 2b. These fiducials correspond to dominant anatomical structures, e.g. points on the diaphragm and vessel centers, and their positions were tracked over time. Considering the target application of US-4DMRI in real-time tumour tracking, a computationally fast image registration method was used (De Luca, Tanner & Székely 2012), which enables real-time position prediction by taking advantage of the recurrence in organ position between different respiratory cycles. We assume the liver at times $t_{i_{\mathrm{US}}}$ and $t_{j_{\mathrm{US}}}$ to be in a comparable

state if the fiducials of $I_{i_{\mathrm{US}}}$ and $I^s_{j_{\mathrm{US}}}$ coincide. Moreover, similar velocities foster a grouping of images at comparable characteristic points of the respiratory cycle: the spatial variation between two temporally consecutive US images near end-exhalation or end-inhalation will be much smaller as compared to the spatial difference of a mid-cycle pair of images. In addition, including the direction of the trajectories avoids matching exhalation frames during inhalation, and vice versa.

Let $\boldsymbol{x}_l(t_{i_{\mathrm{US}}}) \in \mathbb{R}^2$ denote the position of the l-th fiducial at time $t_{i_{\mathrm{US}}}$, with $l \in \{1, \ldots, m\}$ and m being the total number of fiducials. Similarly, let $\Delta\boldsymbol{x}_l(t_{i_{\mathrm{US}}}) = \boldsymbol{x}_l(t_{i_{\mathrm{US}}}) - \boldsymbol{x}_l(t_{i_{\mathrm{US}}-1})$ be the spatial variation of the l-th fiducial between two temporally consecutive US images. We define the similarity measure as

$$S_{\mathrm{Fid}}(I_{i_{\mathrm{US}}}, I^s_{j_{\mathrm{US}}}) = \sum_{l=1}^{m} \|\boldsymbol{x}_l(t_{i_{\mathrm{US}}}) - \boldsymbol{x}_l(t_{j_{\mathrm{US}}})\| + \omega \sum_{l=1}^{m} \|\Delta\boldsymbol{x}_l(t_{i_{\mathrm{US}}}) - \Delta\boldsymbol{x}_l(t_{j_{\mathrm{US}}})\|, \tag{3}$$

with Euclidean norm $\|\cdot\|$ and weight ω. The latter was empirically determined using grid search on a training set.

2.3. Evaluation methods

2.3.1. Leave-one-out experiments Given the image pair $I^s_{i_{\mathrm{US}}}$ and $D^s_{i_{\mathrm{MR}}}$, we identified the best matching US image $I^s_{j^*_{\mathrm{US}}} \in \mathcal{I}_s \setminus \{I^s_{i_{\mathrm{US}}}\}$ such that equation (1) held. The actual MR image $D^s_{i_{\mathrm{MR}}}$ at $t_{i_{\mathrm{US}}}$ served as ground truth and was compared to the optimal solution $D^s_{j^*_{\mathrm{MR}}}$ acquired at the same slice position s but at a different point of time, $t_{j_{\mathrm{US}}}$.

The data was split into a training set acquired at even slice positions $s_{even} \in \{2, 4, \ldots, n\}$, and a validation set with $s_{odd} \in \{1, 3, \ldots, n-1\}$. Quantitative validation involved leave-one-out experiments for all s_{odd} and for each image in the associated subset, that is $\forall I^{s_{odd}}_{i_{\mathrm{US}}} \in \mathcal{I}_{s_{odd}}$. The difference between the selected MR image $D^s_{j^*_{\mathrm{MR}}}$ and the true left-out image $D^s_{i_{\mathrm{MR}}}$ was quantified as the MAD of the pixel intensities contained in a predefined ROI around the liver. For each subject, the ROI was manually specified as the minimum bounding box which contains the entire liver for all respiratory states. In order to achieve optimal image contrast within the ROI, we applied a low-pass image filter.

Note that the design of the leave-one-out experiments implies a reconstruction rate of f^d_{MR} since the MR ground truth images $D^s_{i_{\mathrm{MR}}}$ cannot be acquired at higher frame rates. The supplementary material to this paper provides movies of 4D MR images at different frame rates ranging from $f_{4\mathrm{D}} = f^d_{\mathrm{MR}}$ to $f_{4\mathrm{D}} = f_{\mathrm{US}}$.

2.3.2. Slice selection Having both US images and MR navigators as surrogates for the given data, we investigated whether the same MR images were selected for either of the two methods. Assume we aim to reconstruct an MR volume at time $t_{i_{\mathrm{US}}}$. Let $u \in \{1, \ldots, |\mathcal{I}_s|\}$ denote the index of the optimal MR scan $D^s_{j^*_{\mathrm{MR}}}$ within the subset

Table 2: Statistical results of leave-one-out experiments for tuning of ω. The best results are highlighted in bold font.

ω	0.00	0.25	0.50	0.75	1.00	1.25	1.50
mean	2.32	**2.22**	**2.22**	2.23	2.25	2.26	2.27
median	2.14	**2.08**	**2.08**	2.10	2.12	2.13	2.13
standard deviation	0.93	**0.81**	**0.81**	0.82	0.83	0.84	0.84

$\mathcal{I}_s$ determined by US-4DMRI. Analogously, let $v \in \{1, \ldots, |\mathcal{I}_s|\}$ represent the index of the selected MR scan for navigator-based stacking. We computed the joint sample distribution $p(u, v) \in [0, 1]$ for the complete 4D image, not taking into account the cases where a ground-truth MR image $D^s_{i_{\mathrm{MR}}}$ exists. The probabilities were computed for the validation set only.

3. Experiments and results

The reconstruction was based on $|\mathcal{I}_s| = 30$ images per slice position for Subject 7 and $|\mathcal{I}_s| = 28$ images for the remaining subjects. We omitted noise reduction through averaging and set $N_{\mathrm{avg}} = 1$ for all results below. For an in-depth analysis of the fiducial tracking approach, we refer to (Preiswerk et al. 2014) and (De Luca et al. 2012).

3.1. Parameter tuning

The weight ω in (3) was determined based on leave-one-out experiments on the training set. Table 2 summarizes the mean, median and standard deviations of the resulting error distributions. The results indicate that the stacking performance improves when taking the spatial variations $\Delta \boldsymbol{x}_l$ into account ($\omega > 0$). Table 2 further shows that the proposed similarity measure is robust against the choice of ω. Equal results were obtained for weighting factors $\omega = 0.25$ and $\omega = 0.5$, and the statistical measures increased only slightly for $\omega \geq 0.75$. In the following, $\omega = 0.25$ was selected.

3.2. Slice selection

For the sake of conciseness, we focus on US-4DMRI relying on fiducial tracking for slice selection analysis. Figure 3a shows from left to right the reference US image $I^s_{i_{\mathrm{US}}}$, the best matching US image $I^s_{j^*_{\mathrm{US}}}$ and the absolute intensity difference between the two for a representative case. The tracked US fiducials are indicated with yellow dots and green circles, respectively. Figure 3b displays the corresponding MR ground truth $D^s_{i_{\mathrm{MR}}}$, the optimal data scan $D^s_{j^*_{\mathrm{MR}}}$ and the difference between these. Visual comparison between the US ground truth and the optimal solution reveals a good alignment of the tracked fiducials. Only small intensity differences in both US and MR images can be observed.

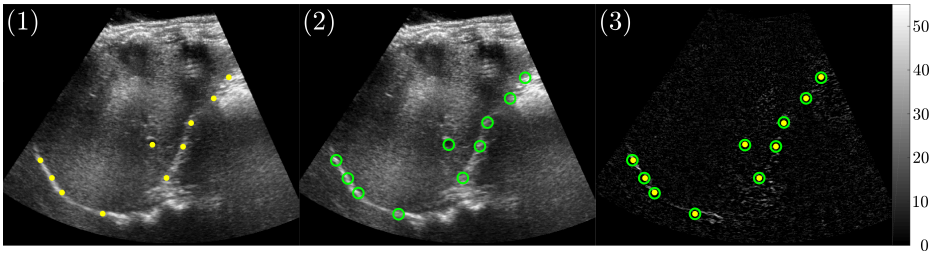

(a)

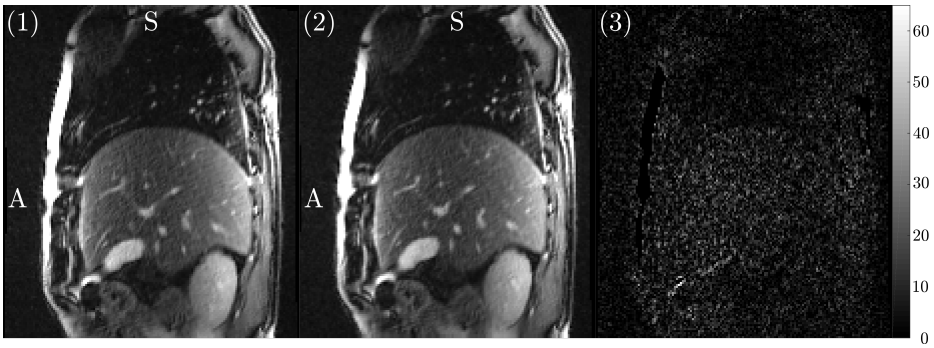

(b)

Figure 3: Slice selection based on US fiducial tracking for Subject 1 and slice position $s = 9$. The images represent from left to right, (1) the ground truth image, (2) the selected optimal image and (3) the absolute intensity difference between (1) and (2). The US and MR image intensities are in the range of 0–255; the intensity differences are defined by the color bars in (3). (a) US images with tracked fiducials, and (b) the corresponding MR scans acquired in sagittal direction.

When comparing the 4D MR images obtained by US-4DMRI and the navigator-based approach, respectively, we find that overall 22.9% of the selected MR scans are identical. Figure 4 shows the 2D histogram of $p(u, v)$ for each subject k separately. The probability value in the upper left corner indicates the percentage of identical MR images for the respective subject, i.e. $p_k := p_k(u = v)$. Note that the histograms do not give information about the superiority of either method. Yet, the joint histograms reveal some interesting insights: for Subject 6, pronounced off-diagonal lines can be observed on either side of the diagonal (highlighted with arrows). The periodic occurrence of the off-diagonal lines suggests that Subject 6 shows a regular respiration pattern with distinctive organ states. Conversely, a less pronounced respiration pattern can be observed for Subject 1 which shows a more uniformly distributed joint probability $p_1(u, v)$.

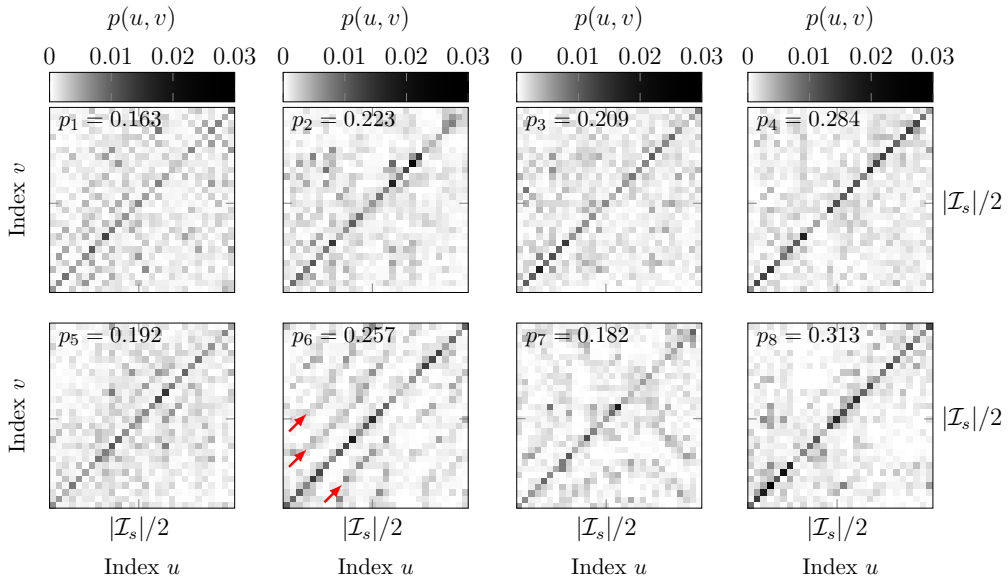

Figure 4: Slice selection illustrated as joint histogram for navigator-based 4D MRI and US-4DMRI, respectively, and for each subject k separately. The probability values p_k denote the percentage of equally selected MR images by both methods, i.e. $p_k = p_k(u = v)$.

3.3. Qualitative validation

Figure 5 shows orthogonal cuts through reconstructed MR volumes of Subject 1 and Subject 6, respectively, at end-exhalation and end-inhalation of a sample respiratory cycle. From left to right, the results for the three stacking methods are presented: (1) navigator-based 4D MRI (Von Siebenthal, Gamper, Boesiger, Lomax, Cattin et al. 2007), (2) US-4DMRI relying on the fiducials' positions and velocities, and (3) intensity-based US-4DMRI. Furthermore, random stacking (4) is shown as upper baseline. If properly stacked, smooth organ boundaries and vessel structures in axial and coronal plane are to be expected.

In both figures, a vertical stripe artifact can be observed as indicated with arrows in the leftmost columns. This artifact is a consequence of the interleaved acquisition scheme and indicates the position of the navigator: as every second MR scan was acquired at the same position, the tissue in that region was excited more frequently and therefore underwent saturation. In the case of US-4DMRI, the stripe artifact will no longer be visible.

Figure 5a and figure 5b reveal additional stacking artifacts at end-inhalation. For US-4DMRI, the dominant vascular structure and the anterior abdominal wall are

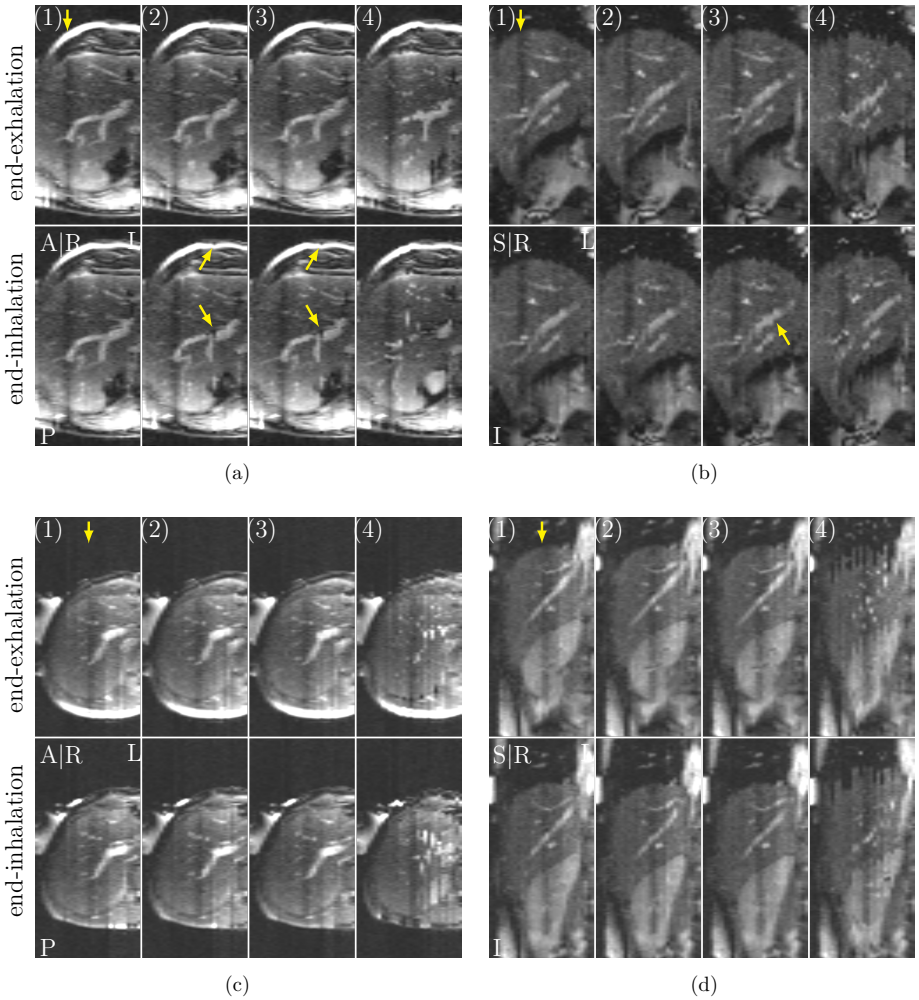

Figure 5: Axial and coronal cuts through stacked MR volumes of (a),(b) Subject 1 and (c),(d) Subject 6 for (1) navigator-based 4D MRI, (2) US-4DMRI relying on fiducial tracking, (3) intensity-based US-4DMRI, and (4) random stacking. The images show the liver at end-exhalation (upper rows) and end-inhalation (lower rows) of a sample respiratory cycle. The arrows in the leftmost column point at the saturation artifacts caused by the interleaved acquisition scheme, while the remaining arrows indicate stacking artifacts.

distorted due to an improperly chosen MR slice. At end-exhalation, no substantial differences were detected between results for the navigator-based approach and US-

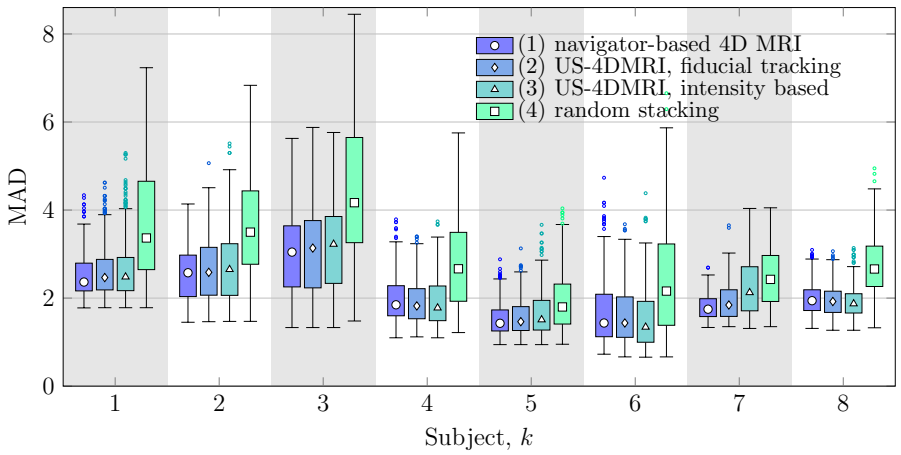

Figure 6: Error distributions of the leave-one-out experiments for each subject k and sorting method (intensity range 0–255). The whiskers comprise all samples within 1.5 times the interquartile range (IQR) above and below the box.

4DMRI, respectively. Note that the qualitative results shown in figure 5a and figure 5b depict the results of Subject 1 for which the navigator-based 4D MRI and US-4DMRI differ most according to the joint histogram in figure 4. Conversely, axial and coronal cuts of Subject 6 in figure 5c and figure 5d show smooth liver boundaries and vascular structures both at end-exhalation and end-inhalation for all stacking methods.

3.4. Quantitative validation

The statistical evaluation presented below is based on paired t-tests; p-values and effect size in terms of Cohen's d are reported. The significance level was set to 1 %.

3.4.1. Results per subject Figure 6 shows the error distributions obtained for stacking methods (1)–(4), as defined in section 3.3, and for each subject k individually. The error distributions contain between $N^d/2 = 390$ and $N^d/2 = 420$ test samples.

In general, methods (1)–(3) performed significantly better than random stacking ($p < 0.001$, $0.35 < d < 1.61$). Comparable results were obtained for stacking methods (1) and (2) where the most significant differences were observed for Subject 1 ($p < 0.001$, $d = 0.22$) and Subject 7 ($p < 0.001$, $d = 0.30$), while for the remaining subjects either no significant difference ($p > 0.03$ $k \in \{6, 8\}$) or a negligible effect size ($d < 0.15$) were found. The same applies when comparing (1) and (3): Cohen's d was in the range of 0.24 and 0.30 for $k \in \{1, 2, 5\}$ and below 0.17 for the remaining data sets. The only exception is Subject 7, where the navigator-based approach clearly outperformed intensity-based US-4DMRI ($p < 0.001$, $d = 0.90$).

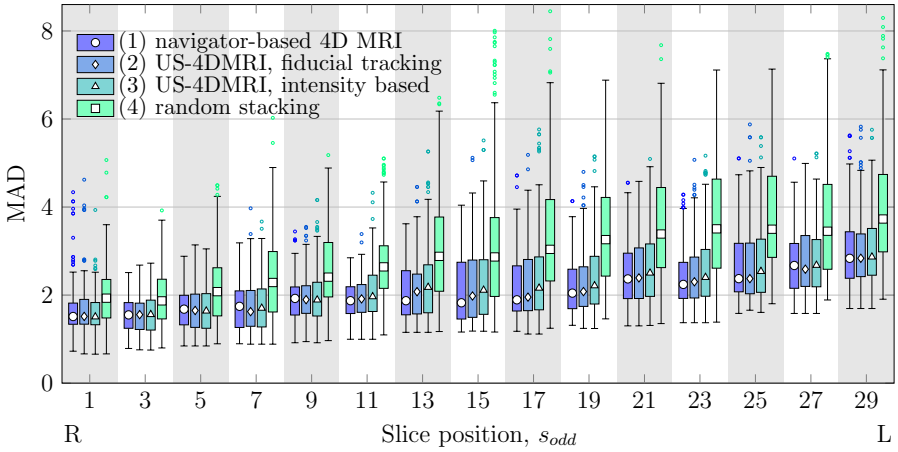

Figure 7: Error distributions of the leave-one-out experiments for each slice position s_{odd} and sorting method (intensity range 0–255). The whiskers have a maximum length of 1.5 IQR.

When comparing (2) and (3), the former outperformed intensity-based US-4DMRI in five out of eight cases. Yet, the difference was either not significant ($p > 0.02$, $k \in \{4, 8\}$) or negligible ($d < 0.20$), with the exception of Subject 7 ($p < 0.001$, $d = 0.65$).

3.4.2. Results per slice position The box plots in figure 7 display the error distributions cumulated over all subjects and for each s_{odd} separately with a total number of 168–226 samples per slice position. Low slice numbers represent the anatomical right (R) side; with increasing s_{odd} the MR slice moves towards the umbilical fissure on the left side (L) of the right liver lobe.

The error for the navigator-based approach and both US-4DMRI was significantly lower than for random stacking ($p < 0.001$, $0.56 < d < 1.23$). In general, the navigator-based approach achieved better results as compared to the US-driven 4D MRI methods. This was observed most clearly for slice positions 11–19 and 23: for these slice positions, (1) outperformed (3) with small yet non-negligible effect size ($0.23 < d < 0.35$). Comparing (1) and (2) either revealed no statistical significant difference ($p > 0.02$, $s_{odd} = 23$) or an effect size below 0.15 ($s_{odd} \in \{11, \ldots, 19\}$).

3.5. Computation times

In order to reconstruct one MR volume, navigator-based 4D MRI and intensity-based US-4DMRI required on average 120 ms and 84 ms, respectively. It is important to note that navigator-based 4D MRI additionally requires image registration for all navigators

since the stacking is based on deformation field differences (Von Siebenthal, Gamper, Boesiger, Lomax, Cattin et al. 2007). The computational time for the registration is not included in the value reported above. For US fiducial tracking, a mean computation time of 9 ms per US image was reported (De Luca et al. 2012). Based on these fiducials, volume reconstruction was performed in 3 ms on average, resulting in a mean computation time of 12 ms per volume. All values were computed for a MATLAB (The MathWorks, Inc., Natick, Massachusetts, USA) implementation on a standard CPU.

4. Discussion

Qualitative analysis of sample MR volumes showed only minor distortions and discontinuities in liver boundaries, emphasizing the feasibility of the proposed US-driven stacking methods. When comparing end-inhalation with end-exhalation volumes, more satisfactory results were obtained in the latter case. We explain this observations with the hysteresis in respiratory motion (Seppenwoolde, Shirato, Kitamura, Shimizu, Van Herk, Lebesque & Miyasaka 2002). Longer time intervals at end-exhalation lead to an increased number of MR scans acquired near exhalation and to improved stacking results.

With regard to quantitative results, small effect sizes in terms of Cohen's d evince that the proposed US-4DMRI is able to compete with the navigator-based 4D MRI independent of the choice of the US similarity measure. A comparison of the two US surrogates suggests that US-4DMRI based on fiducial tracking achieves better results than intensity-based US-4DMRI. Yet, a relevant effect size was measured for one subject only. In terms of computation times, fiducial-based US-4DMRI clearly outperformed the other approaches. Although manual fiducial selection introduces additional complexity to US-4DMRI as compared to the purely intensity-based approach, the shorter computation times might outweigh the extra effort for real-time applications, such as image-guided proton therapy.

Figure 7 shows an increase in the error from the anatomical right to the left side. We explain this observation by the increased presence of vessel structures in the region of the inferior vena cava and the portal vein. Since blood vessels show high image contrast in MRI, the MAD will be higher for slices farther away from the right liver boundary. Cardiac motion might have additional adverse effects on the stacking quality in the region of large blood vessels.

Limitations and future work The number of MR images per slice position available for stacking was $|\mathcal{I}_s| = 30$ or $|\mathcal{I}_s| = 28$ and thus 6 to 8 times smaller than in (Von Siebenthal, Gamper, Boesiger, Lomax, Cattin et al. 2007). The relatively short acquisition duration of 5.5 min per subject implies that long-term effects cannot conclusively be discussed in the present work. However, similar to the navigator-based approach, the use of internal surrogate data potentially enables the proposed US-4DMRI to obtain satisfactory results even in the case of organ drift. Additional experiments with longer scan durations will

be performed in order to evaluate the capability of US-4DMRI to cope with long-term deformations and organ drift.

The number of MR images per slice position $|\mathcal{I}_s|$ further has a direct impact on the achievable temporal resolution of the 4D image: since the MR slices for volume reconstruction are repeatedly selected from constant and finite image sets $\mathcal{I}_s$, the variation in MR volumes is confined too. The supplementary material to this paper showed that visually no difference between the 4D images at $f_{4\mathrm{D}} = 8\,\mathrm{Hz}$ and $f_{4\mathrm{D}} = 16\,\mathrm{Hz}$ could be observed for the given amount of data. In future work, we aim for a temporal resolution of up to 10 Hz or approximately 40 MR volumes per respiratory cycle given lager data sets. The clinical benefit of increased temporal resolution on motion models, however, remains to be shown.

A common limitation of all retrospective slice stacking approaches is their failure of reconstructing anatomically plausible MR volumes if the desired organ state was not captured at each slice position. This issue becomes accentuated for extreme respiration depths or in the presence of coughing. As an extension, (Preiswerk et al. 2016) presented a cough-detector based on the US signal itself. For US-4DMRI an upper threshold to the similarity measure could be applied in order to exclude deficient 3D images (Von Siebenthal, Gamper, Boesiger, Lomax, Cattin et al. 2007). Further extensions to the proposed US-4DMRI will include cardiac motion when the US acoustic window captures the inferior vena cava and its pulsation. Uniquely from other respiratory surrogate methods, US imaging provides internal motion signals at a temporal resolution substantially higher than normal resting heart rate in adults (Aladin, Whelton, Al-Mallah, Blaha, Keteyian, Juraschek, Rubin, Brawner & Michos 2014). Colour Doppler imaging can provide additional information on the speed and the direction of blood flow through vessels (Crowe, Manasseh, Chmielewski, Hachulla, Speicher, Greiser, Müller, De Perrot, Vallée & Salomir 2017). Yet taking cardiac motion into account requires even larger data and might lead to increased scan durations.

With the possibility to monitor internal organ motion outside the MR bore, US-4DMRI bears the potential to enhance online tumour tracking during radiotherapy. However, one major simplification of the proposed setup for image-guided proton therapy is the assumption that the US probe remains attached to the patient's chest for both pretreatment 4D MR imaging and motion estimation during dose delivery. As the US-based similarity measures are sensitive to the imaging plane, a repositioning of the US probe will have adverse effects on the stacking results and motion estimates. Further effort will be needed in order to relax this constraint, for example by investigating the use of skin tattoos to facilitate the repositioning of the US probe. The application of US-4DMRI in radiotherapy demands further examinations on how the US transducer affects the dose delivery.

5. Conclusion

Ultrasound imaging has shown to be a feasible and promising surrogate for retrospective 4D MRI. While most prevalent methods are restricted to reconstruct one single respiratory cycle, US-4DMRI is capable of capturing varying respiration patterns in terms of respiratory depth and frequency far beyond one cycle. Satisfactory MR volumes have been reconstructed showing only minor discontinuities in blood vessels and liver boundaries. Moreover, competitive results were achieved in quantitative leave-one-out experiments when compared to navigator-based 4D MRI. The presented US-4DMRI outperforms navigator-based approaches with respect to reduced acquisition time, increased temporal resolution and availability of the surrogate data outside the MR bore. We envision the application of US-driven 4D MRI in patient-specific motion modelling for dose delivery planning and online tumour tracking in highly conformal, active scanning proton therapies for thoracic and abdominal cancer.

Acknowledgments

This work was supported by the Swiss National Science Foundation, SNSF (CRSII2-127549 and 320030_163330/1).

References

Aladin, A. I., Whelton, S. P., Al-Mallah, M. H., Blaha, M. J., Keteyian, S. J., Juraschek, S. P., Rubin, J., Brawner, C. A. & Michos, E. D. (2014). Relation of resting heart rate to risk for all-cause mortality by gender after considering exercise capacity (the Henry Ford exercise testing project), *The American journal of cardiology* **114**(11): 1701–1706.

Bert, C. & Durante, M. (2011). Motion in radiotherapy: particle therapy, *Physics in medicine and biology* **56**(16): R113.

Blackall, J., Ahmad, S., Miquel, M., McClelland, J., Landau, D. & Hawkes, D. (2006). MRI-based measurements of respiratory motion variability and assessment of imaging strategies for radiotherapy planning, *Physics in Medicine & Biology* **51**(17): 4147.

Buerger, C., Clough, R. E., King, A. P., Schaeffter, T. & Prieto, C. (2012). Nonrigid motion modeling of the liver from 3-D undersampled self-gated golden-radial phase encoded MRI, *IEEE transactions on medical imaging* **31**(3): 805–815.

Cai, J., Chang, Z., Wang, Z., Segars, W. P. & Yin, F.-F. (2011). Four-dimensional magnetic resonance imaging (4D-MRI) using image-based respiratory surrogate: A feasibility study, *Medical physics* **38**(12): 6384–6394.

Crowe, L. A., Manasseh, G., Chmielewski, A., Hachulla, A.-L., Speicher, D., Greiser, A., Müller, H., De Perrot, T., Vallée, J.-P. & Salomir, R. (2017). Spatially Resolved MR-Compatible Doppler Ultrasound: Proof of Concept for Triggering of Diagnostic Quality Cardiovascular MRI for Function and Flow Quantification at 3T, *IEEE Transactions on Biomedical Engineering* .

De Luca, V., Tanner, C. & Székely, G. (2012). Speeding-up image registration for repetitive motion scenarios, *2012 9th IEEE International Symposium on Biomedical Imaging (ISBI)*, IEEE, pp. 1355–1358.

Dinkel, J., Hintze, C., Tetzlaff, R., Huber, P. E., Herfarth, K., Debus, J., Kauczor, H. U. & Thieke, C. (2009). 4D-MRI analysis of lung tumor motion in patients with hemidiaphragmatic paralysis, *Radiotherapy and Oncology* **91**(3): 449–454.

Hugo, G. D. & Rosu, M. (2012). Advances in 4D radiation therapy for managing respiration: Part I–4D imaging, *Zeitschrift für Medizinische Physik* **22**(4): 258–271.

Hui, C., Wen, Z., Stemkens, B., Tijssen, R., van den Berg, C., Hwang, K.-P. & Beddar, S. (2016). 4D MR imaging using robust internal respiratory signal, *Physics in medicine and biology* **61**(9): 3472.

Johnston, E., Diehn, M., Murphy, J. D., Loo, B. W. & Maxim, P. G. (2011). Reducing 4D CT artifacts using optimized sorting based on anatomic similarity, *Medical physics* **38**(5): 2424–2429.

Liu, Y., Yin, F.-F., Chang, Z., Czito, B. G., Palta, M., Bashir, M. R., Qin, Y. & Cai, J. (2014). Investigation of sagittal image acquisition for 4D-MRI with body area as respiratory surrogate, *Medical physics* **41**(10): 101902.

Mickevicius, N. J. & Paulson, E. S. (2017). Investigation of undersampling and reconstruction algorithm dependence on respiratory correlated 4D-MRI for online MR-guided radiation therapy, *Physics in medicine and biology* **62**(8): 2910.

Neto, J. A. G., Elazzazzi, M., Altun, E. & Semelka, R. C. (2008). When should abdominal magnetic resonance imaging be used?, *Clinical Gastroenterology and Hepatology* **6**(6): 610–615.

Paganelli, C., Summers, P., Bellomi, M., Baroni, G. & Riboldi, M. (2015). Liver 4DMRI: A retrospective image-based sorting method, *Medical physics* **42**(8): 4814–4821.

Petrusca, L., Cattin, P., De Luca, V., Preiswerk, F., Celicanin, Z., Auboiroux, V., Viallon, M., Arnold, P., Santini, F., Terraz, S. et al. (2013). Hybrid ultrasound/magnetic resonance simultaneous acquisition and image fusion for motion monitoring in the upper abdomen, *Investigative radiology* **48**(5): 333–340.

Phillips, M. H., Pedroni, E., Blattmann, H., Boehringer, T., Coray, A. & Scheib, S. (1992). Effects of respiratory motion on dose uniformity with a charged particle scanning method, *Physics in medicine and biology* **37**(1): 223.

Preiswerk, F., De Luca, V., Arnold, P., Celicanin, Z., Petrusca, L., Tanner, C., Bieri, O., Salomir, R. & Cattin, P. C. (2014). Model-guided respiratory organ motion prediction of the liver from 2D ultrasound, *Medical image analysis* **18**(5): 740–751.

Preiswerk, F., Toews, M., Cheng, C.-C., Chiou Jr, y. G., Mei, C.-S., Schaefer, L. F., Hoge, W. S., Schwartz, B. M., Panych, L. P. & Madore, B. (2016). Hybrid MRI-Ultrasound acquisitions, and scannerless real-time imaging, *Magnetic Resonance in Medicine* .

Preiswerk, F., Toews, M., Hoge, W. S., Chiou, J.-y. G., Panych, L. P., Wells III, W. M. & Madore, B. (2015). Hybrid Utrasound and MRI Acquisitions for High-Speed Imaging of Respiratory Organ Motion, *International Conference on Medical Image Computing and Computer-Assisted Intervention*, Springer, pp. 315–322.

Rank, C. M., Heußer, T., Buzan, M. T., Wetscherek, A., Freitag, M. T., Dinkel, J. & Kachelrieß, M. (2017). 4D respiratory motion-compensated image reconstruction of free-breathing radial MR data with very high undersampling, *Magnetic resonance in medicine* **77**(3): 1170–1183.

Rohlfing, T., Maurer, C. R., O'dell, W. G. & Zhong, J. (2004). Modeling liver motion and deformation during the respiratory cycle using intensity-based nonrigid registration of gated mr images, *Medical physics* **31**(3): 427–432.

Schwenke, M., Strehlow, J., Haase, S., Jenne, J., Tanner, C., Langø, T., Loeve, A. J., Karakitsios, I., Xiao, X., Levy, Y. et al. (2015). An integrated model-based software for FUS in moving abdominal organs, *International Journal of Hyperthermia* **31**(3): 240–250.

Seppenwoolde, Y., Shirato, H., Kitamura, K., Shimizu, S., Van Herk, M., Lebesque, J. V. & Miyasaka, K. (2002). Precise and real-time measurement of 3D tumor motion in lung due to breathing and heartbeat, measured during radiotherapy, *International Journal of Radiation Oncology Biology Physics* **53**(4): 822–834.

Stemkens, B., Tijssen, R. H., de Senneville, B. D., Heerkens, H. D., van Vulpen, M., Lagendijk, J. J. & van den Berg, C. A. (2015). Optimizing 4-dimensional magnetic resonance imaging data sampling for respiratory motion analysis of pancreatic tumors, *International Journal of Radiation Oncology* Biology* Physics* **91**(3): 571–578.

Stemkens, B., Tijssen, R. H., de Senneville, B. D., Lagendijk, J. J. & van den Berg, C. A. (2016). Image-driven, model-based 3D abdominal motion estimation for MR-guided radiotherapy, *Physics in medicine and biology* **61**(14): 5335.

Tryggestad, E., Flammang, A., Han-Oh, S., Hales, R., Herman, J., McNutt, T., Roland, T., Shea, S. M. & Wong, J. (2013). Respiration-based sorting of dynamic MRI to derive representative 4D-MRI for radiotherapy planning, *Medical physics* **40**(5): 051909.

Von Siebenthal, M., Gamper, U., Boesiger, P., Lomax, A., Cattin, P. et al. (2007). 4D MR imaging of respiratory organ motion and its variability, *Physics in medicine and biology* **52**(6): 1547.

von Siebenthal, M., Székely, G., Lomax, A. J. & Cattin, P. C. (2007). Systematic errors in respiratory gating due to intrafraction deformations of the liver, *Medical physics* **34**(9): 3620–3629.

Wachinger, C., Yigitsoy, M., Rijkhorst, E.-J. & Navab, N. (2012). Manifold learning for image-based breathing gating in ultrasound and MRI, *Medical image analysis* **16**(4): 806–818.

Yamamoto, T., Langner, U., Loo, B. W., Shen, J. & Keall, P. J. (2008). Retrospective analysis of artifacts in four-dimensional CT images of 50 abdominal and thoracic radiotherapy patients, *International Journal of Radiation Oncology Biology Physics* **72**(4): 1250–1258.

Chapter 6

Respiratory Motion Modelling Using cGANs

In the publication presented in this chapter, we investigate the use of a cGAN as regression model for respiratory motion prediction in radiotherapy. Similar to the previous paper, the presented approach builds upon the navigator-based 4D MRI [285] and simultaneously acquired abdominal US imaging. For the navigator-based 4D MRI, the respiratory motion state is reconstructed based on the DVFs extracted from 2D MR navigator slices which are usually not available during radiotherapy. To overcome the lack of MR navigators, we train a cGAN to synthesise such DVFs given an US image as input. Finally, complete 3D MR volumes are predicted based on these synthesised DVFs.

The proposed approach is tested on simultaneously acquired US and lung 4D MRI data sets of two healthy volunteers. Although promising results are achieved, the following publication should be understood as a first proof-of-concept study due to the limited number of data sets.

Publication. The proposed approach was presented in the form of a poster presentation at the *21st International Conference on Medical Image Computing and Computer-Assisted Intervention* (MICCAI), September 2018, Granada, Spain. It was published[1] as part of the conference proceedings [76].

[1] Available online at: https://doi.org/10.1007/978-3-030-00937-3_10, accessed 12 March 2020.

This is the accepted manuscript version of the following article:
Giger A. et al. (2018) Respiratory Motion Modelling Using cGANs. In: Frangi A., Schnabel J., Davatzikos C., Alberola-López C., Fichtinger G. (eds) Medical Image Computing and Computer Assisted Intervention – MICCAI 2018. MICCAI 2018. Lecture Notes in Computer Science, vol 11073. Springer, Cham. https://doi.org/10.1007/978-3-030-00937-3_10

The final authenticated version is available online at https://doi.org/10.1007/978-3-030-00937-3_10.

Respiratory Motion Modelling using cGANs

Alina Giger[1], Robin Sandkühler[1], Christoph Jud[1], Grzegorz Bauman[1,2], Oliver Bieri[1,2], Rares Salomir[3], and Philippe C. Cattin[1]

[1]Department of Biomedical Engineering, University of Basel, Switzerland
[2]Department of Radiology, Division of Radiological Physics, University Hospital Basel, Switzerland
[3]Image Guided Interventions Laboratory, University of Geneva, Switzerland
{alina.giger,christoph.jud}@unibas.ch

Abstract. Respiratory motion models in radiotherapy are considered as one possible approach for tracking mobile tumours in the thorax and abdomen with the goal to ensure target coverage and dose conformation. We present a patient-specific motion modelling approach which combines navigator-based 4D MRI with recent developments in deformable image registration and deep neural networks. The proposed regression model based on conditional generative adversarial nets (cGANs) is trained to learn the relation between temporally related US and MR navigator images. Prior to treatment, simultaneous ultrasound (US) and 4D MRI data is acquired. During dose delivery, online US imaging is used as surrogate to predict complete 3D MR volumes of different respiration states ahead of time. Experimental validations on three volunteer lung datasets demonstrate the potential of the proposed model both in terms of qualitative and quantitative results, and computational time required.

Keywords: Respiratory motion model, 4D MRI, cGAN

1 Introduction

Respiratory organ motion causes serious difficulties in image acquisition and image-guided interventions in abdominal or thoracic organs, such as liver or lungs. In the field of radiotherapy, respiration induced tumour motion has to be taken into account in order to precisely deliver the radiation dose to the target volume while sparing the surrounding healthy tissue and organs at risk. With the introduction of increasingly precise radiation delivery systems, such as pencil beam scanned (PBS) proton therapy, suitable motion mitigation techniques are required to fully exploit the advantages which come with conformal dose delivery [2]. Tumour tracking based on respiratory motion modelling provides a potential solution to these problems, and as a result a large variety of motion models and surrogate data have been proposed in recent years [7].

In this work we present an image-driven and patient-specific motion modelling approach relying on 2D ultrasound (US) images as surrogate data. The proposed approach is targeted primarily but not exclusively at PBS proton therapy of lung tumours. We combine hybrid US and magnetic resonance imaging

2 A. Giger et al.

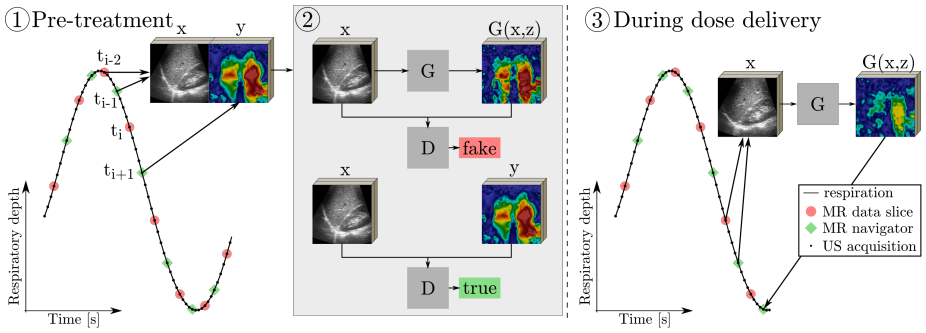

Fig. 1: Schematics of the motion modelling pipeline. See Sec. 2 for details.

(MRI), navigator-based 4D MRI methods [12] and recent developments in deep neural networks [4, 6] into a motion modelling pipeline as illustrated in Fig. 1. In a pre-treatment phase, a regression model between abdominal US images and 2D deformation fields of MR navigator scans is learned using the conditional adversarial network presented in [6]. During dose delivery, US images are used as inputs to the trained model in order to generate the corresponding navigator deformation field, and hence to predict a 3D MR volume of the patient.

Artificial neural networks (ANN) have previously been investigated for time-series prediction in image-guided radiotherapy in order to cope with system latencies [3, 5]. While these approaches rely on relatively simple network architectures, such as multilayer perceptrons with one hidden layer only, a more recent work combines fuzzy logic and an ANN with four hidden layers to predict intra- and inter-fractional variations of lung tumours [8]. Common to the aforementioned methods is that the respiratory motion was retrieved from external markers attached to the patients' chest, either measured with fluoroscopy [5] or LED sensors and cameras [8]. However, external surrogate data might suffer from a lack of correlation between the measured respiratory motion and the actual internal organ motion [12]. To overcome these limitations, the use of US surrogates for motion modelling offers a potential solution. In [9], anatomical landmarks extracted from US images in combination with a population-based statistical shape model are used for spatial and temporal prediction of the liver. Our work has several distinct advantages over [9]: we are able to build patient-specific and dense volume motion models without the need for manual landmark annotation. Moreover, hybrid US/MR imaging has been investigated for out-of-bore synthesis of MR images [10]. A single-element US transducer was used for generating two orthogonal MR slices.

The proposed image-driven motion modelling approach has only become feasible with recent advances in deep learning, in particular with the introduction of generative adversarial nets (GANs) [4]. In this framework, two models are trained simultaneously while competing with each other: a generative model G aims to fool an adversarially trained discriminator D, while the latter learns

to distinguish between real and generated images. Conditional GANs (cGANs) have shown to be suitable for a multitude of image-to-image translation tasks due to their generic formulation of the loss function [6]. We exploit the properties of cGANs in order to synthesize deformation fields of MR images given 2D US images as inputs.

While all components used within the proposed motion modelling framework have been presented previously, to the best of our knowledge, this is the first approach which suggests to integrate deep neural networks into the field of respiratory motion modelling and 4D MR imaging. We believe the strength of this work lies in the novelty of the motion modelling pipeline and underline two contributions: First, we investigate the practicability of cGANs for medical images where only relatively small training sets are available. Second, we present a patient-specific motion model which is capable of predicting complete MR volumes within reasonable time for image-guided radiotherapy. Moreover, thanks to the properties of the applied 4D MRI method and the availability of ground truth MR scans, we are able to quantitatively validate the prediction accuracy of the proposed approach within a proof-of-concept study.

2 Method

Although MR navigators have been proved to be suitable surrogate data for 4D MR imaging and motion modelling [12, 7], this imaging modality is often not available during dose delivery in radiotherapy. Inspired by image-to-image translation, one could think of a two step process to overcome this limitation: first, a cGAN is trained to learn the relation between surrogate images available during treatment and 2D MR images. Second, following the 4D MRI approach of [12], an MR volume is stacked after registering the generated MR navigator to a master image. The main idea of the approach proposed here is to join these two steps into one by learning the relation between abdominal US images and the corresponding deformation fields of 2D MR navigator slices. Directly predicting navigator deformation fields has the major benefit that image registration during treatment is rendered obsolete as it is inherently learned by the neural network. Since this method is sensitive to the US imaging plane, we assume that the patient remains in supine position and does not stand up between the pretreatment data acquisition and the dose delivery. The motion modelling pipeline consists of three main steps as illustrated in Fig. 1 and explained below.

2.1 Data acquisition and image registration

Simultaneous US/MR imaging and the interleaved MR acquisition scheme for 4D MR imaging [12] constitute the first key component as shown in step ① of Fig. 1. For 4D MRI, free respiration acquisition of the target volume is performed using dynamic 2D MR images in sequential order. Interleaved to these so-called data slices, a 2D navigator scan at fixed slice position is acquired. All MR navigator slices are registered to an arbitrary master navigator image in order to

obtain 2D deformation fields. Following the slice stacking approach, the data slices representing the organ of interest in the most similar respiration state are grouped to form a 3D MR volume. The respiratory state of the data slices is determined by comparing the deformation fields of the embracing navigator slices. For further details on 4D MRI, we refer to [12]. Unlike [12], deformable image registration of the navigator slices is performed using the approach proposed in [11], which was specifically developed for mask-free lung image registration.

We combine the 4D MRI approach with simultaneous acquisition of US images in order to establish temporal correspondence between the MR navigators and the US surrogate data. For the US image to capture the respiratory motion, an MR-compatible US probe is placed on the subject's abdominal wall such that the diaphragm's motion is clearly visible. The US probe is fastened tightly by means of a strap passed around the subject's chest.

2.2 Training of the neural network

We apply image-to-image translation as proposed in [6] in order to learn the regression model between navigator deformation fields and US images. The cGAN is illustrated in step ② of Fig. 1: the generator G learns the mapping from the recorded US images x and a random noise vector z to the deformation field y, i.e. $G : \{x, z\} \mapsto y$. The discriminator D learns to classify between real and synthesised image pairs. For the network to be able to distinguish between mid-cycle states during inhalation and exhalation, respectively, we introduce gradient information by feeding two consecutive US images as input to the cGAN. Since the deformation field has two components, one in x and one y direction, the network is trained for two input and two output channels. Moreover, instead of learning the relation between temporally corresponding data of the two imaging modalities, we introduce a time shift: given the US images at times t_{i-2} and t_{i-1}, we aim to predict the deformation field at time t_{i+1}. Together with the previously generated deformation field at time t_{i-1}, we are then able to reconstruct an MR volume at t_i as the estimates of the embracing navigators are known. In real-time applications, this time shift allows for system latency compensation.

2.3 Real-time prediction of deformation fields and stacking

During dose delivery, US images are continuously acquired and fed to the trained cGAN (see step ③ in Fig. 1). The generated deformation fields at times t_{i-1} and t_{i+1} are used to generate a complete MR volume at time t_i by stacking the MR data slices acquired in step ①, analogous to [12].

3 Experiments and Results

Data acquisition The data used in this work was tailored to develop a motion model of the lungs with abdominal US images of the liver and the diaphragm as surrogates. Three hybrid US/MR datasets of two healthy volunteers were

acquired on a 1.5 Tesla MR-scanner (MAGNETOM Aera, Siemens Healthineers, Erlangen, Germany) using an ultra-fast balanced steady-state free precession (uf-bSSFP) pulse sequence [1] with the following parameters: flip angle $\alpha = 35°$, TE = 0.86 ms, TR = 1.91 ms, pixel spacing 2.08 mm, slice thickness 8 mm, spacing between slices 5.36 mm, image dimensions $192 \times 190 \times 32$ (rows $\times$ columns $\times$ slice positions). Coronal multi-slice MR scans were acquired in sequential order at a temporal resolution of $f_{\mathrm{MR}} = 2.5\,\mathrm{Hz}$ which drops to $f_{\mathrm{MR}}/2 = 1.25\,\mathrm{Hz}$ for data slices and navigators considered separately. Simultaneous US imaging was performed at $f_{\mathrm{US}} = 20\,\mathrm{Hz}$ using a specifically developed MR-compatible US probe and an Acuson clinical scanner (Antares, Siemens Healthineers, Mountain View, CA). Although the time sampling points of the MR and the US scans did not exactly coincide, we assumed that corresponding image pairs represent the lungs at sufficiently similar respiration states since f_{US} was considerably higher than f_{MR}. The time horizon for motion prediction was $t_h = 1/f_{\mathrm{MR}} = 400\,\mathrm{ms}$.

For each dataset, MR images were acquired for a duration of 9.5 min resulting in 22 dynamics or complete scans of the target volume. Two datasets of the same volunteer were acquired after the volunteer had been sitting for a couple of minutes and the US probe was removed and repositioned. We treat these datasets separately since the US imaging plane and the position of the volunteer within the MR bore changed. The number of data slices and navigators per dataset was $N = 704$ each. Volunteer 2 was advised to breath irregularly for the last couple of breathing cycles. However, we excluded these data for the quantitative analysis below. The datasets were split into $N_{train} = 480$ training images and $N_{test} = \{224, 100, 110\}$ test images for datasets $\{1, 2, 3\}$, respectively. We assumed that the training data represents the pretreatment data as described in Sec. 2.1. It comprised the first 6.4 min or 15 dynamics of the dataset.

Training details We adapted the PyTorch implementation for paired image-to-image translation [6] in order for the network to cope with medical images and data with two input and two output channels. The US and MR images were cropped and resized to 256×256 pixels. We used the U-Net based generator architecture, the convolutional PatchGAN classifier as discriminator and default training parameters as proposed in [6]. For each dataset, the network was trained from scratch using the training sets described above and training was stopped after 20 epochs or roughly 7 min.

Validation For each consecutive navigator pair of the test set a complete MR volume was stacked using the data slices of the training set as possible candidates. In the following, we compare our approach with a reference method and introduce the following notation: RDF is referred to as the reference stacking method using the deformation fields computed on the actually recorded MR navigator slices, and GDF denotes the proposed approach based on the generated deformation fields obtained as a result of the cGAN.

The 2D histogram in Fig. 2 shows the correlation of the slices selected either by RDF or GDF. The bins represent the dynamics of the acquisition and a strong diagonal line is to be expected if the two methods select the same data slices for

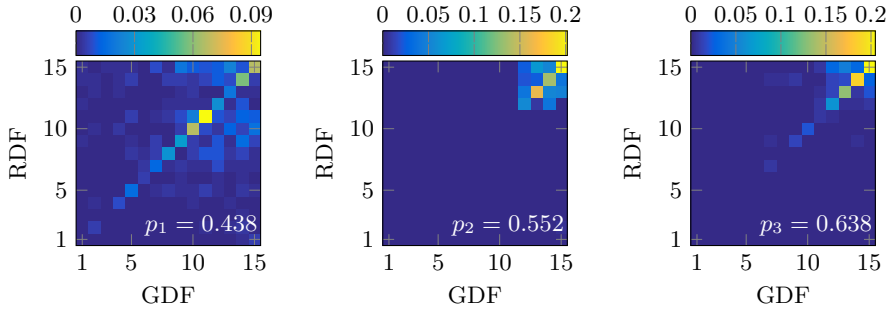

Fig. 2: Slice selection illustrated as joint histogram for reference and generated deformation fields, respectively. From left to right: datasets 1 to 3.

stacking. The sum over the diagonals, that is the percentage of equally selected slices, is indicated as p_k for dataset $k \in \{1, 2, 3\}$. For all datasets the diagonal is clearly visible and the matching rates are in the range of 43.8 % to 63.8 %. While these numbers give a first indication of whether the generated deformation fields are able to stack reasonable volumes, they are not a quantitative measure of quality: two different but very similar data slices could be picked by the two methods which would lead to off-diagonal entries but without affecting the image quality of the generated MR volumes.

The histograms for datasets 2 and 3 suggest a further conclusion: the data slices used for stacking are predominantly chosen from the last four dynamics of the training sets (96.5 % and 81.7 %). Visual inspection of the US images in dataset 2 revealed that one dominant vessel structure appeared more clearly starting from dynamic 11 onwards. This might have been caused by a change in the characteristics of the organ motion, such as organ drift, or a shift of the US probe and emphasises the need for internal surrogate data.

Qualitative comparison of a sample deformation field is shown in Fig. 3a where the reference and the predicted deformations are overlaid. Satisfactory alignment can be observed with the exception of minor deviations in the region of the intestine and the heart. Visual inspection of the stacked volumes by either of the two methods RDF and GDF revealed only minor discontinuities in organ boundaries and vessel structures.

Quantitative results were computed on the basis of image comparison: Each navigator pair of the test set embraces a data slice acquired at a specific slice position. We computed the difference between the training data slice selected for stacking and the actually acquired MR image representing the ground truth. The error was quantified as mean deformation field after 2D registration was performed using the same registration method as in Sec. 2.1 [11]. The median error lies below 1 mm and the maximum error below 3 mm for all datasets and both methods. The average prediction accuracy can compete with previously reported values [9]. Comparing RDF and GDF, slightly better results were achieved for the reference method which is, however, not available during treatment.

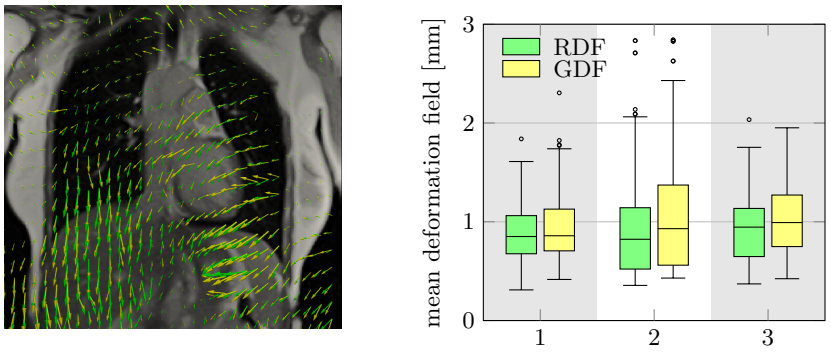

(a) (b)

Fig. 3: Qualitative and quantitative results. (a) Sample motion field of dataset 2 with reference (green) and predicted (yellow) deformations, and (b) error distribution quantified as mean deformation field.

The proposed method required a mean computation time of 20 ms for predicting the deformation field on a NVIDIA Tesla V100 GPU, and 100 ms for slice selection and stacking on a standard CPU. With a prediction horizon of $t_h = 400$ ms, the motion model is real-time applicable and allows for online tracking of the target volume.

4 Discussion and Conclusion

We presented a novel motion modelling framework which is persuasive in several perspectives: the motion model relies on internal surrogate data, it is patient-specific and capable of predicting dense volume information within reasonable computation time for real-time applications, while training of the regression model can be performed within 7 min only.

We are aware, though, that the proposed approach demands further investigation: It shares the limitation with most motion models that respiration states which have not been observed during pretreatment imaging cannot be reconstructed during dose delivery. This includes in particular, extreme respiration depth or baseline shifts due to organ drift. Also, the motion model is sensitive to the US imaging plane, and a small shift of the US probe may have adverse effects on the outcome. Therefore, the proposed framework requires the patients to remain in supine position with the probe attached to their chests. Future work will aim to alleviate this constraint by, for example, investigating the use of skin tattoos for a precise repositioning of the US probe. Furthermore, the motion model relies on a relatively small amount of training data which bears the danger of overfitting. The current implementation of the cGAN includes dropout but one could consider to additionally apply data augmentation on the input images. Further effort will be devoted towards the development of effective data augmen-

tation strategies and must include a thorough investigation of the robustness of cGANs within the context of motion modelling. Moreover, the formulation of a control criterion which is capable of detecting defective deformation fields or MR volumes is considered an additional necessity in future works.

5 Acknowledgement

We thank Tony Lomax, Miriam Krieger, and Ye Zhang from the Centre for Proton Therapy at the Paul Scherrer Institute (PSI), Switzerland, and Pauline Guillemin from the University of Geneva, Switzerland, for fruitful discussions and their assistance with the data acquisition. This work was supported by the Swiss National Science Foundation, SNSF (320030_163330/1).

References

1. Bieri, O.: Ultra-fast steady state free precession and its application to in vivo 1H morphological and functional lung imaging at 1.5 tesla. Magnetic resonance in medicine **70**(3), 657–663 (2013)
2. De Ruysscher, D., Sterpin, E., Haustermans, K., Depuydt, T.: Tumour movement in proton therapy: solutions and remaining questions: a review. Cancers **7**(3), 1143–1153 (2015)
3. Goodband, J., Haas, O., Mills, J.: A comparison of neural network approaches for on-line prediction in IGRT. Medical physics **35**(3), 1113–1122 (2008)
4. Goodfellow, I., Pouget-Abadie, J., Mirza, M., Xu, B., Warde-Farley, D., Ozair, S., Courville, A., Bengio, Y.: Generative adversarial nets. In: Advances in neural information processing systems. pp. 2672–2680 (2014)
5. Isaksson, M., Jalden, J., Murphy, M.J.: On using an adaptive neural network to predict lung tumor motion during respiration for radiotherapy applications. Medical physics **32**(12), 3801–3809 (2005)
6. Isola, P., Zhu, J.Y., Zhou, T., Efros, A.A.: Image-to-Image Translation with Conditional Adversarial Networks. CVPR (2017)
7. McClelland, J.R., Hawkes, D.J., Schaeffter, T., King, A.P.: Respiratory motion models: A review. Med Image Anal **17**(1), 19–42 (2013)
8. Park, S., Lee, S.J., Weiss, E., Motai, Y.: Intra-and inter-fractional variation prediction of lung tumors using fuzzy deep learning. IEEE journal of translational engineering in health and medicine **4**, 1–12 (2016)
9. Preiswerk, F., De Luca, V., Arnold, P., Celicanin, Z., Petrusca, L., Tanner, C., Bieri, O., Salomir, R., Cattin, P.C.: Model-guided respiratory organ motion prediction of the liver from 2D ultrasound. Med Image Anal **18**(5), 740–751 (2014)
10. Preiswerk, F., Toews, M., Cheng, C.c., Chiou Jr, y.G., Mei, C.S., Schaefer, L.F., Hoge, W.S., Schwartz, B.M., Panych, L.P., Madore, B.: Hybrid MRI-Ultrasound acquisitions, and scannerless real-time imaging. Magnetic resonance in medicine **78**(3), 897–908 (2017)
11. Sandkuehler, R., Jud, C., Pezold, S., Cattin, P.C.: Adaptive Graph Diffusion Regularisation for Discontinuity Preserving Image Registration. 8th International Workshop on Biomedical Image Registration (2018)
12. von Siebenthal, M., Szekely, G., Gamper, U., Boesiger, P., Lomax, A., Cattin, P.: 4D MR imaging of respiratory organ motion and its variability. Physics in Medicine & Biology **52**(6), 1547 (2007)

Chapter 7

Inter-fractional Respiratory Motion Modelling from Abdominal Ultrasound: A Feasibility Study

In the feasibility study presented in this chapter, we address the relevant clinical question of how the respiratory motion model performs when the US probe has to be repositioned between multiple fractions. To do so, we evaluate the performance of a respiratory motion model on the basis of lung 4D MRI data sets from five healthy volunteers. For two volunteers, additional data sets were acquired with the US probe repositioned after they had been in upright position for a few minutes. In an attempt to favour robustness over complexity, we performed this analysis using a respiratory motion model which consists of a polynomial correspondence model in combination with a linear autoregressive model for the temporal prediction. In addition, the presented study is based on a recently proposed 4D MRI approach which circumvents the need for image stacking and binning by employing a sophisticated acquisition sequence based on 3D readouts [129].

The preliminary findings presented in this study suggest that the proposed motion model can cope with different US imaging planes due to probe repositioning, however, at the cost of reduced accuracy.

Publication. The proposed approach was presented in the form of a poster presentation at the *Second International Workshop on PRedictive Intelligence In MEdicine* (PRIME) in conjunction with the *22nd International Conference on Medical Image Computing and Computer-Assisted Intervention* (MICCAI), October 2019, Shenzhen, China. It was published[1] as part of the workshop proceedings [75].

[1] Available online at: https://doi.org/10.1007/978-3-030-32281-6_2, accessed 12 May 2020.

This is the accepted manuscript version of the following article:
Giger A. et al. (2019) Inter-fractional Respiratory Motion Modelling from Abdominal Ultrasound: A Feasibility Study. In: Rekik I., Adeli E., Park S. (eds) Predictive Intelligence in Medicine. PRIME 2019. Lecture Notes in Computer Science, vol 11843. Springer, Cham. https://doi.org/10.1007/978-3-030-32281-6_2

The final authenticated version is available online at https://doi.org/10.1007/978-3-030-32281-6_2.

Inter-fractional Respiratory Motion Modelling from Abdominal Ultrasound: A Feasibility Study

Alina Giger[1,2][0000−0001−9644−1991], Christoph Jud[1,2][0000−0001−5514−7999], Damien Nguyen[2,3][0000−0003−2867−5838], Miriam Krieger[4,5][0000−0002−1914−1220], Ye Zhang[4][0000−0003−1608−4467], Antony J. Lomax[4,5], Oliver Bieri[2,3], Rares Salomir[6], and Philippe C. Cattin[1,2][0000−0001−8785−2713]

[1]Center for medical Image Analysis & Navigation,University of Basel, Allschwil, Switzerland
[2]Department of Biomedical Engineering, University of Basel, Allschwil, Switzerland
[3]Department of Radiology, Division of Radiological Physics, University Hospital Basel, Basel, Switzerland
[4]Center for Proton Therapy, Paul Scherrer Institute (PSI), Villigen PSI, Switzerland
[5]Department of Physics, ETH Zurich, Zurich, Switzerland
[6]Image Guided Interventions Laboratory, University of Geneva, Geneva, Switzerland
{alina.giger,christoph.jud}@unibas.ch

Abstract. Motion management strategies are crucial for radiotherapy of mobile tumours in order to ensure proper target coverage, save organs at risk and prevent interplay effects. We present a feasibility study for an inter-fractional, patient-specific motion model targeted at active beam scanning proton therapy. The model is designed to predict dense lung motion information from 2D abdominal ultrasound images. In a pretreatment phase, simultaneous ultrasound and magnetic resonance imaging are used to build a regression model. During dose delivery, abdominal ultrasound imaging serves as a surrogate for lung motion prediction. We investigated the performance of the motion model on five volunteer datasets. In two cases, the ultrasound probe was replaced after the volunteer has stood up between two imaging sessions. The overall mean prediction error is 2.9 mm and 3.4 mm after repositioning and therefore within a clinically acceptable range. These results suggest that the ultrasound-based regression model is a promising approach for inter-fractional motion management in radiotherapy.

Keywords: motion prediction · ultrasound · 4D MRI · radiotherapy

1 Introduction

Motion management is a key element in external beam radiotherapy of thoracic or abdominal tumours prone to respiratory movement. Pioneered in photon therapy, 4D treatment planning and motion monitoring techniques have gained in importance also in the field of particle treatments [13]. Due to higher dose conformity and the absence of radiation dose distal to the Bragg peak, proton therapy enables precise target treatment while spearing healthy tissue and organs at

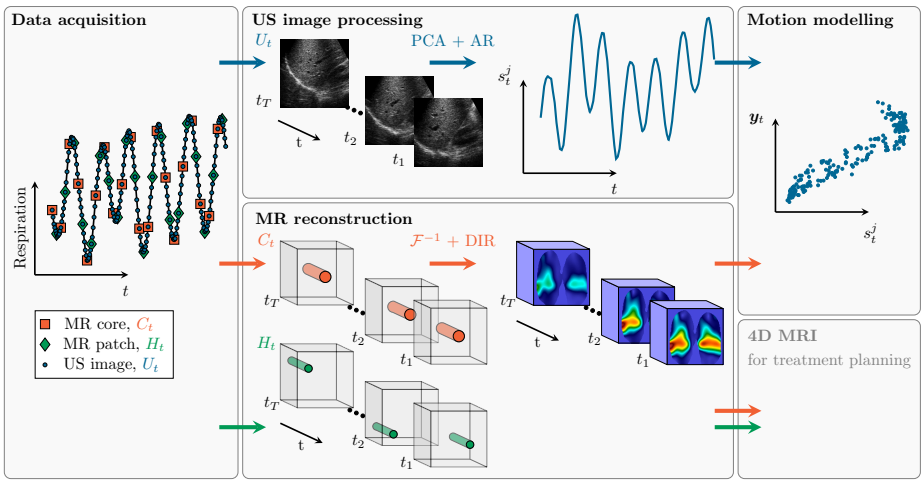

Fig. 1: Illustration of the pretreatment phase. See Sec. 2 and Sec. 3.1 for details.

risk. However, in presence of organ motion, actively scanned proton beam therapies are hampered by interplay effects and inhomogeneous dose distributions [1] emphasising the need for sophisticated motion mitigation strategies, such as rescanning, gating or tracking [1,13]. In tracking, for example, the treatment beam is adapted to follow the tumour motion with the goal to ensure optimal target coverage. To do so, however, predictive methods and motion models are crucial in order to cope with respiratory motion variabilities and system latency.

In the field of radiotherapy, motion variabilities are classified into two categories: intra-fractional and inter-fractional motion variations [6]. Intra-fractional variations refer to motion variations between different respiratory cycles observed within a single treatment session; inter-fractional variations include anatomical and physiological differences between treatment sessions. Such motion variabilities should be considered for both treatment planning and dose delivery [5]. In this context, 4D imaging and motion modelling are widely discussed techniques. Motion models are necessary when direct imaging of the internal motion is not feasible. The idea is to estimate the motion of interest based on more readily available surrogate data. 4D imaging provides dense internal motion information and therefore constitutes an important element for respiratory motion modelling. While 4D imaging is traditionally performed with computed tomography (4D CT), respiratory-correlated magnetic resonance imaging (4D MRI) methods have increasingly been developed in the last decade due to their superior soft-tissue contrast and the lack of radiation dose [12].

In this work, we present an inter-fractional respiratory motion management pipeline for the lungs based on abdominal ultrasound (US) imaging as illustrated in Fig. 1. It involves hybrid US/MR imaging, principal component regression, and a novel 4D MRI technique [4]. The proposed approach follows a typical motion management scheme: In a pretreatment phase, simultaneous US and

MR imaging acquisitions are performed and a motion model is computed. During treatment delivery, online US imaging is used to predict the respiratory motion for tumour tracking. We demonstrate the feasibility of our approach on five healthy volunteer datasets for two of which the US probe has been repositioned between motion modelling and prediction. Although not truly inter-fractional in the sense that there are days or weeks between two acquisitions, the presented data serve as preliminary data in this feasibility study.

US imaging has been proposed for image-guided interventions and radiotherapy before due to its advantages over other imaging modalities and surrogate signals [8]: it provides internal organ motion information at high temporal resolution, and therefore potentially detects phase shifts and organ drift [11], it is non-invasive and available during treatment delivery. However, as the lungs cannot be imaged directly, US guidance has mainly been applied for liver, heart or prostate. In [9], for example, an US-driven respiratory motion model for the liver has been presented. It requires precise co-registration of US and MR images in order to establish correspondence between tracked liver points. Indirect lung tumour tracking strategies based on 2D abdominal US have only been proposed recently [2,7]. Mostafaei et al. [7] combine US imaging and cone-beam CT (CBCT) in order to reduce the CBCT imaging frequency and therefore the imaging dose to the patient. However, the tumour motion is estimated in superior-inferior (SI) direction only. In [2] dense motion information was predicted based on an adversarial neural network. Although promising, it is not clear how this approach performs if the US imaging plane is shifted.

With this work we address the clinically relevant question of how the respiratory motion model performs in case of US probe repositioning between two imaging sessions. The novelty of our work does not primarily lie in the methodological components themselves but rather in their combination into a complete respiratory motion management pipeline. We combine US imaging with a recently presented 4D MRI technique and present first results in a feasibility study.

2 Background

Dense motion estimation is generally represented as a 3D deformation field which can be derived from any 4D imaging technique in combination with deformable image registration (DIR) methods. The 4D MRI sequence applied here uses 3D readouts and, unlike most other approaches, is a time-resolved imaging method [4]. As opposed to respiratory-correlated 4D MRI methods [12], it does not assume periodic respiration but provides continuous motion information. It is based on the assumption that the respiratory motion information is mapped mainly to the low-frequency k-space center. Following this rationale, circular patches at the k-space center $C_t \subset \mathbb{C}^3$ capture low-frequency image components with motion information while peripheral patches $H_t \subset \mathbb{C}^3$ account for image sharpness and structural details. Since these patches consist of a small portion of the k-space only, they can be acquired at a much higher temporal resolution as compared to the entire k-space. In Fig. 1, the 3D k-space is represented as a

cube and the patches are illustrated as cylinders with the height pointing into the phase encoding direction.

Center and peripheral patches are acquired alternately and combined into patch pairs $P_t = \{C_t, H_t\}$. The center patches C_t are transformed to the spatial domain by applying the inverse Fourier transform $I_t = \mathcal{F}^{-1}(C_t)$. Then, a diffeomorphic registration method is applied to obtain the 3D deformation field between a reference image and I_t [10]. For further details, the reader is referred to [4]. In the following, we refer to the vectorised deformation field at time t as $\boldsymbol{y}_t \in \mathbb{R}^d$ with dimension d. Note that the peripheral patches H_t are not required for motion modelling but might be necessary for the treatment planning.

3 Method

3.1 Pretreatment phase

Data acquisition Simultaneous US/MR acquisitions are performed in order to ensure temporal correspondence between the center patches C_t and the US images U_t as shown in Fig. 1. The US imaging plane is chosen such that parts of the liver and the diaphragm motion are clearly visible.

Image processing and reconstruction Following the data acquisition, the 4D MRI is reconstructed and the motion vectors $\boldsymbol{y}_t$ are computed. Given 2D abdominal US images U_t, a low-dimensional respiratory motion surrogate is extracted using principal component analysis (PCA). By selecting only a small subset of principal components the model complexity is reduced. In order to cope with system latencies during dose delivery, it is important for the model to forecast the motion vectors into the future. Let $\boldsymbol{s}_t \in \mathbb{R}^k$ denote the standardised scores of the k most dominant principal components for image U_t. We apply an element-wise autoregressive (AR) model of order p for the time series $\{\boldsymbol{s}_t\}_{t=1}^T$:

$$s_t^j = \theta_0^j + \sum_{i=1}^{p} \theta_i^j s_{t-i}^j + \epsilon_t \quad \forall j \in \{1, \dots, k\}, \tag{1}$$

where s_t^j is the jth element of $\boldsymbol{s}_t$, $\boldsymbol{\theta}^j = \left[\theta_0^j\ \theta_1^j \dots \theta_p^j\right]^T$ denotes the model parameters, and ϵ_t is white noise. The parameters $\boldsymbol{\theta}^j$ are estimated using ordinary least squares. To predict the surrogate n steps ahead of time, the AR model in (1) is repeatedly applied.

Motion modelling In order for the motion model to capture non-linear relationships between the surrogates and the motion estimates, we formulate a cubic regression model. Let $\boldsymbol{x}_t \in \mathbb{R}^{3k+1}$ denote the input vector for the regression model which includes $\boldsymbol{s}_t$, its element-wise square and cube numbers, and a constant bias, i.e. $\boldsymbol{x}_t = \left[1\ s_t^1 \dots s_t^k\ (s_t^1)^2 \dots (s_t^k)^2\ (s_t^1)^3 \dots (s_t^k)^3\right]^T$. The motion model can thus be written as

$$\boldsymbol{y}_t = \boldsymbol{\beta}\boldsymbol{x}_t + \boldsymbol{\epsilon}_t, \tag{2}$$

with regression coefficients $\boldsymbol{\beta} \in \mathbb{R}^{d\times(3k+1)}$ and white noise $\boldsymbol{\epsilon}_t \in \mathbb{R}^d$. Given the pretreatment data $\{\boldsymbol{s}_t, \boldsymbol{y}_t\}_{t=1}^T$, the model parameters $\boldsymbol{\beta}$ are again approximated in the least-squares sense.

3.2 Online motion prediction

Having computed both the AR parameters in (1), and the regression coefficients in (2), the inference during dose delivery is straightforward and computationally efficient. However, since the motion modelling and treatment planning is performed several days or weeks prior to the dose delivery, the US probe has to be reattached to the patients' abdominal wall when they return for the treatment delivery. Although the location of the probe with respect to the patients chest can be marked by skin tattoos or similar approaches, it is hardly possible to recover the exact same imaging plane due to inter-fractional motions, anatomy changes, or different body positions with respect to the treatment couch [13]. The online US images can therefore not be projected onto the PCA basis directly, but a new principal component transformation has to be computed. We use the first minutes of US imaging after the patient has been setup for treatment as training data for recomputing a PCA basis. Since the first principal components capture the most dominant motion information and the scores $\boldsymbol{s}_t$ are standardised, we expect the signals to be comparable. Furthermore, the motion vectors $\boldsymbol{y}_t$ have to be warped in order to correspond to the present anatomy. This requires a 3D reference scan of the patients prior to treatment either using CT or MRI.

The surrogate signal $\boldsymbol{s}_t$ at time t is obtained by projecting the US image U_t onto the new PCA basis. Given the p latest surrogates $\{\boldsymbol{s}_{t-i}\}_{i=0}^{p-1}$, the signal $\boldsymbol{s}_{t+n}$ at time $t+n$ is approximated by applying the AR model n times. Finally, the motion estimate $\boldsymbol{y}_{t+n}$ is computed given equation (2) and warped in order to match the actual patient position.

4 Experiments and Results

Data acquisition The proposed motion management pipeline was tested on 5 healthy volunteers. The 4D MRI sequence [4] was acquired on a 1.5 T MR-scanner (MAGNETOM Aera, Siemens Healthineers, Erlangen, Germany) under free respiration and with the following parameters: TE = 1.0 ms, TR = 2.5 ms, flip angle $\alpha = 5°$, bandwidth 1560 Hz px^{-1}, isotropic pixel spacing 3.125 mm, image matrix $128 \times 128 \times 88$ and field of view $400 \times 400 \times 275$ mm^3 (in LR $\times$ SI $\times$ AP). The radius of C_t and H_t were set to 6 px and 5 px, respectively, resulting in 109 k-space points or 272.5 ms per center patch C_t, and 69 k-space points or 172.5 ms per peripheral patch H_t. The total acquisition time per subject was set to 11.1 min or $T = 1500$ center-peripheral patch pairs, P_t. For the reconstruction of the 4D MRI, a sliding organ mask was created semi-automatically [14].

US imaging was performed simultaneously at $f_{\text{US}} = 15$ Hz on an Acuson clinical scanner (Antares, Siemens Healthineers, Mountain View, CA). A specifically developed MR-compatible US probe was attached to the patient's abdominal

Table 1: Overview of the model settings and the respiratory motion characteristics for each subject s separately. The datasets with US probe repositioning are marked in grey.

s	**model details**			**respiratory motion** [mm]			
	AR model	motion model		training		test	
	train	train	test	μ_{95}	max	μ_{95}	max
1	600	640	200	13.31	40.92	15.65	40.96
2.1	600	470	200	5.68	29.81	4.65	29.96
2.2	600	470	200	5.68	29.81	12.83	45.76
3	600	530	200	4.35	19.80	4.95	19.03
4	600	660	200	6.92	24.49	7.32	23.92
5	600	630	200	5.63	25.74	4.87	16.34
4	–	–	690	6.92	24.49	6.99	27.48
5	–	–	830	5.63	25.74	6.43	25.31

wall by means of a strap. The MRI and US systems were synchronised via optical triggers emitted by the MR scanner after every 6.675 s or 15 patch pairs P_t. The optical signal triggered the US device to record a video for a duration of 5 s. The time gap of 1.675 s was chosen to compensate for the US system latency while storing the video file. As a consequence, however, 4 patch pairs P_t per trigger interval are not usable due to missing US images. Despite this time gap, it sporadically happened that the trigger signal occurred before the preceding video file was stored resulting in an omission of the video just triggered. The time delay between the MR trigger and the start of the US video was negligible.

For subjects 4 and 5, the US probe was removed and reattached after they had been standing for several minutes. The US imaging plane was visually matched with the preceding imaging plane as good as possible. The MR images were aligned based on diffeomorphic image registration of two end-exhalation master volumes and inverse displacement field warping [10,3].

Model details The first 8 US videos, corresponding to 200 images, were used to determine the AR parameters $\boldsymbol{\theta}$. The remaining data was split into a training and test set according to Table 1 in order to estimate $\boldsymbol{\beta}$ and validate the motion model performance, respectively. For each subject, the last 200 US/MR image pairs, or 133.5 s of data acquisition, were used for validation. For subject 2, however, a drastic change in respiratory motion characteristics was observed in the test set; the baseline motion more than doubled as compared to the training set. To take this observation into account, two test sets were created by dividing the last 267 s into equal parts. Below, the test set which includes deep respiratory motion is discussed separately and referred to as 2.2. Table 1 shows the maximum and the baseline respiratory motion for each subject. The baseline motion μ_{95} is defined as the 95th percentile of the deformation field magnitude averaged over all time points.

For subjects 4 and 5, the parameters $\boldsymbol{\theta}$ and $\boldsymbol{\beta}$ were estimated based on the primary dataset. After the probe repositioning, the first 270 US images were used for recomputing the PCA basis. For all the experiments, the number of principal components was set to $k = 3$, and an AR model of order $p = 5$ was built. The surrogate $\boldsymbol{s}_t$ was predicted $n = 2$ steps, or $t_n = n/f_{\mathrm{US}} = 133\,\mathrm{ms}$, into the future.

Validation The predicted deformation field $\hat{\boldsymbol{y}}_t$ was compared to the reference $\boldsymbol{y}_t$. We define the prediction error as the magnitude of the deformation field difference for the masked region including the lungs as well as parts of the liver and the stomach. Fig. 2 exemplarily illustrates the organ mask for volunteer 4 and 5 on a coronal slice of the master volume. In addition, the reference and the predicted deformation field magnitude, and the prediction error are shown. Highest motion magnitudes are observed in the region of the diaphragm. As expected, the prediction errors are higher for both volunteers after repositioning. It can be further observed that the motion model has a tendency to underestimate the respiratory motion. For volunteer 5, this becomes more evident when comparing the respiratory motion characteristics in Table 1 or Fig. 3: the respiratory motion has substantially increased after repositioning and therefore cannot be predicted precisely. Additionally, an organ drift of about 2 mm is observed in volunteer 5 after repositioning if all 830 test samples are considered which further decreases the prediction accuracy. The highest prediction errors are found at the lung boundaries.

Fig. 3 shows the mean prediction error and the respiratory motion for the first 200 test samples. The shaded area marks the 5th and 95th percentile of the prediction error. The respiratory motion is defined as the 95th percentile of the reference deformation field magnitude. Since an end-exhalation master volume was used for registration, in general higher prediction errors are observed at end-inhalation. However, despite the decreased performance of the motion model after repositioning, the mean prediction error is substantially lower than the respiratory motion for most time points.

The box plots in Fig. 4 show the distributions of both the mean prediction error and the 95th percentile computed for each time point. Without US probe repositioning, the mean error is less or equal to 3 mm for all subjects except for volunteer 4 where it shows an outlier at 3.5 mm. The 95th percentile reaches a maximum value of 7.0 mm for volunteer 4 while 95% of the prediction errors for subjects 1, 2.1, and 3 are smaller than 6.0 mm, 5.4 mm, and 5.2 mm, respectively. The last column in Fig. 4 shows the results for the second test set of subject 2 where the respiratory motion was more pronounced as compared to the training data. The maximum values for the mean prediction error and 95th percentile are 12.7 mm and 27.4 mm, respectively.

After US probe repositioning, the mean prediction error is below 8.0 mm and 6.0 mm for volunteers 4 and 5, respectively. There are, however, outliers of up to 14.5 mm for the 95th percentile of volunteer 4. By visual inspection of the prediction errors, it could be observed that these major discrepancies are

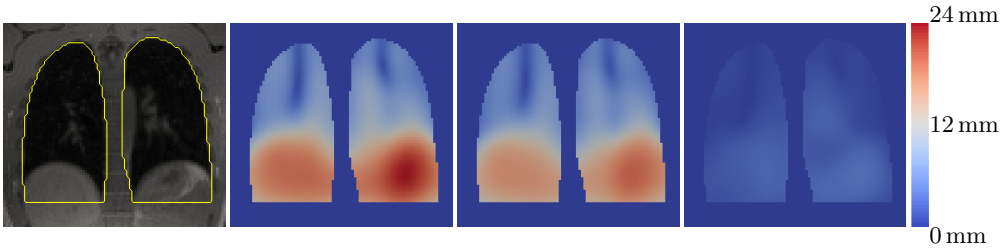

(a) Volunteer 04

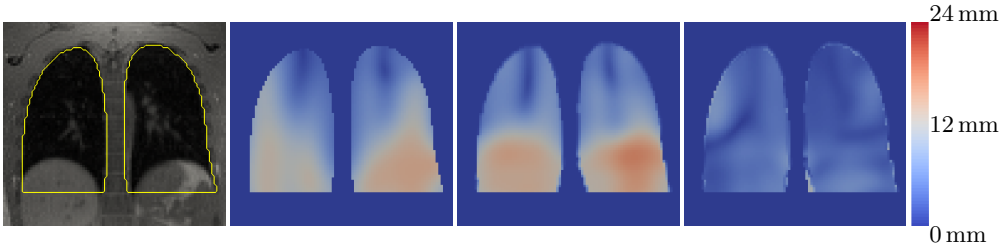

(b) Volunteer 04, with repositioning

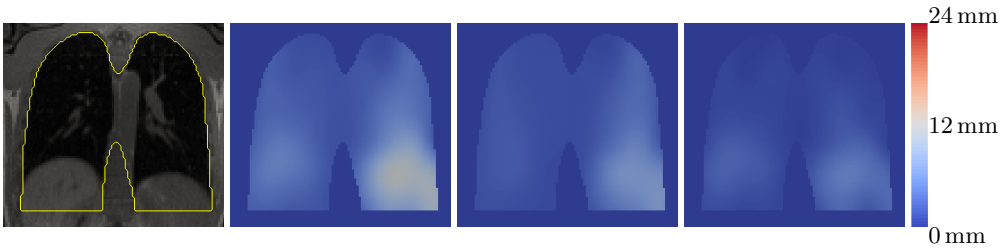

(c) Volunteer 05

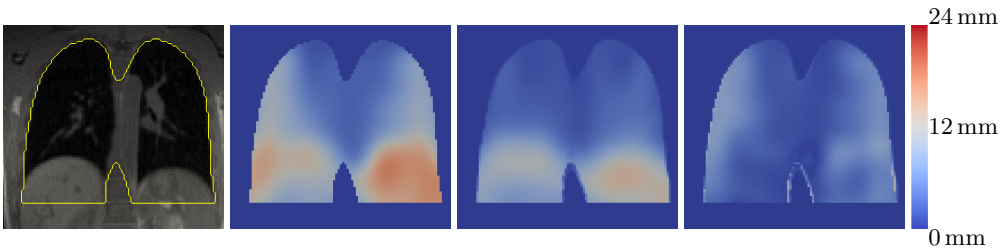

(d) Volunteer 05, with repositioning

Fig. 2: Coronal cuts through sample end-inhalation volumes of volunteer 4 and 5 for both with and without repositioning. From left to right: master volume with the masked region marked in yellow, reference deformation field magnitude, predicted deformation field magnitude, and prediction error.

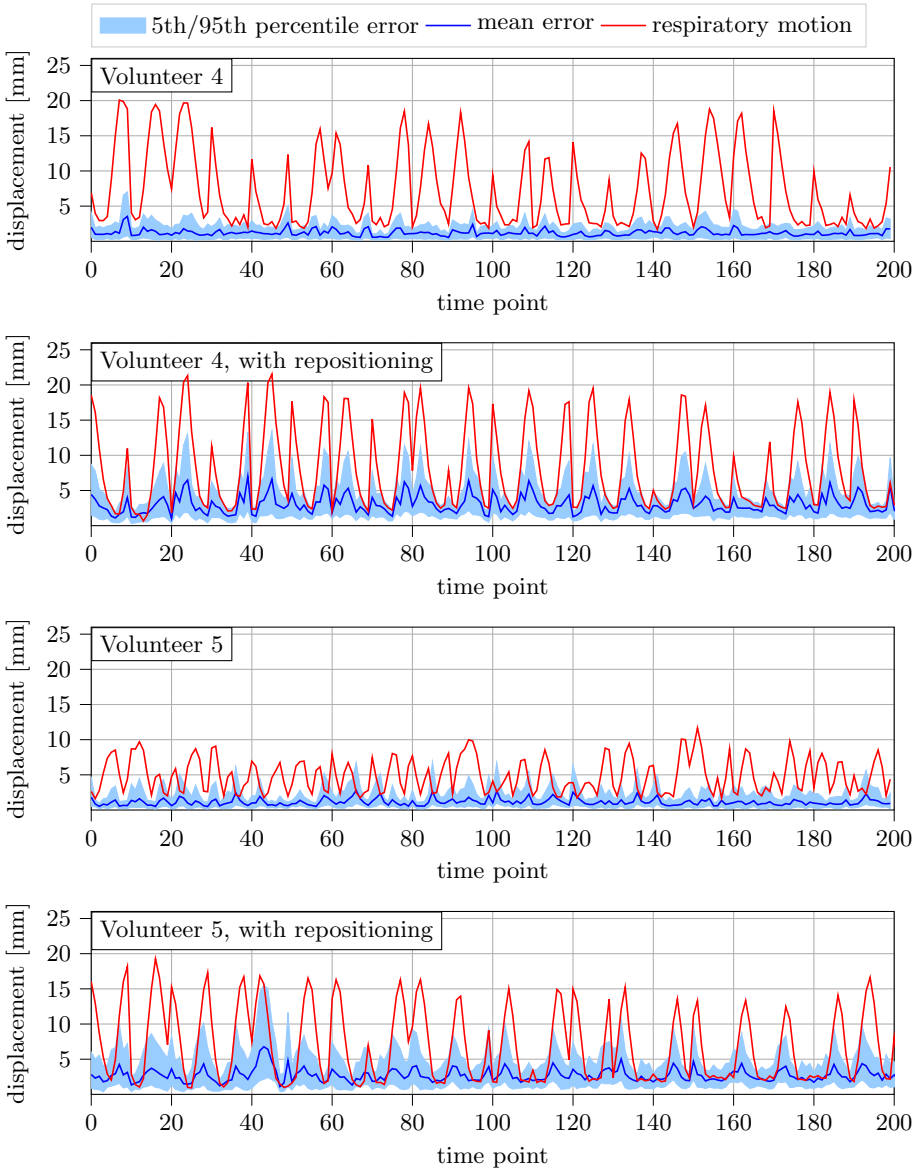

Fig. 3: Respiratory motion and prediction error over time for volunteer 4 and 5. For illustration purposes, only the first 200 test samples after repositioning are shown.

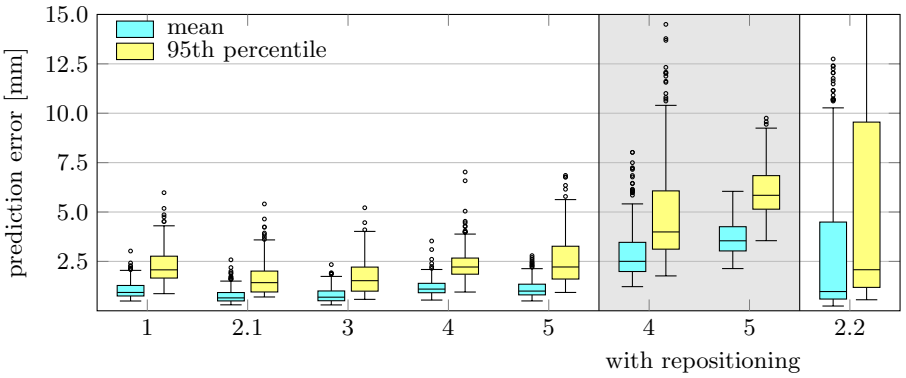

Fig. 4: Prediction error distribution for all volunteers; without (white background) and with (grey background) US probe repositioning. The whiskers of the box plots extend to the most extreme values within 1.5 times the interquartile range.

located in the region of the stomach at the organ mask boundaries. In summary, the overall mean prediction error is 2.9 mm and 3.4 mm for volunteers 4 and 5, respectively.

5 Discussion and Conclusion

In this feasibility study we examined the performance of abdominal US surrogate signals in combination with a novel 4D MRI technique for lung motion estimation. The model predicts dense motion information 133 ms into the future which allows for system latency compensation. The obtained results are similar in terms of accuracy to those presented in previous studies [2,9]. However, we additionally present preliminary findings for inter-fractional motion modelling which involves a repositioning of the US probe. Although the accuracy decreased when compared to intra-fractional modelling, overall mean prediction errors of 2.9 mm and 3.4 mm demonstrate that the proposed US surrogate signal is suitable even if the imaging plane is not identical for two fractions.

The presented results should, however, be treated with caution as the repositioning of the US probe has only been tested on two healthy volunteers and the time interval between the two measurements was in the range of minutes rather than days or weeks. Also, there exists no real ground-truth data for the respiratory motion. The reference deformation field might itself be corrupted due to registration errors. An additional error source is introduced with the alignment of the MR volumes between the two imaging sessions. Since this transformation was computed based on two exhalation master volumes, it might not be accurate for other respiratory states. Moreover, it was observed that the motion model does not generalise well if the respiration characteristics vary substantially as it

was the case for subject 2. Although this limitation is inherent to the problem formulation and occurs in most motion models, it demands further investigations and characterisation. Also, further work is necessary to investigate the effect of dense motion predictions on treatment plan adaptations and dose distribution in proton therapy.

Acknowledgement

We thank Pauline Guillemin from the University of Geneva, Switzerland, for her indispensable support with the data acquisition. This work was supported by the Swiss National Science Foundation, SNSF (320030_163330/1) and the GPU Grant Program of NVIDIA (Nvidia Corporation, Santa Clara, California, USA).

References

1. Bert, C., Durante, M.: Motion in radiotherapy: particle therapy. Physics in Medicine & Biology **56**(16), R113 (2011)
2. Giger, A., Sandkühler, R., Jud, C., Bauman, G., Bieri, O., Salomir, R., Cattin, P.C.: Respiratory Motion Modelling Using cGANs. In: International Conference on Medical Image Computing and Computer-Assisted Intervention. pp. 81–88. Springer (2018)
3. Jud, C., Giger, A., Sandkühler, R., Cattin, P.C.: A localized statistical motion model as a reproducing kernel for non-rigid image registration. In: International Conference on Medical Image Computing and Computer-Assisted Intervention. pp. 261–269. Springer (2017)
4. Jud, C., Nguyen, D., Sandkühler, R., Giger, A., Bieri, O., Cattin, P.C.: Motion Aware MR Imaging via Spatial Core Correspondence. In: International Conference on Medical Image Computing and Computer-Assisted Intervention. pp. 198–205. Springer (2018)
5. Krieger, M., Giger, A., Weber, D., Lomax, A., Zhang, Y.: PV-0422 Consequences of respiratory motion variability in lung 4DMRI datasets. Radiotherapy and Oncology **133**, S219–S220 (2019)
6. McClelland, J.R., Hawkes, D.J., Schaeffter, T., King, A.P.: Respiratory motion models: A review. Med Image Anal **17**(1), 19–42 (2013)
7. Mostafaei, F., Tai, A., Gore, E., Johnstone, C., Haase, W., Ehlers, C., Cooper, D.T., Lachaine, M., Li, X.A.: Feasibility of real-time lung tumor motion monitoring using intrafractional ultrasound and kV cone beam projection images. Medical physics **45**(10), 4619–4626 (2018)
8. O'Shea, Tuathan and Bamber, Jeffrey and Fontanarosa, Davide and van der Meer, Skadi and Verhaegen, Frank and Harris, Emma: Review of ultrasound image guidance in external beam radiotherapy part II: intra-fraction motion management and novel applications. Physics in Medicine & Biology **61**(8), R90 (2016)
9. Preiswerk, F., De Luca, V., Arnold, P., Celicanin, Z., Petrusca, L., Tanner, C., Bieri, O., Salomir, R., Cattin, P.C.: Model-guided respiratory organ motion prediction of the liver from 2D ultrasound. Med Image Anal **18**(5), 740–751 (2014)
10. Sandkühler, R., Jud, C., Andermatt, S., Cattin, P.C.: Airlab: Autograd image registration laboratory. arXiv preprint arXiv:1806.09907 (2018)

11. von Siebenthal, M., Szekely, G., Gamper, U., Boesiger, P., Lomax, A., Cattin, P.: 4D MR imaging of respiratory organ motion and its variability. Physics in Medicine & Biology **52**(6), 1547 (2007)
12. Stemkens, B., Paulson, E.S., Tijssen, R.H.: Nuts and bolts of 4D-MRI for radiotherapy. Physics in Medicine & Biology **63**(21), 21TR01 (2018)
13. Trnková, P., Knäusl, B., Actis, O., Bert, C., Biegun, A.K., Boehlen, T.T., Furtado, H., McClelland, J., Mori, S., Rinaldi, I., et al.: Clinical implementations of 4D pencil beam scanned particle therapy: Report on the 4D treatment planning workshop 2016 and 2017. Physica Medica **54**, 121–130 (2018)
14. Vezhnevets, V., Konouchine, V.: GrowCut: Interactive multi-label ND image segmentation by cellular automata. In: proc. of Graphicon. vol. 1, pp. 150–156. Citeseer (2005)

Chapter 8

Liver-ultrasound based motion modelling to estimate 4D dose distributions for lung tumours in scanned proton therapy

While the previous studies are interesting from a motion modelling point of view, it is not immediately apparent how modelling errors translate into misalignments in the dose distribution. The analysis presented in this chapter addresses this question by investigating the dosimetric impact of lung motion estimation in PBS proton therapy. In a simulation study, respiratory motion information was extracted from 4D MRI of five healthy volunteers and fused with CT scans of two lung cancer patients. Both the US surrogate signal and the motion estimate were projected into a lower-dimensional feature space by performing PCA. The relationship was modelled by means of a GPR model.

We performed the evaluation both in terms of geometrical estimation error and its effect on the dose distribution. The dosimetric errors found in this study suggest that the proposed motion model achieved clinically acceptable results.

Publication. The following manuscript was written in joint first authorship with M. Krieger from PSI. A. Giger developed the motion model while M. Krieger performed the treatment planning and the dose calculations. The manuscript has initially been submitted to the journal *Physics in Medicine & Biology* (PMB) on the 10th of March 2020. The revised manuscript, as presented in this chapter, has been submitted on the 17th of July 2020 and is currently under review.

Liver-ultrasound based motion modelling to estimate 4D dose distributions for lung tumours in scanned proton therapy

Alina Giger[a,b*], Miriam Krieger[c,d*], Christoph Jud[a,b], Alisha Duetschler[c,d], Rares Salomir[e,f], Oliver Bieri[a,g], Grzegorz Bauman[a,g], Damien Nguyen[a,g], Damien C Weber[c,h,i], Antony J Lomax[c,d], Ye Zhang[c], Philippe C Cattin[a,b]

[a] Department of Biomedical Engineering, University of Basel, Allschwil, Switzerland
[b] Center for medical Image Analysis & Navigation, University of Basel, Allschwil, Switzerland
[c] Paul Scherrer Institute (PSI), Center for Proton Therapy, Villigen PSI, Switzerland
[d] Department of Physics, ETH Zurich, Zurich, Switzerland
[e] Image Guided Interventions Laboratory (GR-949), Faculty of Medicine, University of Geneva, Geneva, Switzerland
[f] Radiology Division, University Hospitals of Geneva, Geneva, Switzerland
[g] Department of Radiology, Division of Radiological Physics, University Hospital Basel, Basel, Switzerland
[h] Department of Radiation Oncology, University Hospital Zurich, Zurich, Switzerland
[i] Department of Radiation Oncology, Inselspital Bern, Bern, Switzerland
[*] Both authors contributed equally

E-mail: alina.giger@unibas.ch, miriam.krieger@psi.ch

July 2020

Abstract. Motion mitigation strategies are crucial for scanned particle therapy of mobile tumours in order to prevent geometrical target miss and interplay effects. We developed a patient-specific respiratory motion model based on simultaneously acquired time-resolved volumetric MRI and 2D abdominal ultrasound images. We present its effects on 4D pencil beam scanned treatment planning and simulated dose distributions. Given an ultrasound image of the liver and the diaphragm, principal component analysis and Gaussian process regression were applied to infer dense motion information of the lungs. 4D dose calculations for scanned proton therapy were performed using the estimated and the corresponding ground truth respiratory motion; the differences were compared by dose difference volume metrics. We performed this simulation study on 10 combined CT and 4DMRI data sets where the motion characteristics were extracted from 5 healthy volunteers and fused with the anatomical CT data of two lung cancer patients. Median geometrical estimation errors below 2 mm for all data sets and maximum dose differences of $V_{diff>5\,\%} = 43.2\,\%$ and $V_{diff>10\,\%} = 16.3\,\%$ were found. Moreover, it was shown that abdominal ultrasound imaging allows to monitor organ drift. This study demonstrated the feasibility of the proposed ultrasound-based motion modelling approach for its application in scanned proton therapy of lung tumours.

Keywords: 4DMRI, motion modelling, Gaussian process regression, proton therapy, 4D dose calculation, pencil beam scanning, lung tumour

Submitted to: *Phys. Med. Biol.*

1. Introduction

In recent years, research has focused on understanding and mitigating the effects of respiratory motion on scanned particle therapy. When moving targets such as lung or liver tumours are treated with pencil beam scanned (PBS) proton therapy, geometrical target miss can lead to underdosage at the lateral edge and thus reduce the conformity of the field dose. The interference of the sequential delivery of the proton dose and the motion of the tumour additionally leads to local hot and cold spots, known as the interplay effect (Phillips et al. 1992, Bert & Durante 2011). Over- or underdosage at the distal field occurs due to the sensitivity of the proton beam with respect to the motion induced density variations. All those effects together may lead to a sub-optimal treatment plan which requires detailed investigation for each patient specifically (Chang et al. 2017, Zhang et al. 2018). Integral tools to study the aforementioned effects are 4D dose calculations (4DDCs). These are expansions of conventional 3D dose calculations that include both patient motion and delivery dynamics into the calculations. Various 4DDCs have been developed, see e.g. Bert & Rietzel (2007), Richter et al. (2013), Ammazzalorso & Jelen (2014), Paganetti et al. (2005), Kang et al. (2005), Li et al. (2014), Engwall et al. (2016), Boye, Lomax & Knopf (2013), Krieger et al. (2018), Grassberger et al. (2015), in which patient-specific motion information is the prerequisite for time-resolved dose estimation. Usually, this information is extracted from a pre-treatment respiratory-correlated computed tomography (4DCT) assuming that this average breathing cycle is repeated periodically during the plan delivery. Indeed, it is clear that any single 4DCT cannot capture respiratory variations nor does it provide any real-time information reflecting the real motion scenario during the treatment. However, both above aspects are crucial inputs for accurately estimating or reconstructing the actual dose that a patient receives.

Time-resolved volumetric magnetic resonance imaging (4DMRI) as e.g. developed by von Siebenthal et al. (2007), Giger, Stadelmann, Preiswerk, Jud, De Luca, Celicanin, Bieri, Salomir & Cattin (2018), or Jud et al. (2018) solves the issue of capturing motion variabilities. However, to date no imaging modality can capture and process full 3D lung information in real-time, meaning that some surrogate data is needed in order to estimate the patient motion during dose delivery. An optimal surrogate signal should capture internal motion information which is correlated to the organ motion of interest, expose the patient to no additional radiation dose, and can provide multidimensional surrogate signals. A candidate modality that fulfils all mentioned requirements is abdominal ultrasound (US) imaging. The motion of the liver and diaphragm can be captured in real-time and provides two-dimensional internal information (Giger, Stadelmann, Preiswerk, Jud, De Luca, Celicanin, Bieri, Salomir & Cattin 2018, Preiswerk et al. 2014). Due to physical constraints, direct US imaging of lung tissue is not possible. However, with the help of respiratory motion models, motion characteristics extracted from liver US can be used to estimate lung tumour motion (Mostafaei et al. 2018) and lung deformation (Giger, Sandkühler, Jud, Bauman,

Bieri, Salomir & Cattin 2018, Giger et al. 2019). While Mostafaei et al. (2018) have demonstrated the correlation between diaphragm motion and lung tumour motion in superior-inferior (SI) direction, Giger, Sandkühler, Jud, Bauman, Bieri, Salomir & Cattin (2018) and Giger et al. (2019) have inferred dense lung motion information from 2D abdominal US images. Since we aim to investigate respiratory motion and its variabilities in the context of PBS proton treatment, monitoring 1D tumour motion only is not sufficient as motion information of the surrounding tissue needs to be additionally taken into account (Trnková et al. 2018, Bertholet et al. 2019). Moreover, in contrast to our previous work (Giger et al. 2019), the motion model presented here is based on non-linear methods and therefore potentially has better estimation power.

The aim of this study was to investigate the dosimetric impact of lung motion estimation with the use of online abdominal US imaging and respiratory motion modelling in PBS proton therapy, mainly for two reasons: (1) The performed 4DDCs, when combined with temporal data provided by delivery log files (see e.g. Krieger et al. (2018)), may be used to retrospectively estimate the dose delivered to a patient and, if needed, to adapt the plans accordingly for future fractions (Meijers et al. 2019). (2) The presented framework forms the basis for US-guided proton beam tracking deliveries and, thus, should be understood as one of several steps towards this goal. We simulated realistic treatment scenarios with intra-fractional respiratory motion variabilities on synthetic 4DCT(MRI) data sets. Although similar studies have been performed on 4D data of the liver (Zhang et al. 2013, Zhang et al. 2014, Zhang et al. 2015), this work is the first focusing on the motion model application for lung tumour treatments and the use of abdominal US imaging as a non-invasive and informative surrogate signal.

2. Methods

2.1. Data acquisition

Hybrid US and 4DMRI data sets of five healthy volunteers were acquired under free respiration in a 1.5 T MRI scanner (MAGNETOM Aera, Siemens Healthineers, Erlangen, Germany). Among those, two data sets were acquired with a navigator-based slice-stacking approach (Celicanin et al. 2017) based on an ultra-fast balanced steady-state free precession (ufbSSFP) pulse sequence (Bieri 2013). Multi-slice coronal 2D MR images were acquired in sequential order, alternating with coronal navigator images at a fixed slice position. The remaining three data sets were acquired with a recently presented spoiled gradient echo 4DMRI sequence where core and pseudo-randomly sampled peripheral k-space patches are acquired alternately (Jud et al. 2018). The core patches are used to estimate the spatial relative motion in order to correct the peripheral patches for motion. These motion-corrected patches are subsequently accumulated into a consistent k-space for each motion state. Detailed information about the sequence parameters is listed in table 1. Hereinafter the two 4DMRI sequences are referred to as *slice stacking* and *patch registration* approach, respectively.

The frame rate of the two 4DMRI methods are $f_{\mathrm{MRI}} = 1.25\,\mathrm{Hz}$ and $2.25\,\mathrm{Hz}$, respectively. Simultaneous abdominal US imaging was performed at $f_{\mathrm{US}} = 15\,\mathrm{Hz}$ with an Acuson clinical scanner (Antares, Siemens Healthineers, Mountain View, CA). The system was equipped with a specially designed MR-compatible US linear array transducer consisting of 192 elements (Fraunhofer IBMT, Sulzbach, Germany), equivalent to the Siemens' VF7-3 probe, with central frequency 5 MHz, and bandwidth 4 MHz. The US imaging probe was strapped to the subjects' abdomen and held in place using a home-built casting, as shown in the report of (Santini et al. 2020). The probe was operated in B-mode at 3.3 MHz and covered a maximum field depth of 16 cm and an angular sector of up to 90°. The transmitted acoustic power was adjusted in situ case-specifically and was in the range of −11 to 8 dBm. No interference occurred between the US and the MR acquisitions. Data acquisition was performed for a duration of up to 11 min.

To ensure temporal correspondence between the two imaging modalities, two different strategies were employed. For the 4DMRI based on slice stacking, a continuous US video was acquired whose starting point coincided with the starting point of MR data acquisition within 0.5 to 1.1 s. The synchronisation was achieved via the software user interface of the two systems using a unique button signal sent at the beginning of the acquisition. The two imaging modalities were further temporally aligned in a post-processing step to correct for the residual offset caused by the dissimilar system response times of their software interface command. To do so, both the US images and the MR navigator slices were cropped to a region around the diaphragm based on which the mean image intensity was computed. These respiratory surrogate signals were filtered using a moving average filter before automatic peak detection was performed. Finally, the offset was computed as the time difference between the first peaks associated with end-inhalation for both signals. For the 4DMRI approach based on patch registration, optical output triggers of the MRI scanner were used to automatically start the US acquisitions using a fast hardware interface. One independent trigger signal was sent after every 6.675 s, or 15 MR frames, yielding the record of an US video of 5 s, as offered by the US system. Visual inspection of the extracted mean image intensity signals, computed similarly as described above, revealed that the offset between the two image modalities was negligible. Therefore, no post-processing was required in this case. The time difference of 1.675 s between the MR and US recording windows was chosen deliberately to take into account the US system latency while storing the US files. As a consequence, some MR images have no corresponding US images and were excluded from the motion modelling. Nevertheless, it happened that a trigger was issued before the previous US video was stored resulting in a further loss of US data of up to 7 % as shown in figure 1.

Due to the different frame rates of the 4DMRI and the US video, the sampling points do not perfectly match. However, since the frame rate of the US stream f_{US} is substantially higher than the one of the 4DMRI f_{MRI}, corresponding image pairs were assumed to represent the lungs in a sufficiently similar respiratory state.

Table 1: 4DMRI sequence parameters. The field of view and the image matrix are given in SI × LR × AP direction.

	Slice stacking (Celicanin et al. 2017)	Patch registration (Jud et al. 2018)
Contrast	T2/T1	T1
Flip angle	35°/28°	5°
Echo time	0.86 ms	1.0 ms
Repetition time	1.91 ms	2.5 ms
Bandwidth	2365 Hz px^{-1}	1560 Hz px^{-1}
Field of view	400 × 395.8 × 174.2 mm^3	400 × 400 × 275 mm^3
Image matrix	192 × 190 × 32 px	128 × 128 × 88 px
Core/peripheral patch radii	–	6 px/5 px

2.2. Deformable image registration

To extract motion information from the 4DMRI, volumetric deformable image registration (DIR) between 3D motion 'frames' was applied. For the slice stacking approach, a 3D B-spline based registration method implemented in Plastimatch‡ was used. The reconstructed image volumes were registered to a reference volume at end-exhalation. Conversely, for the patch registration approach, DIR of the core patches transformed to the spatial domain is required for the reconstruction of the 4DMRI in the first place. The resulting deformation vector fields (DVF) were the primary focus for this study and directly used as motion information for the subsequent step. In this case, the image registration was performed using the image registration framework AIRLab, a B-spline transformation model, an isotropic total variation regulariser, and the mutual information similarity measure (Sandkühler et al. 2018). The registration was performed for the lungs only by applying a semi-automatically extracted sliding-organ mask (Vezhnevets & Konouchine 2005). Again, all respiratory states were registered to a reference volume at end-exhalation.

2.3. 4DCT(MRI)

In order to conduct proton dose calculations, information on the relative proton stopping power is needed. This information can be extracted from CT Hounsfield Units (HU) with the use of a calibration curve. However, 4DCT, although capable of capturing motion, only represents one averaged breathing cycle, and does not include motion variability. Motion variabilities can be acquired using 4DMRI as described in the previous subsection. In order to combine these two types of information, synthetic 4DCT(MRI) data sets as described by Boye, Samei, Schmidt, Székely & Tanner (2013), Zhang et al. (2016) and Krieger et al. (2020) were generated.
DVFs extracted from the five 4DMRI data sets were matched to the full-exhale CT scans

‡ `www.plastimatch.org`, accessed: 13.01.2020

of two lung cancer patients§ following the meshing approach described in detail by Boye, Samei, Schmidt, Székely & Tanner (2013). Using this procedure, the two geometries (volunteer MRI and patient CT) are brought to anatomical correspondence by definition and thus the MRI DVFs can be readily transferred to the CT geometry. In order to preserve the sliding boundaries between the lungs and the chest wall, the motion of the chest wall is set to zero. By warping two CT geometries with five MRI motion patterns, ten different geometry/motion combinations were generated, each including 99 to 159 full and variable breathing cycles.
The two CT geometries were deliberately chosen because of their significant difference in size and position: geometry 1 shows a small tumour not attached to neighbouring tissues, geometry 2 contains a larger tumour which is partially attached to the spine. Figure 1 shows the target motion patterns in SI direction for all data sets. For motion 5, a drift of the clinical target volume (CTV) is observable in both CT geometries. A schematic of the target amplitudes and periods is shown in figure 2.

2.4. Motion modelling

A motion model based on Gaussian process (GP) regression was employed in order to estimate the respiratory motion during dose delivery (Williams & Rasmussen 2006). Given the input US image, the model infers the corresponding DVF of the lungs. A schematic overview of the motion model is given in figure 3.

Let $\boldsymbol{x}_t \in \mathbb{R}^{mn}$ denote the vectorised US image of dimension $m \times n$ at time t and analogously $\boldsymbol{y}_t \in \mathbb{R}^{3pqr}$ the vectorised DVF of dimension $p \times q \times r \times 3$. The factor of 3 in $\boldsymbol{y}_t$ is introduced since the voxel values of the DVF are 3-dimensional deformation vectors. Principal component analysis (PCA) has been applied prior to fitting the motion model in order to reduce the dimensionality of $\boldsymbol{x}_t$ and $\boldsymbol{y}_t$ and to remove co-linearities and noise (McClelland et al. 2013). Let $\boldsymbol{\alpha}_t \in \mathbb{R}^u$ and $\boldsymbol{\beta}_t \in \mathbb{R}^v$ represent the principal components (PC) of the US image $\boldsymbol{x}_t$ and the DVF $\boldsymbol{y}_t$, respectively. The number of PCs u and v considered for motion modelling was chosen such that the explained variance is greater than 50 %.

Given a set of M corresponding PCs, $\mathcal{S} = \{(\boldsymbol{\alpha}_t, \boldsymbol{\beta}_t) \,|\, t = 1, \ldots, M\}$, the regression can now be formulated in the feature space. The objective is to find a function $f : \mathbb{R}^u \to \mathbb{R}^v$ which maps the input PCs $\boldsymbol{\alpha}_t$ to the output PCs $\boldsymbol{\beta}_t$ assuming noisy observations:

$$\boldsymbol{\beta}_t = f(\boldsymbol{\alpha}_t) + \boldsymbol{\epsilon}_t, \qquad \boldsymbol{\epsilon}_t \sim \mathcal{N}(\mathbf{0}, \sigma_n^2 I_v), \tag{1}$$

where σ_n^2 denotes the noise variance and I_v the v-dimensional identity matrix. Let $f(\boldsymbol{\alpha}_t)$ be a GP with zero mean and covariance function $k : \mathbb{R}^u \times \mathbb{R}^u \to \mathbb{R}^{v \times v}$, that is

$$f(\boldsymbol{\alpha}_t) \sim \mathcal{GP}(\mathbf{0}, k(\boldsymbol{\alpha}_t, \boldsymbol{\alpha}_{t'})). \tag{2}$$

Then, given the input $\boldsymbol{\alpha}_*$ and the measurements $\mathcal{S}$, the estimate $\boldsymbol{\beta}_*$ can be calculated from the posterior distribution which is again a GP with mean $\boldsymbol{\mu}_S \in \mathbb{R}^v$ and covariance

§ Hugo et al. (2016), Hugo et al. (2017), Balik et al. (2013), Roman et al. (2012), Clark et al. (2013)

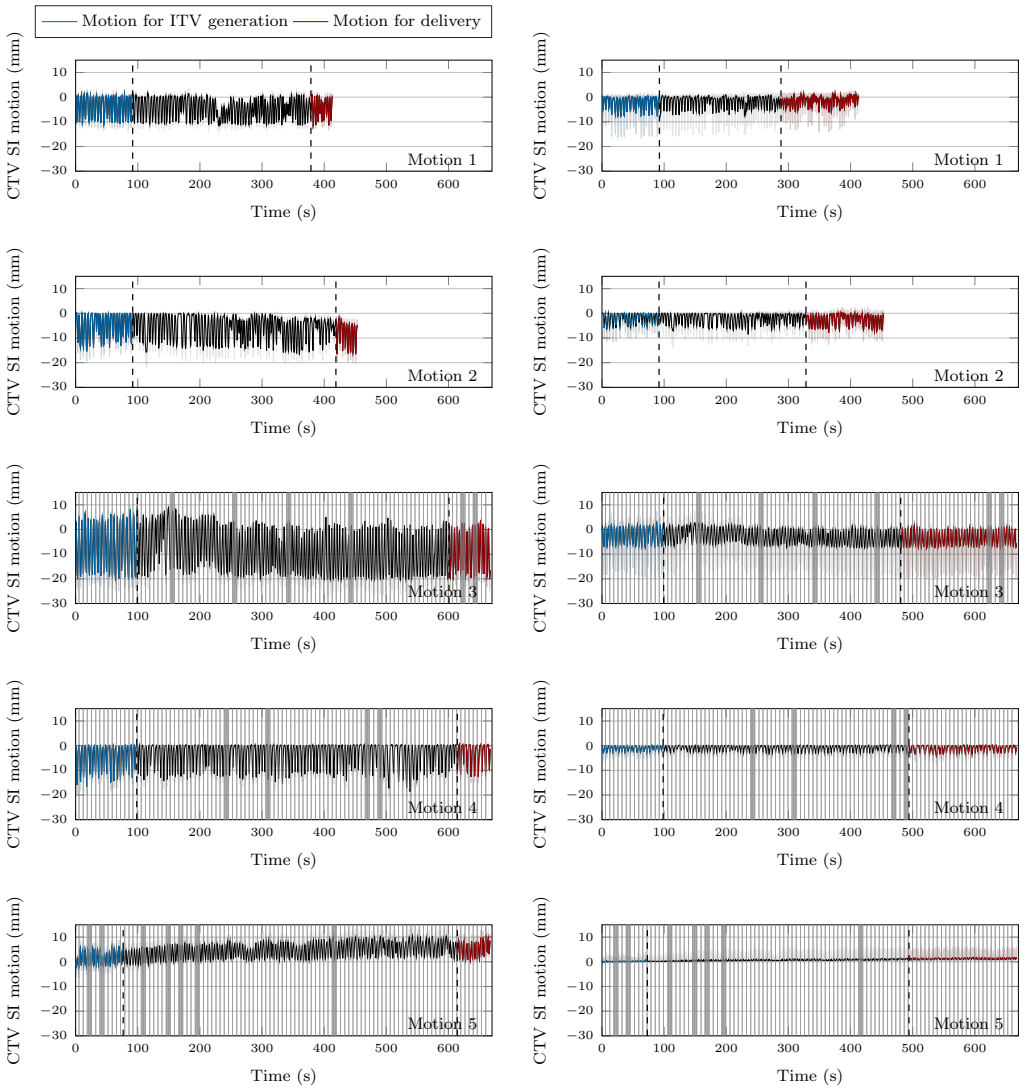

(a) CT geometry 1

(b) CT geometry 2

Figure 1: Motion patterns of the tumour in SI direction for all data sets. The grey shaded areas depict MR motion states without corresponding US frames. The red curve represents the motion for dose delivery and, therefore, the test set for motion modelling. The remaining data (blue and black curve) was split into a training and validation set for motion modelling while the blue curve was additionally used for ITV generation and treatment planning. Solid line: median, shades: 10th to 90th percentile.

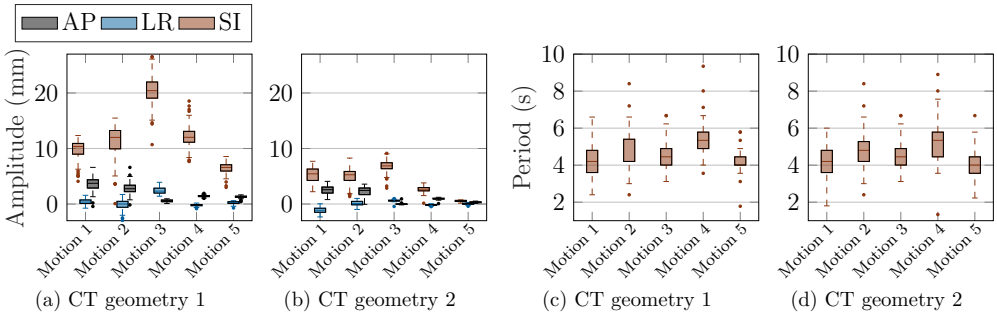

(a) CT geometry 1 (b) CT geometry 2 (c) CT geometry 1 (d) CT geometry 2

Figure 2: Overview over the motion amplitudes in each motion direction (a), (b) and motion periods (c), (d). The boxplots include all breathing cycles in the respective data set. The whiskers extend to the most extreme values still within 1.5 time the inter-quartile range (IQR). SI: superior-inferior, LR: left-right, AP: anterior-posterior.

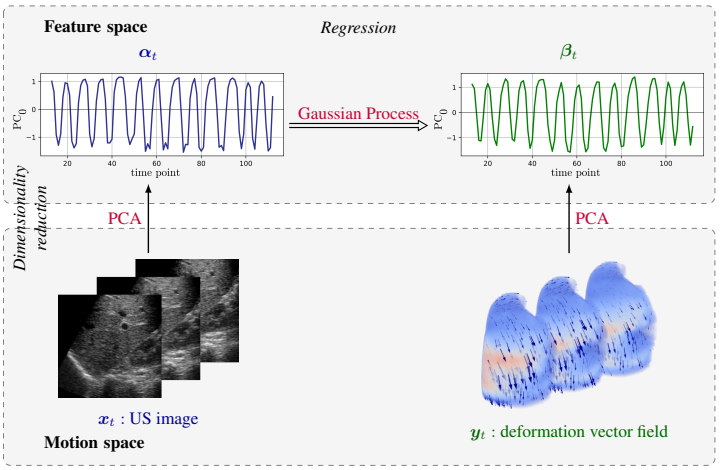

Figure 3: Schematic overview of the motion model.

$k_S \in \mathbb{R}^{v\times v}$ (Williams & Rasmussen 2006):

$$p(\boldsymbol{\beta}_*|\boldsymbol{\alpha}_*, \mathcal{S}) = \mathcal{GP}(\boldsymbol{\mu}_S, k_S). \tag{3}$$

Let $K \in \mathbb{R}^{vM\times vM}$ represent a matrix of the covariance $k(\boldsymbol{\alpha}_i, \boldsymbol{\alpha}_j)$ evaluated for all input training point pairs, $(\boldsymbol{\alpha}_i, \boldsymbol{\alpha}_j)$ with $i, j \in \{1, \dots, M\}$. Similarly, let $K_* \in \mathbb{R}^{vM\times v}$ denote the matrix of the covariance between the test point $\boldsymbol{\alpha}_*$ and the M training points, $k(\boldsymbol{\alpha}_*, \boldsymbol{\alpha}_i)$ with $i \in \{1, \dots, M\}$. Finally, the output training points are collected in a vector $\boldsymbol{b} = \left[\boldsymbol{\beta}_1^T \dots \boldsymbol{\beta}_M^T\right]^T \in \mathbb{R}^{vM}$. The mean and covariance of the posterior can now be

written in closed form using the vM-dimensional identity matrix I_{vM}:

$$\boldsymbol{\mu}_S = K_*^T \left(K + \sigma_n^2 I_{vM}\right)^{-1} \boldsymbol{b}, \tag{4}$$

$$k_S = k\left(\boldsymbol{\alpha}_*, \boldsymbol{\alpha}_*\right) - K_*^T \left(K + \sigma_n^2 I_{vM}\right)^{-1} K_*. \tag{5}$$

Since the respiratory motion in the lungs is expected to be smooth, a Gaussian kernel was chosen as covariance function,

$$k\left(\boldsymbol{\alpha}_t, \boldsymbol{\alpha}_{t'}\right) = \theta_0^2 \exp\left(-\frac{\|\boldsymbol{\alpha}_t - \boldsymbol{\alpha}_{t'}\|^2}{2\theta_1^2}\right) I_v, \tag{6}$$

with scaling parameter θ_0 and characteristic length-scale θ_1. The mean of the posterior distribution $\boldsymbol{\mu}_S$ represents the best estimate of the GP regression. Moreover, the posterior variance k_S can be interpreted as estimation uncertainty and might serve as a confidence value or quality measure (Williams & Rasmussen 2006).

The hyperparameters were manually optimised and set to $\theta_0 = 30$, $\theta_1 = 35$ and $\sigma_n^2 = 1$ for all geometry/motion data sets. The motion data as shown in figure 1 was split into a training, validation and test set. The size of the test set (red curve) was defined as the minimum number of motion states needed for the dose delivery and is in the range of 59 to 88 states for geometry 1 and 210 to 286 states for geometry 2. The remaining data (blue and black curve) was further split into a constant validation set consisting of the last 55 states and a training set of 425 to 913 states.

2.5. 4D treatment planning and dose calculation

As a planning target, we use a previously presented probabilistic ITV concept (Krieger et al. 2020). The ITV50 of the first 20 breathing cycles of each geometry/motion case was used as the target for optimisation. For this, conventional ITVs were first created by unifying all CTV positions of one breathing cycle at a time. By summing up these 20 ITVs, a probability map of the tumour position was generated. The probabilistic ITV50 was then defined as all voxels with a probability of 50 % of being within any ITV calculated from any motion cycle. In order to achieve sufficient target coverage in the static case, a 2 mm margin was added to the ITV50 to define the technical planning target volume (tech-PTV). In this study, the set-up uncertainties were neither considered in the treatment planning nor simulated for the dynamic dose delivery. As planning CT, the definition of Botas et al. (2018) was applied. The density values in the whole CT minus the ITV50 were set to the average value within the first 20 breathing cycles, whereas the density values within the ITV50 were defined as the maximum intensity projection of the same 20 breathing cycles. Thus, every geometry/motion case had its own planning CT and tech-PTV. For both CT geometries, a single field, uniform dose (SFUD) plan with two fields was optimised on the tech-PTV and the planning CT of the respective geometry/motion case due to SFUD's superior stability in the presence of motion (Gorgisyan et al. 2019). The field directions and CTV volumes are shown in figure 4. For the optimisation and the consequent 4D dose calculations, the delivery model of the PSI gantry 2 was used (Pedroni et al. 2004).

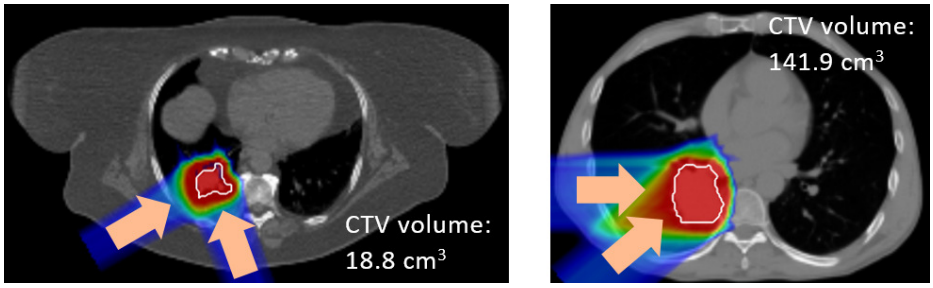

Figure 4: Illustration of the two CT geometries and the beam directions of the treatment plans. Left panel: CT geometry 1, right panel: CT geometry 2.

A ray casting based, deforming grid 4D dose calculation engine as described by Boye, Lomax & Knopf (2013) and validated experimentally by Krieger et al. (2018) was used in order to study the dosimetric effects of the motion estimation. 4DDCs were performed using either the ground truth or the corresponding estimated motion states as input. All motion states of the first *delivery* cycle were used as starting point for the simulation since it is usually unknown in which respiratory state the delivery would start. Depending on the motion pattern, the number of starting phases per field ranged from 5 to 13 (average: 9.2), resulting in 25 to 169 (average: 91.2) scenarios per two-field plan.

2.6. Evaluation

Geometrical error The geometrical estimation error $\boldsymbol{e}_t \in \mathbb{R}^{pqr}$ for motion state t is defined based on the voxel-wise difference between the ground truth and the estimated DVFs. Let $\boldsymbol{v}_t^i \in \mathbb{R}^3$ denote the ground truth deformation vector at voxel $i \in \{1, \ldots, pqr\}$. Similarly, let $\tilde{\boldsymbol{v}}_t^i \in \mathbb{R}^3$ be the estimated deformation vector at voxel i. Then, the i-th entry of the estimation error $\boldsymbol{e}_t$ is given as

$$e_t^i = \|\boldsymbol{v}_t^i - \tilde{\boldsymbol{v}}_t^i\|, \tag{7}$$

where $\|\cdot\|$ denotes the Euclidean norm. Note that the term ground truth refers to the target DVF used to train the model. Although the extracted DVFs do not necessarily represent the real patient motion due to errors introduced by the registration and the 4DCT(MRI) generation, they do still represent a valid ground truth for the motion model.

In order to get a qualitative overview of the error distributions in space, error maps were generated using a colour wash to indicate the spatial distribution of the estimation error, averaged over all motion states.

For a quantitative analysis, the 50th and 95th percentiles of the estimation error within a given volume of interest $\mathrm{VOI}_{\mathrm{geom}}$ were calculated for each respiratory state. Below, the results are reported as a distribution of these percentiles over all motion states. The

VOI_{geom} was defined as all voxels which receive any dose in the static dose calculation and which lie within the lung or the ITV.

Drift analysis The geometrical estimation error was equivalently evaluated as described above in order to investigate the influence of the organ drift on the performance of the motion model. To do so, the training sets for motion 5 and both geometries were divided into equally sized subsets consisting of 220 motion states or 97.9 s each. The quantitative analysis was conducted using each of the 4 subsets for geometry 1 and 3 subsets for geometry 2 as training set while the test set remained unchanged. Subset 1 represents the training motion data from respiratory states 1 to 220, subset 2 from states 221 to 440, and so on. Consequently, there is a decreasing time gap between the training set and the test set for an increasing number of the subset.

Dosimetric error The dose error was calculated as the voxel-wise absolute dose difference between ground truth and estimated 4DDCs. Absolute dose difference volume histograms (DDVHs) were calculated for the CTV and the volume of interest VOI_{dose} defined as all voxels within the CTV plus 20 mm margin, which lie within the lung. Additionally, the median volume percentages for which the absolute dose difference was more than 5 % or 10 % of the prescribed dose, respectively, were calculated ($V_{diff>5\,\%}$, $V_{diff>10\,\%}$).

3. Results

3.1. Geometrical error

Figure 5 shows one sagittal slice through the CT geometries with an error map overlaid for each geometry/motion case. It can be seen that the error tends to become larger towards the edge of the lung. For all scenarios, the tumour lies partly within the high error region and partly within the lower error region. Motions 1 and 2 tend to have larger geometrical errors than motions 3–5. Boxplots of the geometrical estimation error including all motion states are shown in figure 6. It is seen that the 50th and 95th percentile error within the VOI_{geom} for one motion are similar for the two CT geometries. Again, the largest errors of up to 8 mm (95th percentile) are found for motions 1 and 2 (geometries 1 and 2). For motion 3, geometries 1 and 2, the error stays below 4 mm and 2 mm respectively except for a few outlying motion states. Motion 4 and 5 show errors below 2 mm for both CT geometries. When looking at the 50th percentile (median), the errors stay below 3 mm for all cases except for a few outliers. For motions 3–5 it is lower than 1 mm.

3.2. Drift analysis

The drift analysis in figure 7 indicates that the estimation error increases the greater the time gap between the training data and the test data. For both CT geometries,

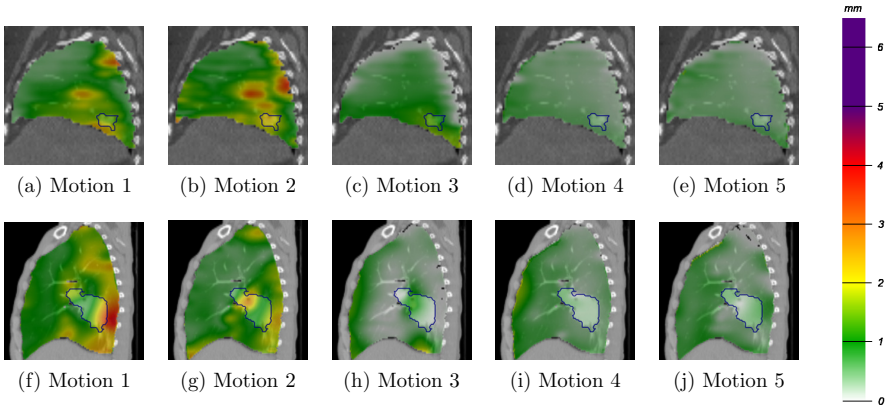

(a) Motion 1 (b) Motion 2 (c) Motion 3 (d) Motion 4 (e) Motion 5

(f) Motion 1 (g) Motion 2 (h) Motion 3 (i) Motion 4 (j) Motion 5

Figure 5: Example sagittal slices to illustrate the spatial error distribution, averaged over time. Top row: CT geometry 1, bottom row: CT geometry 2.

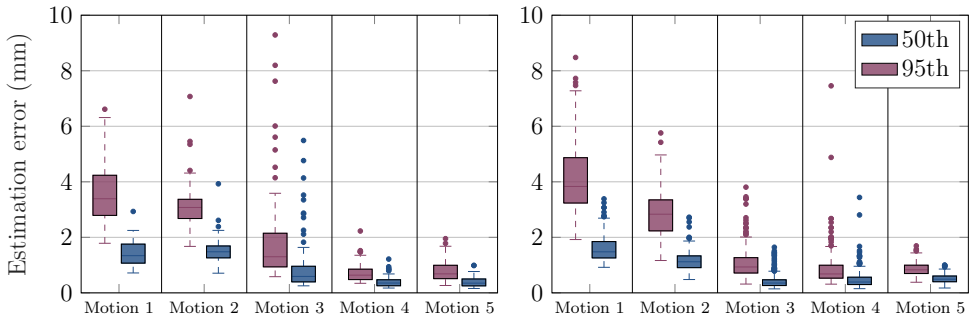

(a) CT geometry 1 (b) CT geometry 2

Figure 6: Motion estimation errors for all geometries and motions. The boxplots indicate the error percentiles of all voxels within the VOI_{geom}. The whiskers include all values within 1.5 IQR.

the estimation error is up to 4 times higher for subset 1 when compared to subset 4. The performance of the motion model is similar when it was trained on the complete training set or subset 4 only.

3.3. Dosimetric error

The influence of the estimation error on the dose distributions is shown in figure 8. The absolute dose difference volume histograms within the CTV and the VOI_{dose} are plotted for each 4DCT(MRI) data set. The solid lines display the median values, whereas the

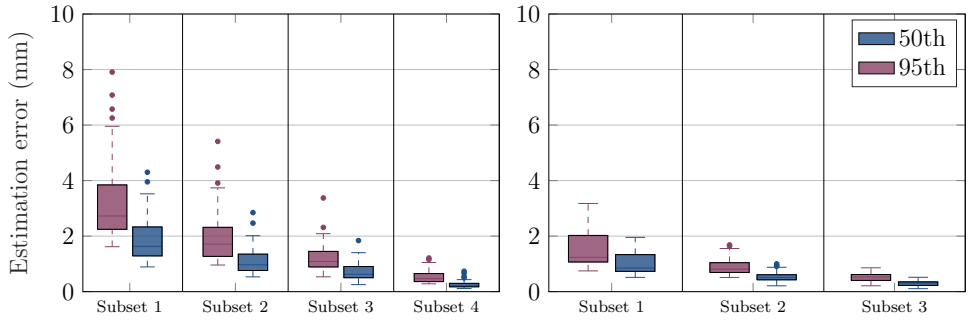

(a) CT geometry 1, motion 5 (b) CT geometry 2, motion 5

Figure 7: Drift analysis for motion 5 and different training subsets. The boxplots indicate the error percentiles of all voxels within the VOI_{geom}. The whiskers include all values within 1.5 IQR.

shaded bands include all possible starting phases (5^2 – 13^2 per two-field plan). It is seen that for CT geometry 2, the dose differences are somewhat lower and the spread due to different starting phases is less pronounced than for CT geometry 1. Motion 3 presents the highest dose differences, whereas the other motions present similar dose differences. When looking at the volumes with a difference of more than 5 % or 10 % (table 2), it is again seen that motion 3 leads to the highest percentages compared to other motion patterns. Again, geometry 2 shows lower values than geometry 1, except for the $V_{diff>10\,\%}$ of motion 4. All $V_{diff>5\,\%}$ values are below 44 %, and even below 30 % if motion 3 is not considered. Similarly, the $V_{diff>10\,\%}$ percentages are below 17 % for all cases and below 9 % when excluding motion motion 3.

4. Discussion

In this work, we have investigated the effects of respiratory motion estimation on the dose distribution in PBS proton therapy of lung tumours. Dense motion information in the lungs was estimated based on abdominal US imaging and patient-specific respiratory motion modelling. Time-resolved 4DCT(MRI) were employed to simulate motion variabilities over a comprehensive time duration of up to 11 min using two different 4DMRI approaches. To take these motion variabilities into account for treatment planning, a recently presented probabilistic ITV definition was applied (Krieger et al. 2020) and two-field SFUD plans were optimised on composite planning CTs.

Good geometrical and dosimetric agreement were achieved, however, with a tendency of higher geometrical errors for the 4DMRI based on slice stacking when compared to the patch registration approach. Due to the reconstruction properties of the latter method, which is based on DIR of low spatial resolution core patch

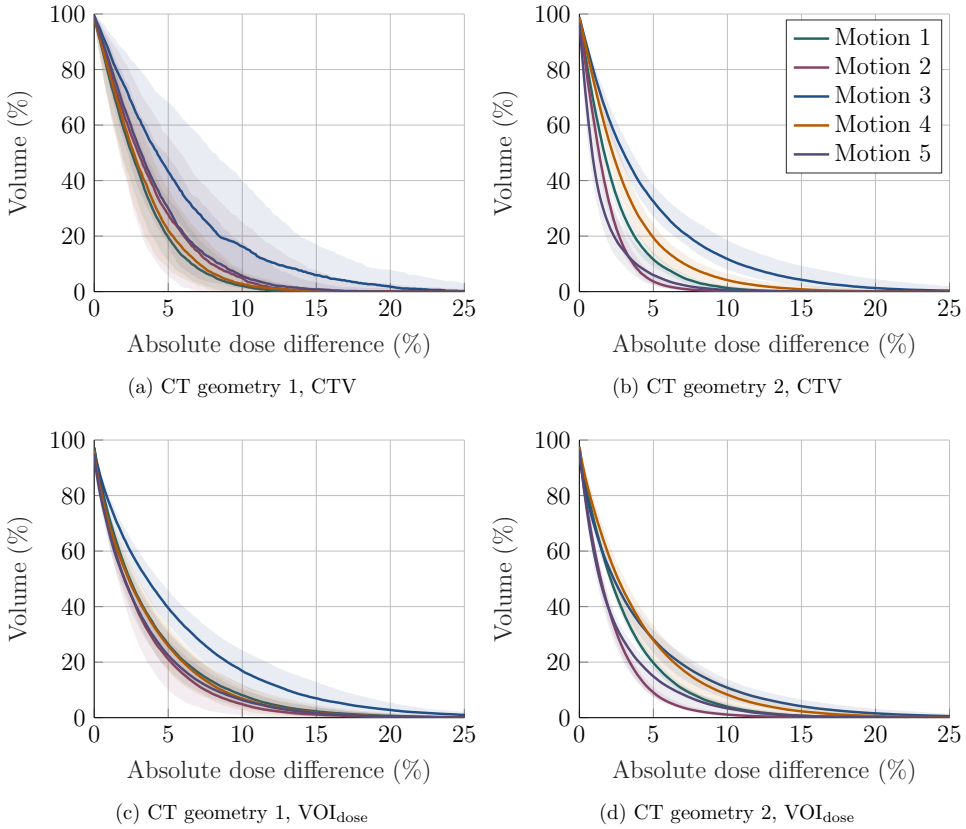

(a) CT geometry 1, CTV

(b) CT geometry 2, CTV

(c) CT geometry 1, VOI_{dose}

(d) CT geometry 2, VOI_{dose}

Figure 8: Absolute dose difference histograms for all geometries and motion cases, evaluated in the CTV and in VOI_{dose}.

reconstructions, the DVFs tend to be smoother and therefore potentially less prone to estimation errors. Additionally, the higher temporal resolution and larger training data sets available for this method may further influence the estimation accuracy positively. With 50th and 95th percentiles estimation errors in the range of 2 mm and 4 mm, respectively, for all geometry/motion cases, the presented respiratory motion model achieves clinically relevant results. It was also demonstrated that higher geometrical errors do not coincide with higher dosimetric errors. This suggests that the presented analysis is robust against the chosen 4DMRI method and, therefore, allows for viable conclusions regarding dosimetric errors. The dosimetric errors found in this study are in a clinically acceptable range, especially because for treatment, a motion mitigation technique such as rescanning can be combined. This has been shown to additionally reduce dosimetric uncertainties due to motion (Krieger et al. 2018, Zhang et al. 2014).

Table 2: Dose difference parameters, analysed in the VOI_{dose} and the CTV.

(a) VOI_{dose}

		Motion 1	Motion 2	Motion 3	Motion 4	Motion 5
$V_{diff>5\,\%}$	CT geom. 1	26.4 %	21.1 %	39.5 %	25.8 %	22.4 %
	CT geom. 2	19.7 %	9.1 %	28.2 %	27.9 %	14.9 %
$V_{diff>10\,\%}$	CT geom. 1	8.1 %	4.8 %	16.8 %	6.9 %	6.3 %
	CT geom. 2	4.0 %	1.1 %	10.8 %	8.3 %	3.4 %

(b) CTV

		Motion 1	Motion 2	Motion 3	Motion 4	Motion 5
$V_{diff>5\,\%}$	CT geom. 1	19.4 %	27.8 %	43.2 %	22.0 %	29.9 %
	CT geom. 2	11.6 %	3.7 %	32.5 %	19.5 %	6.0 %
$V_{diff>10\,\%}$	CT geom. 1	2.1 %	4.8 %	16.3 %	2.8 %	5.7 %
	CT geom. 2	1.3 %	0.2 %	11.8 %	4.1 %	0.6 %

Moreover, reasonable motion estimation performance was achieved for all geometry/motion cases even though the same hyperparameter set was chosen for all cases. This points to the conclusion that the presented motion model is robust with respect to different patient geometries and motion patterns. The fact that no extensive parameter tuning is required for every individual patient, makes this approach feasible for clinical applications. The drift analysis in figure 6 further revealed that the internal motion information provided by the abdominal US imaging was able to record organ drift. That does not necessarily mean that the motion model is able to cope with this long-term changes, however, it might still be used to monitor potential organ drift and to trigger an intervention of the clinicians if needed. Further investigations on prolonged data sets are required and the aim of future studies.

The 4DCT(MRI) data sets are synthetic in the sense that the respiratory motions of healthy volunteers were combined with the geometries of two cancer patients. This further implies that the motion of the CTV was simulated by healthy motion patterns and might not ideally represent pathological motion characteristics. Also, the US images used as motion surrogates do not match the anatomical geometry of the patients. However, we do not expect our findings to change substantially if pathological motion patterns and corresponding patient geometries were used for the analysis. Moreover, the current approach to generate 4DCT(MRI) data sets required the lung volume to be segmented. Consequently, the DVFs were applied to the lung tissue only while the surrounding structures such as the ribs and the skin remained static. However, we are working on a multi-organ numerical 4D phantom to fix this limitation.

For the motion model to be transferred to the clinics, it remains to be shown how the proposed approach performs in the case of inter-fractional motion variabilities. Besides anatomical changes on a day-to-day basis, this further implies dissimilar US imaging

planes due to the required repositioning of the US probe on the patient's abdominal wall. In a first study we have demonstrated the ability of a similar motion model to cope with US probe repositioning (Giger et al. 2019). However, the two data sets were acquired on the same day with only a few minutes in between, therefore not representing truly inter-fractional anatomical changes and motion variabilities.

Given the promising results of the presented study, further improvements are planned for future works. The synchronisation procedure between US and 4DMRI is currently being improved such that future data sets will not suffer from data loss as was the case for the 4DMRI based on patch registration. Instead, we aim for continuous US image acquisition as was the case for the 4DMRI based on slice stacking without, however, the need for subsequent temporal alignment. Further, we aim to extend the current analysis to the case where we simulate 3D tumour tracking by online proton beam adaptions. In this context, we will evaluate the use of the posterior variance of the GP regression as a quality measure for the motion estimation which could then potentially be used to combine tumour tracking and uncertainty-correlated gating.

5. Conclusion

Patient-specific motion modelling based on GP regression and abdominal US surrogates has shown to be a feasible and promising approach to estimate lung motion variabilities and their effects on dose distributions. It offers a possibility to take into account motion variabilities in 4D treatment planning, retrospective actual 4D dose reconstruction and online PBS beam tracking in future.

Acknowledgments

The authors thank Pauline Guillemin from the University of Geneva, Switzerland, for her support during the data acquisitions. This work was supported by the Swiss National Science Foundation, SNSF (project number 320030_163330/1).

References

Ammazzalorso F & Jelen U 2014 *Phys. Med. Biol.* **59**, N91–N99.

Balik S, Weiss E, Jan N, Roman N, Sleeman W C, Fatyga M, Christensen G E, Zhang C, Murphy M J, Lu J, Keall P, Williamson J F & Hugo G D 2013 *Int. J. Radiation Oncology Biol. Phys.* **86**, 372–379.

Bert C & Durante M 2011 *Physics in Medicine & Biology* **56**(16), R113.

Bert C & Rietzel E 2007 *Radiation Oncology* **2:24**.

Bertholet J, Knopf A, Eiben B, McClelland J, Grimwood A, Harris E, Menten M, Poulsen P, Nguyen D T, Keall P et al. 2019 *Physics in Medicine & Biology* **64**(15), 15TR01.

Bieri O 2013 *Magnetic resonance in medicine* **70**(3), 657–663.

Botas P, Grassberger C, Sharp G & Paganetti H 2018 *Phys. Med. Biol.* **63**, 035023.

Boye D, Lomax A J & Knopf A C 2013 *Med. Phys.* **40(6)**, 061702–1 – 061702–11.

Boye D, Samei G, Schmidt J, Székely G & Tanner C 2013 *in* 'Medical Imaging 2013: Image Processing' SPIE. doi: 10.1117/12.2007076.

Celicanin Z, Giger A, Bauman G, Cattin P & Bieri O 2017 *in* 'Proceedings of the ISMRM 25th Annual Meeting and Exhibition' Honolulu, Hawaii, USA.

Chang J Y, Zhang X, Knopf A, Li H, Mori S, Dong L, Lu H M, Liu W, Badiyan S N, Both S, Meijers A, Lin L, Flampouri S, Li Z, Umegaki K, Simone C B & Zhu X R 2017 *International Journal of Radiation Oncology*Biology*Physics* **99**(1), 41.

Clark K, Vendt B, Smith K, Freimann J, Kirby J, Koppe P, Moore S, Phillips S, Maffitt D, Pringle M, Tarbox L & Prior F 2013 *J. Digit. Imaging* **26(6)**, 1045–1057.

Engwall E, Hynning E, Janssens G & Glimelius L 2016 *Int. J. Particle Therapy: Summer 2016* **3(1)**, 71–276.

Giger A, Jud C, Nguyen D, Krieger M, Zhang Y, Lomax A J, Bieri O, Salomir R & Cattin P C 2019 *in* 'International Workshop on PRedictive Intelligence In MEdicine' Springer pp. 11–22.

Giger A, Sandkühler R, Jud C, Bauman G, Bieri O, Salomir R & Cattin P C 2018 *in* 'International Conference on Medical Image Computing and Computer-Assisted Intervention' Springer pp. 81–88.

Giger A, Stadelmann M, Preiswerk F, Jud C, De Luca V, Celicanin Z, Bieri O, Salomir R & Cattin P C 2018 *Physics in Medicine & Biology* **63**(14), 145015.

Gorgisyan J, Lomax A J, Munck af Rosenschöld P, Persson G F, Krieger M, Colvill E, Scherman J, Gagnon-Moisan F, Egloff M, Fattori G, Engelholm S A, Weber D C & Perrin R 2019 *Radiotherapy and Oncology* **134**, 135–142.

Grassberger C, Dowdell S, Sharp G & Paganetti H 2015 *Medical Physics* **42**(5), 2462–2469.

Hugo G D, Weiss E, Sleeman W C, Balik S, Keall P J, Lu J & Williamson J 2016 *Data from 4D Lung Imaging of NSCLC Patients. The Cancer Imaging Archive.*
URL: *http://doi.org/10.7937/K9/TCIA.2016.ELN8YGLE*

Hugo G D, Weiss E, Sleeman W C, Balik S, Keall P J, Lu J & Williamson J 2017 *Med. Phys.* **44**, 762–771.

Jud C, Nguyen D, Sandkühler R, Giger A, Bieri O & Cattin P C 2018 *in* 'International Conference on Medical Image Computing and Computer-Assisted Intervention' Springer pp. 198–205.

Kang Y, Zhang X, Chang J Y, Wang H, Wei X, Liao Z et al. 2005 *Int. J. Radiation Oncology Biol. Phys.* **67**, 906–914.

Krieger M, Giger A, Weber D C, Lomax A J & Zhang Y 2020 *Radiotherapy and Oncology* **145**, 154–161.

Krieger M, Klimpki G, Fattori G, Hrbacek J, Oxley D, Safai S, Weber D C, Lomax A J & Zhang Y 2018 *Physics in Medicine & Biology* **63**(5), 055005.

Li Y, Kardar L, Li H, Cao W, Chang J Y et al. 2014 *Med. Phys.* **41(2)**, 021721.

McClelland J R, Hawkes D J, Schaeffter T & King A P 2013 *Medical image analysis* **17**(1), 19–42.

Meijers A, Jakobi A, Sttzer K, Guterres Marmitt G, Both S, Langendijk J A, Richter C & Knopf A 2019 *Medical Physics* **46**(3), 1140–1149.

Mostafaei F, Tai A, Gore E, Johnstone C, Haase W, Ehlers C, Cooper D T, Lachaine M & Li X A 2018 *Medical physics* **45**(10), 4619–4626.

Paganetti H, Jiang H & Trofimov A 2005 *Phys. Med. Biol.* **50**, 983–990.

Pedroni E, Bearpark R, Böhringer T, Coray A, Duppich J, Forss S, George D, Grossmann M, Goitein G, Hilbes C, Jermann M, Lin S, Lomax A, Negrazus M, Schippers M & Kotrle G 2004 *Zeitschrift für Medizinische Physik* **14**, 25–34.

Phillips M H, Pedroni E, Blattmann H, Boehringer T, Coray A & Scheib S 1992 *Physics in Medicine & Biology* **37**(1), 223.

Preiswerk F, De Luca V, Arnold P, Celicanin Z, Petrusca L, Tanner C, Bieri O, Salomir R & Cattin P C 2014 *Medical image analysis* **18**(5), 740–751.

Richter D, Schwarzkopf A, Trautmann J, Kraemer M, Durante M, Jaekel O & Bert C 2013 *Med. Phys.* **40(5)**, 051722–1 – 051722–17.

Roman N O, Shepherd W, Mukhopadhyay N, Hugo G D & Weiss E 2012 *Int. J. Radiation Oncology Biol. Phys.* **83**, 1566–1572.

Sandkühler R, Jud C, Andermatt S & Cattin P C 2018 *arXiv preprint arXiv:1806.09907* .

Santini F, Gui L, Lorton O, Guillemin P C, Manasseh G, Roth M, Bieri O, Vallée J P, Salomir R & Crowe L A 2020 *Physica Medica* **70**, 161–168.

Trnková P, Knäusl B, Actis O, Bert C, Biegun A K, Boehlen T T, Furtado H, McClelland J, Mori S, Rinaldi I et al. 2018 *Physica Medica* **54**, 121–130.

Vezhnevets V & Konouchine V 2005 *in* 'proc. of Graphicon' Vol. 1 Citeseer pp. 150–156.

von Siebenthal M, Székely G, Gamper U, Boesiger P, Lomax A & Cattin P 2007 *Physics in Medicine & Biology* **52**(6), 1547.

Williams C K & Rasmussen C E 2006 *Gaussian processes for machine learning* Vol. 2 MIT press Cambridge, MA.

Zhang Y, Huth I, Weber D C & Lomax A J 2018 *Radiotherapy and Oncology* **128**(1), 182–188.

Zhang Y, Huth I, Wegner M, Weber D C & Lomax A J 2016 *Radiotherapy and oncology* **121**(2), 281–287.

Zhang Y, Knopf A C, Weber D C & Lomax A J 2015 *Physics in Medicine & Biology* **60**(20), 8141.

Zhang Y, Knopf A, Tanner C, Boye D & Lomax A J 2013 *Physics in Medicine & Biology* **58**(24), 8621.

Zhang Y, Knopf A, Tanner C & Lomax A 2014 *Physics in Medicine & Biology* **59**(24), 7793.

Chapter 9

Liver-ultrasound-guided lung tumour tracking for scanned proton therapy

To take the previous analysis one step further, the study presented in this chapter investigates the performance of the respiratory motion model based on GPR in combination with lung tumour tracking. However, in order to take system latencies into account, the motion model was complemented by an autoregressive model for temporal prediction as described in Chapter 7. Moreover, 4D dose distributions were analysed for both 2D and 3D tracking and retracking. The simulation study was performed based on the same data sets as previously described in Chapter 8.

Although the motion prediction errors only had a minor influence on the dose distributions when compared to the ground truth motions, the study confirms that tracking alone might not be sufficient to effectively mitigate motion effects. Therefore, it is recommended to apply tumour tracking in combination with other motion mitigation techniques, for example rescanning.

Publication. The following manuscript was jointly written with M. Krieger from PSI. Similar to before, A. Giger developed the respiratory motion model and performed the motion predictions; M. Krieger focused on the treatment planning, the dose calculations and the analysis of the results. The manuscript has been submitted to the journal *Physics in Medicine & Biology* (PMB) on the 12th of June 2020 and is currently under review.

Liver-ultrasound-guided lung tumour tracking for scanned proton therapy

Miriam Krieger[a,b*], **Alina Giger**[c,d*], **Christoph Jud**[c,d], **Alisha Duetschler**[a,b], **Rares Salomir**[e,f], **Oliver Bieri**[c,g], **Grzegorz Bauman**[c,g], **Damien Nguyen**[c,g], **Philippe C Cattin**[c,d], **Damien C Weber**[a,h,i], **Antony J Lomax**[a,b], **Ye Zhang**[a]

[a] Paul Scherrer Institute (PSI), Center for Proton Therapy, Villigen PSI, Switzerland
[b] Department of Physics, ETH Zurich, Zurich, Switzerland
[c] Department of Biomedical Engineering, University of Basel, Allschwil, Switzerland
[d] Center for medical Image Analysis & Navigation, University of Basel, Allschwil, Switzerland
[e] Image Guided Interventions Laboratory (GR-949), Faculty of Medicine, University of Geneva, Geneva, Switzerland
[f] Radiology Division, University Hospitals of Geneva, Geneva, Switzerland
[g] Department of Radiology, Division of Radiological Physics, University Hospital Basel, Basel, Switzerland
[h] Department of Radiation Oncology, University Hospital Zurich, Zurich, Switzerland
[i] Department of Radiation Oncology, Inselspital Bern, Bern, Switzerland
[*] Both authors contributed equally

E-mail: miriam.krieger@psi.ch, alina.giger@unibas.ch

May 2020

Abstract. Pencil beam scanned (PBS) proton therapy of lung tumours is hampered by respiratory motion and the motion-induced density changes along the beam path. In this simulation study, we aim to investigate the effectiveness of proton beam tracking for lung tumours both under ideal conditions and in conjunction with a respiratory motion model guided by real-time ultrasound imaging of the liver. Multiple-breathing-cycle 4DMRIs of the thorax and abdominal 2D ultrasound images were acquired simultaneously for five volunteers. Deformation vector fields extracted from the 4DMRI, referred to as ground truth motion, were used to generate 4DCT(MRI) data sets of two lung cancer patients, resulting in 10 data sets with variable motion patterns. Given the 4DCT(MRI) and the corresponding ultrasound images as surrogate data, a patient-specific motion model was built. The model consists of an autoregressive model and Gaussian process regression for the temporal and spatial prediction, respectively. Two-field PBS plans were optimised on the reference CTs, and 4D dose calculations (4DDC) were used to simulate dose delivery for (a) unmitigated motion, (b) ideal 2D and 3D tracking (both beam adaption and 4DDC based on ground truth motion), and (c) realistic 2D and 3D tracking (beam adaption based on motion predictions, 4DDC on ground truth motion). Model-guided tracking retrieved clinically acceptable target dose homogeneity, as seen in a substantial reduction of the D5-D95 % compared to the non-mitigated simulation. Tracking in 2D and 3D resulted in a similar improvement of the dose homogeneity, as did ideal and realistic tracking simulations. In some

cases, however, the tracked deliveries resulted in a shift towards higher or lower dose levels, leading to unacceptable target over- or under-coverage. The presented motion modelling framework was shown to be an accurate motion prediction tool for the use in proton beam tracking. Tracking alone, however, may not always effectively mitigate motion effects, making it necessary to combine it with other techniques such as rescanning.

Keywords: 4DMRI, liver ultrasound, motion modelling, Gaussian process regression, proton therapy, proton beam tracking, pencil beam scanning, lung tumours

Submitted to: *Phys. Med. Biol.*

1. Introduction

In the treatment of thoracic or abdominal tumours, the advantages of pencil beam scanned (PBS) proton therapy are challenged by respiratory motion. Not only lateral target miss but also interplay between the delivery dynamics and the moving tumour can strongly deteriorate the quality of the initially optimised 3D treatment plan (Phillips et al. 1992, Bert & Durante 2011). In order to ensure a safe and effective treatment for tumours affected by respiratory motion employing appropriate motion mitigation strategies is compulsory (Zhang et al. 2018). Indeed, scanned proton deliveries lend themselves to tumour tracking by nature, because each beam position could be adapted in real-time to follow the tumour motion. This probably being the most elegant motion mitigation concept, it is also the most challenging technique to be implemented clinically (Rietzel & Bert 2010). From a motion modelling point of view, the full 3D deformation of the patient's anatomy needs to be known in real-time; motion trajectories of the tumour's centre of mass are not sufficient due to the sensitivity of the proton beam with respect to any changes in tissue density (Bertholet et al. 2019). From a technical point of view, the delivery system needs to support fast changes in the spot position and the proton energy (Grözinger et al. 2008).

A technical implementation of beam tracking in a particle scanning system was presented and validated by Bert et al. (2010). The authors showed that their system is capable of adapting the carbon ion beam in real-time both laterally and in energy and with high accuracy. This was achieved by using the scanning magnets and including a downstream wedge degrader. In order to extract the target motion during treatment, Prall et al. (2014) and Schwaab et al. (2014) indicated the potential of ultrasound (US) guidance for such a tracking system. They performed tracking deliveries for scanned ion beams and found a substantial improvement of target coverage. All of the above studies, however, only considered rigidly moving geometries in a water phantom. Deformable respiratory motion of a real patient geometry has been addressed by Zhang et al. (2013) and Zhang et al. (2014), where online fluoroscopy in beam's-eye-view in combination with a principal component analysis (PCA) motion model were used to estimate liver deformations. Motion of either implanted markers or the diaphragm were extracted to infer dense deformation vector fields (DVFs). The first study showed that both the implanted markers and the diaphragm are appropriate surrogates for estimating the applied 4D dose distribution with high dosimetric accuracy (Zhang et al. 2013). In a further study, the same setup was used to simulate tumour tracking of the liver for proton PBS (Zhang et al. 2014). It was found that indeed, full DVFs are necessary to safely apply proton beam tracking to liver tumours. Moreover, abdominal US imaging was proposed as surrogate signal before both for respiratory motion modelling of the liver (Preiswerk et al. 2014) and for lung tumour tracking (Mostafaei et al. 2018). While the former infers dense DVFs of the liver from a population-based model, the latter predicts the tumour trajectory in superior-inferior direction on a patient-specific basis. However, both studies do not investigate the dosimetric impact of the motion

predictions.

Recently, we have introduced a respiratory motion model that uses Gaussian process regression (GPR, Williams & Rasmussen (2006)) to estimate dense DVFs of the lung using abdominal US images as input (Giger et al. 2020). This framework was used to retrospectively reconstruct the delivered 4D dose distributions by taking into account variable motion patterns. In order to bring tracking treatments closer to clinical implementation, a temporal prediction of the patient motion is imperative. It is important to consider the system latency induced by the time required for US image processing, motion inference, and proton beam adaption. In conventional radiotherpay, the system latency ranges from 50 ms and 115 ms for the VERO system (Depuydt et al. 2011) and the Cyberknife (Hoogeman et al. 2009), respectively, up to several hundreds of milliseconds for multileaf collimator tracking systems (Krauss, Nill, Tacke & Oelfke 2011, Poulsen et al. 2010). Similarly for proton beam therapy, fast energy changes in range of 80 ms for typical range steps of 5 mm were reported (Pedroni et al. 2011, Safai et al. 2012). For the US-based tracking system mentioned above, a latency of 200 ms was reported. However, the major portion of the latency was introduced by non-optimised image processing steps (Prall et al. 2014). To compensate system latencies, various motion prediction models were proposed and compared, among which are linear predictors, support vector regression, atlas-based approaches, Kalman filters, and neural networks (Arnold et al. 2011, Krauss, Nill & Oelfke 2011, Ernst et al. 2013, Preiswerk et al. 2014). While one comparison study reported relatively small differences in prediction accuracy for the different approaches (Krauss, Nill & Oelfke 2011), another study suggests that machine learning methods tend to outperform linear models for increased prediction horizons (Ernst et al. 2013). Yet, the difference between the different prediction models have primarily been discussed from mathematical point of view. The benefits of more advanced motion predictors on the resulting dose distribution is not clear (Knopf et al. 2016).

In this study, we extend our previously presented motion model (Giger et al. 2020) with a linear autoregressive (AR) model (Giger et al. 2019) which allows to forecast the motion information to account for this latency. We investigate the performance of the spatio-temporal motion prediction model in terms of dose restoration for proton beam tracking. We compare these results to ideal tracking where perfect knowledge of the respiratory motion is assumed. As such, this is the first study which quantifies the feasibility of the proposed US-guided respiratory motion model when applied to PBS proton tracking of lung tumours in terms of 4D dose distributions. The presented simulation study is based on comprehensive and realistic motion patterns and, thus, takes into account dense anatomical deformations.

2. Methods

2.1. Image data sets

The same image data sets as in our previous study were used. They are briefly described here, and the interested reader is referred to Giger et al. (2020) for more details.
Simultaneous abdominal US and time-resolved volumetric MRI (4DMRI) of the lungs were acquired of five healthy volunteers under free respiration for 10 min each using two different 4DMRI sequences (Celicanin et al. 2017, Jud et al. 2018). Dense DVFs were extracted from the 4DMRI data sets using deformable image registration of all motion frames with respect to a reference full-exhale frame (`www.plastimatch.org` and Sandkühler et al. (2018)).
Synthetic 4DCT(MRI) data sets (Krieger et al. 2020, Boye, Samei, Schmidt, Székely & Tanner 2013) were generated by warping two lung cancer patient CTs with the DVFs of the volunteers, resulting in 10 combinations of CT geometry and 4DMRI motion patterns, hereinafter referred to as geometry / motion cases. The patient CTs were chosen to differ considerably in terms of position and size as shown in figure 3. Figure 1 shows the motion patterns of the clinical target volume (CTV) in superior-inferior (SI) direction for all data sets. The differences in signal properties, such as duration, missing US frames, or number of states needed for treatment delivery, are induced by the different 4DMRI sequences and synchronisation setups for motions 1 and 2 on the one hand (Celicanin et al. 2017), and motions 3 to 5 on the other hand (Jud et al. 2018).

2.2. Motion modelling

It is imperative to predict the motion vectors into the future since any tracking system inevitably experiences latency, e.g. due to signal processing and transport or time needed to change the spot position and energy. For this reason, the motion model employed in this study is split into two parts: first, the US-based surrogate signal is forecast to some time points ahead using an AR model (Giger et al. 2019); second, a dense DVF of the lungs is predicted using the forecast surrogate signal and a correspondence model based on GPR (Giger et al. 2020). Principal component analysis (PCA) of both the US images and the DVFs was performed in order to reduce the dimensionality of the motion model. By retaining a reduced number of principal components only, the model is less prone to over-fitting and is rendered computationally more efficient, which is important for the online application of such a model. A schematic of the complete motion modelling framework is shown in figure 2.
The data sets were split into three parts as shown in figure 1. The first 300–750 US frames were used to train and validate the AR model, while the last 33–270 US/MR image pairs represented the test set and, thus, were excluded from any model training. The size of the test set was governed by the number of states needed to deliver the respective treatment plan. The remaining data was used for GPR modelling and, for this purpose, split into a training set and a fixed-sized validation set consisting of the

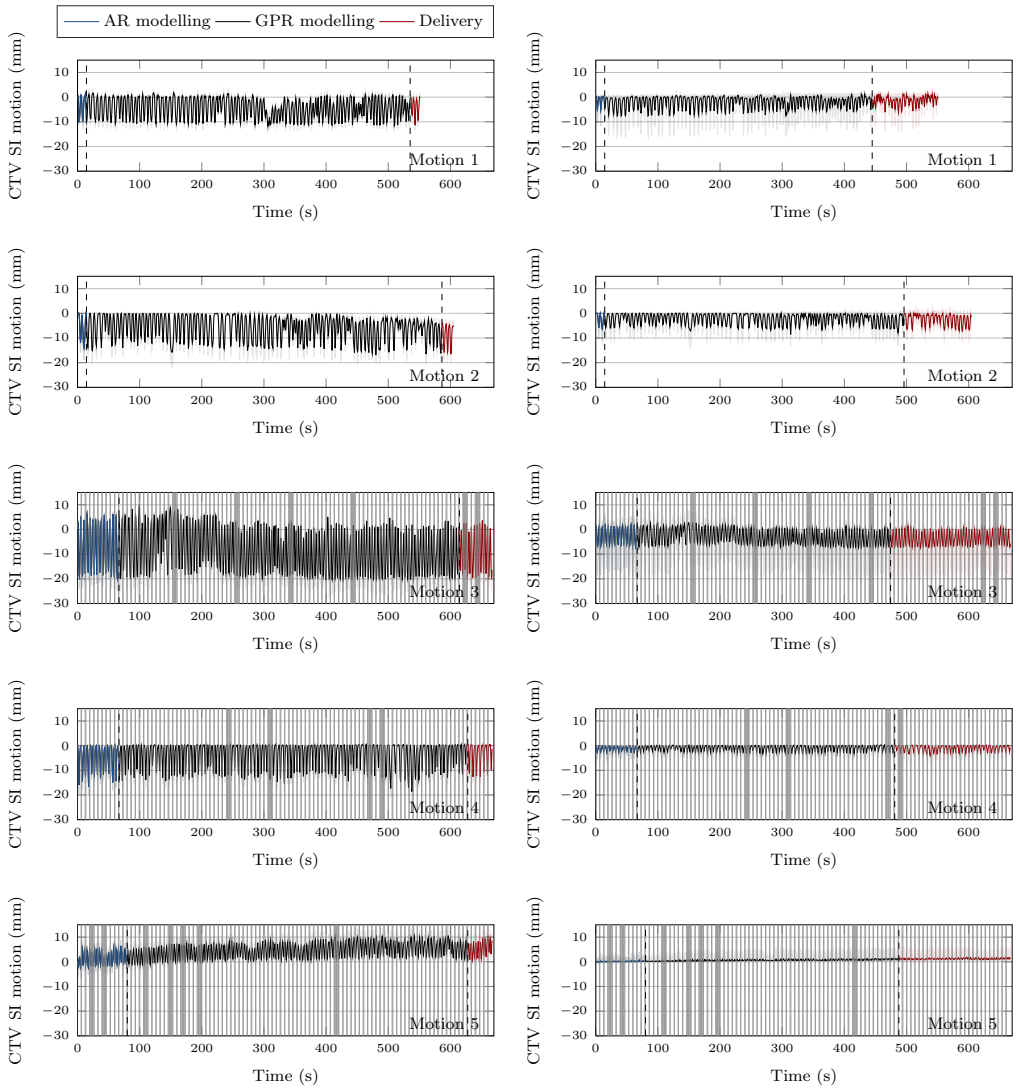

(a) CT geometry 1 (b) CT geometry 2

Figure 1: SI motion of the CTV for all geometry / motion cases. The data sets are split into three parts as highlighted by the vertical dashed lines: AR training and validation sets (blue), GPR training and validation sets (black), and treatment delivery (red). The evaluation of the motion model and tracking algorithms was performed for the last part only (red). Solid line: median, shades: 10th to 90th percentile of all CTV voxels. For motions 3 to 5 some US images were lost due to the synchronisation setup as indicated by the gray areas.

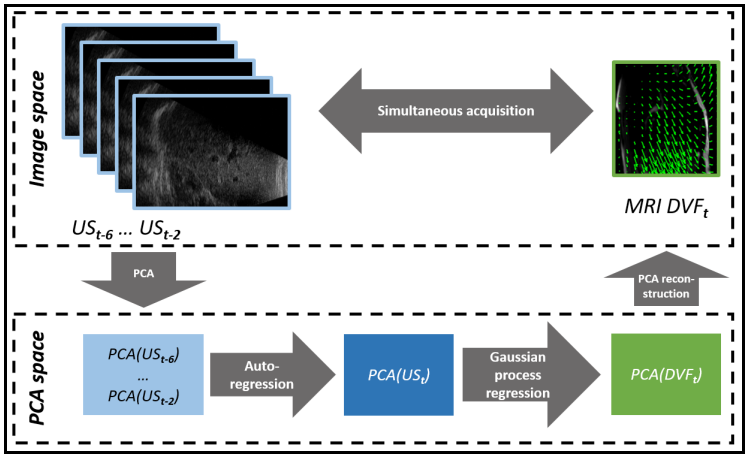

Figure 2: Illustration of the respiratory motion model.

last 50 US/MR image pairs. A detailed overview of all data sets is given in table 1. The DVFs predicted by this model framework are referred to as *predicted motion*, while the DVFs as extracted from the 4DMRI are referred to as the *ground truth motion*. It is important to note that our ground truth DVFs do not necessarily represent the real patient motion patterns. Due to uncertainties in image acquisitions as well as deformable image registrations, the actual patient motion is not known exactly. However, the DVFs extracted from the 4DMRI which were used for both model training and the 4D dose calculations represent a valid ground truth to evaluate the model performance and the resulting dose distributions.

The frame rate of the US acquisition was an order of magnitude higher when compared to the frame rate of the 4DMRI (15 Hz vs. 1.25 to 2.25 Hz). Since the AR model used for the temporal prediction only depends on US images, substantially more training data was available. The GPR model for the spatial prediction relies on US/MR image pairs and, therefore, the data available for training is limited by the frame rate of the 4DMRI. However, for the online application of the correspondence model, the frame rate of the surrogate signal is relevant.

Autoregressive model The autoregressive model used in this study has been described previously (Giger et al. 2019) and, therefore, is only briefly summarised here.
Let $\boldsymbol{\alpha}_t \in \mathbb{R}^u$ describe the vector of the u most dominant principal components of the US image acquired at time t. Furthermore, let α_t^j denote the jth element of the vector $\boldsymbol{\alpha}_t$. The AR model of order p is applied element-wise and its parameters are estimated using ordinary least squares:

$$\alpha_t^j = \vartheta_0^j + \sum_{i=1}^{p} \vartheta_i^j \alpha_{t-i}^j + \epsilon_t \quad \forall j \in \{1, ..., u\},$$

Table 1: Overview over the different data sets used for motion modelling. For AR, all US frames are considered, whereas for GPR, only US/MR image pairs are used.

		AR		GPR		
		Training	Validation	Training	Validation	Test
Geometry 1	Motion 1	280	20	595	50	33
	Motion 2	280	20	659	50	33
	Motion 3	600	150	730	50	60
	Motion 4	600	150	750	50	60
	Motion 5	600	150	720	50	60
Geometry 2	Motion 1	280	20	482	50	146
	Motion 2	280	20	546	50	146
	Motion 3	600	150	520	50	270
	Motion 4	600	150	540	50	270
	Motion 5	600	150	710	50	270

with model parameters $\boldsymbol{\vartheta}^j = \begin{bmatrix}\vartheta_0^j & \dots & \vartheta_p^j\end{bmatrix}^T$ and noise ϵ_t. In order to perform a n-step-ahead forecasting, the model is repeatedly applied.
In this study, the US images were reduced to u principal components such that the explained variance ratio was 10 %. The autoregressive model was of order $p = 5$ and the principal components $\tilde{\boldsymbol{\alpha}}_{\boldsymbol{t}}$ were predicted $n = 2$ steps ahead, resulting in a prediction horizon of 133 ms for the given acquisition parameters.

Gaussian process regression The correspondence model based on GPR has been described in detail in (Giger et al. 2020). Analogously, let $\boldsymbol{\beta}_t \in \mathbb{R}^v$ denote the vector of the v most dominant principal components of the DVF at time t. However, in contrast to the previous work, here the input to the correspondence model is the forecast surrogate signal, $\tilde{\boldsymbol{\alpha}}_{\boldsymbol{t}}$. The number of principal components v was chosen such that 75 % of the explained variance was retained. The parameters of the applied Gaussian covariance function were empirically chosen to be $\theta_0 = 30$, $\theta_1 = 35$, and $\sigma_n^2 = 1$ for all data sets as introduced in Giger et al. (2020).

2.3. Treatment planning and 4D dose calculations

For each CT geometry, a 2-field SFUD (single field, uniform dose) plan was optimised on the reference full-exhale CT scan. As optimisation target, the respective CTV plus a 2 mm margin was used. Since the motion and density variations are taken care of by the tracking simulation, they were not included in the plan optimisation. The field arrangements are illustrated in figure 3.

Several delivery scenarios were simulated, as summarised in table 2. First, the static reference dose distribution was calculated by running a 4D dose calculation (4DDC, see Boye, Lomax & Knopf (2013) and Krieger et al. (2018)) without motion input. Second, the unmitigated 4D dose distributions were calculated as 'worst case reference' by using

(a) CT geometry 1, CTV volume: 18.8 cm^3

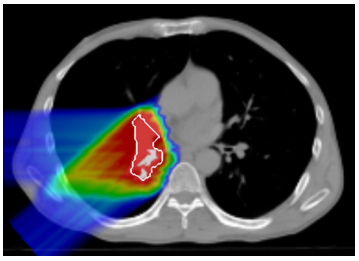

(b) CT geometry 2, CTV volume: 141.9 cm^3

Figure 3: Illustration of the two CT geometries and the corresponding chosen field arrangements.

Table 2: Summary of the simulated dose deliveries. M_{adapt} describes the motion according to which the beam is adapted, M_{calc} describes the motion that is used for the actual dose calculation.

Name	M_{adapt}	M_{calc}	Simulation code
Static	–	–	4D dose calculation
4DDC	–	Ground truth	4D dose calculation
Ideal 2D tracking	Ground truth	Ground truth	2D tracking code
Ideal 3D tracking	Ground truth	Ground truth	3D tracking code
Realistic 2D tracking	Prediction	Ground truth	2D tracking code
Realistic 3D tracking	Prediction	Ground truth	3D tracking code

the ground truth DVFs as respiratory motion. Finally, four different tracking scenarios were simulated by considering different motion compensation approaches. Simulations were performed for both 2D tracking (only adapting the beam laterally) and 3D tracking (adapting the beam laterally and in energy). For both 2D and 3D tracking simulations, *ideal* and *realistic* tracking were distinguished. Ideal tracking assumed perfect motion information for the beam adaptation, meaning that the motion according to which the beam is adapted, M_{adapt}, is equal to the ground truth motion used for the 4DDC, M_{calc}. It thus represents the capability of tracking with perfect knowledge of the deformable motion. Under more realistic conditions, the two motion patterns M_{adapt} and M_{calc} are not equal but rather M_{adapt} is predicted by the model. This scenario is referred to as realistic tracking. All simulations were performed as single deliveries, 9× volumetric rescanning, and 9× volumetric re-tracking (van de Water et al. 2009).
Every dose delivery starts in a certain respiratory state, which is usually not controlled in clinical practice. For this reason, the simulations of each treatment field were started on arbitrary, but different, respiratory states of the first breathing cycle of M_{calc}. The number of respiratory states was in the range of 5–11 for one field, resulting in 25–121

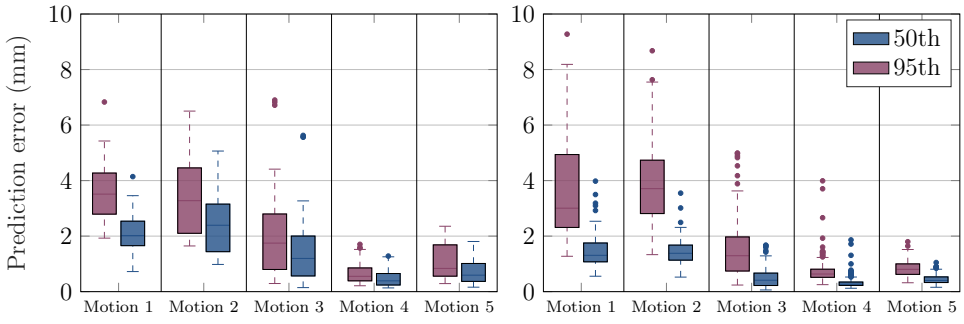

(a) CT geometry 1 (b) CT geometry 2

Figure 4: Spatio-temporal prediction errors for all geometries and motions. The boxplots indicate the error percentiles of all voxels within the CTV and include all predicted motion states. The whiskers expand to the most extreme values within 1.5 times the inter-quartile range.

combinations for a full treatment plan with two fields.

2.4. Analysis

Geometrical error The geometrical prediction error for a motion state t is defined as the Euclidean norm of the voxel-wise vector difference between the ground truth and the predicted DVFs. For a quantitative analysis, the 50th and 95th percentiles of this prediction error within the CTV were calculated for each respiratory state. The results are reported as a distribution of these percentiles over all motion states.

Dosimetric analysis The dosimetric analysis was performed by comparing the dose volume histograms (DVHs) of the different delivery simulations and by evaluating the target dose homogeneity in terms of CTV D5-D95 %.

3. Results

3.1. Geometrical error

Figure 4 summarises the Euclidean geometrical prediction error of the model for all geometry / motion scenarios. The boxes describe the 50th and the 95th percentile of all voxels within the CTV and include all motion states that were predicted by the model and thus used for the dose calculations. It can be observed that, except for a few outlying states, the 50th percentile error is smaller than 4 mm for all geometry / motion scenarios. For motions 3–5, it is even smaller than 2 mm for almost all motion states. A similar pattern is seen for the 95th percentile error: except for a few outliers, all motion

states present an error smaller than 8 mm for all geometry / motion combinations. For motions 3–5, it is smaller than 4 mm for all motion states except some outliers.

3.2. Motion mitigation efficacy of ideal tracking

DVHs for all geometry / motion scenarios for ideal tracking are shown in figure 5, comparing ideal 2D and 3D tracking to either the scenario with no motion mitigation or the static case. Figure 7 additionally compares the CTV dose homogeneity in terms of D5-D95 % for the different tracking scenarios.
It can be seen that for geometry 1, there is a clear under-dosage and severely compromised dose homogeneity for non-mitigated motion cases. Tracking brings the CTV dose homogeneity much closer to the static case for both 2D and 3D tracking, with a slightly better homogeneity for 2D tracking. However, for motions 3 and 4 there is a clear under-dosage of the CTV. In addition, rescanning leads to a smaller dependence of the dose on the starting phase of the simulations, indicated by the more narrow band plots. For motions 1, 2 and 4, re-tracking additionally achieves a result closer to the static case compared to the single-tracking simulations. Motions 3 and 5 do not show an improvement if rescanning is added. For geometry 2, the dose degradation due to missing motion mitigation is much more limited, because the tumour motion amplitudes are much smaller than for geometry 1. For this reason, tracking brings no major improvement compared to non-mitigated simulations. Again, 2D and 3D tracking are very similar, with a slightly improved homogeneity for 2D tracking. Rescanning slightly reduces the dependence on the starting phase.

3.3. Ideal versus realistic tracking

Figure 6 compares the DVHs for ideal and realistic 3D tracking for no rescanning as well as 9× rescanning / re-tracking. It is seen that there are some differences between the two scenarios, originating from the different motion patterns used for beam adaptation. For motion 1, realistic tracking results in lower dose homogeneity due to the larger prediction error already seen in figure 4. This is also confirmed by figure 7. For most of the scenarios however, there are only slight differences in homogeneity between ideal and realistic tracking, meaning that the model provides a suitable motion prediction for tracking, which is also reflected in the geometrical prediction error in figure 4.

4. Discussion

In this study, we presented a framework for proton beam tracking based on abdominal US and a patient-specific respiratory motion model. We made use of simultaneously acquired 4DMRI and 2D US images to train a motion model consisting of two parts: an autoregressive model to forecast the US information ahead in time to cope with system latency, and a Gaussian process regression model to estimate the corresponding dense DVFs inside the lungs. These deformation fields were used to adapt the proton beam

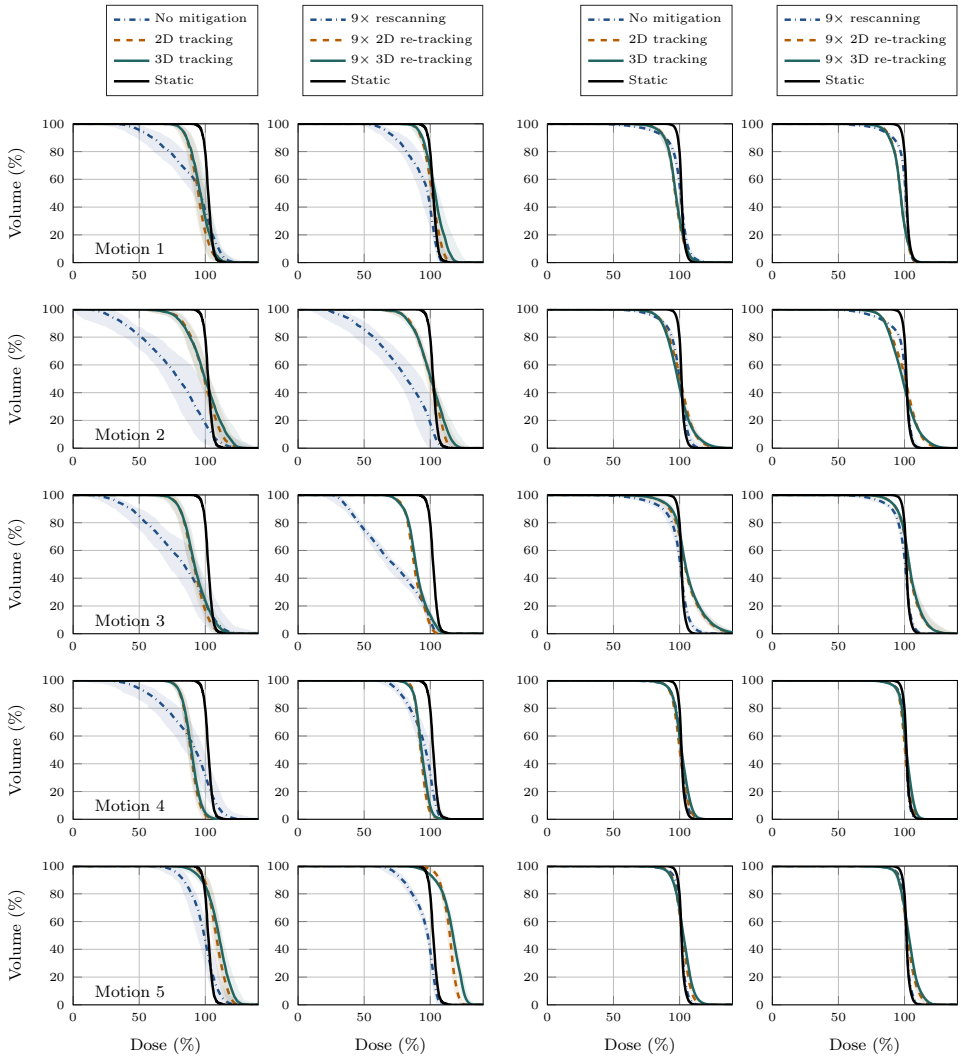

(a) CT geometry 1 (b) CT geometry 2

Figure 5: CTV DVHs for all geometry / motion scenarios for ideal tracking, left: without, right: with 9× rescanning. Purple, solid: no tracking, orange, dashed: ideal 2D tracking, green, solid: ideal 3D tracking, black, solid: static case (no motion included). The shaded bands include all starting phase combinations, whereas the solid lines represent their median.

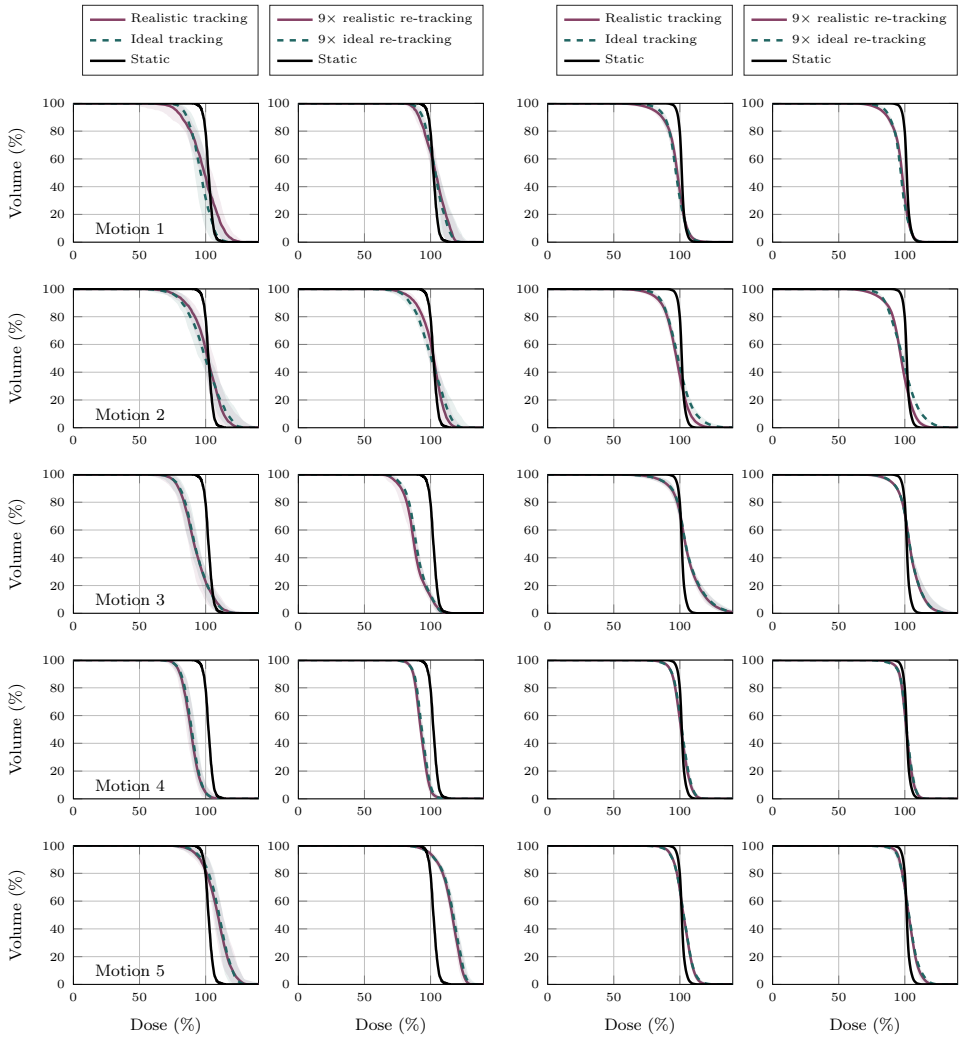

(a) CT geometry 1 (b) CT geometry 2

Figure 6: CTV DVHs for all geometry / motion scenarios for ideal and realistic tracking, left: without, right: with 9× rescanning. Purple, solid: realistic 3D tracking, green, dashed: ideal 3D tracking, black, solid: static case (no motion included). The shaded bands include all starting phase combinations, whereas the solid lines represent their median.

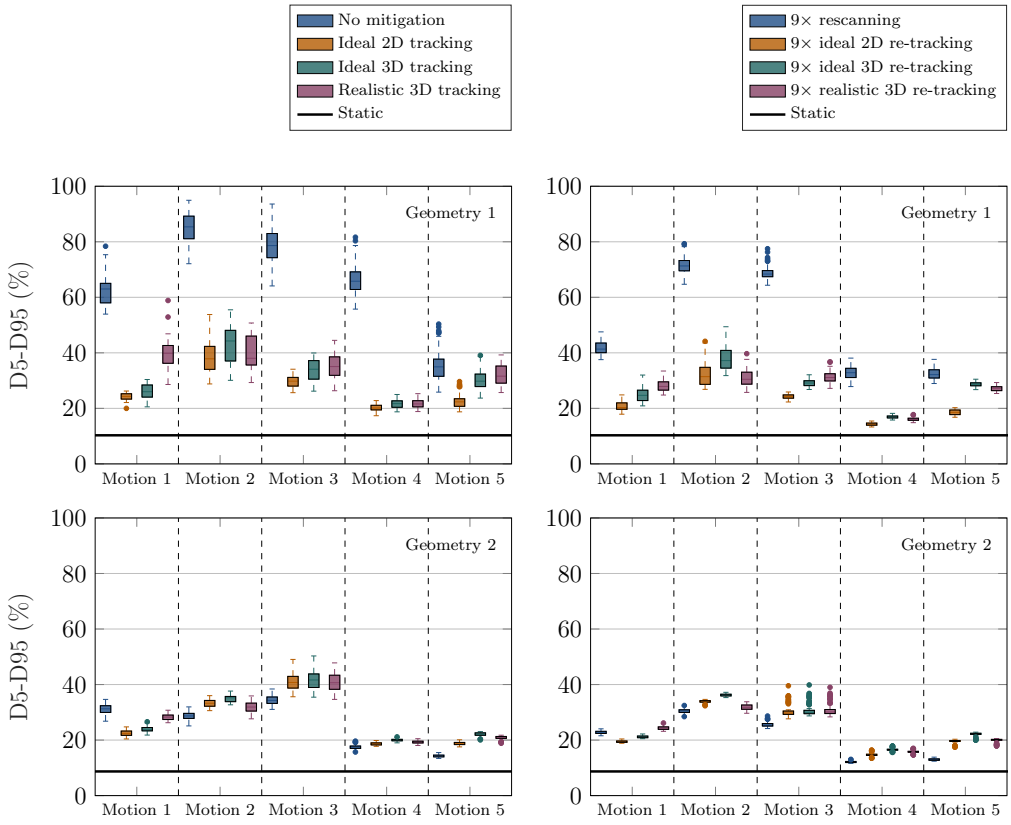

(a) No rescanning (b) 9× rescanning

Figure 7: CTV dose homogeneity in terms of D5-D95 % for all geometry / motion scenarios, (a) without and (b) with rescanning, in comparison to the static case. Top: CT geometry 1, bottom: CT geometry 2. The box plots include simulation results for all starting phases.

laterally and in energy, and thus simulate various tracking scenarios. We have shown that particularly for large tumour motion amplitudes, 2D as well as 3D tracking can substantially improve the target dose homogeneity as compared to a non-mitigated dose delivery. This is true not only for ideal tracking where perfect motion information is assumed, but also for realistic tracking which uses the model's prediction as input for beam position and energy adaptation. Additionally, combining tracking with rescanning (re-tracking) may further improve the target coverage, as seen for cases with motions 1, 2 and 5. Generally, rescanning reduces the dose variations due to different delivery starting phases. For small motion amplitudes, the detrimental effects of the motion were

much smaller, and thus tracking as well as re-tracking brought only minor improvements with respect to the unmitigated delivery.

The prediction horizon of 133 ms is in a reasonable range for tracking systems in radiotherapy. Although no closed loop system latency for proton tracking systems is reported here, we expect the time needed for energy adaption in the range of 80 ms to contribute the major portion of the overall latency for 3D tracking. Thus, we further expect the overall latency to be substantially lower for 2D tracking. Moreover, the linear AR model used here is only one possible prediction approach among many and without doubt the most straightforward one (Krauss, Nill & Oelfke 2011, Ernst et al. 2013). The performance of the motion predictions might in fact be further improved by enhancing the AR model. However, the analysis of the obtained dose distributions suggest that the linear AR model in combination with GPR is sufficient for tumour tracking in PBS proton therapy.

Both parts of the motion model are patient-specific, meaning that they were trained for each geometry / motion pattern separately. This enables the models to estimate patient-specific variability better than a population-based model. However, in order to make such models more suitable for clinical practice, the same parameters were used for all geometry / motion scenarios. Nevertheless, the models were shown to predict the DVFs with reasonable accuracy. This demonstrates the strength of the applied respiratory motion model.

However, one needs to keep in mind that all US and MRI data sets were acquired in one session per volunteer, without any re-positioning of the volunteer or the US probe. In order to apply this tracking framework in clinical practice, the motion models will have to be trained on a pretreatment imaging data set, while the actual treatment, and thus the test set of the model, will happen days or even weeks after the imaging session and will be fractionated over several weeks. It is unclear, therefore, whether and how the motion of a patient will change on an inter-fractional basis, rendering the pretrained motion models less accurate. Additionally, it is impracticable to achieve the same imaging plane of the US probe for every set-up of the patient, posing another challenge to the model. A feasibility study has recently been presented by Giger et al. (2019) to investigate the influence of inter-fractional positioning changes. In this study, the volunteers were asked to stand up between two MRI scans and the US probe was removed. Afterwards, the volunteers and the US probe were repositioned as reproducibly as possible. The motion model trained on the first session resulted in larger prediction errors for the second session, showing the adverse influence of the repositioning. But even in this study, the data sets were not truly inter-fractional since they were acquired within a few minutes after each other. A longitudinal study is therefore planned where the volunteers will be scanned over a time frame of weeks or months. These data sets will lead to more clinically relevant results. Also, for future data acquisition, we will use an improved set-up to synchronise the US and MRI acquisitions, enabling longer imaging sessions without missing US frames.

Since this work is based on the same data as our previous study (Giger et al. 2020),

it inherently has similar limitations. In particular, the analysis was performed on 4DCT(MRI) data sets whose motion is restricted to the lung volume only. Consequently, density heterogeneities proximal to the target, such as ribs, were static in all our calculations. A previous simulation study on simple heterogeneous motion phantoms suggests that tumour tracking in heterogeneous targets may have detrimental effects on the dose distribution (van de Water et al. 2009). In our analysis, such effects were considered by the tracking simulations which altered the spot positions relative to the rib cage. Moreover, the motion extracted from the 4DMRI of healthy volunteers, although realistic, might not perfectly represent the motion characteristics of lung cancer patients. As such, for CT geometry 1 and motions 3 and 4, a clear under-dosage of the CTV was observed. Similarly, for motion 5, an over-dosage was found, even though for all cases tracking improved the dose homogeneity substantially. These changes in the dose level are a result of tumour stretching / compression with respect to the reference state during the delivery. If a tumour is stretched during delivery, the anatomical parts of the tumour move further apart and thus, by applying tracking, the pencil beams will be placed further apart as well. Since the number of protons per spot is unchanged, this will result in a lower proton fluence and thus a lower dose. The analogue explanation holds for tumour compression. It is, however, questionable whether such pronounced stretching or compression of a lung tumour represents reality. In this study, we extracted the motion from healthy volunteers and applied it to a lung cancer case. It is not given that a lung lesion moves in the same way as a healthy lung without any lesion, thus the above described effect may not be an issue for a real lung tumour motion. For this reason, it will be important to extend such a study to real patient data sets, once they will be available.

Due to residual motion effects, tracking alone may not be able to reproduce the dose conformality of the static plan. On the one hand, deformations of the target volume cannot be precluded in real patient data, leading to effects similar to the ones described above. On the other hand, changes of density heterogeneities proximal to the target will distort the shape of the pencil beams, leading to non-nominal dose distributions which in turn can reduce the homogeneity of the total delivered dose. In addition, non-rigid motion of the geometry will lead to inverse interplay effects. In a tracking framework, the beam position is typically adjusted according to the target displacement at Bragg peak depth. However, the anatomy proximal to the Bragg peak does not necessarily move in the same way, particularly in a lung treatment where the rib cage typically exhibits a much smaller motion than a lung tumour. This effect leads to additional deformations of the dose distribution with respect to the patient geometry. The above described residual motion effects could be greatly reduced by combining beam tracking with 4D optimisation methods, as presented for example by Eley et al. (2014). There, the authors include a patient 4DCT in the plan optimisation procedure and optimise the pencil beam weights by assigning each to a certain motion phase of the 4DCT. This method leads to an additional degree of freedom for the optimisation, potentially allowing for better target coverage and healthy tissue sparing. Their approach however

relies on a periodic respiration, which is not realistic, as we have found in this study. Alternatively, the weight of each pencil beam could be re-optimised in an online fashion to correct for motion effects of the previously delivered pencil beams (Lüchtenborg et al. 2011).
The results found in this study suggest that 2D tracking can mitigate the motion effects similarly well as full 3D tracking, even though it does not correct for changes in water-equivalent path length. This is of interest for the clinical implementation of tracking, since one of the major challenges is the fast energy change needed for full 3D tracking. If further studies confirm that 2D tracking is similarly effective as 3D tracking, this would simplify the technical implementation of the tracking framework.

5. Conclusion

In this paper, we demonstrated that the accuracy of the US-guided spatio-temporal motion model was sufficient for PBS proton beam tracking, with comparable plan quality achieved for realistic and ideal tracking. However, the dosimetric advantage of 3D tracking in comparison to rescanning is limited, indicating the necessity of applying online plan optimisation and/or the combination with other motion mitigation strategies.

Acknowledgments

The authors thank Pauline Guillemin from the University of Geneva, Switzerland, for her support during the data acquisitions. This work was supported by the Swiss National Science Foundation, SNSF (project number 320030_163330/1).

References

Arnold P, Preiswerk F, Fasel B, Salomir R, Scheffler K & Cattin P C 2011 *in* 'International Conference on Medical Image Computing and Computer-Assisted Intervention' Springer pp. 623–630.

Bert C & Durante M 2011 *Physics in Medicine & Biology* **56**(16), R113.

Bert C, Gemmel A, Saito N, Chaudhri N, Schardt D, Durante M, Kraft G & Rietzel E 2010 *Radiation Oncology* **5**(61).

Bertholet J, Knopf A, Eiben B, McClelland J, Grimwood A, Harris E, Menten M, Poulsen P, Nguyen D T, Keall P et al. 2019 *Physics in Medicine & Biology* **64**(15), 15TR01.

Boye D, Lomax A J & Knopf A C 2013 *Med. Phys.* **40(6)**, 061702–1 – 061702–11.

Boye D, Samei G, Schmidt J, Székely G & Tanner C 2013 *in* 'Medical Imaging 2013: Image Processing' SPIE. doi: 10.1117/12.2007076.

Celicanin Z, Giger A, Bauman G, Cattin P & Bieri O 2017 *in* 'Proceedings of the ISMRM 25th Annual Meeting and Exhibition' Honolulu, Hawaii, USA.

Depuydt T, Verellen D, Haas O, Gevaert T, Linthout N, Duchateau M, Tournel K, Reynders T, Leysen K, Hoogeman M et al. 2011 *Radiotherapy and Oncology* **98**(3), 365–372.

Eley J G, Newhauser W D, Lüchtenborg R, Graeff C & Bert C 2014 *Physics in Medicine and Biology* **59**(13), 3431–3452.

Ernst F, Dürichen R, Schlaefer A & Schweikard A 2013 *Physics in Medicine & Biology* **58**(11), 3911.

Giger A, Jud C, Nguyen D, Krieger M, Zhang Y, Lomax A J, Bieri O, Salomir R & Cattin P C 2019 *in* 'International Workshop on PRedictive Intelligence In MEdicine' Springer pp. 11–22.

Giger A, Krieger M, Jud C, Duetschler A, Salomir R, Bieri O, Bauman G, Nguyen D, Weber D C, Lomax A, Zhang Y & Cattin P C 2020 *Phys. Med. Biol.* p. Under review.

Grözinger S O, Bert C, Haberer T, Kraft G & Rietzel E 2008 *Radiation Oncology* **3**(1), 34.

Hoogeman M, Prévost J B, Nuyttens J, Pöll J, Levendag P & Heijmen B 2009 *International Journal of Radiation Oncology* Biology* Physics* **74**(1), 297–303.

Jud C, Nguyen D, Sandkühler R, Giger A, Bieri O & Cattin P C 2018 *in* 'International Conference on Medical Image Computing and Computer-Assisted Intervention' Springer pp. 198–205.

Knopf A C, Stützer K, Richter C, Rucinski A, da Silva J, Phillips J, Engelsman M, Shimizu S, Werner R, Jakobi A et al. 2016 *Physica Medica* **32**(7), 874–882.

Krauss A, Nill S & Oelfke U 2011 *Physics in Medicine & Biology* **56**(16), 5303.

Krauss A, Nill S, Tacke M & Oelfke U 2011 *International Journal of Radiation Oncology* Biology* Physics* **79**(2), 579–587.

Krieger M, Giger A, Weber D C, Lomax A J & Zhang Y 2020 *Radiotherapy and Oncology* **145**, 154–161.

Krieger M, Klimpki G, Fattori G, Hrbacek J, Oxley D, Safai S, Weber D C, Lomax A J & Zhang Y 2018 *Physics in Medicine & Biology* **63**(5), 055005.

Lüchtenborg R, Saito N, Durante M & Bert C 2011 *Medical Physics* **38**(10), 5448–5458.

Mostafaei F, Tai A, Gore E, Johnstone C, Haase W, Ehlers C, Cooper D T, Lachaine M & Li X A 2018 *Medical physics* **45**(10), 4619–4626.

Pedroni E, Meer D, Bula C, Safai S & Zenklusen S 2011 *The European Physical Journal Plus* **126**(7), 66.

Phillips M H, Pedroni E, Blattmann H, Boehringer T, Coray A & Scheib S 1992 *Physics in Medicine & Biology* **37**(1), 223.

Poulsen P R, Cho B, Ruan D, Sawant A & Keall P J 2010 *International Journal of Radiation Oncology* Biology* Physics* **77**(2), 600–607.

Prall M, Kaderka R, Saito N, Graeff C, Bert C, Durante M, Parodi K, Schwaab J, Sarti C & Jenne J 2014 *Medical Physics* **41**(4), 041708.

Preiswerk F, De Luca V, Arnold P, Celicanin Z, Petrusca L, Tanner C, Bieri O, Salomir R & Cattin P C 2014 *Medical image analysis* **18**(5), 740–751.

Rietzel E & Bert C 2010 *Medical physics* **37**(2), 449–460.

Safai S, Bula C, Meer D & Pedroni E 2012 *Transl Cancer Res* **1**(3).

Sandkühler R, Jud C, Andermatt S & Cattin P C 2018 *arXiv preprint arXiv:1806.09907* .

Schwaab J, Prall M, Sarti C, Kaderka R, Bert C, Kurz C, Parodi K, Günther M & Jenne J 2014 *Physica Medica* **30**(5), 578 – 582.

van de Water S, Kreuger R, Zenklusen S, Hug E & Lomax A 2009 *Phys. Med. Biol.* **54**, 6549–6563.

Williams C K & Rasmussen C E 2006 *Gaussian processes for machine learning* Vol. 2 MIT press Cambridge, MA.

Zhang Y, Huth I, Weber D C & Lomax A J 2018 *Radiotherapy and Oncology* **128**(1), 182–188.

Zhang Y, Knopf A, Tanner C, Boye D & Lomax A J 2013 *Physics in Medicine & Biology* **58**(24), 8621.

Zhang Y, Knopf A, Tanner C & Lomax A 2014 *Physics in Medicine & Biology* **59**(24), 7793.

Chapter 10

Discussion and Conclusion

The goal of the overall project was to investigate the feasibility and effectiveness of abdominal US imaging as motion surrogate for beam tracking in PBS proton therapy of lung tumours. PBS proton therapy lends itself towards tumour tracking due to the relative ease with which the beam can be adapted to follow the tumour motion. In this context, US imaging is an interesting motion surrogate. Although it is not possible to image lung tumours directly, it provides internal motion information and therefore may allow to monitor organ motion which is uncorrelated to the respiratory motion, in particular organ drift [268, 285, 286]. The work presented here focused on the development of software tools for respiratory motion imaging and prediction based on abdominal US imaging as surrogate.

In a first paper presented in Chapter 5, we propose a US-based 4D MRI method. This approach follows naturally from the treatment setup considered here where simultaneous US/MRI acquisitions are a prerequisite for respiratory motion modelling. The image quality of the presented approach is comparable to the state-of-the-art navigator-based approach [285]. It has, however, the additional benefit of reduced acquisition times and increased temporal resolution. Building upon various 4D MRI approaches, three different motion models were proposed in the following. These included parametric and non-parametric models alike and were based on neural networks in Chapter 6, polynomial regression in Chapter 7, and GPR in Chapter 8. In addition, the effects of US probe repositioning on the prediction accuracy was investigated in Chapter 7, while the subsequent studies in Chapter 8 and Chapter 9 further analysed the impact of the motion predictions on the resulting dose distributions. All of these studies were based on simultaneously acquired US and 4D MRI data sets for surrogate data and motion extraction of two to eight healthy volunteers. For the dosimetric analysis, the motion information of five volunteers was fused with the CT geometries of two lung cancer patients. With mean or median prediction errors generally below $3\,\mathrm{mm}$, all of the presented motion models achieved comparable accuracies with respect to previous studies for intra-fractional motion modelling [219, 303]. Broadly speaking, predictions tend to be more accurate for models trained on motion estimates extracted from the novel 4D MRI based on patch registration [129] when compared to the more widely used navigator-based stacking approach [285]. This observation might be explained by the typically smoother DVF and, in our case, a higher number of training samples for the data sets based on the former 4D MRI approach.

The choice of the respiratory motion model is inherently governed by prior assumptions on the correlation between the surrogate signal and motion estimate as outlined in Chapter 4. Naturally, the different models investigated here differ not only in terms of the underlying assumptions but also regarding their properties and characteristics. Starting with the most straightforward approach, the linear regression model presented in Chapter 7 relies on a linear relationship between the surrogate and the motion estimates. The complexity of the model was manually enhanced by projecting the surrogate vector into a non-linear feature space. Conversely, the neural network presented in Chapter 6 builds on a broad class of nonlinear functions whose parameters are iteratively learned from the training data. The neural network is described by a much larger set of parameters and, therefore, exhibits a substantially increased model complexity when compared to the polynomial regression. Moreover, the encoder-decoder shaped generator network transforms the 2D US image into a low-dimensional coding which in turn is used to reconstruct the DVF of the navigator image. As such, we assume that the model's input and output data share a common feature space. Finally, the GPR proposed in Chapter 8 and Chapter 9 is a non-parametric model where the underlying assumptions are formulated in terms of a kernel function. In particular, the Gaussian kernel used here is based on the assumption that the feature space is smooth [290].

With all models performing comparably well in terms of accuracy, the choice for the model best suited for the application at hand must be based on other criteria. At the risk of oversimplifying, we can state that increased model complexity typically comes with reduced robustness. Indeed, we found that the neural network presented in Chapter 6 is sensitive to small changes in the US images. Although not shown in detail here, we do not expect this approach to perform well in case of substantial organ drift or US probe repositioning. While preliminary results suggest that the linear model in Chapter 7 is able to cope with different US imaging planes introduced by probe repositioning, further studies are required for the GPR model in Chapter 8 and Chapter 9.

A similar analysis holds true for the choice of the temporal prediction model used to cope with system latencies. We opted for a linear AR model as described in Chapter 8 and Chapter 9, although more complex models may further improve the prediction accuracy [65, 150]. It was not the primary goal of this work to develop or compare different temporal prediction models. As such, the AR model used here should only be exemplary and may be replaced with another model in future studies. It is worth noting, however, that the mathematical improvements may not directly translate into clinical benefits. It was suggested that the development of more advanced prediction models may have reached the point of diminishing returns [145].

Following the same reasoning, different types of image processing algorithms to extract both the motion estimates from the 4D MRI and the surrogate signal from the US images could be investigated. Needless to say, the respective problem formulations both encompass entire research fields as outlined in Chapter 4. Since the objective of this project was to investigate the use of respiratory motion models for lung tumour treatment, an indirect motion modelling approach was formulated where the dominant motion information from abdominal US imaging was considered as surrogate signal. Therefore, explicit tracking of liver structures was not a primary necessity. In our first analysis presented in Chapter 5, we compared a learning-based liver vessel tracking approach [54] and a similarity measure based on the image intensities for 4D MRI re-

construction. We found that both approaches performed comparably well. In succeeding studies presented in Chapters 7 to 9, we employed PCA for dimensionality reduction and for respiratory feature extraction. Analogous to above PCA may be replaced by specific tracking algorithms or neural networks, such as autoencoders. Indeed, it would be particularly interesting to investigate the performance of different tracking algorithms when subject to US probe repositioning. The study in Chapter 7 tackles the issue of different imaging planes by normalising the principal components. It is thus based on the assumption that end-exhalation and end-inhalation are similar for the two imaging sessions. Another approach might be to estimate the angle between the US imaging plane and the SI direction and to scale the diaphragm displacement accordingly.

A common challenge in respiratory motion modelling is the lack of ground-truth data and the studies presented here are no exception to this. Different sources of uncertainties arise from data acquisition, in particular 4D imaging, data processing, including motion estimation based on DIR methods or feature extraction algorithms for the surrogate signal, and errors introduced by the motion model [181]. To overcome the issue of missing ground-truth information, respiratory motion models could be validated using motion phantoms. Despite phantoms being a valuable tool, they often only represent a simplified motion pattern giving rise to the question of how realistic they are [276]. Having said this, we believe that the analyses presented in this work provide a good estimate of what accuracy can be achieved with the proposed models. Although most of them were not trained and validated on *real* 4D images and motion estimates, the dense DVF used as basis represent *realistic* and *plausible* motion estimates including motion variabilities and organ drift.

In this context, it is further interesting to highlight one finding from the concluding study in Chapter 9 where we used motion estimates from healthy volunteers to simulate the respiratory motion of lung cancer patients. We observed that for some data sets the tumour tissue was either stretched or compressed resulting in under-dosage or over-dosage. Owing to the design of the study, we may conclude that these effects were introduced by applying the motion characteristics of healthy lung tissue to tumour tissue. This observation in combination with the fact that motion patterns in general and tumour trajectories in particular vary substantially from patient to patient render the use of population-based motion models questionable [138].

However, all of the studies presented here were performed on limited data only – both in terms of the number of data sets and the duration of image acquisition. Therefore, the presented findings should be understood as preliminary results. Extended and systematic analyses, preferably on patient data, are required for motion models to become more clinical adopted. In fact, respiratory motion models, although popular in research, are not widely used in clinical practice [276]. To the best of our knowledge, the only exceptions are the Cyberknife (Accuray Inc. Sunnyvale, CA, USA), and the Vero system (Mitsubishi Heavy Industries, Ltd., Tokyo, Japan and Brainlab AG, Feldkirchen, Germany). These systems, however, predict the tumours' trajectories only which is considered insufficient for proton therapy [19]. Moreover, long-term changes such as tumour shrinkage over the course of treatment may imply the need for model adaptation. Given the lack of patient data, this aspect was beyond the scope of the current work.

Overall, we conclude that abdominal US imaging is an interesting and promising surrogate signal for respiratory motion modelling. Although we did not prove that the US-based motion models are capable of accounting for organ drift, the analysis in Chapter 8 suggests that the

motion information extracted from the US images might still be used to monitor organ drift. Further studies comparing US-based surrogate signals with external markers should be performed to confirm these findings.

Future work

Given the limited amount of data in general and for inter-fractional motion modelling in particular, we see great potential for advancing the presented analyses by extending the current database. Preliminary work for a comprehensive longitudinal study has been developed within the scope of this work. A novel hardware setup for prolonged data acquisition is under development and close to final implementation for an experimental study. It is based on a clinical US imaging system (former Fukuda Denshi, Basel, Switzerland) which was amended for directly transferring the imaging data to standard computers. An MR-compatible US probe for this system was developed at the Fraunhofer IBMT in Sulzbach, Germany, and tested for electromagnetic safety in collaboration with the group for Computer-assisted Applications in Medicine (CAiM) at ETH Zurich, Switzerland. Ethical clearance for 20 subjects, including volunteers and patients, was obtained and first acquisitions should start soon.

Should this longitudinal study proof successful, a rich and comprehensive database will be available for further development and validation of the presented US-based motion modelling approach. Moreover, the improvements in the hardware setup may eventually allow for online application of respiratory motion modelling during treatment delivery.

Conclusion

In this project, we presented different approaches to US-based respiratory motion modelling for lung tumour tracking. A comparison between the obtained results suggests that there is not one optimal motion model per se but different correspondence models perform comparably well. In fact, the uncertainties introduced by the 4D imaging method and motion extraction algorithm further influence the overall performance. Although the results presented here clearly indicate the potential benefit of internal motion surrogates, more studies are needed to directly compare US-based surrogates with external markers. From a dosimetric point of view, the proposed motion model based on GPR was found to result in clinically acceptable dose distributions. This result suggests that the proposed motion modelling framework based on US surrogates is suitable for motion management in PBS proton therapy. However, we further conclude that tumour tracking alone may not always be sufficient to mitigate respiratory motion. Tumour tracking should be applied in combination with other motion mitigation techniques, such as rescanning.

Bibliography

[1] F. Albertini, S. Gaignat, M. Bosshardt, and A. J. Lomax. Planning and optimizing treatment plans for actively scanned proton therapy. *Biomedical Mathematics: Promising Directions in Imaging, Therapy Planning, and Inverse Problems (ed 1). Madison: Medical Physics Pub Corp*, pages 1–18, 2009.

[2] C. Allemani, H. K. Weir, H. Carreira, R. Harewood, D. Spika, X.-S. Wang, F. Bannon, J. V. Ahn, C. J. Johnson, A. Bonaventure, et al. Global surveillance of cancer survival 1995–2009: analysis of individual data for 25 676 887 patients from 279 population-based registries in 67 countries (CONCORD-2). *The Lancet*, 385(9972):977–1010, 2015.

[3] P. Arnold. *Respiratory-induced organ motion compensation for MRgHIFU*. PhD thesis, University of Basel, 2012.

[4] P. Arnold, F. Preiswerk, B. Fasel, R. Salomir, K. Scheffler, and P. C. Cattin. 3D organ motion prediction for MR-guided high intensity focused ultrasound. In *International Conference on Medical Image Computing and Computer-Assisted Intervention*, pages 623–630. Springer, 2011.

[5] J. W. Asaph, J. R. Handy Jr, G. L. Grunkemeier, E. C. Douville, A. C. Tsen, R. C. Rogers, and J. F. Keppel. Median sternotomy versus thoracotomy to resect primary lung cancer: analysis of 815 cases. *The Annals of thoracic surgery*, 70(2):373–379, 2000.

[6] V. Auboiroux, L. Petrusca, M. Viallon, T. Goget, C. D. Becker, and R. Salomir. Ultrasonography-based 2D motion-compensated HIFU sonication integrated with reference-free MR temperature monitoring: a feasibility study ex vivo. *Physics in Medicine & Biology*, 57(10):N159, 2012.

[7] P. Bagan, P. Berna, J. C. Das Neves Pereira, F. Le Pimpec-Barthes, C. Foucault, A. Dujon, and M. Riquet. Sleeve lobectomy versus pneumonectomy: tumor characteristics and comparative analysis of feasibility and results. *The Annals of thoracic surgery*, 80(6):2046–2050, 2005.

[8] E. A. Barnes, B. R. Murray, D. M. Robinson, L. J. Underwood, J. Hanson, and W. H. Roa. Dosimetric evaluation of lung tumor immobilization using breath hold at deep inspiration. *International Journal of Radiation Oncology* Biology* Physics*, 50(4):1091–1098, 2001.

[9] G. Baroni, M. Riboldi, M. F. Spadea, B. Tagaste, C. Garibaldi, R. Orecchia, and A. Pedotti. Integration of enhanced optical tracking techniques and imaging in IGRT. *Journal of radiation research*, 48(Suppl_A):A61–A74, 2007.

[10] M. Baumann, G. Stamatis, and M. Thomas. Therapy of localized non-small cell lung cancer (take home messages). *Lung cancer*, 33:S47–S49, 2001.

[11] M. A. Beckles, S. G. Spiro, G. L. Colice, and R. M. Rudd. Initial evaluation of the patient with lung cancer: symptoms, signs, laboratory tests, and paraneoplastic syndromes. *Chest*, 123(1):97S–104S, 2003.

[12] K. Bernatowicz, A. J. Lomax, and A. Knopf. Comparative study of layered and volumetric rescanning for different scanning speeds of proton beam in liver patients. *Physics in Medicine & Biology*, 58(22):7905, 2013.

[13] K. Bernatowicz, Y. Zhang, R. Perrin, D. C. Weber, and A. J. Lomax. Advanced treatment planning using direct 4D optimisation for pencil-beam scanned particle therapy. *Physics in Medicine & Biology*, 62(16):6595, 2017.

[14] E. B. Bernhardt and S. I. Jalal. Small Cell Lung Cancer. In K. L. Reckamp, editor, *Lung Cancer: Treatment and Research*, pages 301–322. Springer International Publishing, Cham, 2016.

[15] C. Bert and M. Durante. Motion in radiotherapy: particle therapy. *Physics in Medicine & Biology*, 56(16):R113, 2011.

[16] C. Bert, A. Gemmel, N. Saito, and E. Rietzel. Gated irradiation with scanned particle beams. *International Journal of Radiation Oncology* Biology* Physics*, 73(4):1270–1275, 2009.

[17] C. Bert, S. O. Grözinger, and E. Rietzel. Quantification of interplay effects of scanned particle beams and moving targets. *Physics in Medicine & Biology*, 53(9):2253, 2008.

[18] C. Bert, N. Saito, A. Schmidt, N. Chaudhri, D. Schardt, and E. Rietzel. Target motion tracking with a scanned particle beam. *Medical physics*, 34(12):4768–4771, 2007.

[19] J. Bertholet, A. Knopf, B. Eiben, J. McClelland, A. Grimwood, E. Harris, M. Menten, P. Poulsen, D. T. Nguyen, P. Keall, et al. Real-time intrafraction motion monitoring in external beam radiotherapy. *Physics in Medicine & Biology*, 64(15):15TR01, 2019.

[20] J. Boda-Heggemann, A.-C. Knopf, A. Simeonova-Chergou, H. Wertz, F. Stieler, A. Jahnke, L. Jahnke, J. Fleckenstein, L. Vogel, A. Arns, et al. Deep inspiration breath hold-based radiation therapy: a clinical review. *International Journal of Radiation Oncology* Biology* Physics*, 94(3):478–492, 2016.

[21] J. T. Booth, V. Caillet, N. Hardcastle, R. O'Brien, K. Szymura, C. Crasta, B. Harris, C. Haddad, T. Eade, and P. J. Keall. The first patient treatment of electromagnetic-guided real time adaptive radiotherapy using MLC tracking for lung SABR. *Radiotherapy and Oncology*, 121(1):19–25, 2016.

[22] T. Bortfeld, S. B. Jiang, and E. Rietzel. Effects of motion on the total dose distribution. In *Seminars in radiation oncology*, volume 14, pages 41–51. Elsevier, 2004.

[23] G. Bouilhol, M. Ayadi, S. Rit, S. Thengumpallil, J. Schaerer, J. Vandemeulebroucke, L. Claude, and D. Sarrut. Is abdominal compression useful in lung stereotactic body radiation therapy? A 4DCT and dosimetric lobe-dependent study. *Physica Medica*, 29(4):333–340, 2013.

[24] D. Boye, T. Lomax, and A. Knopf. Mapping motion from 4D-MRI to 3D-CT for use in 4D dose calculations: A technical feasibility study. *Medical physics*, 40(6Part1):061702, 2013.

[25] J. D. Bradley, R. Paulus, R. Komaki, G. Masters, G. Blumenschein, S. Schild, J. Bogart, C. Hu, K. Forster, A. Magliocco, V. Kavadi, Y. I. Garces, S. Narayan, P. Iyengar, C. Robinson, R. B. Wynn, C. Koprowski, J. Meng, J. Beitler, R. Gaur, W. Curran, and H. Choy. Standard-dose versus high-dose conformal radiotherapy with concurrent and consolidation carboplatin plus paclitaxel with or without cetuximab for patients with stage IIIA or IIIB non-small-cell lung cancer (RTOG 0617): a randomised, two-by-two factorial phase 3 study. *The Lancet Oncology*, 16(2):187–199, 2015.

[26] F. Bray, J. Ferlay, I. Soerjomataram, R. L. Siegel, L. A. Torre, and A. Jemal. Global cancer statistics 2018: GLOBOCAN estimates of incidence and mortality worldwide for 36 cancers in 185 countries. *CA: a cancer journal for clinicians*, 68(6):394–424, 2018.

[27] J. D. Brierley, M. K. Gospodarowicz, and C. Wittekind. *TNM classification of malignant tumours*. John Wiley & Sons, 2017.

[28] K. R. Britton, G. Starkschall, S. L. Tucker, T. Pan, C. Nelson, J. Y. Chang, J. D. Cox, R. Mohan, and R. Komaki. Assessment of gross tumor volume regression and motion changes during radiotherapy for non-small-cell lung cancer as measured by four-dimensional computed tomography. *International Journal of Radiation Oncology* Biology* Physics*, 68(4):1036–1046, 2007.

[29] A. Bryce-Atkinson, A. McWilliam, T. Marchant, C. Faivre-Finn, G. Whitfield, and M. Van Herk. EP-1713: Feasibility of low dose 4D CBCT in patients with lung cancer. *Radiotherapy and Oncology*, 123:S939–S940, 2017.

[30] G. Buccheri and D. Ferrigno. Lung cancer: clinical presentation and specialist referral time. *European Respiratory Journal*, 24(6):898–904, 2004.

[31] D. A. Bush, G. Cheek, S. Zaheer, J. Wallen, H. Mirshahidi, A. Katerelos, R. Grove, and J. D. Slater. High-dose hypofractionated proton beam radiation therapy is safe and effective for central and peripheral early-stage non-small cell lung cancer: results of a 12-year experience at Loma Linda University Medical Center. *International Journal of Radiation Oncology* Biology* Physics*, 86(5):964–968, 2013.

[32] V. Caillet, J. T. Booth, and P. Keall. IGRT and motion management during lung SBRT delivery. *Physica Medica*, 44:113–122, 2017.

[33] C. Cao, T. D'Amico, T. Demmy, J. Dunning, D. Gossot, H. Hansen, J. He, S. Jheon, R. H. Petersen, A. Sihoe, S. Swanson, W. Walker, and T. D. Yan. Surgery versus SABR for resectable non-small-cell lung cancer. *The Lancet Oncology*, 16(8):e370–e371, 2015.

[34] E. H. Castellanos and L. Horn. Immunotherapy in Lung Cancer. In K. L. Reckamp, editor, *Lung Cancer: Treatment and Research*, pages 203–223. Springer International Publishing, Cham, 2016.

[35] L. I. Cerviño, A. K. Chao, A. Sandhu, and S. B. Jiang. The diaphragm as an anatomic surrogate for lung tumor motion. *Physics in Medicine & Biology*, 54(11):3529, 2009.

[36] J. Y. Chang, S. K. Jabbour, D. D. Ruysscher, S. E. Schild, C. B. Simone, R. Rengan, S. Feigenberg, A. J. Khan, N. C. Choi, J. D. Bradley, X. R. Zhu, A. J. Lomax, and B. S. Hoppe. Consensus Statement on Proton Therapy in Early-Stage and Locally Advanced Non–Small Cell Lung Cancer. *International Journal of Radiation Oncology*Biology*Physics*, 95(1):505–516, 2016. Particle Therapy Special Edition.

[37] J. Y. Chang, R. Komaki, C. Lu, H. Y. Wen, P. K. Allen, A. Tsao, M. Gillin, R. Mohan, and J. D. Cox. Phase 2 study of high-dose proton therapy with concurrent chemotherapy for unresectable stage III nonsmall cell lung cancer. *Cancer*, 117(20):4707–4713, 2011.

[38] J. Y. Chang, H. Li, X. R. Zhu, Z. Liao, L. Zhao, A. Liu, Y. Li, N. Sahoo, F. Poenisch, D. R. Gomez, et al. Clinical implementation of intensity modulated proton therapy for thoracic malignancies. *International Journal of Radiation Oncology* Biology* Physics*, 90(4):809–818, 2014.

[39] J. Y. Chang, S. Senan, M. A. Paul, R. J. Mehran, A. V. Louie, P. Balter, H. J. Groen, S. E. McRae, J. Widder, L. Feng, et al. Stereotactic ablative radiotherapy versus lobectomy for operable stage I non-small-cell lung cancer: a pooled analysis of two randomised trials. *The Lancet Oncology*, 16(6):630–637, 2015.

[40] J. Y. Chang, S. Senan, E. F. Smit, and J. A. Roth. Surgery versus SABR for resectable non-small-cell lung cancer – Authors' reply. *The Lancet Oncology*, 16(8):e374–e375, 2015.

[41] J. Y. Chang, X. Zhang, A. Knopf, H. Li, S. Mori, L. Dong, H.-M. Lu, W. Liu, S. N. Badiyan, S. Both, et al. Consensus guidelines for implementing pencil-beam scanning proton therapy for thoracic malignancies on behalf of the PTCOG thoracic and lymphoma subcommittee. *International Journal of Radiation Oncology* Biology* Physics*, 99(1):41–50, 2017.

[42] N. Chaudhri, N. Saito, C. Bert, B. Franczak, P. Steidl, M. Durante, E. Rietzel, and D. Schardt. Ion-optical studies for a range adaptation method in ion beam therapy using a static wedge degrader combined with magnetic beam deflection. *Physics in Medicine & Biology*, 55(12):3499, 2010.

[43] A. B. Chen, L. Li, A. Cronin, and D. Schrag. Comparative effectiveness of intensity-modulated versus 3D conformal radiation therapy among medicare patients with stage III lung cancer. *Journal of Thoracic Oncology*, 9(12):1788–1795, 2014.

[44] T. Chen, S. Qin, X. Xu, S. K. Jabbour, B. G. Haffty, and N. J. Yue. Frequency filtering based analysis on the cardiac induced lung tumor motion and its impact on the radiotherapy management. *Radiotherapy and Oncology*, 112(3):365–370, 2014.

[45] J. Cho, W. Cheon, S. Ahn, H. Jung, H. Sheen, H. C. Park, and Y. Han. Development of a real-time internal and external marker tracking system for particle therapy: a phantom study using patient tumor trajectory data. *Journal of radiation research*, 58(5):710–719, 2017.

[46] S. G. Chun, C. Hu, H. Choy, R. U. Komaki, R. D. Timmerman, S. E. Schild, J. A. Bogart, M. C. Dobelbower, W. Bosch, J. M. Galvin, et al. Impact of intensity-modulated radiation therapy technique for locally advanced non–small-cell lung cancer: a secondary analysis of the NRG oncology RTOG 0617 randomized clinical trial. *Journal of Clinical Oncology*, 35(1):56, 2017.

[47] A. Cifor, L. Risser, D. Chung, E. M. Anderson, and J. A. Schnabel. Hybrid feature-based diffeomorphic registration for tumor tracking in 2-D liver ultrasound images. *IEEE transactions on medical imaging*, 32(9):1647–1656, 2013.

[48] L. G. Collins, C. Haines, R. Perkel, and R. E. Enck. Lung cancer: diagnosis and management. *American family physician*, 75(1):56–63, 2007.

[49] W. J. Curran Jr, R. Paulus, C. J. Langer, R. Komaki, J. S. Lee, S. Hauser, B. Movsas, T. Wasserman, S. A. Rosenthal, E. Gore, et al. Sequential vs concurrent chemoradiation for stage III non–small cell lung cancer: randomized phase III trial RTOG 9410. *Journal of the National Cancer Institute*, 103(19):1452–1460, 2011.

[50] P. De Leyn, W. Rots, G. Deneffe, P. Nafteux, W. Coosemans, D. Van Raemdonck, G. Decker, and T. Lerut. Sleeve lobectomy for non-small cell lung cancer. *Acta Chirurgica Belgica*, 103(6):570–576, 2003.

[51] V. De Luca, J. Banerjee, A. Hallack, S. Kondo, M. Makhinya, D. Nouri, L. Royer, A. Cifor, G. Dardenne, O. Goksel, et al. Evaluation of 2D and 3D ultrasound tracking algorithms and impact on ultrasound-guided liver radiotherapy margins. *Medical physics*, 45(11):4986–5003, 2018.

[52] V. De Luca, T. Benz, S. Kondo, L. König, D. Lübke, S. Rothlübbers, O. Somphone, S. Allaire, M. L. Bell, D. Chung, et al. The 2014 liver ultrasound tracking benchmark. *Physics in Medicine & Biology*, 60(14):5571, 2015.

[53] V. De Luca, G. Székely, and C. Tanner. Estimation of large-scale organ motion in B-mode ultrasound image sequences: A survey. *Ultrasound in medicine & biology*, 41(12):3044–3062, 2015.

[54] V. De Luca, C. Tanner, and G. Székely. Speeding-up image registration for repetitive motion scenarios. In *2012 9th IEEE International Symposium on Biomedical Imaging (ISBI)*, pages 1355–1358. IEEE, 2012.

[55] V. De Luca, M. Tschannen, G. Székely, and C. Tanner. A learning-based approach for fast and robust vessel tracking in long ultrasound sequences. In *International Conference on Medical Image Computing and Computer-Assisted Intervention*, pages 518–525. Springer, 2013.

[56] T. Depuydt, K. Poels, D. Verellen, B. Engels, C. Collen, M. Buleteanu, R. Van den Begin, M. Boussaer, M. Duchateau, T. Gevaert, et al. Treating patients with real-time tumor tracking using the Vero gimbaled linac system: implementation and first review. *Radiotherapy and Oncology*, 112(3):343–351, 2014.

[57] T. Depuydt, D. Verellen, O. Haas, T. Gevaert, N. Linthout, M. Duchateau, K. Tournel, T. Reynders, K. Leysen, M. Hoogeman, et al. Geometric accuracy of a novel gimbals based radiation therapy tumor tracking system. *Radiotherapy and Oncology*, 98(3):365–372, 2011.

[58] J. Deslauriers, J. Grégoire, L. F. Jacques, M. Piraux, L. Guojin, and Y. Lacasse. Sleeve lobectomy versus pneumonectomy for lung cancer: a comparative analysis of survival and sites or recurrences. *The Annals of thoracic surgery*, 77(4):1152–1156, 2004.

[59] M. F. Dietrich and D. E. Gerber. Chemotherapy for Advanced Non-small Cell Lung Cancer. In K. L. Reckamp, editor, *Lung Cancer: Treatment and Research*, pages 119–149. Springer International Publishing, Cham, 2016.

[60] L. Du, S. N. Waqar, and D. Morgensztern. Multimodality Therapy for NSCLC. In K. L. Reckamp, editor, *Lung Cancer: Treatment and Research*, pages 151–163. Springer International Publishing, Cham, 2016.

[61] J. Dueck, A.-C. Knopf, A. Lomax, F. Albertini, G. F. Persson, M. Josipovic, M. Aznar, D. C. Weber, and P. Munck af Rosenschöld. Robustness of the voluntary breath-hold approach for the treatment of peripheral lung tumors using hypofractionated pencil beam scanning proton therapy. *International Journal of Radiation Oncology* Biology* Physics*, 95(1):534–541, 2016.

[62] M. Durante, R. Orecchia, and J. S. Loeffler. Charged-particle therapy in cancer: clinical uses and future perspectives. *Nature Reviews Clinical Oncology*, 14(8):483, 2017.

[63] J. Ehrhardt, R. Werner, A. Schmidt-Richberg, and H. Handels. Statistical modeling of 4D respiratory lung motion using diffeomorphic image registration. *IEEE transactions on medical imaging*, 30(2):251–265, 2010.

[64] M. Engelsman, M. Schwarz, and L. Dong. Physics controversies in proton therapy. In *Seminars in radiation oncology*, volume 23, pages 88–96. Elsevier, 2013.

[65] F. Ernst, R. Dürichen, A. Schlaefer, and A. Schweikard. Evaluating and comparing algorithms for respiratory motion prediction. *Physics in Medicine & Biology*, 58(11):3911, 2013.

[66] M. Falk, P. Munck af Rosenschöld, P. Keall, H. Cattell, B. C. Cho, P. Poulsen, S. Povzner, A. Sawant, J. Zimmerman, and S. Korreman. Real-time dynamic MLC tracking for inversely optimized arc radiotherapy. *Radiotherapy and oncology*, 94(2):218–223, 2010.

[67] G. Fattori, S. Safai, P. F. Carmona, M. Peroni, R. Perrin, D. C. Weber, and A. J. Lomax. Monitoring of breathing motion in image-guided PBS proton therapy: comparative analysis of optical and electromagnetic technologies. *Radiation oncology*, 12(1):63, 2017.

[68] G. Fattori, M. Seregni, A. Pella, M. Riboldi, L. Capasso, M. Donetti, M. Ciocca, S. Giordanengo, M. Pullia, F. Marchetto, et al. Real-time optical tracking for motion compensated irradiation with scanned particle beams at CNAO. *Nuclear Instruments and Methods in Physics Research Section A: Accelerators, Spectrometers, Detectors and Associated Equipment*, 827:39–45, 2016.

[69] H. Fayad, J.-F. Clément, T. Pan, C. Roux, C. C. Le Rest, O. Pradier, and D. Visvikis. Towards a generic respiratory motion model for 4D CT imaging of the thorax. In *2009 IEEE Nuclear Science Symposium Conference Record (NSS/MIC)*, pages 3975–3979. IEEE, 2009.

[70] M. K. Ferguson and A. G. Lehman. Sleeve lobectomy or pneumonectomy: optimal management strategy using decision analysis techniques. *The Annals of thoracic surgery*, 76(6):1782–1788, 2003.

[71] J. Ferlay, M. Colombet, I. Soerjomataram, C. Mathers, D. Parkin, M. Piñeros, A. Znaor, and F. Bray. Estimating the global cancer incidence and mortality in 2018: GLOBOCAN sources and methods. *International journal of cancer*, 144(8):1941–1953, 2019.

[72] J. Ferlay, M. Ervik, F. Lam, M. Colombet, L. Mery, M. Piñeros, A. Znaor, I. Soerjomataram, and F. Bray. Global Cancer Observatory: Cancer Today. Lyon, France: International Agency for Research on Cancer. Available from: https://gco.iarc.fr/today, accessed 28 January 2020, 2018.

[73] D. Fontanarosa, S. Van der Meer, J. Bamber, E. Harris, T. O'Shea, and F. Verhaegen. Review of ultrasound image guidance in external beam radiotherapy: I. Treatment planning and inter-fraction motion management. *Physics in medicine & biology*, 60(3):R77, 2015.

[74] T. Furukawa, T. Inaniwa, S. Sato, T. Tomitani, S. Minohara, K. Noda, and T. Kanai. Design study of a raster scanning system for moving target irradiation in heavy-ion radiotherapy. *Medical physics*, 34(3):1085–1097, 2007.

[75] A. Giger, C. Jud, D. Nguyen, M. Krieger, Y. Zhang, A. J. Lomax, O. Bieri, R. Salomir, and P. C. Cattin. Inter-fractional Respiratory Motion Modelling from Abdominal Ultrasound: A Feasibility Study. In *International Workshop on PRedictive Intelligence In MEdicine*, pages 11–22. Springer, 2019.

[76] A. Giger, R. Sandkühler, C. Jud, G. Bauman, O. Bieri, R. Salomir, and P. C. Cattin. Respiratory motion modelling using cGANs. In *International Conference on Medical Image Computing and Computer-Assisted Intervention*, pages 81–88. Springer, 2018.

[77] A. Giger, M. Stadelmann, F. Preiswerk, C. Jud, V. De Luca, Z. Celicanin, O. Bieri, R. Salomir, and P. C. Cattin. Erratum: Ultrasound-driven 4D MRI (2018 Phys. Med. Biol. 63 145015). *Physics in Medicine & Biology*, 63(17):179601, 2018.

[78] A. Giger, M. Stadelmann, F. Preiswerk, C. Jud, V. De Luca, Z. Celicanin, O. Bieri, R. Salomir, and P. C. Cattin. Ultrasound-driven 4D MRI. *Physics in Medicine & Biology*, 63(14):145015, 2018.

[79] R. J. Ginsberg and L. V. Rubinstein. Randomized trial of lobectomy versus limited resection for T1 N0 non-small cell lung cancer. *The Annals of Thoracic Surgery*, 60(3):615–623, 1995.

[80] P. Goldstraw, K. Chansky, J. Crowley, R. Rami-Porta, H. Asamura, W. E. Eberhardt, A. G. Nicholson, P. Groome, A. Mitchell, V. Bolejack, et al. The IASLC lung cancer staging project: proposals for revision of the TNM stage groupings in the forthcoming (eighth) edition of the TNM classification for lung cancer. *Journal of Thoracic Oncology*, 11(1):39–51, 2016.

[81] J. H. Goodband, O. C. Haas, and J. Mills. A comparison of neural network approaches for on-line prediction in IGRT. *Medical physics*, 35(3):1113–1122, 2008.

[82] I. Goodfellow, Y. Bengio, and A. Courville. *Deep Learning*. MIT Press, 2016. http://www.deeplearningbook.org.

[83] I. Goodfellow, J. Pouget-Abadie, M. Mirza, B. Xu, D. Warde-Farley, S. Ozair, A. Courville, and Y. Bengio. Generative adversarial nets. In *Advances in neural information processing systems*, pages 2672–2680, 2014.

[84] J. Gorgisyan, A. J. Lomax, P. Munck af Rosenschold, G. F. Persson, M. Krieger, E. Colvill, J. Scherman, F. Gagnon-Moisan, M. Egloff, G. Fattori, et al. The dosimetric effect of residual breath-hold motion in pencil beam scanned proton therapy–An experimental study. *Radiotherapy and Oncology*, 134:135–142, 2019.

[85] J. Gorgisyan, P. Munck af Rosenschold, R. Perrin, G. F. Persson, M. Josipovic, M. F. Belosi, S. A. Engelholm, D. C. Weber, and A. J. Lomax. Feasibility of pencil beam scanned intensity modulated proton therapy in breath-hold for locally advanced non-small cell lung cancer. *International Journal of Radiation Oncology* Biology* Physics*, 99(5):1121–1128, 2017.

[86] C. Graeff. Motion mitigation in scanned ion beam therapy through 4D-optimization. *Physica Medica*, 30(5):570–577, 2014.

[87] C. Graeff, M. Durante, and C. Bert. Motion mitigation in intensity modulated particle therapy by internal target volumes covering range changes. *Medical physics*, 39(10):6004–6013, 2012.

[88] C. Grassberger, S. Dowdell, A. Lomax, G. Sharp, J. Shackleford, N. Choi, H. Willers, and H. Paganetti. Motion interplay as a function of patient parameters and spot size in spot scanning proton therapy for lung cancer. *International Journal of Radiation Oncology* Biology* Physics*, 86(2):380–386, 2013.

[89] C. Grassberger, S. Dowdell, G. Sharp, and H. Paganetti. Motion mitigation for lung cancer patients treated with active scanning proton therapy. *Medical physics*, 42(5):2462–2469, 2015.

[90] A. Grimwood, H. A. McNair, T. P. O'Shea, S. Gilroy, K. Thomas, J. C. Bamber, A. C. Tree, and E. J. Harris. In vivo validation of Elekta's clarity autoscan for ultrasound-based intrafraction motion estimation of the prostate during radiation therapy. *International Journal of Radiation Oncology* Biology* Physics*, 102(4):912–921, 2018.

[91] S. O. Grözinger, C. Bert, T. Haberer, G. Kraft, and E. Rietzel. Motion compensation with a scanned ion beam: a technical feasibility study. *Radiation Oncology*, 3(1):34, 2008.

[92] S. O. Grözinger, E. Rietzel, Q. Li, C. Bert, T. Haberer, and G. Kraft. Simulations to design an online motion compensation system for scanned particle beams. *Physics in Medicine & Biology*, 51(14):3517, 2006.

[93] F. Guida, N. Sun, L. E. Bantis, D. C. Muller, P. Li, A. Taguchi, D. Dhillon, D. L. Kundnani, N. J. Patel, Q. Yan, et al. Assessment of lung cancer risk on the basis of a biomarker panel of circulating proteins. *JAMA oncology*, 4(10):e182078–e182078, 2018.

[94] C. J. Haasbeek, F. J. Lagerwaard, M. E. Antonisse, B. J. Slotman, and S. Senan. Stage I nonsmall cell lung cancer in patients aged $\geq$ 75 years: outcomes after stereotactic radiotherapy. *Cancer: Interdisciplinary International Journal of the American Cancer Society*, 116(2):406–414, 2010.

[95] D. Habermehl, K. Henkner, S. Ecker, O. Jäkel, J. Debus, and S. E. Combs. Evaluation of different fiducial markers for image-guided radiotherapy and particle therapy. *Journal of radiation research*, 54(suppl_1):i61–i68, 2013.

[96] B. Han, M. Najafi, D. T. Cooper, M. Lachaine, R. von Eyben, S. Hancock, and D. Hristov. Evaluation of transperineal ultrasound imaging as a potential solution for target tracking during hypofractionated radiotherapy for prostate cancer. *Radiation Oncology*, 13(1):151, 2018.

[97] K. Han, P. Cheung, P. S. Basran, I. Poon, L. Yeung, and F. Lochray. A comparison of two immobilization systems for stereotactic body radiation therapy of lung tumors. *Radiotherapy and Oncology*, 95(1):103–108, 2010.

[98] S. M. Hanash, E. J. Ostrin, and J. F. Fahrmann. Blood based biomarkers beyond genomics for lung cancer screening. *Translational lung cancer research*, 7(3):327, 2018.

[99] J. Hanley, M. M. Debois, D. Mah, G. S. Mageras, A. Raben, K. Rosenzweig, B. Mychalczak, L. H. Schwartz, P. J. Gloeggler, W. Lutz, et al. Deep inspiration breath-hold technique for lung tumors: the potential value of target immobilization and reduced lung density in dose escalation. *International Journal of Radiation Oncology* Biology* Physics*, 45(3):603–611, 1999.

[100] J. P. Harris, J. D. Murphy, A. L. Hanlon, Q.-T. Le, B. W. Loo Jr, and M. Diehn. A population-based comparative effectiveness study of radiation therapy techniques in stage III non-small cell lung cancer. *International Journal of Radiation Oncology* Biology* Physics*, 88(4):872–884, 2014.

[101] G. Haskins, U. Kruger, and P. Yan. Deep learning in medical image registration: A survey. *Machine Vision and Applications*, 31(1):8, 2020.

[102] T. He, Z. Xue, W. Xie, and S. T. Wong. Online 4-D CT estimation for patient-specific respiratory motion based on real-time breathing signals. In *International Conference on Medical Image Computing and Computer-Assisted Intervention*, pages 392–399. Springer, 2010.

[103] M. P. Heinrich and B. W. Papież. Chapter 13 - Image registration with sliding motion. In S. K. Zhou, D. Rueckert, and G. Fichtinger, editors, *Handbook of Medical Image Computing and Computer Assisted Intervention*, pages 293–318. Academic Press, 2020.

[104] K. A. Higgins, K. O'Connell, Y. Liu, T. W. Gillespie, M. W. McDonald, R. N. Pillai, K. R. Patel, P. R. Patel, C. G. Robinson, C. B. Simone II, et al. National Cancer Database analysis of proton versus photon radiation therapy in non-small cell lung cancer. *International Journal of Radiation Oncology* Biology* Physics*, 97(1):128–137, 2017.

[105] M. Hiraoka, Y. Matsuo, A. Sawada, N. Ueki, Y. Miyaba, M. Nakamura, S. Yano, S. Kaneko, T. Mizowaki, and M. Kokubo. Realization of dynamic tumor tracking irradiation with real-time monitoring in lung tumor patients using a gimbaled x-ray head radiation therapy equipment. *International Journal of Radiation Oncology* Biology* Physics*, 84(3):S560–S561, 2012.

[106] H. Hof, K. K. Herfarth, M. Münter, A. Hoess, J. Motsch, M. Wannenmacher, and J. Debus. Stereotactic single-dose radiotherapy of stage I non–small-cell lung cancer (NSCLC). *International Journal of Radiation Oncology* Biology* Physics*, 56(2):335–341, 2003.

[107] J. D. Hoisak, K. E. Sixel, R. Tirona, P. C. Cheung, and J.-P. Pignol. Correlation of lung tumor motion with external surrogate indicators of respiration. *International Journal of Radiation Oncology* Biology* Physics*, 60(4):1298–1306, 2004.

[108] J. C. Hong and J. K. Salama. Dose escalation for unresectable locally advanced non-small cell lung cancer: end of the line? *Translational Lung Cancer Research*, 5(1), 2016.

[109] M. Hoogeman, J.-B. Prévost, J. Nuyttens, J. Pöll, P. Levendag, and B. Heijmen. Clinical accuracy of the respiratory tumor tracking system of the Cyberknife: assessment by analysis of log files. *International Journal of Radiation Oncology* Biology* Physics*, 74(1):297–303, 2009.

[110] B. Hou, X.-F. Deng, D. Zhou, Q.-X. Liu, and J.-G. Dai. Segmentectomy versus wedge resection for the treatment of high-risk operable patients with stage I non-small cell lung cancer: a meta-analysis. *Therapeutic advances in respiratory disease*, 10(5):435–443, 2016.

[111] N. Howlader, A. M. Noone, M. Krapcho, D. Miller, A. Brest, M. Yu, J. Ruhl, Z. Tatalovich, A. Mariotto, D. R. Lewis, H. S. Chen, E. J. Feuer, and K. A. Cronin. SEER Cancer Statistics Review, 1975-2017, National Cancer Institute. Bethesda, MD, https://seer.cancer.gov/csr/1975_2017/, based on November 2019 SEER data submission, posted to the SEER web site, April 2020.

[112] S. Hughes, J. McClelland, S. Tarte, D. Lawrence, S. Ahmad, D. Hawkes, and D. Landau. Assessment of two novel ventilatory surrogates for use in the delivery of gated/tracked radiotherapy for non-small cell lung cancer. *Radiotherapy and Oncology*, 91(3):336–341, 2009.

[113] G. D. Hugo and M. Rosu. Advances in 4D radiation therapy for managing respiration: part I–4D imaging. *Zeitschrift für medizinische Physik*, 22(4):258–271, 2012.

[114] G. D. Hugo, E. Weiss, W. C. Sleeman, S. Balik, P. J. Keall, J. Lu, and J. F. Williamson. A longitudinal four-dimensional computed tomography and cone beam computed tomography dataset for image-guided radiation therapy research in lung cancer. *Medical physics*, 44(2):762–771, 2017.

[115] ICRU Committee. Report 78: Prescribing, recording, and reporting proton-beam therapy. *Journal of the ICRU*, 7:141–150, 2007.

[116] Intensity Modulated Radiation Therapy Collaborative Working Group. Intensity-modulated radiotherapy: current status and issues of interest. *International Journal of Radiation Oncology* Biology* Physics*, 51(4):880–914, 2001.

[117] S. Ipsen, R. Bruder, E. S. Worm, R. Hansen, P. R. Poulsen, M. Høyer, and A. Schweikard. Simultaneous acquisition of 4D ultrasound and wireless electromagnetic tracking for in-vivo accuracy validation. *Current Directions in Biomedical Engineering*, 3(2):75–78, 2017.

[118] M. Isaksson, J. Jalden, and M. J. Murphy. On using an adaptive neural network to predict lung tumor motion during respiration for radiotherapy applications. *Medical physics*, 32(12):3801–3809, 2005.

[119] P. Isola, J.-Y. Zhu, T. Zhou, and A. A. Efros. Image-to-image translation with conditional adversarial networks. In *Proceedings of the IEEE conference on computer vision and pattern recognition*, pages 1125–1134, 2017.

[120] H. Iwata, M. Murakami, Y. Demizu, D. Miyawaki, K. Terashima, Y. Niwa, M. Mima, T. Akagi, Y. Hishikawa, and Y. Shibamoto. High-dose proton therapy and carbon-ion therapy for stage I nonsmall cell lung cancer. *Cancer*, 116(10):2476–2485, 2010.

[121] S. Iyer, A. Roughley, A. Rider, and G. Taylor-Stokes. The symptom burden of non-small cell lung cancer in the USA: a real-world cross-sectional study. *Supportive Care in Cancer*, 22(1):181–187, 2014.

[122] N. Jegadeesh, Y. Liu, T. Gillespie, F. Fernandez, S. Ramalingam, J. Mikell, J. Lipscomb, W. J. Curran, and K. A. Higgins. Evaluating intensity-modulated radiation therapy in locally advanced non–small-cell lung cancer: results from the national cancer data base. *Clinical lung cancer*, 17(5):398–405, 2016.

[123] M. Jermann. Particle therapy statistics in 2014. *International Journal of Particle Therapy*, 2(1):50–54, 2015.

[124] I. T. Jolliffe and J. Cadima. Principal component analysis: a review and recent developments. *Philosophical Transactions of the Royal Society A: Mathematical, Physical and Engineering Sciences*, 374(2065):20150202, 2016.

[125] C. Jud, A. Giger, R. Sandkühler, and P. C. Cattin. A localized statistical motion model as a reproducing kernel for non-rigid image registration. In *International Conference on Medical Image Computing and Computer-Assisted Intervention*, pages 261–269. Springer, 2017.

[126] C. Jud, N. Möri, B. Bitterli, and P. C. Cattin. Bilateral regularization in reproducing kernel hilbert spaces for discontinuity preserving image registration. In *International Workshop on Machine Learning in Medical Imaging*, pages 10–17. Springer, 2016.

[127] C. Jud, N. Möri, and P. C. Cattin. Sparse kernel machines for discontinuous registration and nonstationary regularization. In *Proceedings of the IEEE Conference on Computer Vision and Pattern Recognition Workshops*, pages 9–16, 2016.

[128] C. Jud, D. Nguyen, A. Giger, R. Sandkühler, M. Krieger, T. Lomax, R. Salomir, O. Bieri, and P. C. Cattin. Accelerated Motion-Aware MR Imaging via Motion Prediction from K-Space Center. *arXiv preprint arXiv:1908.09560*, 2019.

[129] C. Jud, D. Nguyen, R. Sandkühler, A. Giger, O. Bieri, and P. C. Cattin. Motion aware MR imaging via spatial core correspondence. In *International Conference on Medical Image Computing and Computer-Assisted Intervention*, pages 198–205. Springer, 2018.

[130] C. Jud, F. Preiswerk, and P. C. Cattin. Respiratory motion compensation with topology independent surrogates. In *Workshop on imaging and computer assistance in radiation therapy*, 2015.

[131] C. Jud, R. Sandkühler, and P. C. Cattin. An inhomogeneous multi-resolution regularization concept for discontinuity preserving image registration. In *International Workshop on Biomedical Image Registration*, pages 3–12. Springer, 2018.

[132] C. Jud, R. Sandkühler, N. Möri, and P. C. Cattin. Directional averages for motion segmentation in discontinuity preserving image registration. In *International Conference on Medical Image Computing and Computer-Assisted Intervention*, pages 249–256. Springer, 2017.

[133] T. Kanehira, T. Matsuura, S. Takao, Y. Matsuzaki, Y. Fujii, T. Fujii, Y. M. Ito, N. Miyamoto, T. Inoue, N. Katoh, et al. Impact of real-time image gating on spot scanning proton therapy for lung tumors: a simulation study. *International Journal of Radiation Oncology* Biology* Physics*, 97(1):173–181, 2017.

[134] P. Keall, V. Kini, S. Vedam, and R. Mohan. Motion adaptive x-ray therapy: a feasibility study. *Physics in Medicine & Biology*, 46(1):1, 2001.

[135] P. Keall, S. Vedam, R. George, C. Bartee, J. Siebers, F. Lerma, E. Weiss, and T. Chung. The clinical implementation of respiratory-gated intensity-modulated radiotherapy. *Medical Dosimetry*, 31(2):152–162, 2006.

[136] P. J. Keall, H. Cattell, D. Pokhrel, S. Dieterich, K. H. Wong, M. J. Murphy, S. S. Vedam, K. Wijesooriya, and R. Mohan. Geometric accuracy of a real-time target tracking system with dynamic multileaf collimator tracking system. *International Journal of Radiation Oncology* Biology* Physics*, 65(5):1579–1584, 2006.

[137] P. J. Keall, E. Colvill, R. O'Brien, J. A. Ng, P. R. Poulsen, T. Eade, A. Kneebone, and J. T. Booth. The first clinical implementation of electromagnetic transponder-guided MLC tracking. *Medical physics*, 41(2), 2014.

[138] P. J. Keall, G. S. Mageras, J. M. Balter, R. S. Emery, K. M. Forster, S. B. Jiang, J. M. Kapatoes, D. A. Low, M. J. Murphy, B. R. Murray, et al. The management of respiratory motion in radiation oncology report of AAPM Task Group 76. *Medical physics*, 33(10):3874–3900, 2006.

[139] F. M. Khan and J. P. Gibbons. *Khan's the physics of radiation therapy*. Lippincott Williams & Wilkins, 2014.

[140] W. Kilby, J. Dooley, G. Kuduvalli, S. Sayeh, and C. Maurer Jr. The CyberKnife® robotic radiosurgery system in 2010. *Technology in cancer research & treatment*, 9(5):433–452, 2010.

[141] T. Klinder and C. Lorenz. Respiratory motion compensation for image-guided bronchoscopy using a general motion model. In *2012 9th IEEE International Symposium on Biomedical Imaging (ISBI)*, pages 960–963. IEEE, 2012.

[142] T. Klinder, C. Lorenz, and J. Ostermann. Prediction framework for statistical respiratory motion modeling. In *International Conference on Medical Image Computing and Computer-Assisted Intervention*, pages 327–334. Springer, 2010.

[143] A. Knopf, C. Bert, E. Heath, S. Nill, K. Kraus, D. Richter, E. Hug, E. Pedroni, S. Safai, F. Albertini, et al. Special report: Workshop on 4D-treatment planning in actively scanned particle therapy – Recommendations, technical challenges, and future research directions. *Medical physics*, 37(9):4608–4614, 2010.

[144] A.-C. Knopf, T. S. Hong, and A. Lomax. Scanned proton radiotherapy for mobile targets – the effectiveness of re-scanning in the context of different treatment planning approaches and for different motion characteristics. *Physics in Medicine & Biology*, 56(22):7257, 2011.

[145] A.-C. Knopf, K. Stützer, C. Richter, A. Rucinski, J. da Silva, J. Phillips, M. Engelsman, S. Shimizu, R. Werner, A. Jakobi, et al. Required transition from research to clinical application: report on the 4D treatment planning workshops 2014 and 2015. *Physica Medica*, 32(7):874–882, 2016.

[146] F.-M. S. Kong, T. Ritter, D. J. Quint, S. Senan, L. E. Gaspar, R. U. Komaki, C. W. Hurkmans, R. Timmerman, A. Bezjak, J. D. Bradley, B. Movsas, L. Marsh, P. Okunieff, H. Choy, and W. J. Curran. Consideration of Dose Limits for Organs at Risk of Thoracic Radiotherapy: Atlas for Lung, Proximal Bronchial Tree, Esophagus, Spinal Cord, Ribs, and Brachial Plexus. *International Journal of Radiation Oncology*Biology*Physics*, 81(5):1442–1457, 2011.

[147] S. Korreman. Image-guided radiotherapy and motion management in lung cancer. *The British journal of radiology*, 88(1051):20150100, 2015.

[148] N. Kothary, J. J. Heit, J. D. Louie, W. T. Kuo, B. W. Loo Jr, A. Koong, D. T. Chang, D. Hovsepian, D. Y. Sze, and L. V. Hofmann. Safety and efficacy of percutaneous fiducial marker implantation for image-guided radiation therapy. *Journal of vascular and interventional radiology*, 20(2):235–239, 2009.

[149] K. Kraus, E. Heath, and U. Oelfke. Dosimetric consequences of tumour motion due to respiration for a scanned proton beam. *Physics in Medicine & Biology*, 56(20):6563, 2011.

[150] A. Krauss, S. Nill, and U. Oelfke. The comparative performance of four respiratory motion predictors for real-time tumour tracking. *Physics in Medicine & Biology*, 56(16):5303, 2011.

[151] A. Krauss, S. Nill, M. Tacke, and U. Oelfke. Electromagnetic real-time tumor position monitoring and dynamic multileaf collimator tracking using a Siemens 160 MLC: Geometric and dosimetric accuracy of an integrated system. *International Journal of Radiation Oncology* Biology* Physics*, 79(2):579–587, 2011.

[152] H. Krieger. *Grundlagen der Strahlungsphysik und des Strahlenschutzes*, chapter 1, pages 17–51. Springer, Berlin, Heidelberg, 2019.

[153] M. Krieger. *Towards ultrasound-guided proton beam tracking for lung tumours*. PhD thesis, ETH Zurich, 2020.

[154] M. Krieger, A. Giger, R. Salomir, O. Bieri, Z. Celicanin, P. C. Cattin, A. J. Lomax, D. C. Weber, and Y. Zhang. Impact of internal target volume definition for pencil beam scanned proton treatment planning in the presence of respiratory motion variability for lung cancer: A proof of concept. *Radiotherapy and oncology*, 145:154–161, 2020.

[155] M. Krieger, A. Giger, D. Weber, A. Lomax, and Y. Zhang. Consequences of respiratory motion variability in lung 4DMRI datasets. In *Radiotherapy and Oncology*, volume 133, pages S219–S220, 2019.

[156] M. Krieger, K. Klucznik, E. Colvill, M. Peroni, O. Bieri, Z. Celicanin, D. Weber, A. Lomax, and Y. Zhang. Experimental validation of a synthetic 4DCT-MRI approach using an anthropomorphic breathing phantom. In *Radiotherapy and Oncology*, volume 127, page 1140, 2018.

[157] T. Kubiak. Particle therapy of moving targets – the strategies for tumour motion monitoring and moving targets irradiation. *The British journal of radiology*, 89(1066):20150275, 2016.

[158] H. D. Kubo and B. C. Hill. Respiration gated radiotherapy treatment: a technical study. *Physics in Medicine & Biology*, 41(1):83, 1996.

[159] M. Lachaine and T. Falco. Intrafractional prostate motion management with the Clarity Autoscan system. *Medical physics international*, 1, 2013.

[160] G. Landry and C.-h. Hua. Current state and future applications of radiological image guidance for particle therapy. *Medical physics*, 45(11):e1086–e1095, 2018.

[161] S. Lang, J. Zeimetz, G. Ochsner, M. Schmid Daners, O. Riesterer, and S. Klöck. Development and evaluation of a prototype tracking system using the treatment couch. *Medical physics*, 41(2):021720, 2014.

[162] K. Langen and D. Jones. Organ motion and its management. *International Journal of Radiation Oncology* Biology* Physics*, 50(1):265–278, 2001.

[163] X. A. Li, C. Stepaniak, and E. Gore. Technical and dosimetric aspects of respiratory gating using a pressure-sensor motion monitoring system. *Medical physics*, 33(1):145–154, 2006.

[164] Y. Li, L. Kardar, X. Li, H. Li, W. Cao, J. Y. Chang, L. Liao, R. X. Zhu, N. Sahoo, M. Gillin, et al. On the interplay effects with proton scanning beams in stage III lung cancer. *Medical physics*, 41(2):021721, 2014.

[165] Y.-L. Lin. Proton beam therapy in apneic oxygenation treatment of an unresectable hepatocellular carcinoma: A case report and review of literature. *World Journal of Hepatology*, 10(10):772, 2018.

[166] H. H. Liu, P. Balter, T. Tutt, B. Choi, J. Zhang, C. Wang, M. Chi, D. Luo, T. Pan, S. Hunjan, et al. Assessing respiration-induced tumor motion and internal target volume using four-dimensional computed tomography for radiotherapy of lung cancer. *International Journal of Radiation Oncology* Biology* Physics*, 68(2):531–540, 2007.

[167] W. Liu, S. E. Schild, J. Y. Chang, Z. Liao, Y.-H. Chang, Z. Wen, J. Shen, J. B. Stoker, X. Ding, Y. Hu, et al. Exploratory study of 4D versus 3D robust optimization in intensity modulated proton therapy for lung cancer. *International Journal of Radiation Oncology* Biology* Physics*, 95(1):523–533, 2016.

[168] Y. Liu, F.-F. Yin, Z. Chang, B. G. Czito, M. Palta, M. R. Bashir, Y. Qin, and J. Cai. Investigation of sagittal image acquisition for 4D-MRI with body area as respiratory surrogate. *Medical physics*, 41(10):101902, 2014.

[169] A. Lomax. Intensity modulation methods for proton radiotherapy. *Physics in Medicine & Biology*, 44(1):185, 1999.

[170] A. Lomax, T. Boehringer, A. Coray, E. Egger, G. Goitein, M. Grossmann, P. Juelke, S. Lin, E. Pedroni, B. Rohrer, et al. Intensity modulated proton therapy: a clinical example. *Medical Physics*, 28(3):317–324, 2001.

[171] A. J. Lomax. Charged particle therapy: the physics of interaction. *The Cancer Journal*, 15(4):285–291, 2009.

[172] A. J. Lomax, E. Pedroni, H. P. Rutz, and G. Goitein. The clinical potential of intensity modulated proton therapy. *Zeitschrift für Medizinische Physik*, 14(3):147–152, 2004.

[173] O. Lorton, P. C. Guillemin, N. Möri, L. A. Crowe, S. Boudabbous, S. Terraz, C. D. Becker, P. Cattin, R. Salomir, and L. Gui. Self-Scanned HIFU Ablation of Moving Tissue Using Real-Time Hybrid US-MR Imaging. *IEEE Transactions on Biomedical Engineering*, 66(8):2182–2191, 2018.

[174] A. V. Louie, S. Senthi, and D. A. Palma. Surgery versus SABR for NSCLC. *The Lancet Oncology*, 14(12):e491, 2013.

[175] H.-M. Lu, R. Brett, G. Sharp, S. Safai, S. Jiang, J. Flanz, and H. Kooy. A respiratory-gated treatment system for proton therapy. *Medical physics*, 34(8):3273–3278, 2007.

[176] W. Lu, D. A. Low, P. J. Parikh, M. M. Nystrom, I. M. El Naqa, S. H. Wahab, M. Handoko, D. Fooshee, and J. D. Bradley. Comparison of spirometry and abdominal height as four-dimensional computed tomography metrics in lung. *Medical physics*, 32(7Part1):2351–2357, 2005.

[177] M. Makhinya and O. Goksel. Motion tracking in 2D ultrasound using vessel models and robust optic-flow. *Proceedings of MICCAI CLUST*, 20, 2015.

[178] W. A. Mampuya, M. Nakamura, Y. Matsuo, N. Ueki, Y. Iizuka, T. Fujimoto, S. Yano, H. Monzen, T. Mizowaki, and M. Hiraoka. Interfraction variation in lung tumor position with abdominal compression during stereotactic body radiotherapy. *Medical physics*, 40(9):091718, 2013.

[179] D. Manke, K. Nehrke, and P. Börnert. Novel prospective respiratory motion correction approach for free-breathing coronary MR angiography using a patient-adapted affine motion model. *Magnetic Resonance in Medicine: An Official Journal of the International Society for Magnetic Resonance in Medicine*, 50(1):122–131, 2003.

[180] T. Matsuura, N. Miyamoto, S. Shimizu, Y. Fujii, M. Umezawa, S. Takao, H. Nihongi, C. Toramatsu, K. Sutherland, R. Suzuki, et al. Integration of a real-time tumor monitoring system into gated proton spot-scanning beam therapy: An initial phantom study using patient tumor trajectory data. *Medical physics*, 40(7):071729, 2013.

[181] J. R. McClelland, D. J. Hawkes, T. Schaeffter, and A. P. King. Respiratory motion models: a review. *Medical image analysis*, 17(1):19–42, 2013.

[182] J. R. McClelland, S. Hughes, M. Modat, A. Qureshi, S. Ahmad, D. Landau, S. Ourselin, and D. Hawkes. Inter-fraction variations in respiratory motion models. *Physics in Medicine & Biology*, 56(1):251, 2010.

[183] H. A. McNair, J. Brock, J. R. N. Symonds-Tayler, S. Ashley, S. Eagle, P. M. Evans, A. Kavanagh, N. Panakis, and M. Brada. Feasibility of the use of the Active Breathing Co ordinator^{TM}(ABC) in patients receiving radical radiotherapy for non-small cell lung cancer (NSCLC). *Radiotherapy and Oncology*, 93(3):424–429, 2009.

[184] A. Mihai, M. T. Milano, A. Santos, A. Kennedy, P. Thirion, R. S. McDermott, J. Westrup, L. Rock, and J. Armstrong. Treatment completion, treatment compliance and outcomes of old and very old patients treated by dose adapted stereotactic ablative radiotherapy (SABR) for T1-T3N0M0 non-small cell lung cancer. *Journal of Geriatric Oncology*, 10(3):442–448, 2019.

[185] H. Mizuno, O. Saito, M. Tajiri, T. Kimura, D. Kuroiwa, T. Shirai, T. Inaniwa, M. Fukahori, K. Miki, and S. Fukuda. Commissioning of a respiratory gating system involving a pressure sensor in carbon-ion scanning radiotherapy. *Journal of applied clinical medical physics*, 20(1):37–42, 2019.

[186] S. Moore, B. Leung, J. Wu, and C. Ho. Population-based analysis of curative therapies in stage II non-small cell lung cancer: the role of radiotherapy in medically inoperable patients. *Radiation Oncology*, 15(1):1–8, 2020.

[187] S. Mori, C. Graeff, and N. Kanematsu. How should we manage internal margins in four-dimensional dose assessments? *Radiological physics and technology*, 10(4):535–537, 2017.

[188] S. Mori, M. Karube, T. Shirai, M. Tajiri, T. Takekoshi, K. Miki, Y. Shiraishi, K. Tanimoto, K. Shibayama, S. Yasuda, et al. Carbon-ion pencil beam scanning treatment with gated markerless tumor tracking: an analysis of positional accuracy. *International Journal of Radiation Oncology* Biology* Physics*, 95(1):258–266, 2016.

[189] S. Mori, H.-M. Lu, J. A. Wolfgang, N. C. Choi, and G. T. Chen. Effects of interfractional anatomical changes on water-equivalent pathlength in charged-particle radiotherapy of lung cancer. *Journal of radiation research*, 50(6):513–519, 2009.

[190] S. Mori, J. Wolfgang, H.-M. Lu, R. Schneider, N. C. Choi, and G. T. Chen. Quantitative assessment of range fluctuations in charged particle lung irradiation. *International Journal of Radiation Oncology* Biology* Physics*, 70(1):253–261, 2008.

[191] F. Mostafaei, A. Tai, E. Gore, C. Johnstone, W. Haase, C. Ehlers, D. T. Cooper, M. Lachaine, and X. A. Li. Feasibility of real-time lung tumor motion monitoring using intrafractional ultrasound and kV cone beam projection images. *Medical Physics*, 45(10):4619–4626, 2018.

[192] H. Nakamura, N. Kawasaki, M. Taguchi, and K. Kabasawa. Survival following lobectomy vs limited resection for stage I lung cancer: a meta-analysis. *British journal of cancer*, 92(6):1033–1037, 2005.

[193] Y. Y. Nathan, T. A. DeWees, C. Liu, T. B. Daniels, J. B. Ashman, S. E. Beamer, D. E. Jaroszewski, H. J. Ross, H. R. Paripati, J.-C. M. Rwigema, et al. Early Outcomes of Patients With Locally Advanced Non-small Cell Lung Cancer Treated With Intensity-Modulated Proton Therapy Versus Intensity-Modulated Radiation Therapy: The Mayo Clinic Experience. *Advances in Radiation Oncology*, 2019.

[194] National Center for Chronic Disease Prevention and Health Promotion (US), Office on Smoking and Health. *The Health Consequences of Smoking – 50 Years of Progress: A Report of the Surgeon General*, chapter 6. Atlanta (GA): Centers for Disease Control and Prevention (US), 2014. Available from: https://www.ncbi.nlm.nih.gov/books/NBK179276/.

[195] Y. Negoro, Y. Nagata, T. Aoki, T. Mizowaki, N. Araki, K. Takayama, M. Kokubo, S. Yano, S. Koga, K. Sasai, et al. The effectiveness of an immobilization device in conformal radiotherapy for lung tumor: reduction of respiratory tumor movement and evaluation of the daily setup accuracy. *International Journal of Radiation Oncology* Biology* Physics*, 50(4):889–898, 2001.

[196] J. A. G. Neto, M. Elazzazzi, E. Altun, and R. C. Semelka. When should abdominal magnetic resonance imaging be used? *Clinical Gastroenterology and Hepatology*, 6(6):610–615, 2008.

[197] Q.-N. Nguyen, N. B. Ly, R. Komaki, L. B. Levy, D. R. Gomez, J. Y. Chang, P. K. Allen, R. J. Mehran, C. Lu, M. Gillin, et al. Long-term outcomes after proton therapy, with

concurrent chemotherapy, for stage II–III inoperable non-small cell lung cancer. *Radiotherapy and Oncology*, 115(3):367–372, 2015.

[198] A. G. Nicholson, K. Chansky, J. Crowley, R. Beyruti, K. Kubota, A. Turrisi, W. E. Eberhardt, J. Van Meerbeeck, R. Rami-Porta, P. Goldstraw, et al. The International Association for the Study of Lung Cancer Lung Cancer Staging Project: proposals for the revision of the clinical and pathologic staging of small cell lung cancer in the forthcoming eighth edition of the TNM classification for lung cancer. *Journal of Thoracic Oncology*, 11(3):300–311, 2016.

[199] B. M. Oborn, S. Dowdell, P. E. Metcalfe, S. Crozier, R. Mohan, and P. J. Keall. Future of medical physics: real-time MRI-guided proton therapy. *Medical physics*, 44(8):e77–e90, 2017.

[200] E. A. Omari, B. Erickson, C. Ehlers, F. Quiroz, G. Noid, D. T. Cooper, M. Lachaine, and X. A. Li. Preliminary results on the feasibility of using ultrasound to monitor intrafractional motion during radiation therapy for pancreatic cancer. *Medical physics*, 43(9):5252–5260, 2016.

[201] R. Onimaru, H. Shirato, M. Fujino, K. Suzuki, K. Yamazaki, M. Nishimura, H. Dosaka-Akita, and K. Miyasaka. The effect of tumor location and respiratory function on tumor movement estimated by real-time tracking radiotherapy (RTRT) system. *International Journal of Radiation Oncology* Biology* Physics*, 63(1):164–169, 2005.

[202] O. I. Onugha and J. M. Lee. Surgical Treatment of Lung Cancer. In K. L. Reckamp, editor, *Lung Cancer: Treatment and Research*, pages 77–104. Springer International Publishing, Cham, 2016.

[203] L. Osmani, F. Askin, E. Gabrielson, and Q. K. Li. Current WHO guidelines and the critical role of immunohistochemical markers in the subclassification of non-small cell lung carcinoma (NSCLC): Moving from targeted therapy to immunotherapy. In *Seminars in cancer biology*, volume 52, pages 103–109. Elsevier, 2018.

[204] E. Ozkan, C. Tanner, M. Kastelic, O. Mattausch, M. Makhinya, and O. Goksel. Robust motion tracking in liver from 2D ultrasound images using supporters. *International journal of computer assisted radiology and surgery*, 12(6):941–950, 2017.

[205] T. O'Shea, J. Bamber, D. Fontanarosa, S. van der Meer, F. Verhaegen, and E. Harris. Review of ultrasound image guidance in external beam radiotherapy part II: intra-fraction motion management and novel applications. *Physics in Medicine & Biology*, 61(8):R90, 2016.

[206] C. Paganelli, B. Whelan, M. Peroni, P. Summers, M. Fast, T. van de Lindt, J. McClelland, B. Eiben, P. Keall, T. Lomax, et al. MRI-guidance for motion management in external beam radiotherapy: current status and future challenges. *Physics in Medicine & Biology*, 63(22):22TR03, 2018.

[207] H. Paganetti. *Proton Beam Therapy*. 2399-2891. IOP Publishing, 2017.

[208] D. Palma, O. Visser, F. J. Lagerwaard, J. Belderbos, B. J. Slotman, and S. Senan. Impact of introducing stereotactic lung radiotherapy for elderly patients with stage I non–small-cell lung cancer: a population-based time-trend analysis. *Journal of clinical oncology*, 28(35):5153–5159, 2010.

[209] E. Pedroni, R. Bacher, H. Blattmann, T. Böhringer, A. Coray, A. Lomax, S. Lin, G. Munkel, S. Scheib, U. Schneider, et al. The 200-MeV proton therapy project at the Paul Scherrer Institute: Conceptual design and practical realization. *Medical physics*, 22(1):37–53, 1995.

[210] E. Pedroni, E. Egger, G. Munkel, T. Boehringer, B. Schaffner, H. Blattmann, A. Lomax, S. Lin, and A. Coray. Commissioning and Use of the PSI Spot-Scanning Isocentric System for Proton Therapy. 1996. Proceedings of the 14th International Conference on Cyclotrons and their Applications, Cape Town, South Africa.

[211] E. Pedroni, D. Meer, C. Bula, S. Safai, and S. Zenklusen. Pencil beam characteristics of the next-generation proton scanning gantry of PSI: design issues and initial commissioning results. *The European Physical Journal Plus*, 126(7):66, 2011.

[212] L. Petrusca, P. Cattin, V. De Luca, F. Preiswerk, Z. Celicanin, V. Auboiroux, M. Viallon, P. Arnold, F. Santini, S. Terraz, et al. Hybrid ultrasound/magnetic resonance simultaneous acquisition and image fusion for motion monitoring in the upper abdomen. *Investigative radiology*, 48(5):333–340, 2013.

[213] M. H. Phillips, E. Pedroni, H. Blattmann, T. Boehringer, A. Coray, and S. Scheib. Effects of respiratory motion on dose uniformity with a charged particle scanning method. *Physics in Medicine & Biology*, 37(1):223, 1992.

[214] C. Plathow, C. Fink, S. Ley, M. Puderbach, M. Eichinger, I. Zuna, A. Schmähl, and H.-U. Kauczor. Measurement of tumor diameter-dependent mobility of lung tumors by dynamic MRI. *Radiotherapy and oncology*, 73(3):349–354, 2004.

[215] P. R. Poulsen, B. Cho, D. Ruan, A. Sawant, and P. J. Keall. Dynamic multileaf collimator tracking of respiratory target motion based on a single kilovoltage imager during arc radiotherapy. *International Journal of Radiation Oncology* Biology* Physics*, 77(2):600–607, 2010.

[216] M. Prall, R. Kaderka, N. Saito, C. Graeff, C. Bert, M. Durante, K. Parodi, J. Schwaab, C. Sarti, and J. Jenne. Ion beam tracking using ultrasound motion detection. *Medical physics*, 41(4):041708, 2014.

[217] F. Preiswerk. *Modelling and reconstructing the respiratory motion of the liver*. PhD thesis, University of Basel, 2013.

[218] F. Preiswerk, C.-C. Cheng, J. Luo, and B. Madore. Synthesizing dynamic MRI using long-term recurrent convolutional networks. In *International Workshop on Machine Learning in Medical Imaging*, pages 89–97. Springer, 2018.

[219] F. Preiswerk, V. De Luca, P. Arnold, Z. Celicanin, L. Petrusca, C. Tanner, O. Bieri, R. Salomir, and P. C. Cattin. Model-guided respiratory organ motion prediction of the liver from 2D ultrasound. *Medical image analysis*, 18(5):740–751, 2014.

[220] F. Preiswerk, M. Toews, C.-C. Cheng, J.-y. G. Chiou, C.-S. Mei, L. F. Schaefer, W. S. Hoge, B. M. Schwartz, L. P. Panych, and B. Madore. Hybrid MRI-Ultrasound acquisitions, and scannerless real-time imaging. *Magnetic resonance in medicine*, 78(3):897–908, 2017.

[221] A. Protik, M. van Herk, M. Witte, and J.-J. Sonke. The impact of breathing amplitude on dose homogeneity in intensity modulated proton therapy. *Physics and Imaging in Radiation Oncology*, 3:11–16, 2017.

[222] J. A. Purdy. Current ICRU definitions of volumes: limitations and future directions. In *Seminars in radiation oncology*, volume 14, pages 27–40. Elsevier, 2004.

[223] B. Raaymakers, J. Lagendijk, J. Overweg, J. Kok, A. Raaijmakers, E. Kerkhof, R. Van der Put, I. Meijsing, S. Crijns, F. Benedosso, et al. Integrating a 1.5 T MRI scanner with a 6 MV accelerator: proof of concept. *Physics in Medicine & Biology*, 54(12):N229, 2009.

[224] J. E. Reiff. Internal Target Volume (ITV). In L. W. Brady and T. E. Yaeger, editors, *Encyclopedia of Radiation Oncology*, page 385. Springer Berlin Heidelberg, Berlin, Heidelberg, 2013.

[225] E. Rietzel and C. Bert. Respiratory motion management in particle therapy. *Medical physics*, 37(2):449–460, 2010.

[226] E. Rietzel and G. T. Chen. Deformable registration of 4D computed tomography data. *Medical physics*, 33(11):4423–4430, 2006.

[227] E.-J. Rijkhorst, D. Heanes, F. Odille, D. Hawkes, and D. Barratt. Simulating dynamic ultrasound using MR-derived motion models to assess respiratory synchronisation for image-guided liver interventions. In *International Conference on Information Processing in Computer-Assisted Interventions*, pages 113–123. Springer, 2010.

[228] J. Rodriguez-Canales, E. Parra-Cuentas, and I. I. Wistuba. Diagnosis and Molecular Classification of Lung Cancer. In K. L. Reckamp, editor, *Lung Cancer: Treatment and Research*, pages 25–46. Springer International Publishing, Cham, 2016.

[229] M. Rosu and G. D. Hugo. Advances in 4D radiation therapy for managing respiration: part II–4D treatment planning. *Zeitschrift für Medizinische Physik*, 22(4):272–280, 2012.

[230] J. M. Rubin, M. Feng, S. W. Hadley, J. B. Fowlkes, and J. D. Hamilton. Potential use of ultrasound speckle tracking for motion management during radiotherapy: preliminary report. *Journal of Ultrasound in Medicine*, 31(3):469–481, 2012.

[231] D. Rueckert, L. I. Sonoda, C. Hayes, D. L. Hill, M. O. Leach, and D. J. Hawkes. Non-rigid registration using free-form deformations: application to breast MR images. *IEEE transactions on medical imaging*, 18(8):712–721, 1999.

[232] D. E. Rumelhart, R. Durbin, R. Golden, and Y. Chauvin. Backpropagation: The basic theory. *Backpropagation: Theory, architectures and applications*, pages 1–34, 1995.

[233] S. Safai, C. Bula, D. Meer, and E. Pedroni. Improving the precision and performance of proton pencil beam scanning. *Translational Cancer Research*, 1(3), 2012.

[234] S. Sampath. Treatment: Radiation Therapy. In K. L. Reckamp, editor, *Lung Cancer: Treatment and Research*, pages 105–118. Springer International Publishing, Cham, 2016.

[235] R. Sandkühler, S. Andermatt, G. Bauman, S. Nyilas, C. Jud, and P. C. Cattin. Recurrent Registration Neural Networks for Deformable Image Registration. In *Advances in Neural Information Processing Systems*, pages 8755–8765, 2019.

[236] R. Sandkühler, C. Jud, S. Andermatt, and P. C. Cattin. AirLab: Autograd image registration laboratory. *arXiv preprint arXiv:1806.09907*, 2018.

[237] R. Sandkühler, C. Jud, S. Pezold, and P. C. Cattin. Adaptive graph diffusion regularisation for discontinuity preserving image registration. In *International Workshop on Biomedical Image Registration*, pages 24–34. Springer, 2018.

[238] A. Santiago, U. Jelen, F. Ammazzalorso, R. Engenhart-Cabillic, P. Fritz, W. Mühlnickel, W. Enghardt, M. Baumann, and A. Wittig. Reproducibility of target coverage in stereotactic spot scanning proton lung irradiation under high frequency jet ventilation. *Radiotherapy and Oncology*, 109(1):45–50, 2013.

[239] F. Santini, L. Gui, O. Lorton, P. C. Guillemin, G. Manasseh, M. Roth, O. Bieri, J.-P. Vallée, R. Salomir, and L. A. Crowe. Ultrasound-driven cardiac MRI. *Physica Medica*, 70:161–168, 2020.

[240] S. Sarudis, A. Karlsson Hauer, J. Nyman, and A. Bäck. Systematic evaluation of lung tumor motion using four-dimensional computed tomography. *Acta Oncologica*, 56(4):525–530, 2017.

[241] H. Sato, S. Toyooka, J. Soh, K. Hotta, K. Katsui, H. Yamamoto, S. Sugimoto, T. Oto, S. Kanazawa, K. Kiura, et al. The feasibility of median sternotomy with or without thoracotomy for locally advanced non-small cell lung cancer treated with induction chemoradiotherapy. *The Annals of thoracic surgery*, 102(3):985–992, 2016.

[242] A. Schätti, D. Meer, and A. Lomax. First experimental results of motion mitigation by continuous line scanning of protons. *Physics in Medicine & Biology*, 59(19):5707, 2014.

[243] A. Schätti, M. Zakova, D. Meer, and A. Lomax. Experimental verification of motion mitigation of discrete proton spot scanning by re-scanning. *Physics in Medicine & Biology*, 58(23):8555, 2013.

[244] A. Schätti, M. Zakova, D. Meer, and A. Lomax. The effectiveness of combined gating and re-scanning for treating mobile targets with proton spot scanning. An experimental and simulation-based investigation. *Physics in Medicine & Biology*, 59(14):3813, 2014.

[245] S. M. Schellhammer, A. L. Hoffmann, S. Gantz, J. Smeets, E. van der Kraaij, S. Quets, S. Pieck, L. Karsch, and J. Pawelke. Integrating a low-field open MR scanner with a static proton research beam line: proof of concept. *Physics in Medicine & Biology*, 63(23):23LT01, 2018.

[246] J. M. Schippers and A. J. Lomax. Emerging technologies in proton therapy. *Acta Oncologica*, 50(6):838–850, 2011.

[247] D. Schmitt, S. Nill, F. Roeder, D. Gompelmann, F. Herth, and U. Oelfke. Motion monitoring during a course of lung radiotherapy with anchored electromagnetic transponders. *Strahlentherapie und Onkologie*, 193(10):840–847, 2017.

[248] J. Schwaab, M. Prall, C. Sarti, R. Kaderka, C. Bert, C. Kurz, K. Parodi, M. Günther, and J. Jenne. Ultrasound tracking for intra-fractional motion compensation in radiation therapy. *Physica Medica*, 30(5):578–582, 2014.

[249] M. Schwarz, G. M. Cattaneo, and L. Marrazzo. Geometrical and dosimetrical uncertainties in hypofractionated radiotherapy of the lung: a review. *Physica medica*, 36:126–139, 2017.

[250] S. Senan, M. A. Paul, and F. J. Lagerwaard. Treatment of early-stage lung cancer detected by screening: surgery or stereotactic ablative radiotherapy? *The Lancet Oncology*, 14(7):e270–e274, 2013.

[251] Y. Seppenwoolde, R. I. Berbeco, S. Nishioka, H. Shirato, and B. Heijmen. Accuracy of tumor motion compensation algorithm from a robotic respiratory tracking system: a simulation study. *Medical physics*, 34(7):2774–2784, 2007.

[252] Y. Seppenwoolde, H. Shirato, K. Kitamura, S. Shimizu, M. Van Herk, J. V. Lebesque, and K. Miyasaka. Precise and real-time measurement of 3D tumor motion in lung due to breathing and heartbeat, measured during radiotherapy. *International Journal of Radiation Oncology* Biology* Physics*, 53(4):822–834, 2002.

[253] S. Shimizu, N. Miyamoto, T. Matsuura, Y. Fujii, M. Umezawa, K. Umegaki, K. Hiramoto, and H. Shirato. A proton beam therapy system dedicated to spot-scanning increases accuracy with moving tumors by real-time imaging and gating and reduces equipment size. *PloS one*, 9(4), 2014.

[254] A. M. Shinde and A. Dashti. Palliative Care in Lung Cancer. In K. L. Reckamp, editor, *Lung Cancer: Treatment and Research*, pages 225–250. Springer International Publishing, Cham, 2016.

[255] H. Shirato, Y. Seppenwoolde, K. Kitamura, R. Onimura, and S. Shimizu. Intrafractional tumor motion: lung and liver. In *Seminars in radiation oncology*, volume 14, pages 10–18. Elsevier, 2004.

[256] D. S. K. Sihono, L. Vogel, C. Weiß, J. Thölking, F. Wenz, F. Lohr, J. Boda-Heggemann, and H. Wertz. A 4D ultrasound real-time tracking system for external beam radiotherapy of upper abdominal lesions under breath-hold. *Strahlentherapie und Onkologie*, 193(3):213–220, 2017.

[257] C. Silva, D. Mateus, M. Eiras, and S. Vieira. Calypso® 4D localization system: a review. *Journal of Radiotherapy in Practice*, 13(4):473–483, 2014.

[258] J. Skowronek. Brachytherapy in the treatment of lung cancer–a valuable solution. *Journal of contemporary brachytherapy*, 7(4):297, 2015.

[259] F. Soldà, M. Lodge, S. Ashley, A. Whitington, P. Goldstraw, and M. Brada. Stereotactic radiotherapy (SABR) for the treatment of primary non-small cell lung cancer; Systematic review and comparison with a surgical cohort. *Radiotherapy and Oncology*, 109(1):1–7, 2013.

[260] J.-J. Sonke and J. Belderbos. Adaptive Radiotherapy for Lung Cancer. *Seminars in Radiation Oncology*, 20(2):94–106, 2010. Adaptive Radiotherapy.

[261] J.-J. Sonke, J. Lebesque, and M. Van Herk. Variability of four-dimensional computed tomography patient models. *International Journal of Radiation Oncology* Biology* Physics*, 70(2):590–598, 2008.

[262] A. Sotiras, C. Davatzikos, and N. Paragios. Deformable medical image registration: A survey. *IEEE transactions on medical imaging*, 32(7):1153–1190, 2013.

[263] B. Stemkens, E. S. Paulson, and R. H. Tijssen. Nuts and bolts of 4D-MRI for radiotherapy. *Physics in Medicine & Biology*, 63(21):21TR01, 2018.

[264] B. Stemkens, R. H. Tijssen, B. D. de Senneville, H. D. Heerkens, M. Van Vulpen, J. J. Lagendijk, and C. A. van den Berg. Optimizing 4-dimensional magnetic resonance imaging data sampling for respiratory motion analysis of pancreatic tumors. *International Journal of Radiation Oncology* Biology* Physics*, 91(3):571–578, 2015.

[265] B. Stemkens, R. H. Tijssen, B. D. De Senneville, J. J. Lagendijk, and C. A. Van Den Berg. Image-driven, model-based 3D abdominal motion estimation for MR-guided radiotherapy. *Physics in Medicine & Biology*, 61(14):5335, 2016.

[266] A. Stewart, B. Parashar, M. Patel, D. O'Farrell, M. Biagioli, P. Devlin, and S. Mutyala. American Brachytherapy Society consensus guidelines for thoracic brachytherapy for lung cancer. *Brachytherapy*, 15(1):1–11, 2016.

[267] T. E. Stinchcombe. Targeted Therapies for Lung Cancer. In K. L. Reckamp, editor, *Lung Cancer: Treatment and Research*, pages 165–182. Springer International Publishing, Cham, 2016.

[268] S. Takao, N. Miyamoto, T. Matsuura, R. Onimaru, N. Katoh, T. Inoue, K. L. Sutherland, R. Suzuki, H. Shirato, and S. Shimizu. Intrafractional baseline shift or drift of lung tumor motion during gated radiation therapy with a real-time tumor-tracking system. *International Journal of Radiation Oncology* Biology* Physics*, 94(1):172–180, 2016.

[269] M. Tashiro, T. Ishii, J.-i. Koya, R. Okada, Y. Kurosawa, K. Arai, S. Abe, Y. Ohashi, H. Shimada, K. Yusa, et al. Technical approach to individualized respiratory-gated carbon-ion therapy for mobile organs. *Radiological physics and technology*, 6(2):356–366, 2013.

[270] N. L. S. T. R. Team. Reduced lung-cancer mortality with low-dose computed tomographic screening. *New England Journal of Medicine*, 365(5):395–409, 2011.

[271] R. H. Tijssen, M. E. Philippens, E. S. Paulson, M. Glitzner, B. Chugh, A. Wetscherek, M. Dubec, J. Wang, and U. A. van der Heide. MRI commissioning of 1.5 T MR-linac systems–a multi-institutional study. *Radiotherapy and Oncology*, 132:114–120, 2019.

[272] R. Timmerman, R. Paulus, J. Galvin, J. Michalski, W. Straube, J. Bradley, A. Fakiris, A. Bezjak, G. Videtic, D. Johnstone, et al. Stereotactic body radiation therapy for inoperable early stage lung cancer. *Jama*, 303(11):1070–1076, 2010.

[273] A. Torshabi, A. Pella, M. Riboldi, and G. Baroni. Targeting accuracy in real-time tumor tracking via external surrogates: a comparative study. *Technology in cancer research & treatment*, 9(6):551–561, 2010.

[274] E. Tran, B. Eiben, A. Wetscherek, U. Oelfke, G. Meedt, D. Hawkes, and J. McClelland. Respiratory motion models built using MR-derived signals and different amounts of MR image data from multi-slice acquisitions. ICCR, 2019.

[275] S. H. Tretbar, H. J. Hewener, D. Speicher, T. Barthscherer, A. Bongers, J. W. Jenne, and M. Günther. MR-compatible ultrasound research platform for motion tracking to reduce motion induced artifacts in MR imaging. In *2013 IEEE International Ultrasonics Symposium (IUS)*, pages 553–556. IEEE, 2013.

[276] P. Trnková, B. Knäusl, O. Actis, C. Bert, A. K. Biegun, T. T. Boehlen, H. Furtado, J. McClelland, S. Mori, I. Rinaldi, et al. Clinical implementations of 4D pencil beam scanned particle therapy: report on the 4D treatment planning workshop 2016 and 2017. *Physica Medica*, 54:121–130, 2018.

[277] E. Tryggestad, A. Flammang, S. Han-Oh, R. Hales, J. Herman, T. McNutt, T. Roland, S. M. Shea, and J. Wong. Respiration-based sorting of dynamic MRI to derive representative 4D-MRI for radiotherapy planning. *Medical physics*, 40(5):051909, 2013.

[278] S. Van de Water, R. Kreuger, S. Zenklusen, E. Hug, and A. J. Lomax. Tumour tracking with scanned proton beams: assessing the accuracy and practicalities. *Physics in Medicine & Biology*, 54(21):6549, 2009.

[279] N. C. van der Voort van Zyp, J.-B. Prévost, M. S. Hoogeman, J. Praag, B. van der Holt, P. C. Levendag, R. J. van Klaveren, P. Pattynama, and J. J. Nuyttens. Stereotactic radiotherapy with real-time tumor tracking for non-small cell lung cancer: Clinical outcome. *Radiotherapy and Oncology*, 91(3):296–300, 2009.

[280] P. E. Van Schil and J. Van Meerbeeck. Surgery or radiotherapy for early-stage lung cancer – a potential comparison bias. *The Lancet Oncology*, 14(10):e390, 2013.

[281] S. Vedam, P. Keall, V. Kini, and R. Mohan. Determining parameters for respiration-gated radiotherapy. *Medical physics*, 28(10):2139–2146, 2001.

[282] S. Vijayan, S. Klein, E. F. Hofstad, F. Lindseth, B. Ystgaard, and T. Langö. Validation of a non-rigid registration method for motion compensation in 4D ultrasound of the liver. In *2013 IEEE 10th international symposium on biomedical imaging*, pages 792–795. IEEE, 2013.

[283] V. Vishnevskiy, T. Gass, G. Szekely, C. Tanner, and O. Goksel. Isotropic total variation regularization of displacements in parametric image registration. *IEEE transactions on medical imaging*, 36(2):385–395, 2016.

[284] L. Vogel, D. S. K. Sihono, C. Weiss, F. Lohr, F. Stieler, H. Wertz, S. von Swietochowski, A. Simeonova-Chergou, F. Wenz, M. Blessing, et al. Intra-breath-hold residual motion of image-guided DIBH liver-SBRT: an estimation by ultrasound-based monitoring correlated with diaphragm position in CBCT. *Radiotherapy and Oncology*, 129(3):441–448, 2018.

[285] M. von Siebenthal, G. Székely, U. Gamper, P. Boesiger, A. Lomax, and P. Cattin. 4D MR imaging of respiratory organ motion and its variability. *Physics in Medicine & Biology*, 52(6):1547, 2007.

[286] M. von Siebenthal, G. Székely, A. J. Lomax, and P. C. Cattin. Systematic errors in respiratory gating due to intrafraction deformations of the liver. *Medical physics*, 34(9):3620–3629, 2007.

[287] A. M. Walling, J. C. Weeks, K. L. Kahn, D. Tisnado, N. L. Keating, S. M. Dy, N. K. Arora, J. W. Mack, P. M. Pantoja, and J. L. Malin. Symptom prevalence in lung and colorectal cancer patients. *Journal of pain and symptom management*, 49(2):192–202, 2015.

[288] S. Webb. *Intensity-modulated radiation therapy*. CRC Press, 2015.

[289] C. P. Wild, E. Weiderpass, and B. W. Stewart, editors. *World Cancer Report: Cancer Research for Cancer Prevention*. Lyon, France: International Agency for Research on Cancer, 2020. Available from: http://publications.iarc.fr/586.

[290] C. K. Williams and C. E. Rasmussen. *Gaussian processes for machine learning*, volume 2. MIT press Cambridge, MA, 2006.

[291] T. Willoughby, J. Lehmann, J. A. Bencomo, S. K. Jani, L. Santanam, A. Sethi, T. D. Solberg, W. A. Tomé, and T. J. Waldron. Quality assurance for nonradiographic radiotherapy localization and positioning systems: report of Task Group 147. *Medical physics*, 39(4):1728–1747, 2012.

[292] R. R. Wilson. Radiological use of fast protons. *Radiology*, 47(5):487–491, 1946.

[293] J. P. Wisnivesky, C. I. Henschke, S. Swanson, D. F. Yankelevitz, J. Zulueta, S. Marcus, and E. A. Halm. Limited resection for the treatment of patients with stage IA lung cancer. *Annals of surgery*, 251(3):550–554, 2010.

[294] G. A. Woodard, K. D. Jones, and D. M. Jablons. Lung Cancer Staging and Prognosis. In K. L. Reckamp, editor, *Lung Cancer: Treatment and Research*, pages 47–75. Springer International Publishing, Cham, 2016.

[295] World Health Organization. Burning opportunity: clean household energy for health, sustainable development, and wellbeing of women and children. 2016. Available form: https://www.who.int/airpollution/publications/burning-opportunities/en/.

[296] T. Yamamoto, U. Langner, B. W. Loo Jr, J. Shen, and P. J. Keall. Retrospective analysis of artifacts in four-dimensional CT images of 50 abdominal and thoracic radiotherapy patients. *International Journal of Radiation Oncology* Biology* Physics*, 72(4):1250–1258, 2008.

[297] S. S. Yom, Z. Liao, H. H. Liu, S. L. Tucker, C.-S. Hu, X. Wei, X. Wang, S. Wang, R. Mohan, J. D. Cox, et al. Initial evaluation of treatment-related pneumonitis in advanced-stage non–small-cell lung cancer patients treated with concurrent chemotherapy and intensity-modulated radiotherapy. *International Journal of Radiation Oncology* Biology* Physics*, 68(1):94–102, 2007.

[298] S. Zenklusen, E. Pedroni, and D. Meer. A study on repainting strategies for treating moderately moving targets with proton pencil beam scanning at the new Gantry 2 at PSI. *Physics in Medicine & Biology*, 55(17):5103, 2010.

[299] T. Zhang, H. Keller, M. J. O'Brien, T. R. Mackie, and B. Paliwal. Application of the spirometer in respiratory gated radiotherapy. *Medical physics*, 30(12):3165–3171, 2003.

[300] X. Zhang, M. Günther, and A. Bongers. Real-time organ tracking in ultrasound imaging using active contours and conditional density propagation. In *International Workshop on Medical Imaging and Virtual Reality*, pages 286–294. Springer, 2010.

[301] X. Zhang, Y. Li, X. Pan, L. Xiaoqiang, R. Mohan, R. Komaki, J. D. Cox, and J. Y. Chang. Intensity-modulated proton therapy reduces the dose to normal tissue compared with intensity-modulated radiation therapy or passive scattering proton therapy and enables individualized radical radiotherapy for extensive stage IIIB non-small-cell lung cancer: a virtual clinical study. *International Journal of Radiation Oncology* Biology* Physics*, 77(2):357–366, 2010.

[302] Y. Zhang, I. Huth, M. Wegner, D. C. Weber, and A. J. Lomax. Surface as a motion surrogate for gated re-scanned pencil beam proton therapy. *Physics in Medicine & Biology*, 62(10):4046, 2017.

[303] Y. Zhang, A. Knopf, C. Tanner, D. Boye, and A. J. Lomax. Deformable motion reconstruction for scanned proton beam therapy using on-line x-ray imaging. *Physics in Medicine & Biology*, 58(24):8621, 2013.

[304] Y. Zhang, A. Knopf, C. Tanner, and A. Lomax. Online image guided tumour tracking with scanned proton beams: a comprehensive simulation study. *Physics in Medicine & Biology*, 59(24):7793, 2014.

[305] Y. Zhang, A.-C. Knopf, D. C. Weber, and A. J. Lomax. Improving 4D plan quality for PBS-based liver tumour treatments by combining online image guided beam gating with rescanning. *Physics in Medicine & Biology*, 60(20):8141, 2015.

[306] S. Zhi, M. Kachelrieß, and X. Mou. High-quality Initial Image-guided 4D CBCT Reconstruction. *Medical Physics*, 2020.

Curriculum Vitae

Alina Giger

Curriculum Vitae

Education

Since 04.2016	**PhD in Biomedical Engineering** Department of Biomedical Engineering, University of Basel Supervisor: Prof. Dr. Philippe C. Cattin Topic: *Ultrasound-based motion modelling for the lungs in scanned proton therapy*
09.2013–06.2016	**MSc in Robotics, Systems and Control**, ETH Zurich Master's thesis: *Breathing Motion Compensation for the Laser Osteotome*
09.2010–09.2013	**BSc in Mechanical Engineering**, ETH Zurich Bachelor's thesis: *Control and evaluation of the pneumatic system of the Robotic Sensory Trainer*

Referees

	Prof. Dr. Philippe C. Cattin Head of Department of Biomedical Engineering Gewerbestrasse 14 4123 Allschwil, Switzerland
phone	+41 61 207 54 00
e-mail	philippe.cattin@unibas.ch
	Prof. Dr. Antony J. Lomax Center for Proton Therapy, Paul Scherrer Institute 5232 Villigen PSI West, Switzerland
phone	+41 56 310 35 23
e-mail	tony.lomax@psi.ch

List of Publications

2020

M. Krieger, **A. Giger**, C. Jud, A. Duetschler, R. Salomir, O. Bieri, G. Bauman, D. Nguyen, P. C. Cattin, D. C. Weber, A. J. Lomax, and Y. Zhang. Liver-ultrasound-guided lung tumour tracking for scanned proton therapy, 2020. *Under review in Physics in Medicine & Biology*

A. Giger, M. Krieger, C. Jud, A. Duetschler, R. Salomir, O. Bieri, G. Bauman, D. Nguyen, D. C. Weber, A. J. Lomax, Y. Zhang, and P. C. Cattin. Liver-ultrasound based motion modelling to estimate 4D dose distributions for lung tumours in scanned proton therapy, 2020. *Under review in Physics in Medicine & Biology*

O. A. Pusterla, F. Santini, G. Bauman, R. Heule, **A. Giger**, Ph. C. Cattin, S. Safai, S. Kozerke, and O. Bieri. 4D-MRI of Thorax and Abdomen with Variable Contrast at 1.5T. In *Proceedings of the ISMRM 28th Annual Meeting and Exhibition*, 2020

M. Krieger, **A. Giger**, R. Salomir, O. Bieri, Z. Celicanin, Ph. C. Cattin, A. J. Lomax, D. C. Weber, and Y. Zhang. Impact of internal target volume definition for pencil beam scanned proton treatment planning in the presence of respiratory motion variability for lung cancer: A proof of concept. *Radiotherapy and oncology*, 145:154–161, 2020

2019

A. Giger, C. Jud, D. Nguyen, M. Krieger, Y. Zhang, A. J. Lomax, O. Bieri, R. Salomir, and Ph. C. Cattin. Inter-fractional Respiratory Motion Modelling from Abdominal Ultrasound: A Feasibility Study. In *International Workshop on PRedictive Intelligence In MEdicine*, pages 11–22. Springer, 2019

M. Krieger, **A. Giger**, D. C. Weber, A. J. Lomax, and Y. Zhang. Consequences of respiratory motion variability in lung 4DMRI datasets. In *Radiotherapy and Oncology*, volume 133, pages 219–220. Elsevier, 2019

T. Ronchetti, C. Jud, P. M. Maloca, S. Orgül, **A. Giger**, C. Meier, H. P. Scholl, R. K. M. Chun, Q. Liu, C.-H. To, et al. Statistical framework for validation without ground truth of choroidal thickness changes detection. *PloS one*, 14(6):e0218776, 2019

2018 **A. Giger**, M. Stadelmann, F. Preiswerk, C. Jud, V. De Luca, Z. Celicanin, O. Bieri, R. Salomir, and Ph. C. Cattin. Ultrasound-driven 4D MRI. *Physics in Medicine & Biology*, 2018

A. Giger, R. Sandkühler, C. Jud, G. Bauman, O. Bieri, R. Salomir, and Ph. C. Cattin. Respiratory Motion Modelling using cGANs. In *International Conference on Medical Image Computing and Computer-Assisted Intervention*. Springer, 2018

C. Jud, D. Nguyen, R. Sandkuehler, **A. Giger**, O. Bieri, and Ph. C. Cattin. Motion Aware MR Imaging via Spatial Core Correspondence. In *International Conference on Medical Image Computing and Computer-Assisted Intervention*. Springer, 2018

2017 **A. Giger**, C. Jud, and Ph. C. Cattin. Respiratory motion compensation for the robot-guided laser osteotome. *International Journal of Computer Assisted Radiology and Surgery*, pages 1–12, 2017

C. Jud, **A. Giger**, R. Sandkühler, and Ph. C. Cattin. A Localized Statistical Motion Model as a Reproducing Kernel for Non-rigid Image Registration. In *International Conference on Medical Image Computing and Computer-Assisted Intervention*, pages 261–269. Springer, 2017

Z. Celicanin, **A. Giger**, G. Bauman, Ph. C. Cattin, and O. Bieri. Temporally-resolved volumetric imaging (4DMRI) of the lungs. In *Proceedings of the ISMRM 25th Annual Meeting and Exhibition*, 2017

Awards

2019 2nd prize at the ICCR Rising Stars Competition

International Conference on the Use of Computers in Radiation Therapy (ICCR), Montreal, Canada